Delft University of Technology

Fluorescent Nuclear Track Detectors for Alpha Particle Measurement

Kouwenberg, Jasper

Important note
To cite this publication, please use the final published version (if applicable).
Please check the document version above.

Fluorescent Nuclear Track Detectors for Alpha Particle Measurement

PROEFSCHRIFT

ter verkrijging van de graad van doctor
aan de Technische Universiteit Delft
op gezag van Rector Magnificus
Prof. dr.ir. T.H.J.J. van der Hagen,
voorzitter van het College voor Promoties,
in het openbaar te verdedigen op
5 juli 2018, 15:00

door

Jasper Johannes Marcellianus KOUWENBERG
Ingenieur in Biomedical Engineering, Technische Universiteit Delft, Nederland
geboren te Voorburg, Nederland

PROMOTIECOMMISSIE

Dit proefschrift is goedgekeurd door de promotor en copromotoren.

Samenstelling promotiecommissie bestaat uit:

Rector magnificus,	voorzitter
Prof. dr. H. Th. Wolterbeek	TU Delft, promotor
Dr. ir. A. G. Denkova	TU Delft, copromotor
Dr. A. J. J. Bos	TU Delft, copromotor

Onafhankelijke leden:

|	
Prof. dr. Pieter Doorenbos	TU Delft
Prof. dr. ir. Harry van der Graaf	TU Delft
Prof. dr. Adriaan Houtsmuller	Erasmus MC
Prof. dr. Brigitte Reniers	Universiteit Hasselt (België)

Printed in the Netherlands.

By Randall Munroe. Source: https://xkcd.com/931/

TABLE OF CONTENTS

Chapter 1

Introduction

METASTATIC CANCER

Increased life expectancies and better treatments for (mainly) infectious and coronary disease have led to cancer becoming one of the most common causes of death in the Netherlands. Incidence has risen to approximately 100.000 new cases per year, causing almost 45.000 deaths yearly in the Netherlands (de Nederlandse Kankerregistratie, 2015). Less visible to the public is the average survival chance 5 years after diagnosis, which has increased significantly from 38% in 1980 to 64% in 2011. These improvements can be attributed to more knowledge, better detection and diagnosis, and improved treatment methodologies developed by the scientific community. A reason for the still prevalent cancer mortality in modern times is expressed superbly in the illustration on page 3 (*https://xkcd.com/931/*). One of the distinct characteristic of malignant tumors (cancer) is the lack of respect for anatomical borders. Cancerous tumors grow uncontrollably; penetrating blood vessels and other parts of the organ of origin. When cells break off the main growth, they can settle in other parts of the body, forming metastases (small 'new' tumors). While the main growth is often detectable and treatable using radiotherapy or surgery, the survival probability decreases rapidly once metastases have formed. Metastases are often too small to detect using conventional imaging techniques (X-ray, CT, PET, SPECT), and patients therefore can undergo chemotherapy, hormone therapy, external beam radiation therapy, or a combination of these, as an attempt to combat these metastases, even after removal of the primary tumor mass (Chia et al., 2007; Rusthoven et al., 2009). These treatments are however only occasionally effective. Moreover, chemotherapy, the most common form of treatment, has significant side effects due to atrophy in fast differentiating tissues (Chabner and Roberts, 2005). One alternative approach to deal with these metastases is injection of radionuclides (radioactive atoms) attached to some targeting agent in the bloodstream. The targeting agent circulates through the body and delivers the radionuclides to metastases automatically, potentially circumventing the detection and manual targeting issue, while the targeting prevents (severe) normal tissue complications caused by chemotherapy (Elgqvist et al., 2014; Miederer et al., 2008; Sgouros et al., 2010). During the last 10 years, Dr. ir. A. G. Denkova has led the effort to use polymersomes, small artificial vesicles, to carry and retain the alpha emitting radioisotope actinium-225 and its daughters (Chapter 7). The polymersomes can be used to deliver the actinium isotopes to metastases, yielding a large absorbed dose within the cancerous cells, while minimizing the negative effects in healthy tissue.

ALPHA RADIATION

Being the most energetic of the four forms of natural radioactive decay, alpha radiation, consisting of a helium atom stripped of its electrons, deposits large quantities of energy in very small volumes. Alpha radiation is very 'bulky' compared to beta (electron), gamma (photon)

and neutron radiation, yielding up to a 1000 fold larger loss per traversed distance (linear energy transfer, LET) than beta radiation, as well as having a very short range in matter (Ziegler, 2010). For example, most alpha radiation will have lost all its kinetic energy within 10 cm of air or 0.1 mm of water. It is therefore unable to penetrate the skin, but can nevertheless be very dangerous when it originates within the body. The large LET means that particles create a wake of dense ionizations in matter. When cellular DNA is exposed to such high concentrations of ionizations, the DNA becomes damaged, often leading to aggregations of damage too complex to repair for the cell, thereby killing the cell effectively (Antonelli et al., 2015; Hu et al., 2005). Research has shown that this effect can lead to a 10 fold increase in lethality between gamma and alpha radiation (Tracy et al., 2015). This high lethality combined with the short range, makes alpha emitting radioisotopes a promising candidate for the treatment of metastases. The high lethality ensures effective killing of the growths, while the short range of the alpha particles will help spare the healthy tissue. Research on the application of alpha radiation for the treatment of cancer spans (radio) chemistry, radiobiology, alpha spectroscopy, (micro-) dosimetry and (pre-) clinical studies. (radio) chemistry is involved with the design of molecular, antibody and nanoparticle carriers for alpha emitting radioisotopes. Radiobiology focuses on the effects of alpha radiation on cells, and looks, for example, at the damage induced by alpha radiation in DNA and tries to describe the factors involved in the high lethality of this type of radiation. Accurate alpha radiobiology relies for a large part on the alpha spectroscopy and (micro-) dosimetry. These primarily physics-based fields work on the development of experimental and mathematical tools for the measurement or prediction of various physical quantities of alpha radiation (fields) in-vivo and in-vitro. Alpha spectroscopy is involved with the measurement of quantities, including the energy and trajectory vector, of an alpha radiation field. Alpha dosimetry measures the absorbed dose, a measure for the amount of energy deposited in a certain mass, by alpha radiation. Since the absorbed dose and particle energy spectrum are often the fundamental quantities used for the quantification of cell survival, DNA damage and other biological factors, precise alpha spectroscopy and dosimetry is paramount of alpha radiation research (Sgouros et al., 2010). Alpha microdosimetry attempts to measure or predict doses induced by alpha radiation in very small volumes (e.g. cell nuclei). Especially the application of this field in radiobiology is relatively new and researchers attempt to use the microdosimetry-related quantities to better explain the biological effects seen with alpha radiation (Sato and Furusawa, 2012; Van Den Heuvel, 2014). Advances in these fields are partly hampered by the lack of accurate and diverse tools for alpha radiation spectroscopy, dosimetry and microdosimetry.

ALPHA RADIATION MEASUREMENT

The short range of this radiation makes it hard to measure, since alpha particles cannot penetrate the outer walls of most radiation measurement tools. Numerous techniques are however available for detection, spectroscopy and dosimetry of alpha radiation.

The most commonly found commercial alpha spectrometers are silicon-based semiconducting detectors. When the fluence is low and individual alpha particles can be distinguished within the semiconductor detector, the charge created by the alpha particle inside the semiconducting material can be used to measure the energy of individual particles. These detectors boast substantial some advantages, allowing for sub-millimeter measurement volumes while maintaining a good energy resolution (Chaudhuri et al., 2013; Wang et al., 2012). Plastic nuclear track detectors (PNTD), like the polymer plastic CR-39, are commonly used to visualize individual alpha particles. PNTDs utilize chemical changes induced by passing ionizing particles inside the detector. After irradiation, the detector is submersed in a chemical solution that breaks down the polymer at a fixed rate. Chemical alterations induced by ionizing particles accelerate this process, creating holes in the detector where ionizing particles passed through it. CR-39 detectors have been used extensively in alpha radiation spectroscopy and dosimetry (Wertheim et al., 2010). The required chemical processing, limited resolution, poor energy resolution, small dose range, lack of reusability and inability to work with living matter (living cells) has hampered the widespread adoption of this technique for alpha radiation measurement, especially in radiobiology. A notable recent development is the so-called alpha camera, which uses a CCD camera behind a scintillator, a material that locally produces visible light when interacting with an ionizing particle, to map the concentration of alpha-emitting radionuclides in slices of tissue (Back and Jacobsson, 2010).

The field of alpha radiation dosimetry is diverse, including, but no limited to, optically stimulated luminescence dosimeter (OSLD), radiochromic film, ionization chambers and, as mentioned, PNTD. Ionization chambers utilize the charge created in gas by passing ionizing particles to count particles and measure the absorbed dose inside the gas chamber. Most commercially available ionization chambers are however not very effective for alpha radiation dosimetry. In addition to the wall thickness of most ionization chambers, does the high ionization density of alpha particles introduce non-linear effects in the charge produced per unit of deposited energy (Böhm, 1976). A special ionization chamber called the extrapolation chamber uses an adjustable gas chamber volume and an adjustable electric potential across the chamber to identify these non-linear effects, allowing for very precise alpha radiation dosimetry (Böhm et al., 1991). Extrapolation chambers are however rare, expensive and large, making them inaccessible for most researchers. OSLD and thermoluminescence dosimeters (TLD) are very popular for personnel dosimetry, delivering a broad dose range and ease-of-use at a relatively low cost. However, both OSLD and TLD are limited in their ability to

distinguish particle charge and energy and require extensive calibration (Akselrod, 2011; Oster et al., 2010). These detectors are therefore not often used for alpha dosimetry. Lastly, radiochromic film is commonly applied because it is relatively easy to use. Similar to PNTD does radiochromic film utilize chemical changes in the detector, yielding a change of color of the film following irradiation. Often being self-developing, the user only needs to image to film after irradiation using a conventional scanner. While change in color of the film can be correlated to absorbed dose, it has been shown that this process is very sensitive to LET and angle of incidence of the particles (Aydarous and Ghazaly, 2013), making absolute (alpha) radiation dosimetry unfeasible. It nevertheless remains a popular tool for field homogeneity verification.

While the mentioned technologies do not cover the whole fields of alpha radiation spectroscopy and dosimetry, it can be concluded that, as of yet, no single method exist that simultaneously offers a high spatial and energy resolution, ease-of-use, reusability and a bio-compatible surface.

FLUORESCENT NUCLEAR TRACK DETECTOR

The fluorescent nuclear track detectors (FNTD) is a novel type of track detectors that allow for individual particle track visualization at a sub-100 nm scale. These detectors, introduced by M. Akselrod et al. in 2006 (M. S. Akselrod et al., 2006), consist of an aluminum oxide crystal (sapphire) with carbon and magnesium defects. These defects form so-called color centers that capture ionized electrons liberated by passing ionizing particles to undergo radiochromic transformations. FNTDs can therefore be read-out after irradiation using fluorescence microscopy, most commonly using a confocal laser scanning microscopy, to yield 3D images of the tracks stored within the crystal. Due to the wide optical energy gap of aluminum oxide (9.5 eV), storage of the captured electrons is stable, allowing the detectors to be read-out multiple times and up to years after irradiation. While FNTDs have been used extensively for proton, heavy ion and gamma spectroscopy and dosimetry, studies using alpha radiation are almost non-existent. The penetration of alpha particles in FNTDs is low at sub-10 micrometer, but sufficient for imaging using the mentioned microscopy technique. The combination of high resolution, affordability, reusability, versatility and size make these detectors to be prime candidates for alpha spectroscopy, dosimetry and even microdosimetry and radiobiology. FNTDs are discussed in detail in chapter 2.

THESIS OVERVIEW

Alpha radionuclide therapy has great potential for the treatment of metastases, but requires maturation before it can be applied safely and successfully in the clinic. As mentioned, current research efforts lack proper tools for alpha radiation spectroscopy, (micro-)dosimetry and

radiobiology. FNTDs have proven to excel in these areas for proton and heavy ion (accelerator) therapy, but their potential for alpha radiation is yet untouched. This thesis attempts to build and validate methods to make FNTDs a 4 in 1 tool for alpha spectroscopy, dosimetry, microdosimetry and radiobiology. Additionally, based on publicly available pharmacokinetic data for previously publishes alpha radionuclide carriers, the pros and cons of various carriers are identified.

To summarize:

Chapter 2 gives a detailed overview of the properties and the applications of FNTDs in radiation science. The production of FNTDs, formation and analysis of tracks, spectroscopy and dosimetry of ion and gamma radiation and applications in radiobiology are covered.

Chapter 3 introduces a new algorithm for the reconstruction of measured ion tracks in FNTDs. Since most high-resolution fluorescence microscopy techniques produce series of 2D images of the fluorescence at various depth in the crystal, reconstruction of the fluorescence in the 2D images was required to obtain the 3D tracks.

Chapter 4 describes the methods developed to use FNTDs together with the algorithm shown in chapter 3 to measure various quantities, including energy, of individual alpha tracks. This chapter also shows the first application of structured illumination microscopy, a fast super-resolution fluorescence microscopy technique, for FNTDs.

Chapter 5 builds upon chapter 3 and 4 and uses the individual tracks to shows the potential of FNTDs for alpha dosimetry. A novel alpha irradiation setup is introduced for future radiobiology research. Dose rate measurements of the setup were performed using both FNTDs and an extrapolation chamber for validation of the proposed FNTD dosimetry methods.

Chapter 6 combines theory and practice of alpha microdosimetry. A novel experimental alpha microdosimetry method for cell monolayer is proposed using the setup mentioned in chapter 5, the individual alpha track measured in chapter 4 and a cancer cell line (U87). The results of this one-of-a-kind method are used together with simulation of alpha radiation in models for micro-tumors or metastases (spheroids) to quantify the effects of localized energy deposition of alpha particles on the survival of cells.

Chapter 7 attempts to model the pharmacokinetics and dosimetry of various types of alpha radionuclide carriers and free daughter radionuclides, in order to evaluate the effects of carrier internalization, recoil retention and circulation time.

REFERENCES

Akselrod, M.S., Yoder, R.C., Akselrod, G.M., 2006. Confocal fluorescent imaging of tracks from heavy charged particles utilising new Al2O3:C,Mg crystals. *Radiat. Prot. Dosimetry* 119(1–4), 357–362. https://doi.org/10.1093/rpd/nci664

Akselrod, M.S., 2011. Fundamentals of materials, techniques, and instrumentation for OSL and FNTD dosimetry. *AIP Conf. Proc.* 1345(2011), 274–302. https://doi.org/10.1063/1.3576173

Antonelli, F., Campa, A., Esposito, G., Giardullo, P., Belli, M., Dini, V., Meschini, S., Simone, G., Sorrentino, E., Gerardi, S., Cirrone, G.A.P., Tabocchini, M. a., 2015. Induction and Repair of DNA DSB as Revealed by H2AX Phosphorylation Foci in Human Fibroblasts Exposed to Low- and High-LET Radiation: Relationship with Early and Delayed Reproductive Cell Death. *Radiat. Res.* 183, 417–431. https://doi.org/10.1667/RR13855.1

Aydarous, A., Ghazaly, M. El, 2013. Characterization of HD-V2 Gafchromic Film for Measurement of Spatial Dose Distribution from Alpha Particle of 5.5 MeV. *Int. J. Math. Comput. Phys. Electr. Comput. Eng.* 7(7), 1279–1281.

Back, T., Jacobsson, L., 2010. The alpha-Camera: A Quantitative Digital Autoradiography Technique Using a Charge-Coupled Device for Ex Vivo High-Resolution Bioimaging of alpha-Particles. *J. Nucl. Med.* 51(10), 1616–1623. https://doi.org/10.2967/jnumed.110.077578

Böhm, J., Ambrosi, P., Wernli, C., 1991. Measurement of the Depth-Dose Curve of 240Pu Alpha Particles. *Radiat. Prot. Dosimetry* 39(1), 191–194. https://doi.org/10.1017/CBO9781107415324.004

Böhm, J., 1976. Saturation corrections for plane-parallel ionization chambers. *Phys. Med. Biol.* 21(5), 754–759. https://doi.org/10.1088/0031-9155/21/5/004

Chabner, B.A., Roberts, T.G., 2005. Timeline: Chemotherapy and the war on cancer. *Nat. Rev.* 5(1), 65–72. https://doi.org/10.1038/nrc1529

Chaudhuri, S.K., Zavalla, K.J., Mandal, K.C., 2013. High resolution alpha particle detection using 4H-SiC epitaxial layers: Fabrication, characterization, and noise analysis. *Nucl. Instruments Methods Phys. Res. A* 728, 97–101. https://doi.org/10.1016/j.nima.2013.06.076

Chia, S.K., Speers, C.H., D'Yachkova, Y., Kang, A., Malfair-Taylor, S., Barnett, J., Coldman, A., Gelmon, K.A., O'Reilly, S.E., Olivotto, I.A., 2007. The impact of new chemotherapeutic and hormone agents on survival in a population-based cohort of women with metastatic breast cancer. *Cancer* 110(5), 973–979. https://doi.org/10.1002/cncr.22867

de Nederlandse Kankerregistratie, 2015. Cijfers over kanker [WWW Document]. URL http://www.cijfersoverkanker.nl/

Elgqvist, J., Frost, S., Pouget, J.P., Albertsson, P., 2014. The Potential and Hurdles of Targeted Alpha Therapy – Clinical Trials and Beyond. *Front. Oncol.* 3, 324. https://doi.org/10.3389/fonc.2013.00324

Hu, B., Han, W., Wu, L., Feng, H., Liu, X., Zhang, L., Xu, A., Hei, T.K., Yu, Z., 2005. In situ visualization of DSBs to assess the extranuclear/extracellular effects induced by low-dose alpha-particle irradiation. *Radiat. Res.* 164(3), 286–291. https://doi.org/10.1667/RR3415.1

Miederer, M., Scheinberg, D.A., McDevitt, M.R., 2008. Realizing the potential of the Actinium-225 radionuclide generator in targeted alpha-particle therapy applications. *Adv. Drug Deliv. Rev.* 60(12), 1371–1382. https://doi.org/10.1038/jid.2014.371

Oster, L., Horowitz, Y.S., Podpalov, L., 2010. OSL and TL in TLD-100 following alpha and beta irradiation: Application to mixed-field radiation dosimetry. *Radiat. Meas.* 45(10), 1130–1133. https://doi.org/10.1016/j.radmeas.2010.06.017

Rusthoven, K.E., Kavanagh, B.D., Cardenes, H., Stieber, V.W., Burri, S.H., Feigenberg, S.J., Chidel, M.A., Pugh, T.J., Franklin, W., Kane, M., Gaspar, L.E., Schefter, T.E., 2009. Multi-Institutional Phase I/II Trial of Stereotactic Body Radiation Therapy for Liver Metastases. *J. Clin. Oncol.* 27(10), 1572–1578. https://doi.org/10.1200/JCO.2008.19.6329

Sato, T., Furusawa, Y., 2012. Cell Survival Fraction Estimation Based on the Probability Densities of Domain and Cell Nucleus Specific Energies Using Improved Microdosimetric Kinetic Models. *Radiat. Res.* 178(4), 341–356. https://doi.org/10.1667/RR2842.1

Sgouros, G., Roeske, J.C., McDevitt, M.R., Palm, S., Allen, B.J., Fisher, D.R., Brill, A.B., Song, H., Howell, R.W., Akabani, G., Bolch, W.E., Brill, A.B., Fisher, D.R., Howell, R.W., Meredith, R.F., Sgouros, G., Wessels, B.W., Zanzonico, P.B., 2010. MIRD Pamphlet No. 22 (abridged): radiobiology and dosimetry of alpha-particle emitters for targeted radionuclide therapy. *J. Nucl. Med.* 51(2), 311–328. https://doi.org/10.2967/jnumed.108.058651

Tracy, B.L., Stevens, D.L., Goodhead, D.T., Hill, M.A., 2015. Variation in RBE for Survival of V79-4 Cells as a Function of Alpha-Particle (Helium Ion) Energy. *Radiat. Res.* 184(1), 33–45. https://doi.org/10.1667/RR13835.1

Van Den Heuvel, F., 2014. A closed parameterization of DNA-damage by charged particles, as a function of energy - A geometrical approach. *PLoS One* 9(10). https://doi.org/10.1371/journal.pone.0110333

Wang, G., Fu, K., Yao, C.S., Su, D., Zhang, G.G., Wang, J.Y., Lu, M., 2012. GaN-based PIN alpha particle detectors. *Nucl. Instruments Methods Phys. Res. A* 663(1), 10–13. https://doi.org/10.1016/j.nima.2011.09.003

Wertheim, D., Gillmore, G., Brown, L., Petford, N., 2010. A new method of imaging particle tracks in solid state nuclear track detectors. *J. Microsc.* 237(1), 1–6. https://doi.org/10.1111/j.1365-2818.2009.03314.x

Ziegler, J.F., Ziegler, M.D., Biersack, J.P., 2010. SRIM - The stopping and range of ions in matter (2010). *Nucl. Instruments Methods Phys. Res. B* 268(11–12), 1818–1823. https://doi.org/10.1016/j.nimb.2010.02.091

Chapter 2

Fluorescent Nuclear Track Detectors – review of past, present and future of the technology

M.S. Akselrod[1] and J.J.M. Kouwenberg[2]

[1] Landauer, Inc., Crystal Growth Division, 723½ Eastgate St., Stillwater, OK 74074, USA
[2] Radiation, Science & Technology, Delft University of Technology, Mekelweg 15, Delft, the Netherlands

ABSTRACT

Fluorescent Nuclear Track Detector technology is a passive luminescent integrating detector technology having important advantages in measuring neutrons, heavy ions and even photons. FNTD is based on new aluminum oxide crystals doped with carbon and magnesium impurities (Al_2O_3:C,Mg) and confocal laser scanning fluorescent microscopy technique. The production and optical characteristics of Mg-doped aluminum oxide are discussed in details, as well as the progress made in the read-out instrumentation. Since the introduction of the technology, FNTDs have been successfully used for a wide range of applications in mixed neutron-gamma fields, medical dosimetry and radiobiological research and the results of these tests are discussed in detail.

INTRODUCTION

Neutron and heavy charged particle dosimetry is considered the most difficult task in radiation dosimetry. Neutrons are not directly ionizing particles with wide dynamic range of energies and doses. Heavy charge particles also might have very wide range of linear energy transfer (LET) and penetration range in matter. Active neutron instruments like ^{3}He-based counters, Rem-meters and Bonner Sphere spectrometers are typically bulky, require long preparation, calibration and readout time and are prone to failure because of batteries and complex electronics. In turn passive integrating detectors like TLD and OSLD are very compact, reusable and reliable, as they do not have batteries or imbedded electronics. They do not require much preparation and post processing, although they do not have the alarming and dose rate indication capabilities.

Novel passive integrating fluorescent nuclear track detectors (FNTDs), developed by Landauer, Inc. (Akselrod and Akselrod, 2006; G. M. Akselrod et al., 2006; Sykora et al., 2007, 2008a, 2009) have demonstrated a promising performance for dosimetry of neutrons, protons and other heavy charged particles. The FNTD is based on a single crystal of aluminum oxide doped with carbon and magnesium, and having aggregate oxygen vacancy defects - Al_2O_3:C,Mg (Akselrod et al., 2003; Sanyal and Akselrod, 2005). The crystals are grown by the Czochralski technique and detectors are produced in different sizes and shapes depending on the final application (Figure 2-1). Thin 500 μm polished wafers with diameter as large as 60 mm for radiation field imaging can be produced. The tracks of recoil protons and other heavy charge particles, or even delta electrons generated in a crystalline detector are forming bright objects on dark background in fluorescent contrast, are imaged digitally and processed using a high resolution readout system based on confocal laser scanning fluorescence microscopy technique (Akselrod et al., 2014a; Diaspro, 2001; Sykora et al., 2008b). Specialized data acquisition and image processing software allows for automatic readout of multiple detectors in two modes: track

counting in a low dose range of neutrons and analog, power spectral integral (PSI) mode for high doses of neutrons, charge particles and photons. This article is a review of the advancements of the FNTD technology during the last decade. We cover the fundamentals of FNTD crystal's defects, optical properties and production, the readout process and advances in both fast and super-resolution readout, the application in neutron spectroscopy and dosimetry, gamma dosimetry, LET spectroscopy of ions and radiobiological research.

Figure 2-1: Al₂O₃:C,Mg single crystal (top), polished wafer (bottom right), FNTDs (bottom middle) and OSL slide with FNTD chip covered by three converters (polyethylene, Teflon and Li-glass) (bottom left).

## CRYSTAL GROWTH, DEFECTS AND OPTICAL SPECTROSCOPY OF ALUMINUM OXIDE CRYSTALS

Crystal growth

Al_2O_3:C,Mg crystals are synthesized using the Czochralski (CZ) crystal growth method (Akselrod and Bruni, 2012) the technique of pulling the crystal out of the melt by first deeping-in a seed of the same material of desired crystallographic orientation in the melt with simultaneous seed rotation. Today the Czochralski technique is the major industrial growth method for virtually all semiconductor materials that melt congruently as well as a variety of oxide crystals. Sapphire with desired impurities is melted above the crystallization point of 2050 °C in a highly reduced atmosphere (Figure 2-2).

Oxygen vacancy defects are introduced by growing the crystal in the presence of hot graphite to obtain a low partial oxygen pressure around 10^{-20} Pa. By dissolving carbon monoxide at a preferred concentration during crystal growth into the melt, carbon dopants are formed during the crystallization. It is believed that secondary effects of the presence of carbon monoxide

during crystal growth involve the creation of oxygen vacancies. Magnesium is added in the form of a Mg-compound, often MgO or $MgAl_2O_4$, to the raw material.

FNTD detectors are cut from the Al_2O_3:C,Mg crystal along the optical *c*-axis in different shapes, although commonly found as 8 x 4 x 0.5 mm³ plates (Figure 2-1). One large side of the detector is polished to optical quality. To reduce background luminescence, detectors are thermally annealed with a special heating profile up to 650 °C for 17h and optically bleached with a frequency tripled 349 nm Nd:YLF pulsed laser light. Annealing or optical bleaching can be repeated to erase fluorescent tracks in a detector, allowing it to be reused.
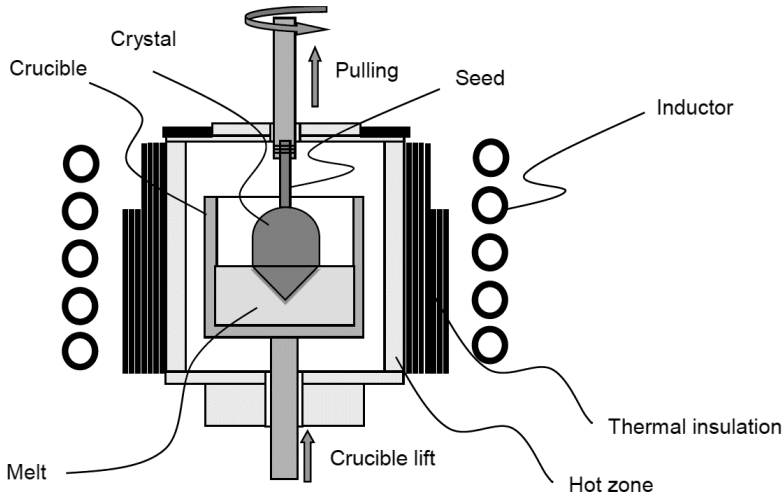
Figure 2-2: Schematic diagram of the Czochralski crystal growth process (Akselrod and Bruni, 2012).

Crystallography, defect structure and spectroscopy

α-Al_2O_3 has a rigid, slightly distorted hexagonal close-packed sub-lattice of O^{2-}ions with Al^{3+} ions occupying two out of every three octahedral interstices (Figure 2-3). Each O^{2-} ion is surrounded by four tetrahedral nearest-neighbor Al^{3+} ions. Point defects in the crystal (vacancies, interstitials and impurities) in a certain circumstances can produce optically active defects, known as color centers or luminescent centers. Ionized electrons produced in the crystal by radiation can be captured by said color centers, thereby altering their net charge and consequently their optical properties (Akselrod et al., 1998). A fundamental advantage of Al_2O_3 is its wide optical energy gap of 9.5 eV that allows one to engineer deep localized electronic states, traps and luminescent centers with the high thermal and optical stability required for radiation detection applications.

Crystal growth in highly reducing atmosphere stimulate creation of single oxygen vacancies occupied by two electrons and usually denoted as F-centers, and identified by strong optical absorption band at 205 nm and emission band at 420 nm with 35 ms lifetime (Lee and Crawform, 1979) , while absorption bands at 230 and 255 nm with emission at 330 nm and very short lifetime of 2 ns are assigned to transitions in single oxygen vacancy with just one electron and denoted as F^+-centers (Akselrod et al., 1990; Evans and Stapelbroek, 1978). F and F^+-centers have been studies in detail and play a key role in the TL and OSL mechanisms of Al_2O_3:C (Akselrod et al., 1990, 1998; Yukihara et al., 2015).
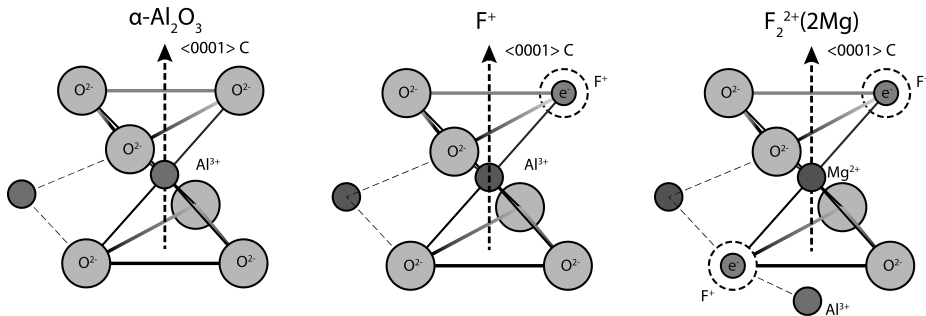
*Figure 2-3: Lattice structure of α- Al_2O_3:C,Mg and its important defects: a) simplified ideal lattice cell, b) single oxygen vacancy with one electron – F^+ center and c) aggregate defect consistent of two oxygen vacancies charge compensated by two Mg^{2+}-ions.*

Al_2O_3:C,Mg crystals have much more complex defects created during crystal growth process that result in multiple types of color centers with different absorption and emission bands. In addition to single vacancy defects (F and F^+-centers) which dominate in Al_2O_3:C crystals, double vacancy defects (denoted as F_2-type color centers) associated and not associated with Mg-impurity ions (Figure 2-3c). They were identified and assigned to different emission-excitation and absorption bands (Figs. 4, 5 and 6). The crystals have yellow-green coloration due to a 435 nm absorption band associated with aggregate F_2^{2+}(2Mg) color centers consisting of two oxygen vacancies and charge-compensated by two magnesium ions (Figure 2-3c) (Akselrod et al., 2003). F_2^{2+}(2Mg) centers efficiently capture free electrons during irradiation and undergo photochromic (Figure 2-4) and radiochromic transformations into a three-electron state forming F_2^+(2Mg) centers (G. M. Akselrod et al., 2006; Sykora and Akselrod, 2010a). The F_2^+(2Mg) centers have excitation bands centered at 335 and 620 nm with emission centered at 750 nm (Figure 2-5, Figure 2-6). Similar types of defects produced by thermo-chemical reduction of Mg-doped sapphire crystals were reported by Ramirez *et al*. (Ramirez et al., 2005).
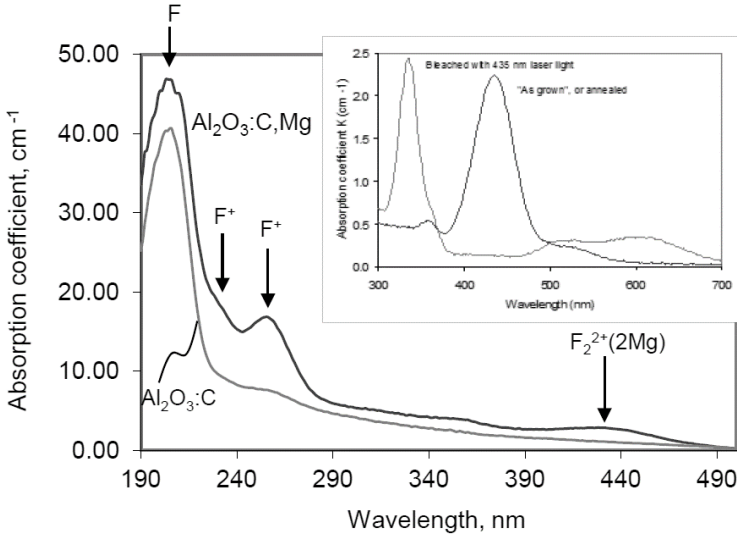
Figure 2-4: Optical absorption bands in Al₂O₃:C and Al₂O₃:C,Mg crystals and photochromic transformation in the latter one under the 435 nm pulsed laser light (Akselrod et al., 2003).
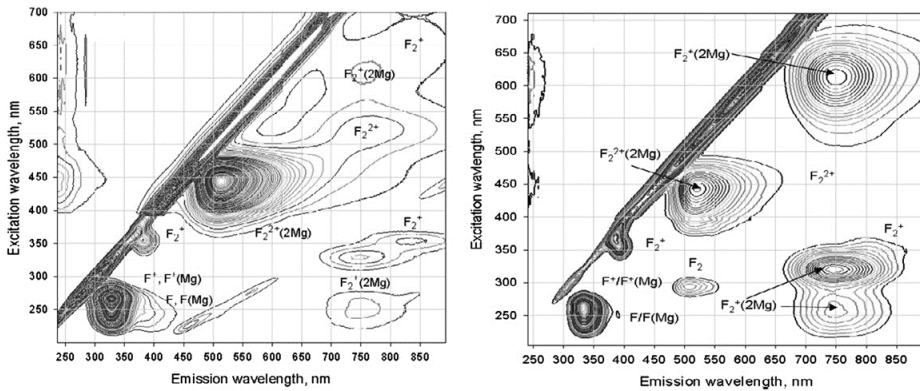

Figure 2-5: Photoluminescence bands in Al₂O₃:C,Mg crystals (a) before and (b) after irradiation with 143 Gy from a 90Sr/90Y beta source (Akselrod and Sykora, 2011).
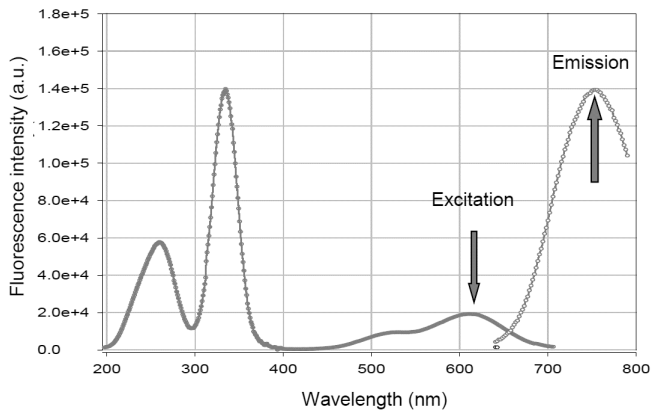
Figure 2-6: Excitation and emission spectra of F^{2+} (2Mg)-centers (Sanyal and Akselrod, 2005).

The most important advantage of this new crystal for practical applications is that the color centers undergo efficient radiochromic transformations as a function of dose (**Error! Reference source not found.**). Functioning as charge storage, these color centers are thermally stable up to 600° C (Figure 2-7). The lifetime of their luminescence is short ~ 9 ns for an F^{2+}(2Mg) center emitting at 520 nm and 75 ns for an F_2^+(2Mg) center emitting at 750 nm (Figure 2-8) which allows for fast laser scanning in imaging applications. That lifetime is almost a million times faster than the 35 ms lifetime of F-center luminescence in OSL material based on Al_2O_3:C crystals. This is in contrast with the OSL process, including one in Al_2O_3:C, where the photoionization of traps during optical stimulation is followed by the recombination of charge on luminescent centers and results in partially destructive readout. Both physical processes - intra-center fluorescence and recombination luminescence during OSL readout have their own practical advantages and disadvantages.
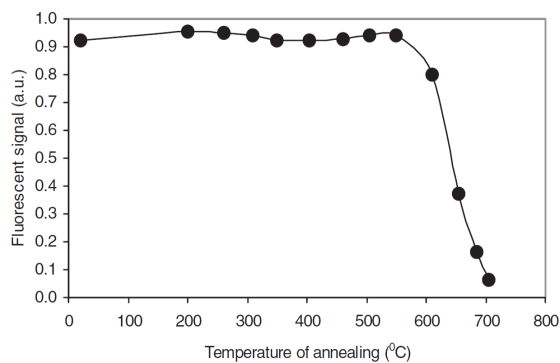
Figure 2-7: Thermal stability and erasure of fluorescent signal produced by F^{2+} (2Mg)-centers by thermal annealing of Al_2O_3:C,Mg crystal (G. M. Akselrod et al., 2006).
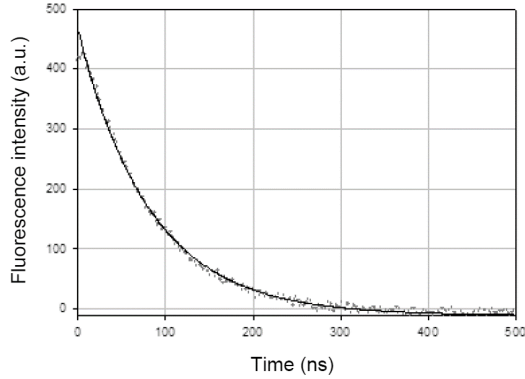
Figure 2-8: Fluorescence decay of F^{2+} (2Mg)-centers emission band at 750 nm having 75 ns lifetime (Akselrod et al., 2003).

The main advantage of OSL is the possibility to use inexpensive powdered phosphors imbedded in plastic to detect very low doses (~1 μSv) by measuring single photons of radiation-induced luminescent above very low background signal. Another advantage of OSL is an easy bleaching/erasing of detectors for reusable applications. At the same time OSL detectors are, at least partially, erased during readout and are sensitive to ambient light requiring light-tight packaging and handling in low or even red light conditions. In turn, RPL materials are typically not sensitive to ambient light, can be read multiple times without erasure, but show relatively high background signal even before irradiation and cannot measure very low doses. Plus their optical erasure is more technically challenging, but possible using multiphoton ionization process. Thermal erasure of RPL phosphors is also possible.
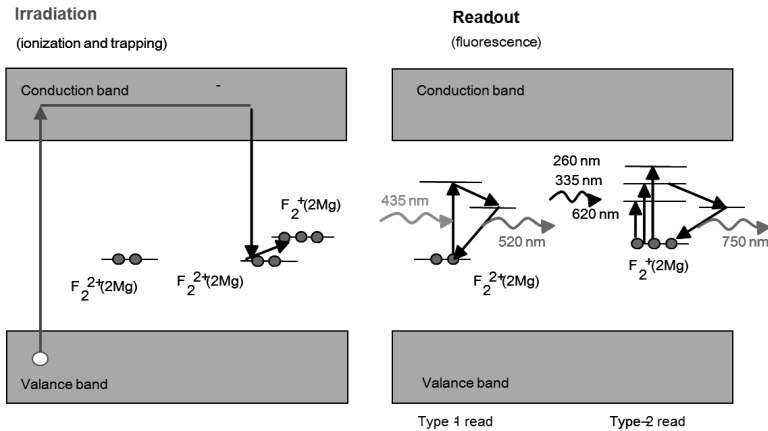
Figure 2-9. Schematic band diagram of defect levels in Al_2O_3:C,Mg crystals explaining electronic processes during irradiation and optical readout using radio-photo-luminescent process (Akselrod et al., 2003).

ADVANCES IN FNTD INSTRUMENTATION

Due to the short relaxation time of F_2^+(2Mg)-centers, FNTDs can be readout using fast confocal laser scanning fluorescence measurement systems (Akselrod and Sykora, 2011). Confocal laser scanning microscopy (CLSM) was first used to readout FNTDs and offers a high spatial resolution, reaching near-diffraction limit at 240×240×940 nm³ measured as FWHM (Chapter 3). Confocal microscopy technique allows one to discriminate the fluorescence induced in a tight focal laser spot within the track volume from the background fluorescence induced by the laser beam in surrounding crystal volume. Figure 2-10 shows an example of the fluorescent image (2D x-y scan) where the bright spots are produced by recoil protons produced by Am-Be neutrons in polyethylene converter mounted on top of the FNTD crystal during the irradiation. The scan is typically performed by the FNTD reader system at 2 μm depth in single crystal sapphire detector. The bright fluorescent feature are actually cross-section part of the track within the confocal thickness of the scanned layer. In dosimetry application the dose of neutrons is proportional to the track density determined from statistically significant track counts obtained from multiple images of large detector area and processed by a specialized image processing routine.
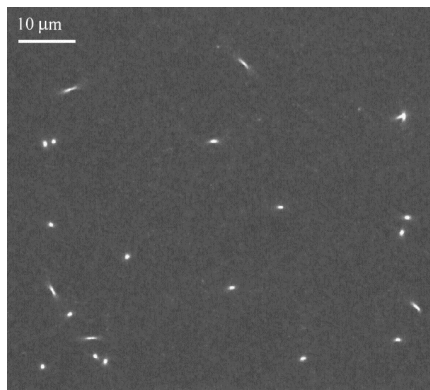
Figure 2-10: Example of fluorescent 2D image of recoil proton tracks induced by fast neutrons and obtained by scanning the laser beam at 2 μm depth in single crystal sapphire detector covered by polyethylene converter. Actually the fluorescent track spots are cross-section part of tracks within the thickness of the scanned layer (Sykora et al., 2008b).

A simplified optical diagram of a CLSM is shown in Figure 2-11. Light from a 635nm laser diode is scanned by 1D or 2D galvanometer system and focused in a small volume in the crystal by the high NA objective lens. The resulting fluorescence emission is collected by the same objective (epi-luminescent mode) passes through the same optics and galvanometers (descanning), separated from the excitation laser light by a dichroic mirror and focused

through a pinhole and long-pass filters onto the avalanche photodiode (APD) detector. A pinhole placed in front of the APD photodetector filters off out-of-focus fluorescence for optimal spatial resolution and reduced background fluorescent signal. The CLSM creates 2D images formed by fluorescence intensity as a function of the laser beam position in FNTD by raster scanning of the focused laser beam inside the crystal and digitizing the fluorescent signal voxel by voxel.
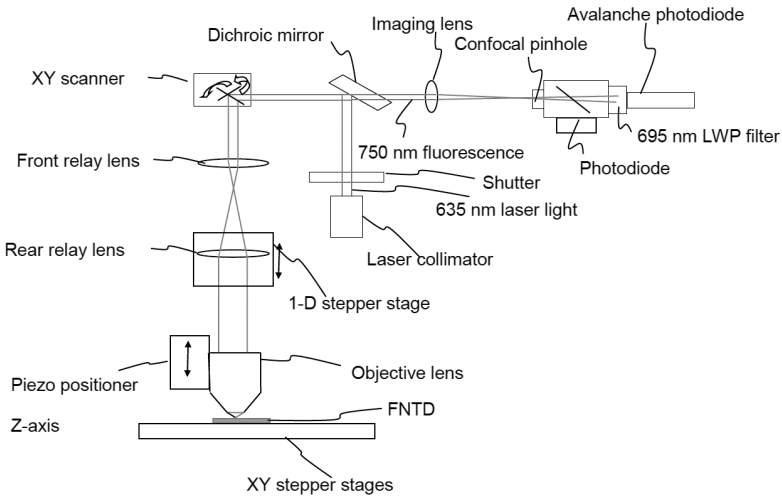
Figure 2-11: Simplified schematic of a CLSM used for FNTD read-out (Sykora et al., 2008b).
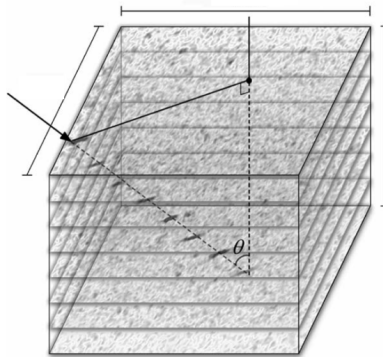
Figure 2-12: Stack of 2D images obtained at different depth in the crystal with the trajectory obtained by interconnecting and measuring the centroid of each fluorescent bright spot (here in negative contrast) identified on each image (G. M. Akselrod et al., 2006).

3D images are created by recording series of 2D images at various pre-set depths in the crystal. A 3D volumetric image can be then reconstructed from the stack of 2D images by any commercial or free software packages (Figure 2-12). CLSMs from a number of manufacturers (Leica, Zeiss, Olympus) can be used for FNTD read-out when outfitted with the appropriate lasers, photodetectors and filters for the mentioned excitation and emission wavelengths. Avalanche photo-detectors (APDs) are however a better choice since conventional photomultiplier tubes have insufficient detection efficiency at wavelengths >700 nm. An example of a typical CLSM image of recoil protons traversing an FNTD is shown in Figure 2-10. Each bright spot was produced by a single proton passing through the detector. Note that the shape and intensity of the spots varies among the track, which is caused by the difference in proton angle of incidence and asymmetric shape of the excitation laser focal spots of CLSM systems, which resembles an ellipsoid having a longer axis in direction along the optical axis of the objective lens (Figure 2-13). Image and track processing and analyses are described in more details in the section *"Application of FNTD in radiation dosimetry"*.
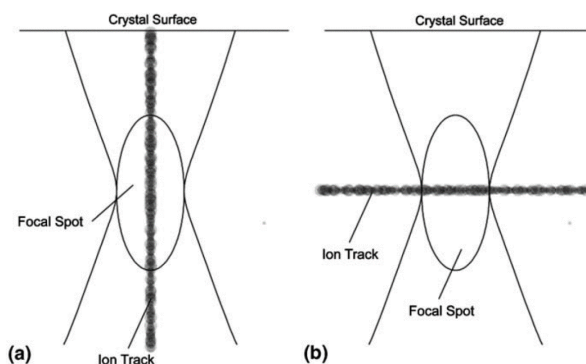
Figure 2-13: Illustration of the effect of the focal spots asymmetry on the illumination of ion tracks at different angle (M. S. Akselrod et al., 2006). The convex lines indicate the excitation laser beam, where the maximum intensity in the focal spots is visualized as an ellipse. A track perpendicular to the crystal surface will produce a near 3-times higher fluorescence intensity than tracks propagating along the crystal surface due to the larger portion of fluorescent track contained within the excitation laser focal spot (Bartz et al., 2014).

Automatic FNTD reader design

A photo of the commercial automatic FNTD reader manufactured by Landauer is shown on Figure 2-14. The reader is produced in two variants – neutron dosimetry system (model FXR-700N) with 2D scanning performed with fast axis scanning by a single galvanometer and slow scanning by one of a 2D translation stages. Surface position determination and setting the scan depth is performed by the piezo actuator of the high numerical aperture dry objective lens

(Nikon 100×, 0.95 NA). The reader can scan automatically up to 184 detectors on a tray, their engraved IDs are automatically read and fluorescent images are scanned and processed automatically according to predetermined algorithm with configurable parameters (Akselrod et al., 2014a).

The second variant of the reader (model FXR-700R) is designed for research laboratories. It has two galvanometer for 2D scanning of the detector crystal in a static position of the tray to obtain stacks of images scanned at different depth in the crystal for 3D imaging and track trajectory reconstruction (Greilich et al., 2013; Klimpki et al., 2016). Massive scanning of multiple detectors and multiple image stacks on the same detector is easily configurable in a software. Precise surface position and depth of scanning setting for each detector is determined automatically by the reflection of the laser light peak position measured with a second APD or photodiode.
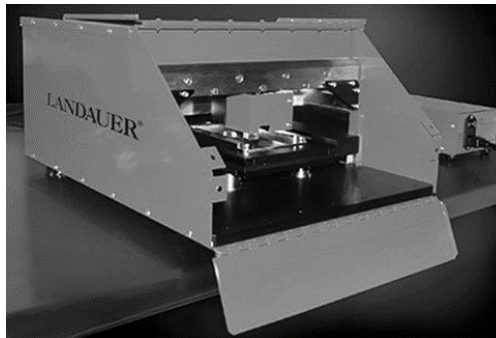
Figure 2-14: Commercial automatic FNTD reader produced by Landauer (Akselrod et al., 2014a).

Further improvements in FNTD instrumentation was lately achieved by introducing crystal coloration determination before starting the confocal laser scanning (Akselrod et al., 2014b). This technique allowed estimation of detector photon and neutron sensitivity for high dose analog mode without doing individual calibration by irradiating, reading and bleaching of each detector.

Application of super-resolution microscopy techniques for FNTD imaging

Significant improvements in high resolution imaging have been made since the initial introduction of FNTDs. The resolution of CLSM is limited by the diffraction limit: the smallest detail that can be resolved using photons. This limit is determined by the wavelengths of the excitation and emission lights and translates to approximately into 240 x 240 x 940 nm^3 (x, y,

z) voxels for the best available oil-emersion lenses. Over the last two decades, a number of techniques surpassing this physical limitation have become commercially available and two were used for FNTD read-out to visualize sub-micrometer sized tracks, namely structured illumination microscopy (SIM) (Gustafsson, 2000, Chapter 4) and stimulated emission depletion (STED) (Greilich et al., 2013; Hell, 2003).

STED employs two pulsed overlapping laser beams: the primary laser beam that stimulates the excitation transition of the luminescent centers and a secondary high peak power and doughnut-shaped laser beam with the wavelength corresponding to the emission transition. This second laser beam depletes (and temporarily disables) fluorescent centers excited by the primary beam within a small volume outside the center of the primary stimulation laser beam (Figure 2-15).
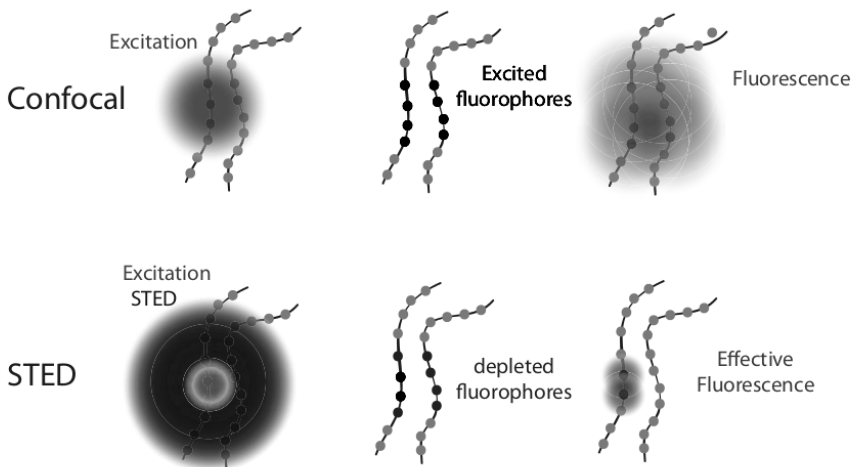
Figure 2-15: Illustration of the STED principle compared to CLSM for imaging of fluorophores (or fluorescent centers). While employing a similar, diffraction limited, excitation spots, the number of functioning fluorophores are reduced with STED due to quenching/depletion of excited luminescent centers on the periphery of the primary excitation beam using donut shaped secondary depletion beam (Scientific Volume Imaging, 2017).

In STED careful adjustment of the peak power, duration and delay time between both laser beam pulses allow the reduction of the emitting volume of FNTD crystal down to 80 nm in lateral (x,y) direction. (Figure 2-16, left) (Niklas et al., 2017). The data collected after irradiation of FNTD crystals with ion having different LET indicate that the observed track spot widths contain information on the energy distribution when the dimensions are larger than ~90 nm. The STED measurements identified the FWHM to be a limited proxy for the LET of individual ions, similar to the track spot intensity but less dependent on detector sensitivity.

STED could be an excellent candidate for 3D track imaging and validation of Monte Carlo simulation of a track structure.

SIM is a wide-field microscopy technique which employs a raster of laser lines, instead of a scanning single focused laser beam, to excite the whole image plane at once. Fluorescent images obtained at various rotational positions of the excitation raster are recorded to retrieve information from the frequency space outside the observable region. This technique yields a two-fold increase in spatial resolution compared to CLSM (Figure 2-16, right). SIM might be faster than STED and CLSM since no raster-scanning is required, but computationally intensive in the reconstruction stage of image processing. It was shown for alpha tracks in FNTDs that the superior resolution of SIM estimated the scattering of particles better than CLSM (Chapter 4).
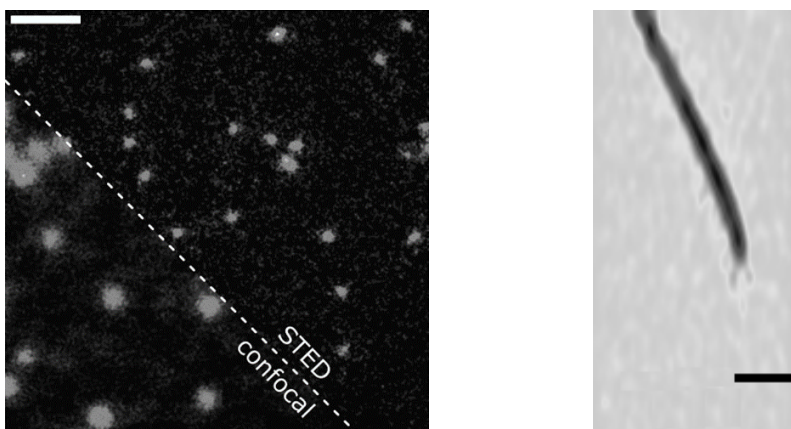
Figure 2-16: (left) Comparison of confocal and Stimulation Emission Depletion (STED) imaging of ion tracks in FNTD (Niklas et al., 2017). (right) Alpha tracks imaged using Structural Illumination Microscopy (SIM) (Chapter 4). Scale bars are 1 µm.

The time required to scan a 100 x 100 x 10 µm FNTD volume varies greatly depending on the used methodology and required signal-to-noise ratio. SIM and CLSM are relatively fast and take between 2 and 30 minutes. STED is slow due to pulsed stimulation and multiple illumination steps and can take up to several hours for imaging at high resolutions.

Annealing, bleaching and reusability of FNTDs

FNTDs can be read with red laser light multiple times without erasure, but at the same time the detectors can be erased and reused multiple times after thermal annealing or optical bleaching. As was shown in the 'Crystallography, defect structure and spectroscopy' and Figure 2-7, radiation-induced fluorescent signal in FNTDs is stable up to 600 °C but can be

successfully thermally annealed by heating the crystals to 650 °C. Thermal annealing fully erases the radiation-induced signal but increases the relatively high background fluorescent signal and optically bleaching with pulsed UV laser light using two-photon absorption photoionization process is needed (see examples in Table 2-1). The main criteria of FNTD image quality is a signal-to-noise ratio (SNR), parameter obtained from the standard crystal sample irradiated in vacuum with ^{241}Am alpha particles from 200 mm distance to produce identical tracks propagating normally to the crystal surface and resulting in bright round fluorescent spots. SNR in this case is defined as ratio of average of alpha particle fluorescent track amplitudes and one standard deviation of the fluorescent background surrounding the tracks. A special FNTD laser bleaching system is available from Landauer for erasing the accumulated dose before the next use of the detectors. The system allows loading up to 1000 detectors on four trays and bleaching them automatically with the bleaching time of 30 s per one detector.

Table 2-1: Improvements as result of different detector treatments (Sykora and Akselrod, 2010a).

Crystal state	Background fluorescence (a.u.)	Alpha track fluorescent amplitude (a.u.)	Signal-to-noise ratio
As-grown	65 ± 2	22	9.4
Annealed	235 ± 3	38	13.6
Bleached 325 nm	22 ± 1	38	40.0
Bleached 260 and 325 nm	33 ± 1	45	47.4

APPLICATION OF FNTD IN RADIATION DOSIMETRY

Dosimetry of neutrons at low doses

Personal neutron dosimetry remains the most difficult dosimetry task since no single method is able to deliver the required energy and dose response, detector sensitivity and accuracy that is necessary (ISO 21909-1 standard). One of the first applications of FNTDs was therefore measurement of neutrons. While neutrons themselves produce no detectable signal in FNTDs at low doses and neutron energies, products of nuclear reactions between neutrons and a neutron converter produce easily detectable tracks. Converters containing high content of hydrogen, like polyethylene (PE), for fast neutron detection and ^{6}Li- and ^{10}B-containing compounds, having high neutron capture cross-section and resulting in (n,α) reactions, for thermal and intermediate energy neutrons were tested. Track detectors, including FNTDs, have traditionally measured neutron dose by proportionally relating track density of nuclear reaction products to the incident neutron fluence and dose (Figure 2-17).

Unlike Plastic Nuclear Track Detectors (PNTD), Al_2O_3:C,Mg is also sensitive to low linear energy transfer (LET) radiation including secondary electrons resulting from interactions of photons

with the crystal. Neutron radiation is usually accompanied by gamma radiation. If the dose of gamma radiation is above several cGy, then the fluorescence induced by overlapping secondary delta electron tracks can interfere with the signal induced by recoil protons making it difficult to detect and count neutron induced tracks. An advanced image processing method was developed as a technique to determine the correct dose in mixed gamma-neutrons fields (Sykora and Akselrod, 2010b).

Thermal neutrons could be detected in FNTDs via the production of alpha particles and tritium ions in 6LiF or 6Li-glass and that fast neutrons could be observed via recoil protons produced in polyethylene (PE) (M. S. Akselrod et al., 2006). From the range in the FTND, alpha particles (helium ions) could be distinguished from tritium ions. A more extensive study involved irradiations using fast neutron in air and on a PMMA phantom using PE, 6LiF and 10B converters, and moderated neutrons with TLD-100 and TLD-600 as converters (Sykora et al., 2008b). The absorbed dose was calculated using the track density and detector sensitivity expressed in tracks per 1 mm^2 and per 1 mSv of neutron dose. A linear relation between absorbed doses and track densities was observed. FNTDs proved superior to CR-39 PNTDs, depending on the source of plastic, with up to a four times increase in detection efficiency and a 100 times higher saturation dose.
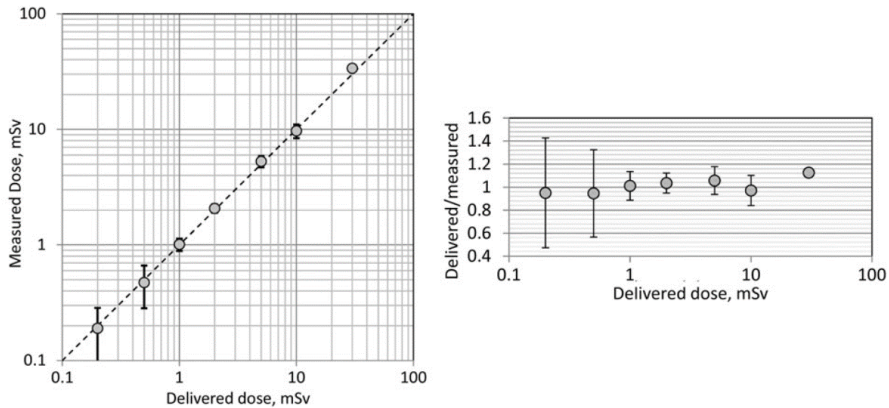
Figure 2-17: Measured neutron doses as a function of delivered doses (top). 1:1 line represented as a dashed line. Error bars represent 1 standard deviation. Detectors were irradiated with 241AmBe neutrons. In the bottom chart, measured dose and standard deviations were normalized to the delivered dose (Akselrod et al., 2014a).

To tackle the strong neutron energy dependence of the detector sensitivity (Figure 2-18) it was proposed to use to use two different methods (Sykora et al., 2009). Fist is to calculate the ratio of track densities measured behind two converters made of PE and 6Li-based compound

(Figure 2-19). Estimated neutron energies were in good agreement with the reference values for median neutron energies between 40 keV and 4 MeV. The second method is to measure the track density behind PE converter as a function of depth in the crystal, as recoil proton penetration depth depends on the initial neutron energy. This second technique produced good results for high energy neutrons in the range from 1 MeV to 19.6 MeV (Figure 2-20) (Sykora et al., 2009).
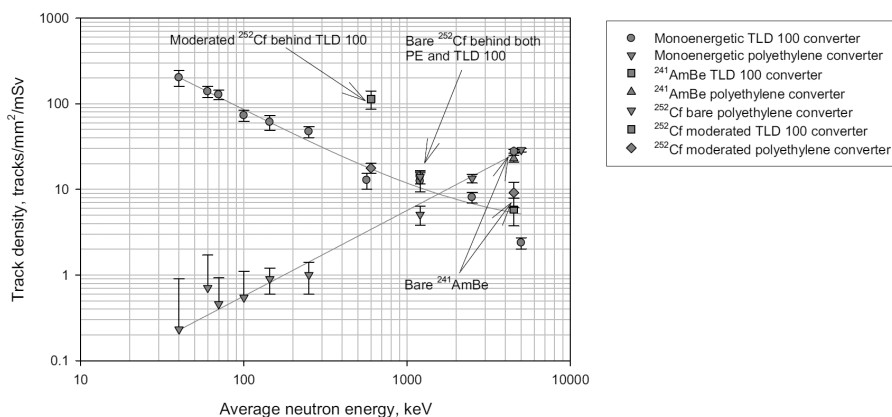
Figure 2-18: Neutron energy dependence of FNTDs irradiated at NPL (UK) and PTB (Germany) with mono-energetic and broad spectrum neutrons (Sykora et al., 2009).
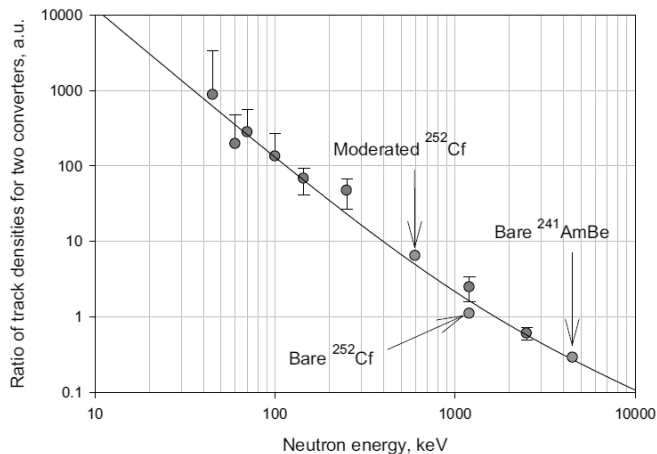
Figure 2-19: Track density ratio measured in FNTDs behind TLD-100 and PE converters as an estimator of neutron energies (Sykora et al., 2009).
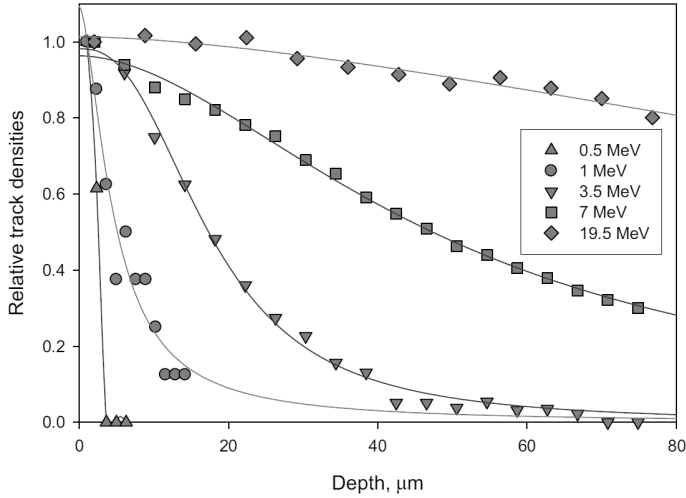
Figure 2-20: Track densities for FNTDs covered with PE converter as a function of scanning depth for high energy mono-energetic neutrons (Sykora et al., 2009).

Dosimetry of neutrons at high doses

Spatial frequency analysis of fluorescent images (Sykora and Akselrod, 2010c) provides a new approach to determine the dose of radiation through evaluation of the modulation of the fluorescence intensity within images acquired from an irradiated FNTD. The modulation of fluorescence intensity is caused by non-uniform distribution of ionization produced by charged particles (either neutron-induced recoil protons or photon-induced secondary electrons). Although gamma photons may be incident on the crystal in a uniform manner, the amount and localization of energy deposition has a microscopic and statistical variation as described by a microdosimetric approach (Rossi and Zaider, 1996).

Quantitative evaluation of fluorescence Intensity modulation can be determined by spatial frequency analysis of the image illustrated by Figure 2-21. The image is converted into the spatial frequency domain by the discrete Fourier transform (DFT) defined by:

$$F(k,l) = \frac{1}{N^2} \sum_{m=0}^{N-1} \sum_{n=0}^{N-1} f(m,n) e^{-\frac{2\pi i}{N}(km+ln)}$$

(2-1)

where *f(m,n)* is the intensity of the original image in the spatial domain at points *m* and *n, k* and *l* are spatial frequencies and F(0,0) represents the DC offset of the image. The power spectral density of the image is calculated by squaring the magnitude of the Fourier transform.

Integrating the power spectral density over specially selected frequency range in the image provides the parameter – Power Spectrum Integral (PSI) which was found to be proportional to the absorbed dose:

$$PSI = \int_{k_0}^{k} \int_{l_0}^{l} \left| f(k,l) \right|^2 dk dl \ \propto \ D$$
(2-2)

where, k_0 and l_0 are the initial spatial frequencies of interest.
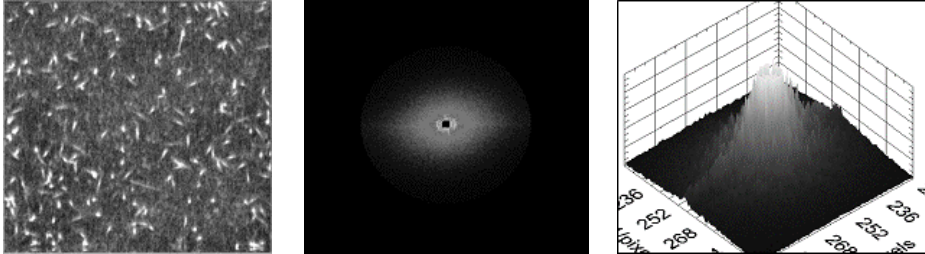
Figure 2-21: Processing of high photon and neutron dose images using the spatial frequency domain, Discrete Fourier Transforms and the Power Spectrum Integral as the dose-indicating parameter (Sykora and Akselrod, 2010c).

The so-called "analog" technique using PSI was successfully used to discriminate neutron and photon radiation induced signal produced behind PE and PTFE converters. Signal induced in FNTD behind PE converter is combination of neutron and photon doses, whereas signal behind the PTFE converter that does not contain hydrogen is proportional only to photon dose (Sykora and Akselrod, 2010b). A linear relation between the PSI and the high neutron dose in combination with track counting technique at low doses allows one to measure neutrons in a wide dynamic range between 0.1 mSv and 10 Sv (Figure 2-22) with up to a 1:3 neutron to gamma dose ratio. Correcting for nonlinearity of dose response neutron and photon doses can be measured up to 30 Gy. Correction of detector sensitivity on crystal coloration using green fluorescence intensity, a feature available in the fast automated reader, allows to determine the doses within +/-30% limits without individual detector calibration using radiation sources (Figure 2-23) (Akselrod et al., 2014a). The ability to measure mixed neutron-gamma fields over a wide energy (thermal to 20 MeV neutrons) and dose (0.1 mSv to 30 Sv) range with energy discrimination and detector reusability make the FNTD a very promising candidate for personal neutron dosimetry.
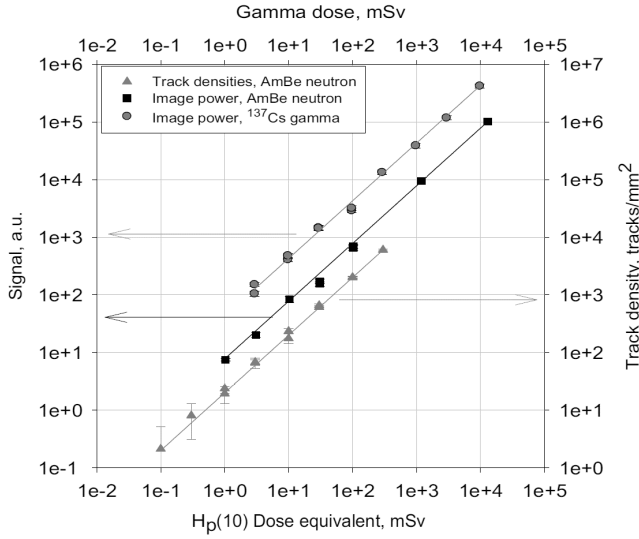
Figure 2-22. Dose dependences of FNTDs irradiated with neutrons and photons and measured in track counting and analog PSI mode (Sykora and Akselrod, 2010c).
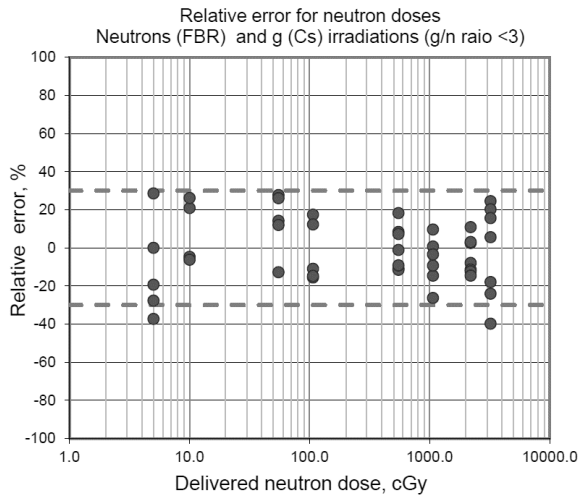
Figure 2-23: Uncertainties of high neutron dose determination using FNTDs with sensitivities determined coloration measurements using blue light induced green fluorescence (Akselrod et al., 2014b).

Criticality dosimetry

Fluorescent nuclear track detectors (FNTDs) are suggested for criticality dosimetry of neutrons and photons (Harrison et al., 2017a). The depth profiles of the fluorescent signal from FNTDs after exposure to high doses of broad spectrum neutron fields from four different sources were analyzed using the power spectrum integral (PSI) measured at increasing depths within the Al_2O_3:C,Mg crystals and show difference for different neutron spectra (Figure 2-24). The depth profiles are compared to Monte Carlo simulations of energy deposition of recoil protons as a function of depth in aluminum oxide for the same four neutron sources. An algorithm for estimating the median neutron energy and neutron dose correction factors was developed and successfully tested. This algorithm includes the use of several correction and calibration functions, but the main parameter – median neutron energy is obtained by fitting the depth profile with an exponential function and determining the depth at which the PSI value reduced 1/e times.
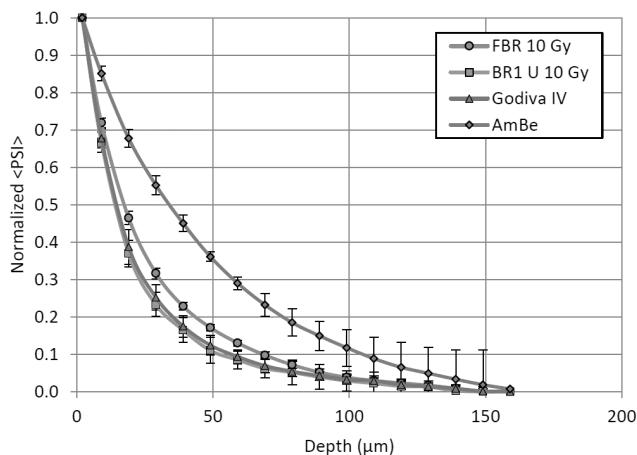
Figure 2-24: Experimental neutron-induced FNTD PSI signal depth profiles for four different neutron sources normalized to values obtained at 2 mm depth. The corresponding experimental uncertainties are ±1 standard deviation (Harrison et al., 2017a).

Gamma and X-Ray dosimetry using integral fluorescent signal

The simplest way to measure the absorbed dose of photons is to use RPL technique with 335 nm UV or 635 nm red LED illuminators and 750 nm luminescence of Al_2O_3:C,Mg crystals (G. M. Akselrod et al., 2006; Harrison et al., 2017b). The useful dose dynamic range of these type of measurements is limited relatively to OSL or confocal scanning with PSI technique and covers only 4 decades mostly due to elevated background signal even after optical bleaching (Figure

2-25). FNTDs also found application in Microbeam Radiation Therapy (MRT), where high doses of collimated, quasi-parallel arrays of X-ray beams between 50 and 600 keV are used to increase therapeutic efficiency (Bräuer-Krisch et al., 2010). In collaboration with the European Synchrotron Radiation facility in Grenoble, France, FNTDs were irradiated with 50 µm wide and 400 µm spaced x-ray microbeams with doses up to 30 Gy (Bartz et al., 2011a). A 1 µm spatial resolution of dose mapping was achieved and a linear relation between fluorescence and dose was observed. The main goal of this research was to demonstrate the performance of FNTD as a quality control tool for MRT with the peak dose and peak-to-valley dose ratio as the main parameters to be monitored.
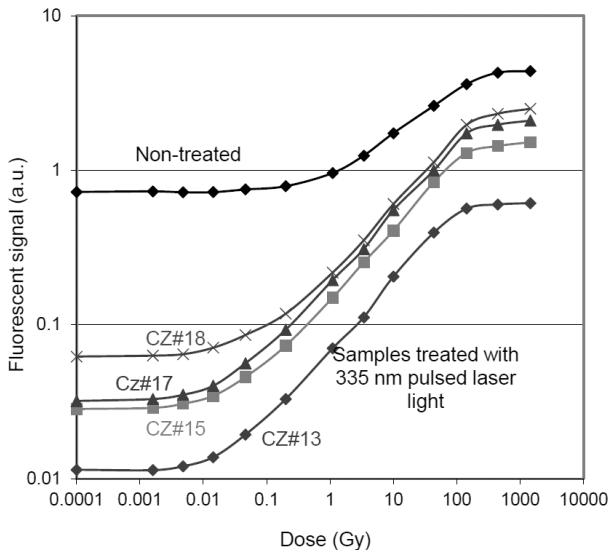
Figure 2-25: Dose dependence of 750 nm fluorescent light from Al2O3:C,Mg crystals under 337 nm excitation in as-grown (non-treated) and bleached with 335 nm pulsed laser light (G. M. Akselrod et al., 2006).

Imaging and dosimetry of high energy ion beams used in radiotherapy

In radiobiology and radiotherapy research it is important not only to image and count the number of ion tracks, but it is critical to measure each incoming charge particle's LET and to estimate the contribution to dose from both projectile and target atoms fragments (Figure 2-26). FNTD technology have been successful in measuring the LET of wide range of ions with different energies from protons to Xe ions (G. M. Akselrod et al., 2006; Bartz et al., 2014; Greilich et al., 2016; Klimpki et al., 2013; Sykora et al., 2008b). Because of stochastic nature of energy deposition along the ion track FNTDs need to be read using confocal scanning in stacks

of 2D images (Figure 2-12) (G. M. Akselrod et al., 2006), where the depth spacing is limited by the optical system point spread function axial dimension. Fluorescent intensity of tracks was proposed as a measure of LET. Several corrections including track incidence angle, microscope's field of view curvature, spherical aberrations and crystal coloration non-uniformity have to be applied to minimize the LET spectral line width (Bartz et al., 2014). The minimal LET spectral line width of 2.5% at FWHM was demonstrated with 290 MeV C-ions produced by HIMAC accelerator in Japan. Spectral lines of fragments starting from 2He through 5B were resolved and automatically processed by the image processing routine. Proton tracks were also visible but at that time could not be processed and quantized automatically.
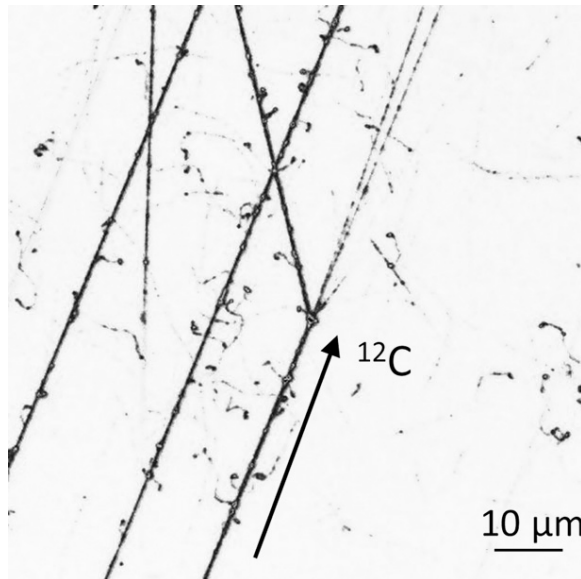
Figure 2-26: Example of carbon ion tracks passing through a FNTD. The arrow indicates a track of a primary carbon ion which undergoes a nuclear reaction (fragmentation). The smaller curly tracks surrounding the primary particles and fragments are high energy delta electrons. The fluorescence intensity of the track corresponds to the energy deposited in the crystal volume (Greilich et al., 2013).

Another parameter that was investigated as a measure of LET and atomic number Z is fluorescent track width (FWHM) (Bartz et al., 2014; Klimpki et al., 2016; Sykora et al., 2008a). Both fluorescent intensity and track width should increase with the increase of the particle LET and Z, but measurements of a track size are limited by the resolution of the employed microscopy technique and in case of confocal microscopy the increase in track size is measurable only at relatively high LETs when track size exceeds the lateral size of optical system PSF. It is important to emphasize that FWHM of a track fundamentally should not depend on crystal properties whereas fluorescent intensity of a track strongly depends on

detector crystal coloration and require calibration of each crystal. Although the absorbed dose within the heavy ion tracks can reach hundreds of Gy there are no signs of color center saturation even at LETs above 10,000 keV/μm (Figure 2-27).
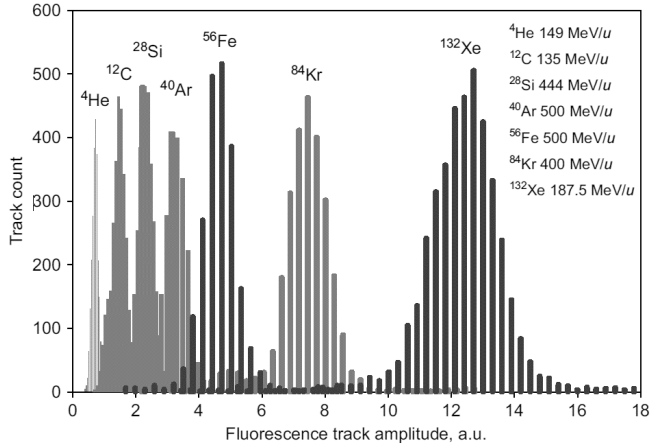
Figure 2-27: Mean track amplitude histogram for various elements at indicated energies in bare FNTDs (Sykora et al., 2008a).
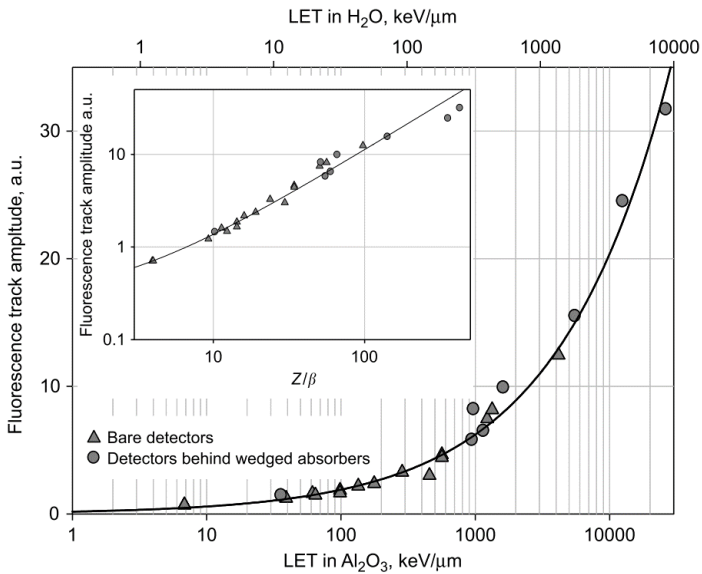
Figure 2-28: LET in Al_2O_3:C,Mg versus fluorescence track amplitude. The insert shows the relation between the fluorescence track amplitude and Z/β, where Z is the effective charge of the ion and β is the relativistic ion velocity (Sykora et al., 2008a).

Various studies have been dedicated to the relation between fluorescence intensity and LET. While a direct relation between fluorescence intensity and LET was observed for protons (Bartz et al., 2011b; Sawakuchi et al., 2016), it is hypothesized that color center saturation is reached at low LETs, resulting in a complex relation between fluorescence intensity and LET for heavy ions. In addition to fluorescence increase, enlargement of the track diameter was observed for particles with $LET_\infty H_2O > 100$ keV/µm (Sykora et al., 2008a). Sykora et al. were the first to produce a direct relation between the fluorescence track amplitude, given by the average fluorescence intensity of the track, and the LET (Figure 2-28), for multiple ions with a $LET_\infty H_2O$ ranging from 2.2 to 8767 keV/µm (Sykora et al., 2008a). Niklas et al. showed similar results for the maximum fluorescence intensity and showed the track diameter is related to the maximum delta ray range (Niklas et al., 2013a). Following these results, Klimpki et al. proposed a hyperbolic relation between the fluorescence intensity fluctuation, related to the stochastic nature of energy deposition of ionizing particles, and the LET (Klimpki et al., 2016). From this fluctuation of intensity, the authors concluded that the LET is best estimated from the intensity straggling below LET of 10 keV/µm. This method is advantageous compared to the track intensity approach since it is independent of FNTD sensitivity. FNTDs offer excellent measurement efficiency over a wide range of LETs and ion charges but more efforts for the standardization of LET and the ion charge calibration are required. The introduction of the fast automated reader (Akselrod et al., 2014a) already initiated part of this process by automating the readout, surface detection and FNTD sensitivity calibration.
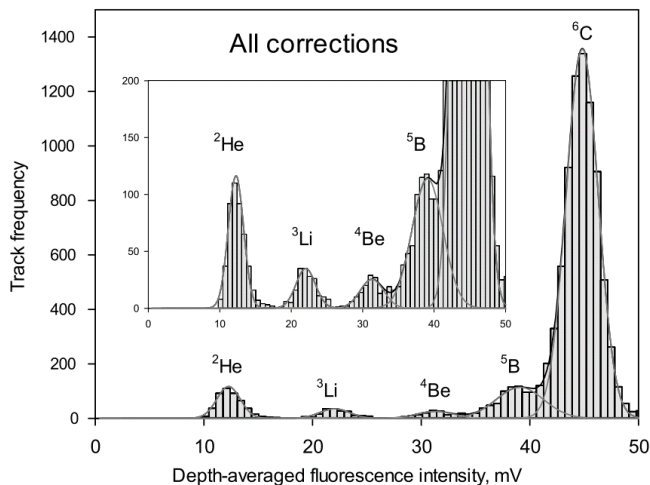
Figure 2-29: Spectrum of fluorescent track intensities of primary 290 MeV C-ions and their nuclear fragments produced when the carbon beam penetrates through 63 mm of PMMA absorber. The peaks corresponding to the different fragment nuclei are marked (Bartz et al., 2014).

In addition to fluorescence based methods, ion ranges in Al_2O_3:C,Mg have been used to estimate alpha particle energies (Bartz et al., 2013) and others (Chapter 3, Chapter 4). The new approach reduced the measured energy uncertainty of alpha particles down to the expected straggling in Al_2O_3 and is superior to intensity based approaches since no corrections for fluorescence intensity and detector sensitivity are required. However, since the maximum depth that CLSM can reach is in the range of 100 μm, only particle beams with low energies can be measured using this technique. By irradiating the FNTD from the side and measuring the fluorescence parallel to the ion beam, Klimpki et al. reported less than 3% deviation from tabulated SRIM data for the ranges of C, Mg, S, Fe and Xe ions in the FNTD (Klimpki et al., 2013).

Several authors reported a near 100% detection efficiency of primary particles in various ion beams compared to the reference fluence and the fluence measured using CR-39 PNTDs (G. M. Akselrod et al., 2006; Osinga et al., 2013, 2014a). It was found that the fluence of secondary particles, produced by fragmentation of the primary beam, was underestimated by the FNTD approach compared to simulation. This is the result of the relatively low LET and possibly high angle of incidence of fragments (Klimpki et al., 2016). Osinga et al. showed a 5 fold underestimation of H, He and Li-fragments in a carbon beam (Osinga et al., 2014b).

Track-based dosimetry remains challenging due to the uncertainties in charge, LET and fluence. Osinga et al. reported differences in absorbed doses between a fluence-based FNTD approach, including fragments, and ionization chamber measurements of 2.4% and 4.5% for respectively 142.66 MeV protons and 270.55 MeV/u carbon ions (Osinga et al., 2014b). The mass stopping powers for the primary and secondary particles in this study were estimated in advance. Klimpki et al. employed both fluence and LET measurements to estimate the absorbed dose from a degraded carbon beam to yield a 15% deviation from the expected dose. It was assumed that the relatively large underestimation of 9% was the result of LET and angular uncertainties. The authors argue that the large number of undetected low-LET fragments might be the cause of the found deviation in dose (Klimpki et al., 2016). At higher doses and corresponding ion fluencies, the overlap of tracks becomes problematic. Sykora and Akselrod therefore proposed to use the power spectrum integral (PSI) instead of track counting for dose estimation (Sykora and Akselrod, 2010b). In this approach, the Fourier transformed special frequency spectrum of the fluorescent image is calculated and integrated, excluding the lowest frequencies to avoid background contribution. The PSI approach is able to deal with much higher doses than track counting, but suffers from crystal coloration dependency of LET and requires detectors calibration (Bartz et al., 2014). Due to this LET dependency, significant overestimation of the absorbed dose in the Bragg peak of modulated proton beams was observed. It can therefore be concluded that FNTDs offer excellent opportunities for ion track visualization and radiobiology research via charge and LET spectroscopy, but further research is required before it can be used as independent dosimeter in therapeutic ion beams.

FNTDS IN RADIOBIOLOGY

Aluminum oxide, and therefore the FNTD, is a biocompatible material which means that the detector is non-toxic and cells can grow and thrive on these detectors. This has led to some very innovative uses of FNTDs for radiobiology. In radiobiology, the damage induced in the cell, and mainly in the DNA, is of major importance in improving the effectiveness of the radiotherapy treatment of cancerous tissue and reducing the chance of inducing secondary cancer in healthy tissue. Niklas et al. were the first to combine FNTDs with cell cultures on top of the detector to create a hybrid detector (Cell-Fit-HD) (Niklas et al., 2013b). Various fluorescent markers for cell organelles, nuclei and damages induced in the DNA are commercially available. Tracks in the FNTD, cell geometry and DNA damage can therefore be measured using the same CLSM using a single hybrid detector. FNTDs covered with human lung adenocarcinoma epithelial (A549) cells, a type of lung cancer, were irradiated using a 270.5 MeV/u carbon beam. The cell nuclei were visualized using HOECHST staining and Double Strand Breaks (DSB), a form of DNA damage which is hard to repair and likely to induce cell death, were visualized using γ-H2AX staining. This required the cells to be killed and fixated before imaging. By imaging both the cell layer and the FNTD after irradiation, the induced DNA damage could be determined on a per-track basis (Figure 2-30).

Other studies involved more cell types and staining to produce similar results (Niklas et al., 2013c). Kodaira et al. showed that the Cell-Fit-HD approach also works in live cells when using 53BP1-GFP staining (Figure 2-31), which was an important step required to allow the study of DNA damage and repair over time (Kodaira et al., 2015).
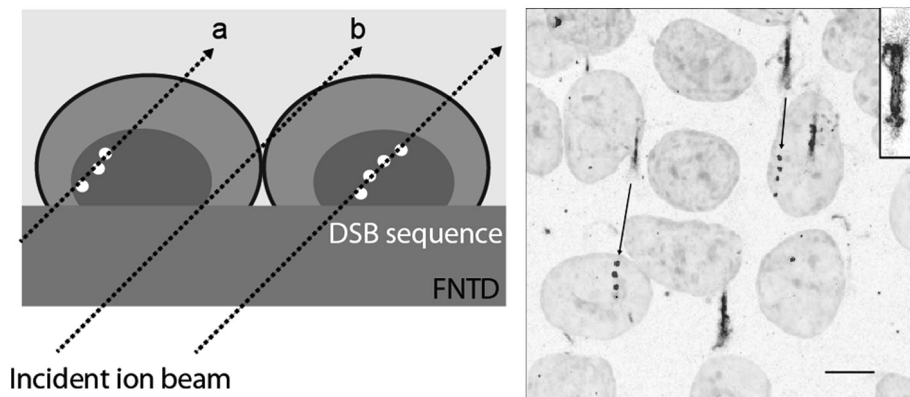
Figure 2-30: Schematic depiction of the acquired FNTD stack proximate to the detector surface (left). A superposition of cellular response as maximum intensity z-projection. The arrows connect the DSB sequences with the corresponding ion tracks. Scale bar is 5 μm (right) (Niklas et al., 2013b).
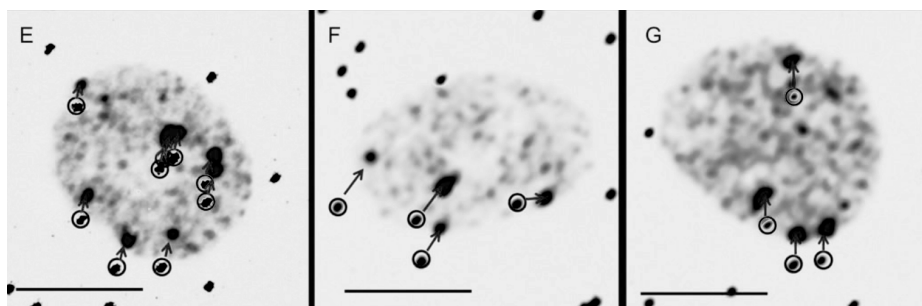
Figure 2-31: Co-localization of double strand breaks and ion tracks using FNTDs in HT1080 fibrosarcoma cells. The DNA DSBs are shown as light grey dots while the circled dots indicate neon ion tracks. Scale bars are 10 µm. The difference in position of the DNA damage and neon ion track spots was caused by cell movement between irradiation and imaging, a natural process unrelated to the FNTD surface or imaging technique (Kodaira et al., 2015).

The Cell-Fit-HD tool was later extended to include clonogenic survival studies (Dokic et al., 2015). These studies look at the fraction of surviving cells following radiation treatment and generally require a large number of cells for statistical significance. The dose to cells and related DNA damage was estimated from the ion tracks in the whole FNTD and the formation of colonies was followed over time. This approach allows the user to study the fate of individual cells and determine factors involved in the survival or death of cells. For radiobiology studies the FNTD crystals became available in various sizes and thicknesses down to 100 µm to better accommodate biological experiments in incubator sample holders able to keep the mammalian cells at 36 °C temperature (Figure 2-32, bottom).

McFadden et al. built a custom first-of-its-kind CLSM that could be placed in a beamline (McFadden et al., 2016). Utilizing fast scanning of the FNTD and cell layer enabled the authors to follow the formation of DNA damage induced by proton radiation in near real-time using their unique experimental setup (Figure 2-32).

Niklas et al. recently adapted the Cell-Fit-HD approach to image the cell layer using wide-field microscopy instead of CLSM. This greatly reduced the imaging time and phototoxicity. This allows for cell kinetics studies on a larger time scale than was possible using only CLSM. These developments offer great opportunities for DNA repair and RBE studies (Dokic et al., 2016), which are considered the fields that require more research for effective heavy ion radiotherapy.
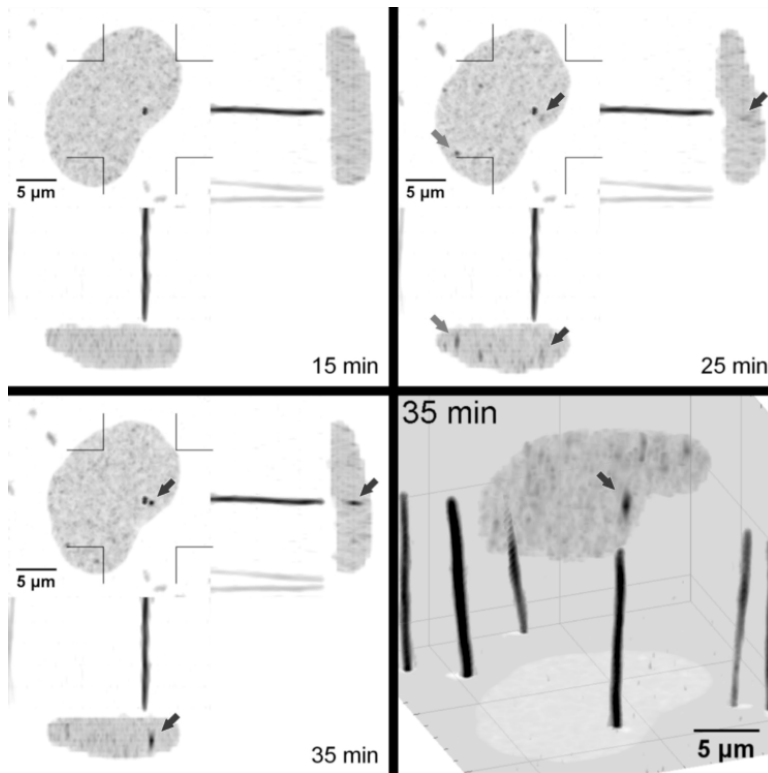
Figure 2-32: Proton tracks passing through a HT1080 cell nucleus and evaluation of DSB foci (indicated dots) over time. Crosshairs - the field of view for the perpendicular projections; Arrows - proton track-induced foci. (McFadden et al., 2016).

For alpha radiation, where the very short range of alpha particles prevent dosimetry methods akin to the techniques described above, we developed a method using U87 Glioblastoma cell imaging with large numbers of alpha tracks measured using FNTDs to determine the dose distribution within the nucleus of U87 cell monolayers (Chapter 6).

It is expected that the described techniques involving FNTD technology will have a significant impact on the field of ion radiobiology. The ability to visualize and follow the development and repair of radiation induced damage should help to unravel the complex mechanism involved in radiation induced cell death. The death and repair mechanisms play an important role in precise determination of the radiation quality and in the design of targeted therapy where moderation of repair mechanism in cancerous cells can greatly increase the treatment efficiency and therapeutic margin - the amount of effective dose than can safely be deposited in target sites before unwanted side-effect occur.

CONCLUSIONS AND OUTLOOK

While initially designed for optical data storage, the unique Al_2O_3:C,Mg-based fluorescent nuclear track detector has grown to become a diverse tool in radiation dosimetry. FNTDs utilize the radiochromic transformations of color centers to visualize the traversal of ionizing particles at a sub-micrometer resolution. Optical and thermal stability of these color centers allow for non-destructive read-out without the need for etching or post-processing, and the detectors can be stored for years without a loss of a signal. Together with the reusability after optical bleaching FNTDs offer significant advantages over other radiation detection techniques. Their small size and physical robustness provide important advantages for numerous applications in radiation dosimetry and spectroscopy.

Utilization of confocal laser scanning fluorescent microscopy for sub-micrometer imaging of the detectors is novel and allows the user to visualize energy depositions in the crystal in 3D with great accuracy. With the introduction of an automated FNTD reader investigator's time required to image a single or multiple detectors has greatly been reduced, paving the way for large scale commercialization of the technology in neutron dosimetry and fundamental research. Additionally, two super-resolution techniques have been successfully used to image ion tracks within the FNTD at resolution below 100 nanometer, providing a valuable tool for future validation of complex Monte Carlo simulations of ion track structures and novel microdosimetric models.

Large number of publications studying the characteristics of FNTDs after irradiation with photons, neutrons and high energy ions have been produced over the past decade. It has been shown that FNTDs are able to discriminate fast and moderated neutrons and can separate neutron and gamma doses in mixed neutron-gamma fields over a wide dose range from 100 μSv to 30 Sv. Using fluorescence intensity, spot size and/or straggling within the fluorescent tracks, various authors were able to discriminate particle charge and LET in both proton and heavy ions with a near 100% detection efficiency. The detectors have also been successfully demonstrated for the quality assurance of synchrotron microbeams and ion beams.

There are still numerous challenges and improvements expected from the FNTD technology. Advances in crystal growth should improve the uniformity of crystals coloration and reduction of background signal. Faster readout instrumentation and image processing software should improve detectability and spectroscopy of low LET protons and even delta electrons.

The biggest advances are expected in radiobiology use of FNTDs where cell-cultures stained with fluorescent markers and grown on top of biologically inert Al_2O_3:C,Mg crystals can be irradiated and imaged in real time or post factum. Ion tracks, imaged by FNTD, and DNA double-strand breaks were already successfully co-localized both after cell fixation and in real-time. This new type of hybrid detector is expected to have a large impact on the field of

radiobiology, where the ability to relate ion traversals, with corresponding charge and LET, to induced radiation damage over time can shed light on the complex mechanism of DNA damage repair and radiation quality. With these rapid developments over the last few years, further developments for the coming years can be expected.

REFERENCES

Akselrod, M.S., Kortov, V.S., Kravetsky, D.J., Gotlib, V.I., 1990. Highly Sensitive Thermoluminescent Anion-Defective Alpha-Al2O3: C Single Crystal Detectors. *Radiat. Prot. Dosimetry.* 32(1), 15-20.

Akselrod, M.S., Lucas, A.C., Polf, J.C., McKeever, S.W.S., 1998. Optically stimulated luminescence of Al2O3. *Radiat. Meas.* 29(3), 391–399. https://doi.org/10.1016/S1350-4487(98)00061-4

Akselrod, M.S., Akselrod, A.E., Orlov, S.S., Sanyal, S., Underwood, T.H., 2003. Fluorescent aluminum oxide crystals for volumetric optical data storage and imaging applications. *J. Fluoresc.* 13, 503–511.

Akselrod, M.S., Akselrod, A.E., 2006. New Al2O3:C,Mg crystals for radiophotoluminescent dosimetry and optical imaging. *Radiat. Prot. Dosimetry* 119(1–4), 218–221. https://doi.org/10.1093/rpd/nci663

Akselrod, G.M., Akselrod, M.S., Benton, E.R., Yasuda, N., 2006. A novel Al2O3 fluorescent nuclear track detector for heavy charged particles and neutrons. *Nucl. Instruments Methods Phys. Res. B* 247(2), 295–306. https://doi.org/10.1016/j.nimb.2006.01.056

Akselrod, M.S., Yoder, R.C., Akselrod, G.M., 2006. Confocal fluorescent imaging of tracks from heavy charged particles utilising new Al2O3:C,Mg crystals. *Radiat. Prot. Dosimetry* 119(1–4), 357–362. https://doi.org/10.1093/rpd/nci664

Akselrod, M.S., Sykora, G.J., 2011. Fluorescent nuclear track detector technology - A new way to do passive solid state dosimetry. *Radiat. Meas.* 46(12), 1671–1679. https://doi.org/10.1016/j.radmeas.2011.06.018

Akselrod, M.S., Bruni, F.J., 2012. Modern trends in crystal growth and new applications of sapphire. J. *Cryst. Growth* 360(1), 134–145. https://doi.org/10.1016/j.jcrysgro.2011.12.038

Akselrod, M.S., Fomenko, V.V., Bartz, J.A., Haslett, T.L., 2014a. Automatic neutron dosimetry system based on Fluorescent Nuclear Track Detector Technology. *Radiat. Prot. Dosimetry* 161(1), 86–91.

Akselrod, M.S., Fomenko, V.V., Bartz, J.A., Ding, F., 2014b. FNTD radiation dosimetry system enhanced with dual-color wide-field imaging. *Radiat. Meas.* 71, 166–173. https://doi.org/10.1016/j.radmeas.2014.05.026

Bartz, J.A., Sykora, G.J., Bräuer-Krisch, E., Akselrod, M.S., 2011a. Imaging and dosimetry of synchrotron microbeam with aluminum oxide fluorescent detectors. *Radiat. Meas.* 46(12), 1936–1939. https://doi.org/10.1016/j.radmeas.2011.04.003

Bartz, J.A., Sykora, G.J., Underwood, T.H., Nichiporov, D.N., Sawakuchi, G.O., Akselrod, M.S., 2011b. Evaluation of aluminum oxide fluorescent and OSL detectors in proton radiotherapy beams. *Radiat. Meas.* 46(12), 1974–1978. https://doi.org/10.1016/j.radmeas.2011.05.047

Bartz, J.A., Zeissler, C.J., Fomenko, V.V., Akselrod, M.S., 2013. An imaging spectrometer based on high resolution microscopy of fluorescent aluminum oxide crystal detectors. *Radiat. Meas.* 56, 273–276. https://doi.org/10.1016/j.radmeas.2013.01.041

Bartz, J.A., Kodaira, S., Kurano, M., Yasuda, N., Akselrod, M.S., 2014. High resolution charge spectroscopy of heavy ions with FNTD technology. *Nucl. Instruments Methods Phys. Res. B* 335, 24–30. https://doi.org/10.1016/j.nimb.2014.05.019

Bräuer-Krisch, E., Rosenfeld, A., Lerch, M., Petasecca, M., Akselrod, M.S., Sykora, G.J., Bartz, J.A., Ptaszkiewicz, M., Olko, P., Berg, A., Wieland, M., Doran, S., Brochard, T., Kamlowski, A., Cellere, G., Paccagnella, A., Siegbahn, E.A., Prezado, Y., Martinez-Rovira, I., Bravin, A., Dusseau, L., Berkvens, P., 2010. Potential high resolution dosimeters for MRT. *AIP Conf. Proc.* 1266, 89–97. https://doi.org/10.1063/1.3478205

Diaspro, A., 2001. Confocal and Two-Photon Microscopy: Foundations, Applications and Advances. Wiley-Liss.

Dokic, I., Niklas, M., Zimmermann, F., Mairani, A., Seidel, P., Krunic, D., Jäkel, O., Debus, J., Greilich, S., Abdollahi, A., 2015. Correlation of Particle Traversals with Clonogenic Survival Using Cell-Fluorescent Ion Track Hybrid Detector. *Front. Oncol.* 5, 275. https://doi.org/10.3389/fonc.2015.00275

Dokic, I., Mairani, A., Niklas, M., Zimmermann, F., Jäkel, O., Debus, J., Haberer, T., Abdollahi, A., 2016. Next generation multi-scale biophysical characterization of high precision cancer particle radiotherapy using clinical proton , helium- , carbon- and oxygen ion beams. *Oncotarget* 7(35), 56676–56689. https://doi.org/10.18632/oncotarget.10996

Evans, B.D., Stapelbroek, M., 1978. Optical Properties of the F+-center in Crystalline Al2O3. *Phys. Rev. B* 18(12), 7089–7098.

Greilich, S., Osinga, J.M., Niklas, M., Lauer, F.M., Klimpki, G.M., Bestvater, F., Bartz, J.A., Akselrod, M.S., Jäkel, O., 2013. Fluorescent nuclear track detectors as a tool for ion-beam therapy research. *Radiat. Meas.* 56, 267–272. https://doi.org/10.1016/j.radmeas.2013.01.033

Greilich, S., Jansen, J., Grischa, M.K., Kouwenberg, J.J.M., Neuholz, A., Pfeiler, T., Rahmanian, S., Stadler, A., Ulrich, L., 2016. Dosimetry for ion-beam therapy using fluorescent nuclear track detectors and an automated reader , 1–36, 2017, arXiv:1610.05054.

Gustafsson, M.G.L., 2000. Surpassing the lateral resolution limit by a factor of two using structured illumination microscopy. *J. Microsc.* 198(2), 82–87. https://doi.org/10.1046/j.1365-2818.2000.00710.x

Harrison, J., Moreno, B., Van Hoey, O., Mihailescu, L.C., Vanhavere, F., Million, M., Fomenko, V., Akselrod, M.S., 2017a. Characterization of fluorescent nuclear track detectors as criticality dosimeters. *Radiat. Meas.* https://doi.org/10.1016/j.radmeas.2017.03.036

Harrison, J., Moreno, B., van Hoey, O., Mihailescu, L.C., Vanhavere, F., Million, M., Fomenko, V. V., Akselrod, M.S., 2017b. Characterization of fluorescent nuclear track detectors as criticality dosimeters II. Radiat. Prot. Dosimetry https://doi.org/10.1093/rpd/ncx236

Hell, S.W., 2003. Toward fluorescence nanoscopy. *Nat. Biotechnol.* 21(11), 1347–1355. https://doi.org/10.1038/nbt895

Klimpki, G.M., Osinga, J.M., Herrmann, R., Akselrod, M.S., Jäkel, O., Greilich, S., 2013. Ion range measurements using fluorescent nuclear track detectors. *Radiat. Meas.* 56, 342–346. https://doi.org/10.1016/j.radmeas.2013.03.014

Klimpki, G.M., Mescher, H., Akselrod, M.S., 2016. Fluence-based dosimetry of proton and heavier ion beams using single track detectors. *Phys. Med. Biol.* 61(3), 1021–1040.

Kodaira, S., Konishi, T., Kobayashi, A., Maeda, T., Farizal, T.A., Ahmad, T., Yang, G., Akselrod, M.S., Furusawa, Y., Uchihori, Y., 2015. Co-visualization of DNA damage and ion traversals in live mammalian cells using fluorescent nuclear track detector. *J. Radiat. Res.* 56(2), 360–365. https://doi.org/10.1093/jrr/rru091

Lee, K.H., Crawform, J.H., 1979. Luminescence of the F-center in Sapphire. Phys. Rev. B 19(6), 3217–3221.

McFadden, C.H., Hallacy, T.M., Flint, D.B., Granville, D.A., Asaithamby, A., Sahoo, N., Akselrod, M.S., Sawakuchi, G.O., 2016. Time-Lapse Monitoring of DNA Damage Colocalized With Particle Tracks in Single Living Cells. *Int. J. Radiat. Oncol. Biol. Phys.* 96(1), 221–227. https://doi.org/10.1016/j.ijrobp.2016.04.007

Niklas, M., Melzig, C., Abdollahi, A., Bartz, J.A., Akselrod, M.S., Debus, J., Jäkel, O., Greilich, S., 2013a. Spatial correlation between traversal and cellular response in ion radiotherapy - Towards single track spectroscopy. *Radiat. Meas.* 56, 285–289. https://doi.org/10.1016/j.radmeas.2013.01.060

Niklas, M., Abdollahi, A., Akselrod, M.S., Debus, J., Jäkel, O., Greilich, S., 2013b. Subcellular spatial correlation of particle traversal and biological response in clinical ion beams. *Int. J. Radiat. Oncol. Biol. Phys.* 87(5), 1141–1147. https://doi.org/10.1016/j.ijrobp.2013.08.043

Niklas, M., Greilich, S., Melzig, C., Akselrod, M.S., Debus, J., Jäkel, O., Abdollahi, A., 2013c. Engineering cell-fluorescent ion track hybrid detectors. *Radiat. Oncol.* 8, 141. https://doi.org/10.1186/1748-717X-8-141

Niklas, M., Henrich, M., Jäkel, O., Engelhardt, J., Abdollahi, A., Greilich, S., 2017. STED microscopy visualizes energy deposition of single ions in a solid-state detector beyond diffraction limit. *Phys. Med. Biol.* 62(9), N180–N190. https://doi.org/10.1088/1361-6560/aa5edc

Osinga, J.M., Akselrod, M.S., Herrmann, R., Hable, V., Dollinger, G., Jäkel, O., Greilich, S., 2013. High-accuracy fluence determination in ion beams using fluorescent nuclear track detectors. *Radiat. Meas.* 56, 294–298. https://doi.org/10.1016/j.radmeas.2013.01.035

Osinga, J.M., Ambrožová, I., Pachnerová Brabcová, K., Akselrod, M.S., Jäkel, O., Davídková, M., Greilich, S., 2014a. Single track coincidence measurements of fluorescent and plastic nuclear track detectors in therapeutic carbon beams. *J. Instrum*. 9, P04013. https://doi.org/http://dx.doi.org/10.1088/1748-0221/9/04/P04013

Osinga, J.M., Brons, S., Bartz, J.A., Akselrod, M.S., Jäkel, O., Greilich, S., 2014b. Absorbed dose in ion beams : Comparison of ionization- and fluence-based measurements. *Radiat. Prot. Dosimetry* 161(1–4), 387–392. https://doi.org/10.1093/rpd/ncu004

Ramirez, R., Tardio, M., Gonzalez, R., Chen, Y., Kokta, M.R., 2005. Photochromism of vacancy-related defects in thermochemically reduced alpha-Al2O3: Mg single crystals. *Appl. Phys. Lett.* 86(8), 1–3. https://doi.org/10.1063/1.1870130

Rossi, H.H., Zaider, M., 1996. Microdosimetry and Its Applications. Springer-Verlag, Berlin.

Sanyal, S., Akselrod, M.S., 2005. Anisotropy of optical absorption and fluorescence in Al2 O3: C,Mg crystals. *J. Appl. Phys.* 98(3). https://doi.org/10.1063/1.1999032

Sawakuchi, G.O., Ferreira, F.A., McFadden, C.H., Hallacy, T.M., Granville, D.A., Sahoo, N., Akselrod, M.S., 2016. Nanoscale measurements of proton tracks using fluorescent nuclear track detectors. *Med. Phys.* 43(5), 2485–2490. https://doi.org/10.1118/1.4947128

Scientific Volume Imaging, 2017. https://svi.nl/STEDMicroscopy [WWW Document].

Sykora, G.J., Akselrod, M.S., Salasky, M., Marino, S.A., 2007. Novel Al2O3:C,Mg Fluorescent Nuclear Track Detectors for Passive Neutron Dosimetry. *Radiat. Prot. Dosimetry* 126(1–4), 278–283.

Sykora, G.J., Akselrod, M.S., Benton, E.R., Yasuda, N., 2008a. Spectroscopic properties of novel fluorescent nuclear track detectors for high and low LET charged particles. *Radiat. Meas.* 43, 422–426. https://doi.org/10.1016/j.radmeas.2007.11.009

Sykora, G.J., Salasky, M., Akselrod, M.S., 2008b. Properties of novel fluorescent nuclear track detectors for use in passive neutron dosimetry. *Radiat. Meas.* 43(2–6), 1017–1023. https://doi.org/10.1016/j.radmeas.2007.12.038

Sykora, G.J., Akselrod, M.S., Vanhavere, F., 2009. Performance of fluorescence nuclear track detectors in mono-energetic and broad spectrum neutron fields. *Radiat. Meas.* 44(9–10), 988–991. https://doi.org/10.1016/j.radmeas.2009.10.027

Sykora, G.J., Akselrod, M.S., 2010a. Photoluminescence study of photochromically and radiochromically transformed Al2O3:C,Mg crystals used for fluorescent nuclear track detectors. *Radiat. Meas.* 45(3–6), 631–634. https://doi.org/10.1016/j.radmeas.2009.11.022

Sykora, G.J., Akselrod, M.S., 2010b. Novel fluorescent nuclear track detector technology for mixed neutron-gamma fields. *Radiat. Meas.* 45(3–6), 594–598. https://doi.org/10.1016/j.radmeas.2010.01.037

Sykora, G.J., Akselrod, M.S., 2010c. Spatial frequency analysis of fluorescent nuclear track detectors irradiated in mixed neutron-photon fields. *Radiat. Meas.* 45(10), 1197–1200. https://doi.org/10.1016/j.radmeas.2010.08.022

Yukihara, E.G., Doull, B., Ahmed, M., Brons, S., Tessonnier, T., Jäkel, O., Greilich, S., 2015. Time-resolved optically stimulated luminescence of Al2O3:C for ion beam therapy dosimetry. *Phys. Med. Biol.* 60(17), 6613–6638. https://doi.org/10.1088/0031-9155/60/17/6613

Chapter 3

A 3D Feature Point Tracking Method for Ion Radiation

J.J.M. Kouwenberg[1], L. Ulrich[2,3], O. Jäkel[2,3,4], S. Greilich[2,3]

[1] Radiation, Science & Technology, Delft University of Technology, Mekelweg 15, Delft, the Netherlands

[2] Division of Medical Physics in Radiation Oncology, German Cancer Research Center (DKFZ), Im Neuenheimer Feld 280, 69120 Heidelberg, Germany

[3] Heidelberg Institute for Radiation Oncology (HIRO), National Center for Radiation Research in Oncology, Im Neuenheimer Feld 280, 69120 Heidelberg, Germany

[4] Heidelberg Ion-Beam Therapy Center (HIT), Im Neuenheimer Feld 450, 69120 Heidelberg, Germany

ABSTRACT

A robust and computationally efficient algorithm for automated tracking of high densities of particles travelling in (semi-) straight lines is presented. It extends the implementation of Sbalzarini and Koumoutsakos and is intended for use in the analysis of single ion track detectors. By including information of existing tracks in the exclusion criteria and a recursive cost minimization function, the algorithm is robust to variations on the measured particle tracks. A trajectory relinking algorithm was included to resolve the crossing of tracks in high particle density images. Validation of the algorithm was performed using Fluorescent Nuclear Track Detectors (FNTD) irradiated with high- and low (heavy) ion fluences and showed less than 1% faulty trajectories in the latter.

INTRODUCTION

The therapeutical use of (heavy) charged particles such as protons, helium or heavier ions in external radiotherapy has gained increased attention over the last years (Hanin and Zaider, 2014; Loeffler and Durante, 2013; Nelson, 2015). In addition, alpha emitters are steadily gaining importance in radionuclide therapy and are even explored in clinical trials (de Kruijff et al., 2015; Elgqvist et al., 2014; Jadvar and Quinn, 2013; Kratochwil et al., 2014; Sartor et al., 2012). The cell killing efficiency per deposited energy by these radiation types can differ significantly from that of mega-voltage X-ray or electrons. This hampers the transfer of clinical experience in dosage and calls for new reference data. Due to the large variation in energy deposition by single ions on micrometer scales, these data have also to be acquired on a cellular level using suitable detector systems. One example for such assays is the Cell-Fit-HD which relies on the use of Fluorescent Nuclear Track Detectors (FNTD) (Niklas et al., 2013a, 2013c) to record 3D data on the path and the energy loss of individual ions. Spatial resolution in the (sub)micrometer range can be achieved in this case when applying confocal laser scanning microscopy for read-out. Other examples include semiconductor detectors and the work done using microbeam facilities (Grad et al., 2012; Hei et al., 2009; Prise and Schettino, 2011; Schettino et al., 2010).

The relatively low cost, biocompatibility and ease-of-use of these detectors result in a wide range of potential applications (Akselrod et al., 2014a; Bartz et al., 2014; Klimpki et al., 2016). However, the automated identification and evaluation of ion tracks using post processing of the fluorescence image data depends significantly on dedicated tracking algorithms.

Feature point tracking, i.e. tracking of points that represent physical particles, is an area of active development with many applications from biology (Chetverikov and Verestói, 1999) to computer vision (Luo et al., 2015). To the best knowledge of the authors, currently available algorithms are impractical or incompatible with the specific requirements of ion beam data

such as crossing of tracks and high numbers of tracks per area. Fluences exceeding 10^7 cm^{-2}, corresponding to 1000 tracks on a 100x100 μm^2 field of view, are often found in clinical beams. On the other hand, ions travel mostly in straight lines which is an excellent property to be used for discrimination between potential tracks. This property has not been fully exploited up to now.

We therefore present here an extension of the algorithm of Sbalzarini and Koumoutsakos (Sbalzarini and Koumoutsakos, 2005), Levy and Incardona (Levy and Incardona, 2014) and the implementation in the MOSAIC Toolsuite for ImageJ (Schneider et al., 2012) and FIJI (Schindelin et al., 2012). A robust and computationally efficient algorithm for the reconstruction of fluorescent ion tracks could be established by introducing a cost function aimed at specific characteristics of ion interactions in matter and adding both a recursive cost minimization function and a track relinking algorithm.

METHOD

Fluorescent nuclear track detector

Detection of ion tracks was done using FNTDs cut from a single crystal of aluminum oxide doped with carbon and magnesium produced by Landauer Inc. (Stillwater, Oklahoma, USA). The dopants produce local charge imbalances in the lattice, known as color centers, which can trap secondary electrons induced by traversing ions and thereby undergo radiochromic transformations (G. M. Akselrod et al., 2006). Exciting the color centers with a 633 nm HeNe laser produces fluorescence at 750 nm, which allows for read out with a Confocal Laser Scanning Microscope (CLSM). The high color center density and low background fluorescence allows for a large range in detectable Lineal Energy Transfer (LET) (Bartz et al., 2014). A track of an ion is visible as a bright spot against a low intensity background, where the intensity of the spot is dependent on the LET (Niklas et al., 2013d). We will refer to the observed spots as 'feature points'. It is important to note that a feature point does not necessarily represent a physical particle due to the possibility of false-positive detection due to noisy or defect samples.

Feature point detection

This paper largely follow the notation of Sbalzarini and Koumoutsakos (2005) to enhance clarity. FNTD readout commonly yields a stack of $n = 1 \dots N$ image slices, each X by Y pixels in size, thereby representing a volume V in the FNTD. Detection of spots in the slices was done using Levy's algorithm for feature point extraction as found in the MOSAIC ToolSuite plugin for ImageJ and FIJI, yielding for each slice image A_n a set of feature points P^{A_n} for intensity threshold I and feature point radius r. The amount of feature points in P^{A_n} is given by

$\dim(P^{A_n})$. Feature points are viewed in Euclidian space where x and y represent the pixel numbers in the respective directions, while z represents the depth in the image stack as given by the slice number n.

Feature point linking

Trajectories are formed by linking feature points in P^{A_n} to feature points in subsequent slices $P^{A_{n+k}}$ where $k = 1 \dots R$ and R is the user-specified link range. Due to the different focus of application, linking is done between feature points in depths (slice dimension) rather than in time (frame dimension) as in Sbalzarini and Koumoutsakos (2005). This, however, does not affect the generality of the following considerations.

By applying a cost function to each feature point combination, the cost matrix $C^{A_n} \in \mathbb{R}^{\dim(P^{A_n}) \times \sum \dim(P^{A_{n+k}})}$ is constructed. Since the method used in this paper employs a recursive minimization function for linking instead of a common assignment problem approach, there is no longer a need for matrix filling using the dummy feature points found in Sbalzarini and Koumoutsakos (2005) when $\dim(P^{A_n}) \neq \dim(P^{A_{n+k}})$. The association matrix given by Sbalzarini and Koumoutsakos (2005) is replaced by an association vector $G^{A_n} \in \mathbb{R}^{\dim(P^{A_n})}$, containing the indices of the linked partners for the feature points in P^{A_n}. Trajectories are later extracted by following the indices in G^A. The values of G^{A_n} are set to 0 to represent the absence of links.

Linking cost function

Let $C_{i,j}^{A_n} = \sum_{\text{feature}} \phi_{i,j}^{feature}$. Each feature $\phi_{i,j}^{feature}$ penalizes the mismatch of a specific characteristic between feature point i in P^{A_n} and feature point j in $P^{A_{n+k}}$, so that $C_{i,j}^{A_n}$ is a compressed representation of the matching of these characteristics. Assuming each feature point i has only one true linking partner j, finding the lowest the linking cost in $C_{i,j}^{A_n}$ for each feature point i will approximate the solution to minimizing the cost matrix, i.e. $\sum_i \min C_{i,j}^{A_n} \approx \min \sum_i C_{i,j}^{A_n}$, for a fraction of the calculation time. Heavy ions can safely assumed to follow an approximately straight path with constant velocity considering the typical track-lengths assessed in an FNTD, i.e. several tens of micrometers. Cumulative effects of small-angle coulomb-scattering are tolerated by the algorithm, while the frequency of large-angle events can be – even at the end of the particle range – considered to be rare and their impact on the track reconstruction (splitting of one track into two tracks with corresponding total length) as benign. Four features are used for the linking of feature points in this method. Some of these features find their basis in the work of Sbalzarini and Koumoutsakos, Levy and Incardona, but were modified to better serve the tracking of ions with these characteristics.

Features

To filter unlikely linking candidates, the first feature describes the distance between feature points which is given by the squared distance between feature points i and j.

$$\phi_{i,j}^{\text{distance}} = w_d^2 \begin{cases} \left|d_{i,j}\right|^2 + (n_j - n_i)^2, & \left|d_{i,j}\right|^2 + (n_j - n_i)^2 \le d_{p,max} \\ \infty, & \text{elsewhere} \end{cases} \qquad (3\text{-}1)$$

Where w_d is the user-specified distance weight factor, $d_{i,j}$ is the linking distance in the x-y plane and $d_{p,max}$ is the user-specified maximum linking distance. In order to favor constant intensities, the second feature is based on the likeness of the zero and second order intensity momenta.

$$\phi_{i,j}^{\text{intensity}} = \frac{w_i^2}{\pi \cdot r^2} \sum_{x=-r}^{r} \sum_{y=-r}^{r} (1 + x^2 + y^2) \cdot \begin{cases} \left|I_{x,y}^j - I_{x,y}^i\right|, & x^2 + y^2 \le r^2 \\ 0, & \text{elsewhere} \end{cases} \qquad (3\text{-}2)$$

Where w_i is the user-specified feature weight factor, r is the feature point radius and $I_{x,y}^p$ is the pixel intensity at position x, y from the center of feature point p. The third feature is given as the absolute velocity difference, where $v_{i,j}$ is the link velocity vector as given by eq. (3-4).

$$\phi_{i,j}^{\text{velocity}} = w_v^2 \begin{cases} \left| \left|v_{i,j}\right|^2 - \left|\bar{v}_i^H\right|^2 \right|, & \left|\bar{v}_i^H\right|^2 > 0 \\ 0, & \text{elsewhere} \end{cases} \qquad (3\text{-}3)$$

$$v_{i,j} = \begin{bmatrix} \Delta\text{x}/\Delta z \\ \Delta\text{y}/\Delta z \end{bmatrix} = \frac{1}{n_j - n_i} \begin{bmatrix} x_j - x_i \\ y_j - y_i \end{bmatrix} \qquad (3\text{-}4)$$

w_v is the user-specified velocity weight factor and $\bar{v}_i^H$ is the average link velocity vector of the last H feature points in the trajectory of feature point i, where H is specified by the user. When feature point i is not part of an existing trajectory, $\bar{v}_i^H$ is set to zero. The final feature is based on the angle between the $\bar{v}_i^H$ and $v_{i,j}$.

$$\phi_{i,j}^{\text{angle}} = w_a^2 \begin{cases} f(\theta_{i,j})^2 & |d_{i,j}| > {}^{r_p}\!/_2, |\bar{v}_i^H|^2 > 0, |\theta_{i,j}| \le \theta_{p,max} \\ \beta \cdot f(\theta_{p,max})^2 & |d_{i,j}| > {}^{r_p}\!/_2, |\bar{v}_i^H|^2 = 0 \\ \gamma \cdot f(\theta_{p,max})^2 & |d_{i,j}| \le {}^{r_p}\!/_2 \\ \infty & \text{elsewhere} \end{cases} \tag{3-5}$$

$$f(\theta_{i,j}) = \frac{\alpha}{2}\left[\cos\theta_{i,j} - 1\right] = \frac{\alpha}{2}\left[\frac{(v_{i,j} \cdot v_i^H)}{|v_{i,j}||v_i^H|} - 1\right] \tag{3-6}$$

Where w_a is the user-specified angle weight factor, r_p is the allowed particle drift, usually given by the particle radius r, and $\theta_{p,max}$ is user-specified maximum allowed feature point linking angle. To allow for small noise variations in tracks perpendicular to the z-axis, a standard cost value is used for links with $|d_{i,j}| \le {}^{r_p}\!/_2$. However, since continuation of existing tracks is favoured, β was chosen higher than 1. It was experimentally found by applying the method to the set of alpha tracks given in the section "*241Am Alpha radiation energy estimation*" that $\alpha = d_{max}$, $\beta = 6/5$ and $\gamma = 1$ were good values. Both β and γ were set (close) to 1 in order to simplify the interpretation of the angle cost factor for the user.

When the link range $R \ge 2$, an extra criteria is introduced in order to prevent multiple links to feature point j. If $j \in G$, i.e. feature point j has already been linked to from one of the previous image slices, and the current link $C_{i,j}^{A_n}$ exceeds the cost of the previous link, then $C_{i,j}^{A_n}$ is to ∞ to prevent suboptimal replacements of links during feature point linking.

Link cost minimization

Feature point linking is performed by applying a recursive minimization function which aims to find the best linking candidate i for each feature point j in $P^{A_{n+k}}$, given that each feature point can only be linked once. When feature point i was already linked, i.e. $G_i^{A_n} > 0$, and the cost for linking feature point j to i is lower than the cost of the existing link, the existing link is replaced and the function calls itself to find the next best link for delinked feature point $j = G_i^{A_n}$ in $P^{A_{n+k}}$. This process is halted when no new link with cost lower than C_{max}, the maximum allowed linked cost, which was experimentally chosen as $4\,d_{p,max}^2$, can be found. A pseudo-code representation of the function is on the next page.

```
Function FindBestLink (feature point j)
  cost = C_max,    candidate = -1
  for each feature point i do
    if C_{i,j}^{A_n} < cost && C_{i,j}^{A_n} < C_{i,G_i^{A_n}}^{A_n} then
        candidate = i, cost = C_{i,j}^{A_n}
  End
  if candidate == -1 then
    no link found, return
  if G_candidate^{A_n} == -1 then
    G_candidate^{A_n} = j, return
  else then
    old_j = G_candidate^{A_n} , G_candidate^{A_n} = j
    Call self to find next best link for feature point old_j:
  end
```

Trajectory relinking

The restriction that each feature point can only be in one trajectory leads to broken trajectories when particles overlap during crossing of tracks. Relinking of trajectories is therefore required for high particle density experiments. Let T^A be a set of trajectories in A, where each trajectory contains a set of linked feature points $\hat{p}_l$ and let $\dim(T^A)$ be the number of trajectories in A. By applying a cost function to each trajectory combination, a cost vector $D^{l,A} \in \mathbb{R}^{\dim(T^A)}$ can be constructed for each trajectory $l = 1\ldots\dim(T^A)$ so that $D_m^{l,A} = \sum_{\text{feature}} \phi_{l,m}$, where m represents the relinking candidates in T^A. Note that due to the symmetry $D_m^{l,A} = D_l^{m,A}$, only $m = l + 1 \ldots \dim(T^A)$ needs to be calculated and $D_{m=1..l}^{l,A}$ can be set to ∞.

Features

Since trajectory relinking uses the same trajectory data as the former linking process, the five proposed features for trajectory relinking are similar to those found for feature point linking. The ^{first} and ^{last} superscripts are used to indicate the first and last feature point and their respective properties in the given trajectory. For simplification of the expressions in this section, let t_1 and t_2 represent respectively the first and last starting trajectory. t_1 and t_2 are then given for each combination l, m so that $n_{t_2}^{first} \geq n_{t_1}^{first}$. In order to allow trajectories to bridge a maximum of one whole feature point linking step, a scenario where a particle disappears or is unavailable for linking for R slices, the first feature given in eq. (3-7) is introduced.

$$\phi_{t_1,t_2}^{\text{z-order}} = \begin{cases} 0, 0 \leq n_{t_2}^{first} - n_{t_1}^{last} \leq 2R + 1 \\ \infty, \qquad \text{elsewhere} \end{cases} \qquad (3\text{-}7)$$

Unlikely relinking candidates are filtered using eq. (3-1) with $i = t_1^{last}$, $j = t_2^{first}$, $d_{p,max} = d_{t,max}$, where $d_{t,max}$ is the user-specified maximum trajectory relinking distance. $w_{distance}$ was set to the same user-specified value as for feature point linking. Let $\bar{v}_{t_1}$ and $\bar{v}_{t_2}$ represent the average velocity vectors for respectively t_1 and t_2. The averaged linking vector $\bar{v}_{t_1,t_2}$ between the Q closest endpoint pairs in the trajectories is given by:

$$\bar{v}_{t_1,t_2} = \frac{1}{Q} \sum_{q=0}^{Q-1} \frac{1}{n_{t_2}^{first+q} - n_{t_1}^{last-q}} \begin{bmatrix} x_{t_2}^{first+q} - x_{t_1}^{last-q} \\ y_{t_2}^{first+q} - y_{t_1}^{last-q} \end{bmatrix} \tag{3-8}$$

Where Q is the number of endpoints used for averaging which showed the best experimental results for $Q = 3$. To ensure alignment between the trajectories as well as the trajectories and the linking vector, the third feature penalizes difference between these respective velocity vectors.

$$\phi_{t_1,t_2}^{align} = w_a^2 \begin{cases} f(\theta_a)^2 & |\theta_a| \leq \theta_{t,max} \ \& \ |\theta_b| \leq \theta_{t,max} \\ \infty & \text{elsewhere} \end{cases} \tag{3-9}$$

Where θ_a is the angle between $\bar{v}_{t_1}$ and $\bar{v}_{t_2}$ and θ_b is the angle between $(\bar{v}_{t_1} + \bar{v}_{t_2})/2$ and $\bar{v}_{t_1,t_2}$. $\theta_{t,max}$ is the maximum allowed trajectory relinking angle. $\theta_{t,max}$ was set to $\theta_{p,max}$ in the code implementation for these experiments due to the high similarity between these parameters. The last two features are given by the intensity and velocity features as used for feature point linking using the track averages.

Trajectory relinking

Trajectory l is linked to trajectory $M = \min_m D^{l,A}$ if $D_m^{l,A} \leq D_{max}$, where D_{max} is a user-specified maximum linking cost, usually given as a function of $d_{t,max}$. By merging l into M, i.e. $\hat{p}_M = \hat{p}_l \ || \ \hat{p}_M$, during linking, the newly merged trajectory is considered for further cost function evaluations. Due to the small number of trajectories and relinking candidates, this simplified cost minimization approach was found to be sufficient.

Code implementation

The linking procedure described was implemented in Java 1.6 as part of a larger collection of FNTD related routines (the 'FNTD package') and uses various FIJI classes. Also, some MOSAIC Toolsuite classes were extended to allow for storage of the feature points and their respective information required for this method, while maintaining compatibility with the MOSAIC

feature point detection routine. Execution of the Java code and analyses of the results were done using the FNTD package (v0.8.1) for the R language (R Core Development Team, 2011) (v3.2.2). The sources for both the R routines and the Java code are freely available at Github (*https://github.com/FNTD*). For Fiji, the latest version of the plugin is provided via the update site at *http://sites.imagej.net/FNTD*. Installation and usage instructions are available at *https://fntd.dkfz.de/fntd/index.php/Main_Page.*

VALIDATION

High fluence synchrotron carbon ion irradiation algorithm comparison

The improvement that can be achieved with the described algorithm is especially distinct for very complex particle fields. The benefit is illustrated at an FNTD irradiated in the rising flank of a Spread-Out Bragg Peak (SOBP) of a clinical 12C ion beam. RW3 water equivalent plastic slabs (PTW Freiburg GmbH) were used as phantom material. The irradiation consisted of 18 separate beams leading to a SOBP located at a depth of 10 to 15 cm. The FNTD was positioned at 8.5 cm where the total particle fluence reaches a maximum. This represents a clinically relevant, but at the same time most challenging, situation for identifying trajectories due to the large amount of secondary fragments in the beam, which yield a significant variation in fluorescence intensity and track direction.

The FNTDs were read out using the Landauer FXR700RG automated reader, a CLSM dedicated to FNTD readout which uses a 100x 0.95 air objective in combination with an Avalanche Photo Diode (APD) (Akselrod et al., 2014a). A readout stack of 20 images with an image size of 200x200 μm^2 (1024 x 1024 pixel) and 5 μm separation between the slices was acquired. A zoomed section of the first slice is shown in Figure 3-1.

The background was subtracted using the histogram-based 'background subtractor' from the MOSAIC ToolSuite (Cardinale, 2010). The intensity decrease near the edges of the FOV and deeper in the sample were corrected using field-of-view non-uniformity and spherical aberration corrections as presented in (Bartz et al., 2014). Particle tracks were reconstructed both with the presented 3D feature point tracking method and with the algorithm of Sbalzani and Koumoutsakos (Sbalzarini and Koumoutsakos, 2005) and Levy and Incardona (Levy and Incardona, 2014), from now on referred to as 'previous method'. In both cases particle segmentation was achieved with a relative threshold of 5%, a particle radius of 3 pixels and no cut-off value in order to avoid outlier discrimination. Particle linking was performed with the parameters listed in Table 3-1.
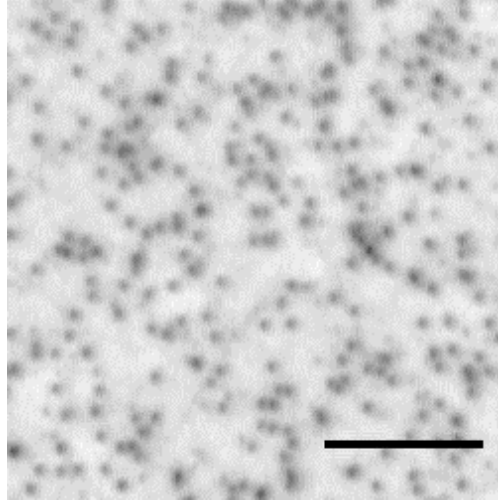
Figure 3-1: 2x zoomed fluorescence image of first slice of a stack in the FNTD. The scale bar corresponds to 16 μm.

Table 3-1: Feature point linking parameters for the 12C irradiated samples. Values used for the two linking methods are listed separately.

Parameter	Previous method	Proposed method	Parameter	Previous method	Proposed method
I	5%.		w_d	1	1
$r = r_p$	-	4 px	w_i	1	1
$d_{p,max}$	15 px	15 px	w_v	-	1
R	2	2	w_a	-	1
$\theta_{p,max}$	-	20°	$d_{t,max}$	-	40 px

Since very short trajectories are likely to be caused by the linking of erroneously segmented features or the incorrect linking of true particles the minimum trajectory length was set to 5 slices.

Figure 3-2 visualizes a comparison between the tracks reconstructed in sections of the image with the previous method (a,c,e) and with the proposed method (b,d,f). The images show the projection of the reconstructed tracks along the z-axis and thus correspond to a zoomed section of the readout volume.

A crucial constraint for the production of physically reasonable tracks is the maximum track angle $\theta_{p,max}$. In the previous method this parameter was not implemented. In Figure 3-2 all

numbered tracks 1-10 show unphysically strong bends. With the proposed method the corresponding feature points were linked differently since the maximum allowed linking angle was set to 20° with respect to the average link velocity vector of the last H=3 feature points. The angle threshold also prevents linking of parallel tracks like performed for track 2.
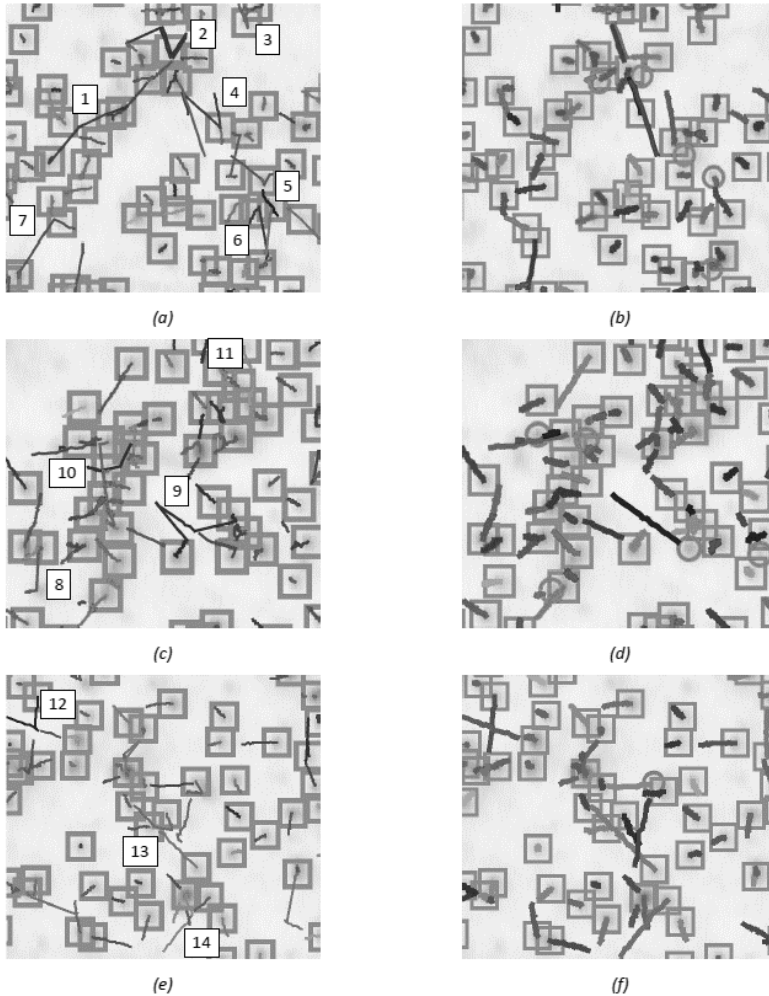
Figure 3-2: Tracks produced by the implementation of Sbalzarini and Koumoutsakos, Levy and Incardona (left), compared to the proposed method (right). Squares indicate a tracked feature point while lines indicate projections of a track. Circles represent tracked feature points that were not assigned to a track. Track shade and thickness between the methods do not correspond. The numbered tracks are described in the text.

Since the presented algorithm performs a recursive minimization of the cost function instead

of an assignment problem approach all feature points are more likely to be linked to the best linking candidate. The different approaches can for example result in an altered assignment of feature points to tracks as in location 11. The points belonging to the green and pink tracks are also considered in the presented algorithm but distributed differently among the two tracks.

The choice and interplay of features included into the cost function in the presented method leads to a strongly improved reconstruction of crossing trajectories compared to the previous method. This effect is very beneficial for experiments with complex high fluence particle fields. Improved linking can e.g. be seen for tracks 12, 13 and 14 in the bottom row of Figure 3-2.

As described earlier, the proposed method enables relinking of trajectories with very similar features. Tracks break apart if corresponding feature points are tracked incompletely. This occasionally happens with tracks of secondary particles with low fluorescence intensity and large track angles with respect to the z-axis or crossing tracks which overlap in one or more image slices. As shown in the top row of Figure 3-3 the benefit for linking of crossing tracks compared to the previous method (cf. bottom row of Figure 3-2) is partly due to the implementation of track relinking (track 13 and 14). The bottom row of Figure 3-3 shows another comparison between the linking results without (a,c) and with (b,d) relinking for crossing trajectories (15 and 16) and for a secondary particle track (17).
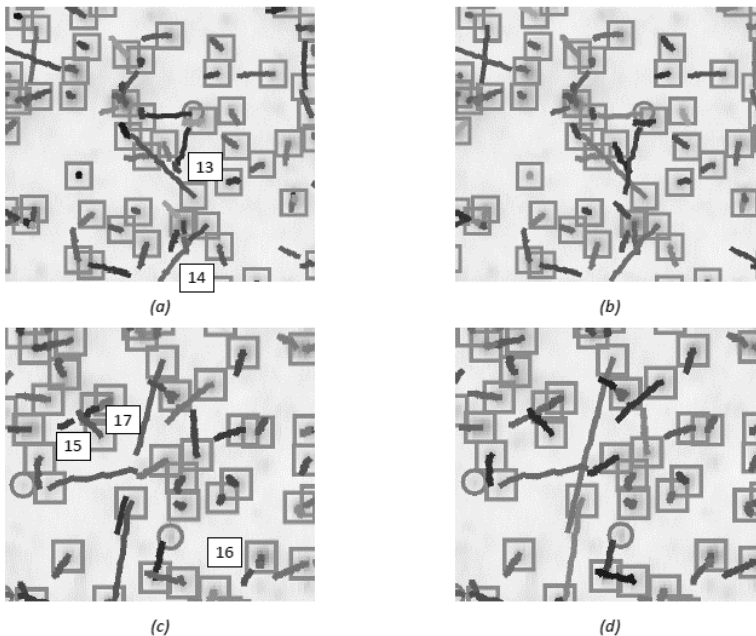
Figure 3-3: Tracks produced by the proposed algorithm with (left) and without relinking (right). The numbered features are explained in the text.

241Am alpha radiation energy estimation

An FNTD was irradiated from the top with a circular 241Am source, with $r_{source} \gg r_{FNTD}$ and 2.5 mm air between the source and the FNTD so that the irradiation was unidirectional. The expected fluence in the FNTD was 1.25×10^6 cm^{-2}, which corresponds roughly to the scenario of a cell study with 1 alpha track per 10 μm diameter cell. The FNTD was read-out using a Carl Zeiss LSM710 with a 63x 1.40 oil-immersion objective and two fiber-coupled, photon-counting APDs (Klimpki et al., 2016). 6 separate image stacks, each containing 42 slices, were obtained. Each image slice contained 1024 x 1024 pixels with pixel dimensions 0.13 x 0.13 x 0.47 μm^3 (x, y, z). The surface location was obtained via measurement of the surface reflection using the second APD parallel to the fluorescent measurement.

Feature point detection was performed with an absolute threshold just above the background noise threshold and a relatively large feature point radius of 6 pixels, as to prevent the detection of multiple feature points within an elongated spot. Again, the cut-off value was not set in order to avoid outlier discrimination. The feature point linking routine was executed with the parameters given in Table 3-2.
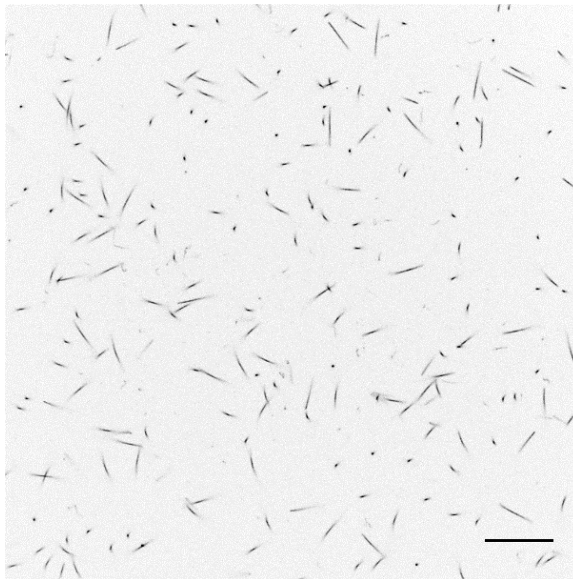

Figure 3-4: FNTD irradiated with alpha particles produced by the decay of 241Am. Note the wide variety of incidence angles (as seen from the elongated shapes), the crossing of tracks and presence of highly energetic delta rays. The scale bar corresponds to 16 μm.

Table 3-2: Feature point linking parameters for 241Am irradiation linking.

	Value		**Value**
I	35 a.u.	w_d	0.5
$r = r_p$	5 px	w_i	1
$d_{p,max}$	30 px	w_v	0.1
R	3	w_a	1
$\theta_{p,max}$	20°	$d_{t,max}$	50 px
H	5	D_{max}	$1 \cdot C_{max}$

Since the feature point detection routine was built for circular spots, ion tracks with very high angles of incidence let to detection and linking artefacts due to their elongated appearance. Tracks spanning less than 8 slices or with fitted angles $\theta > 50$ degrees were therefore removed. When inclusion of these tracks is critical for the user, more sophisticated, and computationally intensive, detection algorithms are available which to recognize more complex shapes (Arganda-Carreras et al., 2014; Rizk et al., 2014). However, extra effort is required to make these algorithms output the feature points in a compatible format.

The reference fluence Φ_{adj} was calculated taking into account the maximum angle of acceptance θ:

$$\Phi_{\mathrm{adj}}(\theta) = \Phi \cdot (1 - \cos\theta) \tag{3-10}$$

where Φ is the fluence for the entire hemisphere (solid angle = pi). A total of 509 tracks was found after filtering, while the adjusted reference fluence was 489 ± 44. A total of 39 tracks originated from trajectory relinking, exemplifying the significance of this added routine.

For further analysis of the tracks, tracks ending close to the border of the image were removed, due to their likelihood having a part of the track lying out of bounds, thereby appearing as an artefact. The penetration length of each track was calculated from the incidence angle and the depth of the last feature point in respect to the surface. Refinement of the exact endpoint was based on the intensity of the last few feature points. Knowing the penetration depth and the thickness of the layer of air, the total traversed distance and thereby the equivalent range in water for each track could be calculated. The range in water to initial kinetic energy translation table was obtained using SRIM (Ziegler, 2010). The resulting calculated initial alpha kinetic energy was 5451 ± 310 keV (Figure 3-6). The limited z-resolution, energy loss straggling, detector noise and the unknown thickness of the activity layer added to the uncertainty. However, artefact can be identified as tracks with a measured energy far away from the given distribution curve relating incident angle and length. From Figure 3-6 it was estimated that this was the case for less than 1% of the reconstructed trajectories.
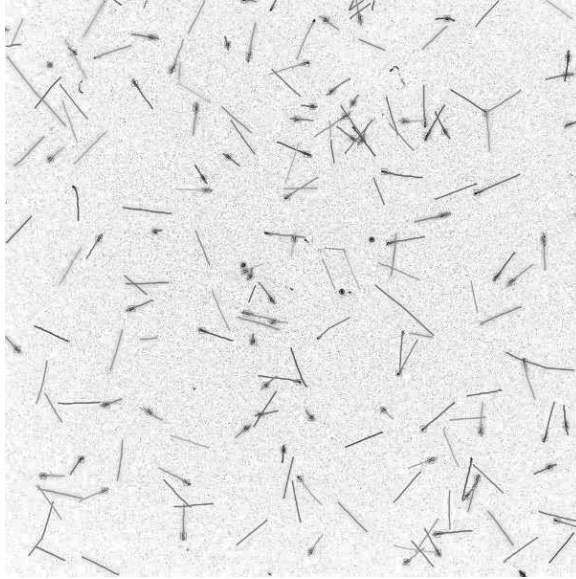
*Figure 3-5: Linking of the sample in Figure 3-4 with the parameters in Table 3-2. Feature points are correctly linked in crowded areas and no artefacts are visible. The elongated spots from particles with very high angles of incidence led to detection of multiple feature points.*
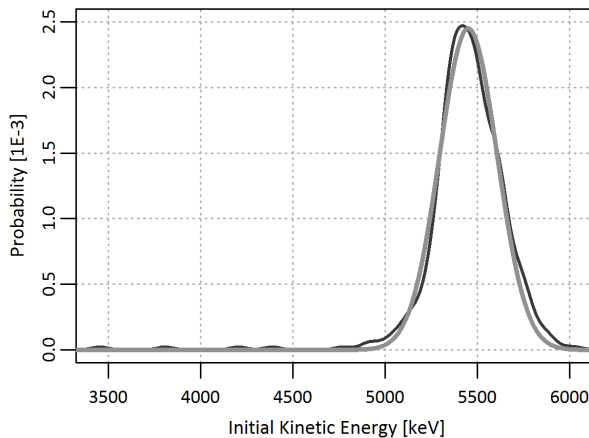
Figure 3-6: The calculated initial kinetic energy distribution in dark grey with the Gaussian fit shown in light gray.

Parameter Sensitivity Analysis and Usability

A one-at-a-time parameter sensitivity analysis was performed on the measured alpha tracks. The effect of varying each parameter on the fitted mean energy, fluence and RMSE of the fit were measured while the rest of the parameters was as given in Table 3-2. The detailed results are given in Appendix A. In summary, it was found that the 13 parameters can be subdivided in two general categories: fine-tuning parameters, parameters that (mildly) influence the algorithm over a wide range, and threshold parameters, parameters that influence the algorithm only from a specific value, similar to an on/off-switch (Table 3-3).

The algorithm proved to be stable and failed only when critical aspects were disabled. For example, setting the maximum linking distance to very small values yielded a large deviation from the expected behaviour. Most of variables are robust and serve a role in fine-tuning the algorithm to obtain the best results for the specific application. Some parameters reflect a physical property and can be estimated using the available data, namely intensity threshold I, particle radius r, maximum displacement $d_{p,max}$, particle drift r_p, maximum linking angle $\theta_{p,max}$ and the maximum trajectory relinking distance $d_{t,max}$. The remaining seven parameters require an initial guess from the user. Three of these parameters, namely distance weight w_d, angle weight w_a and relink cost D_{max} are threshold values and therefore require manual iterating to find their working values. This can be done quickly and interactively using the Fiji implementation. The remaining four parameters are fine-tuning parameters and are expected to be work over a wide range of values. While the number of parameters can in principle be reduced given the above findings and using default values for specific applications, they provide the experienced user with flexibility.

CONCLUSION

The combination of an iterative cost minimization function and a trajectory relinking algorithm in addition to a specialized cost function aimed at favouring constant trajectories, resulted in a fast and accurate algorithm for single ion track reconstruction that could be validated for both high and low fluence samples. Linking of particles and relinking of trajectories using one thread for 45000 (2900) particles took 4.43 (0.16) seconds on an Intel(R) Core(TM) i5-560M 2.67 GHz processor, compared to 32.16 (13.25) seconds for the old implementation. The high fluence SOBP carbon-12 experiment tested the algorithm for high fluences with up 2000 tracks per 512x512 pixel image, a scenario that could not be tracked reliably with existing methods. A clear increase in fragmentations was visible, despite their high angles of incidence and relatively low SNR. It is expected that these fluences are at the limit of this algorithm, partly due to difficulty of detecting the correct feature points for these scenarios. The low fluence 241Am alpha irradiation experiment showed a low artefact count with less than 1% faulty

trajectories and a calculated fluence that closely matched the expected value. It was found that most input variables could be chosen intuitively by the user and an appropriate set of parameters could usually be found within one or two iterations. The Fiji plugin allows for easy and quick optimization of the linking parameters without the need for prior programming knowledge, while the R shell is best used for linking of larger sample sets and trajectory data analyses.

Table 3-3: Feature point linking parameter properties.

Category	Parameter	Type	Sensitivity	Physical property
Feature Point Selection	I	Fine-tuning	Strong	Yes
	r	Fine-tuning	Strong	Yes
Feature Point Linking	$d_{p,max}$	Threshold	-	Yes
	R	Fine-tuning	Low	No
	r_p	Fine-tuning	Mild	Yes
	$\theta_{p,max}$	Fine-tuning	Mild	Yes
	H	Fine-tuning	Low	No
	w_d	Threshold	-	No
	w_i	Fine-tuning	Low	No
	w_v	Fine-tuning	Strong	No
	w_a	Threshold	-	No
Trajectory Relinking	$d_{t,max}$	Threshold	-	Yes
	D_{max}	Threshold	-	No

ACKNOWLEDGEMENTS

REFERENCES

Akselrod, G.M., Akselrod, M.S., Benton, E.R., Yasuda, N., 2006. A novel Al2O3 fluorescent nuclear track detector for heavy charged particles and neutrons. *Nucl. Instr. Methods B* 247(2), 295–306. https://doi.org/10.1016/j.nimb.2006.01.056

Akselrod, M.S., Fomenko, V.V., Bartz, J.A., Haslett, T.L., 2014. Automatic neutron dosimetry system based on Fluorescent Nuclear Track Detector Technology. *Radiat. Prot. Dosimetry* 161(1), 86–91.

Arganda-Carreras, I., Kaynig, V., Schindelin, J., Cardona, A., Seung, H.S., 2014. Trainable Weka Segmentation : A Machine Learning Tool for Microscopy Image Segmentation.

Bartz, J.A., Kodaira, S., Kurano, M., Yasuda, N., Akselrod, M.S., 2014. High resolution charge spectroscopy of heavy ions with FNTD technology. *Nucl. Instr. Methods B* 335, 24–30. https://doi.org/10.1016/j.nimb.2014.05.019

Cardinale, J., 2010. Histogram-based background subtractor for ImageJ.

Chetverikov, D., Verestói, J., 1999. Feature Point Tracking for Incomplete Trajectories. *Computing* 62(4), 321–338. https://doi.org/10.1007/s006070050027

de Kruijff, R., Wolterbeek, H.T., Denkova, A.G., 2015. A Critical Review of Alpha Radionuclide Therapy— How to Deal with Recoiling Daughters? *Pharmaceuticals* 8(2), 321–336. https://doi.org/10.3390/ph8020321

Elgqvist, J., Frost, S., Pouget, J.P., Albertsson, P., 2014. The Potential and Hurdles of Targeted Alpha Therapy – Clinical Trials and Beyond. *Front. Oncol.* 3(January), 1–9. https://doi.org/10.3389/fonc.2013.00324

Grad, M., Harken, A., Randers-Pehrson, G., Attinger, D., Brenner, D.J., 2012. An ultra-thin Schottky diode as a transmission particle detector for biological microbeams. *J. Instrum.* 7, 1–22. https://doi.org/10.1088/1748-0221/7/12/P12001

Hanin, L., Zaider, M., 2014. On the probability of cure for heavy-ion radiotherapy. *Phys. Med. Biol.* 59(14), 3829–3842. https://doi.org/10.1088/0031-9155/59/14/3829

Hei, T.K., Ballas, L.K., Brenner, D.J., Geard, C.R., 2009. Advances in radiobiological studies using a microbeam. *J. Radiat. Res.* 50 Suppl A(0 0), A7–A12. https://doi.org/10.1269/jrr.08135S

Jadvar, H., Quinn, D.I., 2013. Targeted α-particle therapy of bone metastases in prostate cancer. *Clin. Nucl. Med.* 38(12), 966–71. https://doi.org/10.1097/RLU.0000000000000290

Klimpki, G.M., Mescher, H., Akselrod, M.S., 2016. Fluence-based dosimetry of proton and heavier ion beams using single track detectors. *Phys. Med. Biol.* 61(3), 1021–1040.

Kratochwil, C., Giesel, F.L., Bruchertseifer, F., Mier, W., Apostolidis, C., Boll, R., Murphy, K., Haberkorn, U., Morgenstern, A., 2014. 213Bi-DOTATOC receptor-targeted alpha-radionuclide therapy induces remission

in neuroendocrine tumours refractory to beta radiation: a first-in-human experience. *Eur. J. Nucl. Med. Mol. Imaging* 41(11), 2106–2119. https://doi.org/10.1007/s00259-014-2857-9

Levy, G., Incardona, P., 2014. MOSAIC ParticleTracker 2D and 3D [WWW Document]. http://mosaic.mpi-cbg.de/ParticleTracker/.

Loeffler, J.S., Durante, M., 2013. Charged particle therapy--optimization, challenges and future directions. *Nat. Rev. Clin. Oncol.* 10(7), 411–424. https://doi.org/10.1038/nrclinonc.2013.79

Luo, N., Sun, Q., Chen, Q., Ji, Z., Xia, D., 2015. A Novel Tracking Algorithm via Feature Points Matching. *PLoS One* 10(1), e0116315. https://doi.org/10.1371/journal.pone.0116315

Nelson, B., 2015. A beam of hope for heavy ion radiotherapy: Promising clinical results and better designs are adding new momentum to the push for more proton and carbon ion radiotherapy centers. *Cancer Cytopathol.* 123(8), 445–446. https://doi.org/10.1002/cncy.21598

Niklas, M., Greilich, S., Melzig, C., Akselrod, M.S., Debus, J., Jäkel, O., Abdollahi, A., 2013a. Engineering cell-fluorescent ion track hybrid detectors. *Radiat. Oncol.* 8, 141. https://doi.org/10.1186/1748-717X-8-141

Niklas, M., Melzig, C., Abdollahi, A., Bartz, J.A., Akselrod, M.S., Debus, J., Jäkel, O., Greilich, S., 2013b. Spatial correlation between traversal and cellular response in ion radiotherapy - Towards single track spectroscopy. *Radiat. Meas.* 56, 285–289. https://doi.org/10.1016/j.radmeas.2013.01.060

Niklas, M., Bartz, J.A., Akselrod, M.S., Abdollahi, A., Jäkel, O., Greilich, S., 2013c. Ion track reconstruction in 3D using alumina-based fluorescent nuclear track detectors. *Phys. Med. Biol.* 58(18), N251-66. https://doi.org/10.1088/0031-9155/58/18/N251

Prise, K.M., Schettino, G., 2011. Microbeams in radiation biology: Review and critical comparison. *Radiat. Prot. Dosimetry* 143(2–4), 335–339. https://doi.org/10.1093/rpd/ncq388

R Core Development Team, 2011. R: A Language and Environment for Statistical Computing, R Foundation for Statistical Computing, Vienna, Austria.

Rizk, A., Paul, G., Incardona, P., Bugarski, M., Mansouri, M., Niemann, A., Ziegler, U., Berger, P., Sbalzarini, I.F., 2014. Segmentation and quantification of subcellular structures in fluorescence microscopy images using Squassh. *Nat. Protoc.* 9(3), 586–96. https://doi.org/10.1038/nprot.2014.037

Sartor, O., Maalouf, B.N., Hauck, C.R., Macklis, R.M., 2012. Targeted use of Alpha Particles: Current Status in Cancer Therapeutics. *J. Nucl. Med. Radiat. Ther.* 3(4). https://doi.org/10.4172/2155-9619.1000136

Sbalzarini, I.F., Koumoutsakos, P., 2005. Feature point tracking and trajectory analysis for video imaging in cell biology. *J. Struct. Biol.* 151(2), 182–195. https://doi.org/10.1016/j.jsb.2005.06.002

Schettino, G., Al Rashid, S.T., Prise, K.M., 2010. Radiation microbeams as spatial and temporal probes of subcellular and tissue response. *Mutat. Res.* 04(1–3), 68–77. https://doi.org/10.1016/j.mrrev.2010.01.005

Schindelin, J., Arganda-Carreras, I., Frise, E., Kaynig, V., Longair, M., Pietzsch, T., Preibisch, S., Rueden, C., Saalfeld, S., Schmid, B., Tinevez, J., White, D.J., Hartenstein, V., Eliceiri, K., Tomancak, P., Cardona, A., 2012.

Fiji: an open-source platform for biological-image analysis. *Nat. Methods* 9(7), 676–682. https://doi.org/10.1038/nmeth.2019

Schneider, C. a, Rasband, W.S., Eliceiri, K.W., 2012. NIH Image to ImageJ: 25 years of image analysis. *Nat. Methods* 9(7), 671–675. https://doi.org/10.1038/nmeth.2089

Ziegler, J.F., Ziegler, M.D., Biersack, J.P., 2010. SRIM - The stopping and range of ions in matter (2010). *Nucl. Instruments Methods Phys. Res. Sect. B* 268(11–12), 1818–1823. https://doi.org/10.1016/j.nimb.2010.02.091

APPENDIX A

- □ Fluence (%, left)
- ● Fitted Mean Energy (%, left)
- ◆ RMSE (a.u., right)
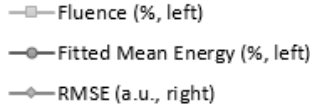
Fluence and the fitted mean energy are given as percentage of their expected value and are displayed on the left axis. RMSE is given in arbitrary units, given on the right axis, and serves as an indicator of the goodness-of-fit. A high RMSE in combination with a high or low fitted mean energy indicates a large number of faulty tracks.
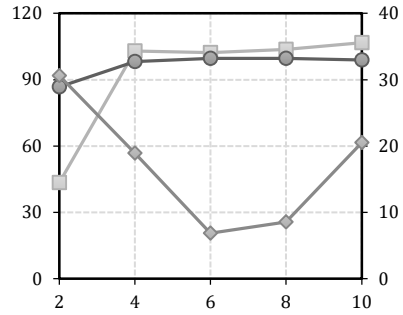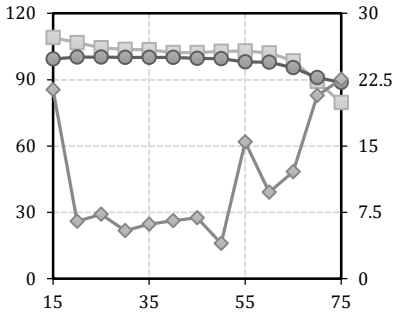
Intensity Threshold I (a.u.) – *Fine Tuning*

Particle Radius r (px) – *Fine Tuning*
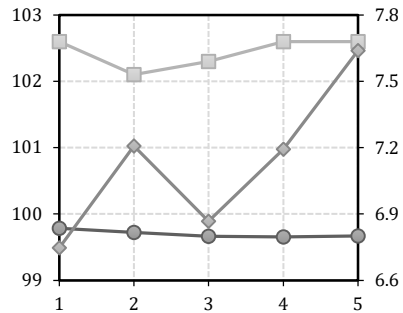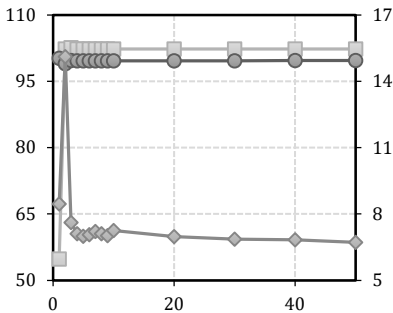
Maximum Distance $d_{p,max}$ (px) – *Threshold*

Linkrange R (slices) – *Fine Tuning*
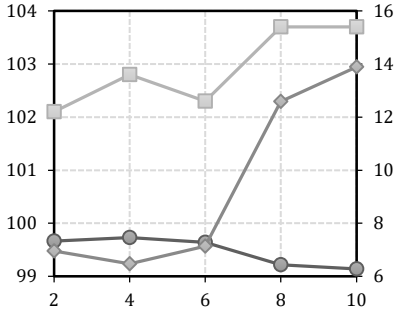
Particle Drift r_p (px) – Fine Tuning
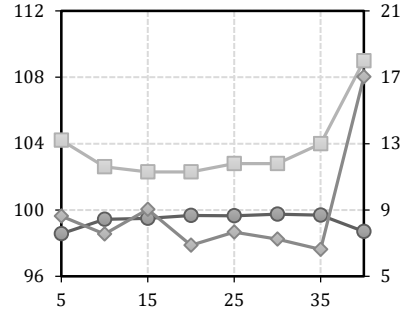
Maximum Angle $\theta_{p,max}$ (°) – Fine Tuning
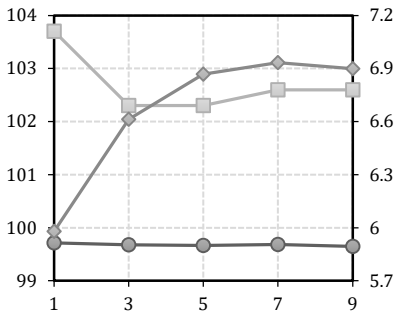
Angle History H (-) – Fine Tuning
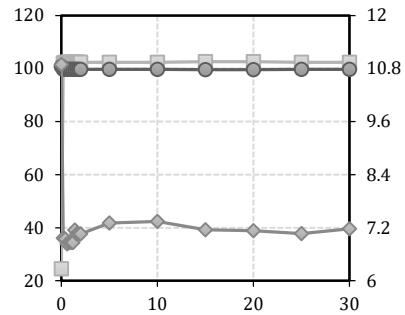
Distance Weight w_d (-) – Threshold
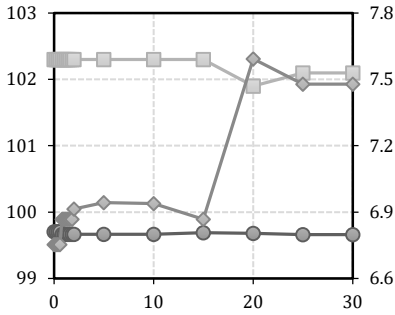
Intensity Weight w_i (-) – Fine Tuning
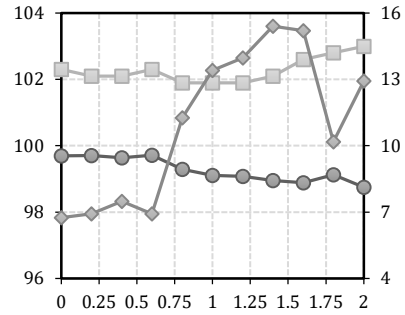
Velocity Weight w_v (-) – Fine Tuning
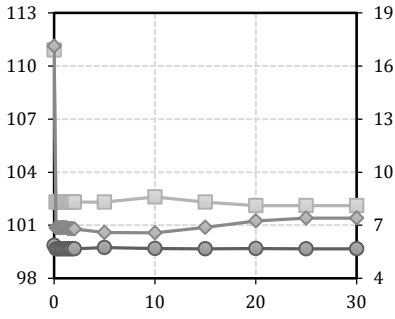
Angle Weight w_a (-) – Threshold
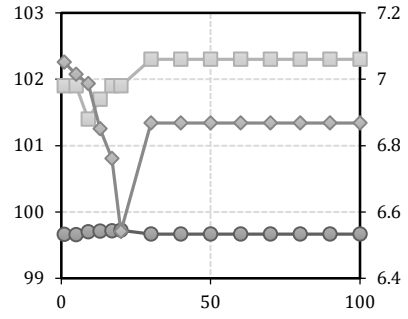
Relink Distance $d_{t,max}$ (px) – Threshold
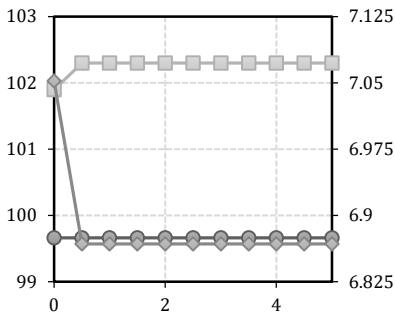
Relink Cost D_{max} (-) – Threshold

Chapter 4

Alpha particle spectroscopy using FNTD and SIM super-resolution microscopy

J.J.M. Kouwenberg[1,*], G.J. Kremers[2,*], J.A. Slotman[2], H.T. Wolterbeek[1], A.B. Houtsmuller[2], A.G. Denkova[1], A.J.J. Bos[1]

[1] Radiation, Science & Technology, Delft University of Technology, Mekelweg 15, Delft, the Netherlands
[2] Erasmus Optical Imaging Centre, Erasmus MC, 's-Gravendijkwal 230, Rotterdam, the Netherlands
* These authors contributed equally to this work

ABSTRACT

Structured Illumination Microscopy (SIM) for the imaging of alpha particle tracks in Fluorescent Nuclear Track Detectors (FNTD) was evaluated and compared to Confocal Laser Scanning Microscopy (CLSM). FNTDs were irradiated with an external alpha source and imaged using both methodologies. SIM imaging resulted in improved resolution, without increase in scan time. Alpha particle energy estimation based on the track length, direction and intensity produced results in good agreement with the expected alpha particle energy distribution. A pronounced difference was seen in the spatial scattering of alpha particles in the detectors, where SIM showed an almost 50 % reduction compared to CLSM. The improved resolution of SIM allows for more detailed studies of the tracks induced by ionizing particles. The combination of SIM and FNTDs for alpha radiation paves the way for affordable and fast alpha spectroscopy and dosimetry.

INTRODUCTION

The use of alpha particle emitting radionuclides for the treatment of cancer is increasing rapidly (Bandekar et al., 2014; Jadvar and Quinn, 2013; Sartor et al., 2012; Sofou et al., 2004). Alpha radiation has a high Lineal Energy Transfer (LET), a measure for the amount of energy deposited per distance traveled, which leads to high biological effectiveness (Franken et al., 2011; Tracy et al., 2015) and insensitivity to the oxygen concentration in the tumor (Barendsen et al., 1966; Sgouros et al., 2010). This can be a promising prospect for the treatment of tumors resistant to conventional radiation therapy (Elgqvist et al., 2014). Unfortunately, to this day alpha radiation spectroscopy and dosimetry remain challenging due to the short range of alpha particles (less than 100 μm in water) (Sgouros et al., 2010). Improvements in such measurements are expected to greatly enhance the development of alpha particle mediated cancer treatment.

Fluorescent Nuclear Track Detectors (FNTD) have shown to be an excellent tool for alpha radiation research (Chapter 3, Sykora et al., 2009), offering a high spatial resolution in combination with fast and stable read-out using Confocal Laser Scanning Microscopy (CLSM). FNTDs are aluminum oxide crystals with carbon and magnesium dopants, giving them a characteristic green color (M. S. Akselrod et al., 2006). The dopants introduce defects in the crystal, called color centers, that undergo radiochromic transformations when irradiated (G. M. Akselrod et al., 2006). These transformed color centers are very stable and are fluorescent with an excitation wavelength of ~650 nm and emission at 750 nm. The FNTD can therefore be imaged using fluorescence microscopy to yield high-resolution images of the tracks induced by passing alpha particles in the crystal (Bartz et al., 2013). The direction, length and spatial scattering of these tracks is used to calculate the initial energies and directions of alpha

particles. From this the various characteristics of the alpha radiation field, like absorbed dose rate and biological effectiveness, can be deduced. The spatial and energy resolutions of alpha tracks in FNTDs are however restricted by the resolution limit of CLSM. Here, we investigated the use of an alternative fluorescence super-resolution microscopy technique, Structured Illumination Microscopy (SIM) (Gustafsson et al., 2008; Lukosz and Marchand, 1963), for FNTD read-out, utilizing both its fast read-out and high spatial resolution to improve spatial and energy resolution in alpha radiation measurement.

MATERIALS AND METHODS

FNTD Irradiation

Al_2O_3:C,Mg Fluorescent Nuclear Track Detectors (Landauer, Inc., Glenwood, Illinois, United States), kindly donated by Landauer, Inc., were irradiated using a 1.1 cm diameter 394 kBq 241Am source with an estimated 1.3 µm layer of americium oxide and a 2 µm protective gold layer (Czech Metrological Institute, Brno, Czech Republic), placed behind a 3D printed honeycomb collimator. The honeycomb collimator restricted outgoing alpha particles to a maximum vertical angle of ~45 degrees, a requirement for sufficient penetration in the FNTD (Chapter 3). Four 8 x 4 x 0.5 mm^3 FNTDs were irradiated at a 5.00 ± .05 mm distance from the source for 267 s each above the center of the collimator to induce an approximate water equivalent dose of 1 Gy in the detector.

FNTD Read-out

Small arbitrarily chosen volumes near the center of the FNTDs were read-out using both CLSM and SIM super-resolution microscopy. The measured volumes were not the same for both devices. A Leica SP5 (Leica Microsystems, Mannheim, Germany) with an Avalanche Photo Diode (APD) behind a Chroma Technology ET655lp 655nm long pass filter (Chroma Technology Corp., Bellows Falls, Vermont, United States) together with a 633 nm excitation laser was used in the CLSM read-out. A HCX PL APO CS 63x 1.4NA Oil objective, 2.5 zoom factor, 40 Hz scan speed and 2 times line averaging were used to yield 96 x 96 x 490 nm^3 sized voxels in a 98 x 98 x 10 µm^3 read-out volume. Imaging of one read-out volume took 25 minutes and no post-processing was performed on the resulting images.

SIM imaging was performed on a Zeiss Elyra PS1 with an Andor iXon DU 885 EMCCD camera (Carl Zeiss AG, Oberkochen, Germany) behind a LP655 filter with a Plan Apochromat DIC 63x 1.4 NA Oil objective and 642 nm laser excitation with 500 ms exposure times and EM gain set at 30. Samples were illuminated with a spatial line pattern that was shifted in 5 phases and rotated in 5 orientations. The raw images were reconstructed (Gustafsson et al., 2008) into a high resolution 3D-dataset using the Zeiss 2012 PS1 ZEN software. Reconstruction was done

using the default sectioning values (100, 83, 83) and automatic noise filtering. No correction was made for anisotropy and the results were baseline shifted. The SIMcheck toolbox (Ball et al., 2015) was used to evaluate the SIM reconstruction results. SIM reconstruction yielded 39.7 x 39.7 x 144 nm^3 sized voxels in a 75 x 75 x 10 μm^3 read-out volume. Imaging of one read-out volume took 18 minutes.

Signal-to-noise ratios (SNR) were calculated via:

$$SNR(\pm \sigma) = \frac{\mu_t(\pm \sigma_t) - \mu_b}{\sigma_b} \qquad (4\text{-}1)$$

where μ_t and σ_t are respectively the mean and standard deviation of the measured track intensities, while μ_b and σ_b are respectively given by the mean and standard deviation of the background intensity.

Resolution measurement

A line was fitted through the maximum Z projection of all tracks in a field of view in FIJI (Schindelin et al., 2015). A Gaussian model was fitted to the average intensity profile perpendicular to the track at a single pixel spacing, using the non-linear least squares algorithm in the software package R version 3.2.2 (R Core Development Team, 2011). Track diameter was defined as the FWHM (Full width half maximum) calculated via:

$$FWHM = 2\sqrt{2ln2} \; \sigma \qquad (4\text{-}2)$$

Where σ is the fitted standard deviation.

Particle tracking

The fluorescent tracks produced by the alpha particles in the FNTDs consist of series of fluorescent spots in the 2D images. Track reconstruction is required for further analysis of the tracks. The fluorescent spots were used for track reconstruction using an expanded version of in-house built software. Spots in the 2D images were connected to reconstruct the tracks based on proximity and similarity in trajectory and intensity. This procedure is described in more detail in a previous chapter (Chapter 3). A summary of the tracking parameters used in said chapter for the CLSM and SIM sets are given in Table 4-1. I is the intensity threshold for spot selection, r and r_p are related to the spot size and drift, $d_{p,max}$ and $d_{t,max}$ are related to the maximum distance between spots for linking, R and H control the minimum number of spots per track and the amount of spots used for track averaging, $\theta_{p,max}$ is the maximum allowed angle and w_d, w_i, w_v and w_a are the weighting factors for respectively distance, intensity, velocity and angle. D_{max} is the maximum allowed cost for track relinking.

Range estimation

Let l be a set of trajectories in image stack A, where each trajectory contains a set of N points p_i (Figure 4-1). Each point can be described using its coordinates x_i, y_i, z_i, given in voxels from the image stack origin, and intensity I_i. The intensity was taken as the average of the 5 center voxels of a spot while the x and y coordinates followed from intensity weighting of the same voxels. Each coordinate is given as the far corner of a voxel, i.e. the first voxel is given by (1,1,1).

Table 4-1: Feature point linking parameters for CLSM and SIM

Parameter	CLSM	SIM	Parameter	CLSM	SIM
I	3 a.u.	5500 a.u.	w_d	0.5	0.5
$r = r_p$	6 px	6 px	w_i	1	0.2
$d_{p,max}$	10 px	20 px	w_v	0.5	1
R	3	3	w_a	1	1
$\theta_{p,max}$	30°	30°	$d_{t,max}$	30 px	40 px
H	4	4	D_{max}	$10 \cdot C_{max}$	$10 \cdot C_{max}$

Reflectance imaging was used to establish the angle of the surface plane. In cases where the location of the surface plane was later located using the lengths of the measured tracks, 25% of the measured tracks were used for surface plane localization, while the remaining 75% of the tracks were used for spectroscopy purposes (see Results and Discussion). Let the surface plane of image stack A obtained from the maximum reflectance be given by $\Psi_A(x, y, z) \equiv \psi_x x + \psi_y y - z = -z_0$, so that the corrected z-coordinate is given by:

$$z_i' = z_i - \psi_x x_i - \psi_y x_i - z_0 \tag{4-3}$$

The length $L'_{l,i}$ of track l at point i is then given by:

$$L'_{l,i} = \sum_{j=1}^{i-1} \sqrt{s_x^2(x_{j+1} - x_j)^2 + s_y^2(x_{j+1} - x_j)^2 + \left(f(z'_{j+1}) - f(z'_j)\right)^2} \tag{4-4}$$

Where s_x, s_y are the voxel sizes in μm in the x and y direction as given by the microscopy control software. f is a function for the depth correction required for the refractive index mismatch between the immersion oil (n = 1.518) of the objective and Al₂O₃ (n = 1.765), given by eq. (13) in Van Elburg et al. (Van Elburg et al., 2007). The total penetration of track l follows from the length of the track and the intersection of the initial track direction with Ψ_A. Since the slope of the surface plane is often small compared to the slope of the tracks, the distance between p_1 and the point of intersect can be simplified to:

$$L_{l,i} = L'_{l,i} + \frac{f(z'_1)}{\sqrt{1 + \chi_l^2 + \gamma_l^2}}$$

(4-5)

Where χ_l is the linear slope between $s_x x_i$ and $s_z(z'_1) \cdot z'_1$, and γ_l is the linear slope between $s_y y_i$ and $s_z(z'_1) \cdot z'_1$, both based on the first 5 points.
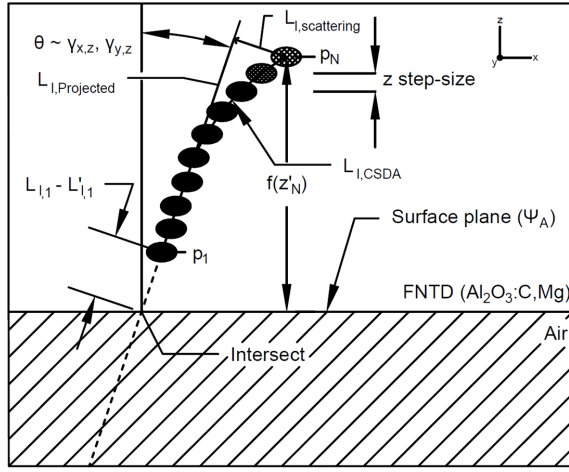
Figure 4-1: Schematic of an alpha particle penetrating a FNTD, producing a series of fluorescent spots (p_1 .. p_n) in the CLSM and SIM images. The depth in the FNTD of a spot p_i is given by $f(z'_i)$, and the separation between spots in the z-direction is determined by the respective step-size of the measurement. The initial trajectory of the particle upon entering the FNTD ($\gamma_{x,z}$, $\gamma_{y,z}$) is determined using the first 5 spots of the track. The distance traveled through the FNTD by the alpha particle before the first spot is measured, is determined using this trajectory and the surface plane of the FNTD. The lateral scattering ($L_{l,scattering}$) is given by the perpendicular deviation from the initial trajectory of the track, measured at the last fluorescent spot within the track. Fluorescence intensity decay at the end of a track is illustrated by the change in the brightness of the spots.

The position of the end of the track was refined using the fluorescence intensity I. Since the color center concentration in the FNTDs is low (G. M. Akselrod et al., 2006), color center saturation inside the track is expected to occur at a Linear Energy Transfer (LET) far below the average LET of an alpha track. For samples with a good SNR, an exponential function was fitted to the fluorescence intensity I_i as function of track length $L_{l,i}$ in accordance with the dose profile of the alpha track (Cucinotta et al., 1998):

$$I_{fit}(L_{l,i}) = a + (1-a)(1 - e^{-b \cdot (L_{l,i} - L_{l,N})})$$

(4-6)

Where the parameters a and b were fitted using the implementation of the Broyden–Fletcher–Goldfarb–Shanno algorithm as found in software package R version 3.2.2. The endpoint of the track was chosen at $I_{fit} = 95$ % since it is theorized that color center saturation happens at LETs far below those of alpha particles. The drop in intensity therefore indicates the end of the alpha particle track. Residual energy deposition is the result of high energy delta rays travelling beyond the path of the alpha particle (Scholz and Kraft, 1996). The fitting was limited to 2.5 μm from the endpoint to avoid faulty fitting due to scattering of the alpha particle within the track. For cases where the SNR was too low for accurate fitting, the endpoint was chosen, when possible, as the last point with an intensity above the mean track intensity minus the track intensity standard deviation. When either method failed, no further refinement was attempted.

The detour factor is an indicator for the deviation of the track from a straight line of a particle in a material and is defined as:

$$Detour\ factor \equiv \frac{L_{l,projected}}{L_{l,CSDA}} \tag{4-7}$$

Where $L_{l,projected}$ is the track length projected onto the initial track direction vector and $L_{l,CSDA}$ is the Continuous Slowing Down Approach (CSDA) range which is given here by the procedural track length as described by eq. (4-5). The scattering is defined here as the deviation from the projected orthogonal to the projection vector ($L_{l,scattering}$). The relative scattering can then be expressed as:

$$Relative\ scattering \equiv \frac{L_{l,scattering}}{L_{l,CSDA}} \tag{4-8}$$

The code framework for track following and calculation was written in a combination of the software packages R version 3.2.2 and Java version 8.

Energy calculation

Alpha particles originate in a 1.3 μm thick Am_2O_3 layer and pass through a 2 μm layer of gold and then a 5 mm air layer before entering the FNTD. Using the approximated initial direction vector $z = \chi_l x + \gamma_l y$, the path length through the kth layer, denoted as $\tau_l^{(k)}$, could be estimated using the equation below, assuming that the track passes through the whole layer.

$$\tau_l^{(k)} = \frac{t^k}{\sqrt{1 + \chi_l^2 + \gamma_l^2}} \tag{4-9}$$

Where t^k is the thickness of the kth layer. This approach ignores scattering in either layer. The

path length of an alpha particle can be related to its loss of energy using translation tables, which in this case were obtained from the ASTAR application by the National Institute of Standards and Technology, USA (NIST) (Berger et al., 2005). The energy loss of an alpha particle passing through a layer is then given by:

$$\Delta e_l^{(k)} = e_l^{(k-1)} - e_{mat}\left[R_{mat}\left(e_{l,0}^{(k-1)}\right) - \tau_l^{(k)}\right] \tag{4-10}$$

where e_{mat} is a conversion function for the residual range to the corresponding energy in a material and R_{mat} acts as the inverse of e_{mat} and $e_l^{(k-1)}$ is the particle's energy the moment it leaves layer $k-1$ and enters the kth layer. The total energy of an alpha particle then follows from iteration of eq. (4-10) for each layer including the FNTD, where $\tau_l^{(FNTD)}$ was given by the refined track length. When the depth z_0 of the surface plane could not be found, it could be retrieved by optimization of z_0 for $\left|e_{peak} - e_{Am241}\right| \approx 0$, where e_{peak} is the peak in the measured energy distribution for image stack A and e_{Am241} is the mean alpha energy for 241Am.

FLUKA simulation

A simulation was built in FLUKA 2011.2c.5 (Ferrari et al., 2011) to measure the energy distribution of alpha particles entering the FNTD. The collimator was modelled as the material BLACKHOLE to improve calculation speed. The source was modeled as an infinitely thin layer halfway within the americium oxide layer, which was modeled using the same density, but with gold atoms to approximate americium atoms since higher Z atoms are not available in FLUKA. The energies of 10^7 incoming alpha particles were measured with the FLUKA function USRBDX in 30 keV bins.

RESULTS AND DISCUSSION

To compare SIM and CLSM imaging for FNTD-based alpha particle spectroscopy, four randomly chosen areas were scanned using both modalities. Since the range of an alpha particle in matter is directly related to its energy, the surface plane for both the SIM and CLSM scans were found by matching the calculated pathlength of alpha particle tracks through the FNTD, together with the observed angle of incidence and known pathlength through the air and source, to the energy of alpha particles emitted by the source. Am-214 emits alpha particles with 2 possible energies: 5486 keV (85% chance) and 5443 keV (15% chance). The energy difference of 43 keV would not be expected to be distinguished due to the thickness of the test material and variations in angle of incidence that would degrade the fidelity of the energies impinging on the FNTD. Indeed, even conventional alpha spectrometers can be challenged by

this energy separation for thick specimens. An average alpha particle energy of 5480 keV was therefore assumed.

Figure 4-2 shows a close-up of an area imaged with CLSM and SIM, respectively. The full field of view of the scans is shown in supplement 1.
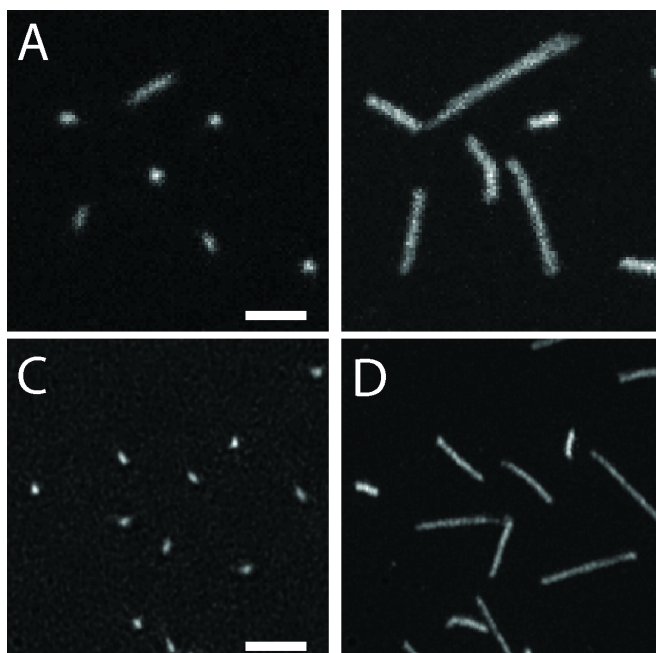
Figure 4-2: Close-up of FNTDs irradiated with alpha radiation and imaged with CLSM (A and B) and SIM (C and D). Panels A and C show single images and panels B and D show the maximum projection of the 3D image stacks. Scale bars are 2 micrometer. Note that panels A and B show a different field of view than panels C and D.

In single optical sections nuclear fluorescent tracks appeared as round or elongated spots (Figure 4-2A,C and supplement 1A). Round spots referred to alpha particles, which propagated nominally perpendicular to the FNTD surface (i.e. the imaging plane). Spot elongation was caused by a combination of the incident angle of the alpha particle trajectory with the FNTD and the optical slice thickness of the microscope. Shallow angle tracks were identified by more elongated spots in single sections and their apparent increase in length in a maximum projection along the z axis (Figure 4-2B, D and supplement 1B, D). Spot elongation was less for SIM, as a result of the improved optical sectioning capability. SIM imaging yielded a SNR (14.4 ± 4.8) comparable to CLSM (13.9 ± 3.6).

The radial track profile was predicted to be in the order of 3 to 100 nm (Cucinotta et al., 1998).

Here, we measured the radial track profile as the FWHM perpendicular to the length of the alpha tracks. As expected, the SIM images showed smaller track diameters (FWHM 209 ± 69 nm), compared to CLSM (FWHM 322 ± 19 nm). The fact that these values are somewhat higher than the theoretical resolution limits for SIM (140 nm) and CLSM (280 nm; pinhole 1 airy unit) might be explained by the large difference in wavelength between excitation (647 nm) and emission (750 nm). In addition, the anisotropic properties of the FNTD material (see below) could have negatively affected the measured track width. However, it is noteworthy that the radial track profile found in FNTDs irradiated with 3 MeV protons (LET in Al_2O_3: 35 keV/μm) and 1094 MeV carbon ions (LET in Al_2O_3: 90 keV/ μm), imaged by stimulated emission depletion (STED) microscopy, yielded comparable track diameters of respectively 196 ± 28 nm and 240 ± 29 nm (FWHM) (Niklas et al., 2017). 3.7 MeV alpha particles, used for this work, have a LET in Al_2O_3 of 308 keV/μm (Berger et al., 2005).

For SIM imaging the orientation of the FNTD on the microscope was important, due to the optically anisotropic properties of Al_2O_3:C,Mg (Akselrod et al., 2003). The FNTDs were cut with the "c" optical axis along the long axis of the chip (M. S. Akselrod, personal communication). Hence the "c" optical axis was perpendicular to the optical axis of the microscope and more than one refractive index could be observed in the imaging plane. We expected that polarization dependent fluctuations in the fluorescence yield might adversely affect SIM image reconstruction. To test this, FNTDs were imaged at different orientations. Shadow images were observed next to the fluorescent tracks, but appeared to be absent when FNTDs were oriented at 0° (supplement 2). The expected variation in the separation distance between the shadow images and the main fluorescent track should be dependent on the track's angle of incidence relative to the detector surface and therefore the thickness of the FNTD through which the imaging is performed. These observations still need to be compared to the theoretical separation based on track depth and crystallographic orientation of the FNTD. Nevertheless, all subsequent SIM measurements were done under conditions that eliminated the observation. In addition, we used the SIMcheck toolbox (Ball et al., 2015) to identify putative problems with the 3D-SIM reconstructions. This analysis verified that the raw and processed SIM data were of good quality and showed no evidence for common SIM reconstruction issues (Supplement 3).

Because of the increased resolution of SIM compared to CLSM, we expected SIM imaging of FNTDs to allow for more detailed studies of the tracks induced by ionizing particles. Plotting the normalized fluorescence intensity as function of distance from the track resulted in the intensity profiles shown in Figure 4-3. Note that the visible gaps are the result of the discrete step-size in z-direction. An exponential intensity decay is seen at the end of the tracks for both methodologies, but is more evident with SIM. This allowed for the intensity endpoint fitting approach given in eq. (4-6).
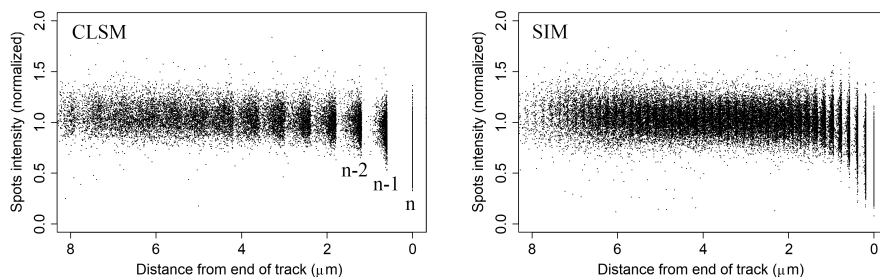
Figure 4-3: Scatter plot of the normalized fluorescence intensity of spots as function of distance from the last detected spot (indicated by n) in their respective track. An exponential decay of fluorescence is visible for CLSM (left) and SIM (right). Note that the distance between two spots for a track perfectly perpendicular to the z-axis is given by the step-size (Figure 4-1) of the image stack in the z-direction (~0.6 μm for CLSM, ~0.18 μm for SIM), hence the visible gaps in the figures. This distance increases when the track is more slanted (eq. (4-5)). The decrease in fluorescence intensity at the end of the measured tracks indicate that alpha particles come to halt within the measured tracks. The point where the alpha particle came to a halt can therefore be estimated using eq. (4-6).

Distributions of the calculated alpha particles energies after endpoint refinement are given in Figure 4-4, together with the distribution obtained from FLUKA simulations. Both the distributions from CLSM and SIM match closely with the expected energy distributions, yielding standard deviations of respectively 306 and 284 keV, compared to 208 keV in the simulation. The exact uncertainty of this method due to noise and resolution for alpha particle energy measurement is unknown, since the true energy distribution is unknown. While the FLUKA simulation serves as an indicator for the true distribution, this simulation does not account for manufacturing errors in the collimator and degradation of the source.
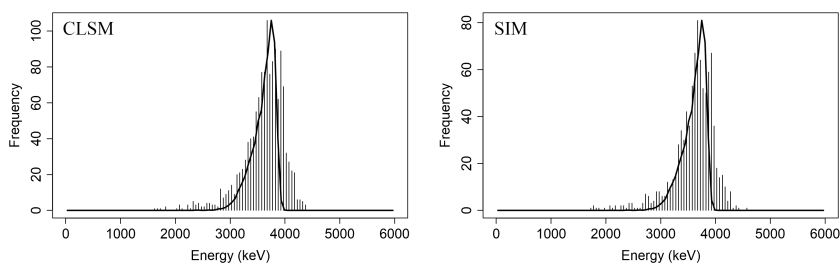
Figure 4-4: The energy distribution of alpha particles upon entering the FNTDs for CLSM (left) and SIM (right), calculated using the lengths of the tracks within the FNTD using the described methods. The black line indicates the expected energy distribution obtained from simulations of the experimental setup using the FLUKA software. Peak values for CLSM and SIM were respectively 3682 and 3678 keV.

The true energy distribution can therefore reasonably be expected to be broader than the simulation is showing. Nevertheless, for both imaging modalities the proposed method showed a better energy resolution than would likely be achievable using track width or track intensity based methods for alpha radiation (Klimpki et al., 2016; Sykora et al., 2008a). It is however important to note that the method proposed in this work is only applicable for tracks ending within the FNTD, which is only the case for (very) low energy ions, whereas the other methods can be used for all types of tracks.

The detour factor and relative scattering distributions are given in respectively Figure 4-5 and Figure 4-6. Given a mean entrance alpha energy of approximately 3900 keV in the FNTD, NIST reports a detour factor in Al_2O_3 of 0.984 (Berger et al., 2005).
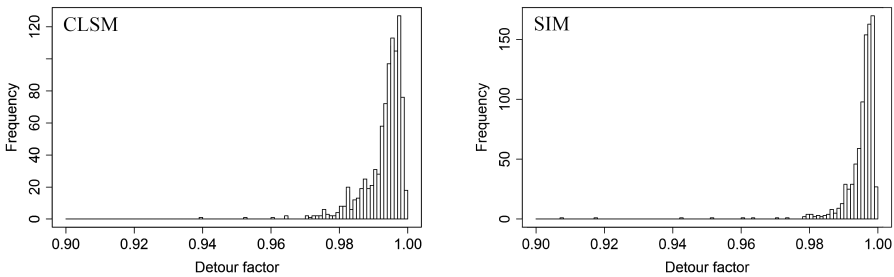
Figure 4-5: The detour factor distribution of alpha particles penetrating a FNTD as measured using CLSM (left) and SIM (right). A detour factor of 1 indicates that the particle followed a perfectly straight track through the FNTD, while a value close to zero indicates a large deviation from its initial trajectory upon entering the FNTD. The median values for CLSM and SIM were respectively 0.995 and 0.997.
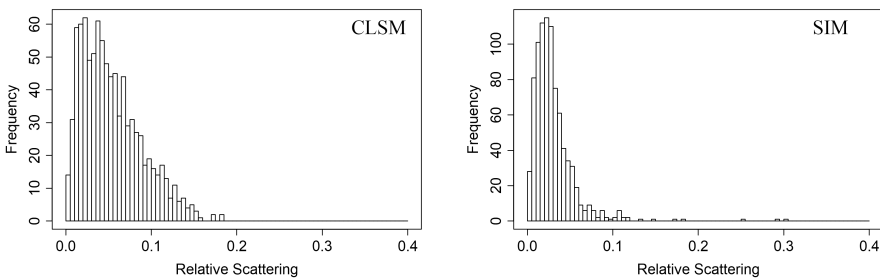
Figure 4-6: The relative scattering distribution of alpha particles penetrating a FNTD as measured using CLSM (left) and SIM (right). A relative scattering of 0 indicates a perfectly straight track. The median values for CLSM and SIM were respectively 0.047 and 0.025. Both CLSM and SIM samples were irradiated under the same experimental conditions, indicating that the resolution of CLSM is insufficient to properly measure the scattering of alpha particles.

The mean detour factors for CLSM and SIM were respectively 0.993 and 0.995. As shown in Figure 4-5 and Figure 4-6, SIM showed an almost 50 % reduction in measured scattering compared to CLSM for the same experiment conditions (Figure 4-6), which was most likely the result of the improved resolution of the SIM images, enabling more accurate track reconstruction. These results might be an indication that the simulation approach (Lewis, 1950) used by NIST to estimate the spatial scattering of alpha particles overestimates said scattering of alpha particles in Al_2O_3. While uncertainty evaluation of particle ranges and scattering is difficult at these low energies, stopping power uncertainties up to 10% for 100 keV alpha particles were reported (ICRU, 1993). Further research is however required to thoroughly estimate the uncertainty in scattering estimation using FNTDs before any concrete conclusions regarding the accuracy of the scattering simulations can be made. While these results on itself are not expected to make an impact, the overestimation suggests that this method might find its use in Monte Carlo and cross-section validation for low energy ions, a domain that is difficult to validate. Validation of scattering and stopping power data for low energy alpha particles is important for accurate microdosimetry in alpha radionuclide therapy, a field that studies the effects of alpha radiation on a small (sub-)micron scale and thereby mainly depends on simulation data (Chouin et al., 2007; Kvinnsland et al., 2001; Roeske and Stinchcomb, 1997). The low C and Mg dopant concentrations are expected to be too low to influence the scattering significantly. Figure 4-7 displays tracks with weak and strong scattering to illustrate that the calculated scattering could be verified via visual inspection.
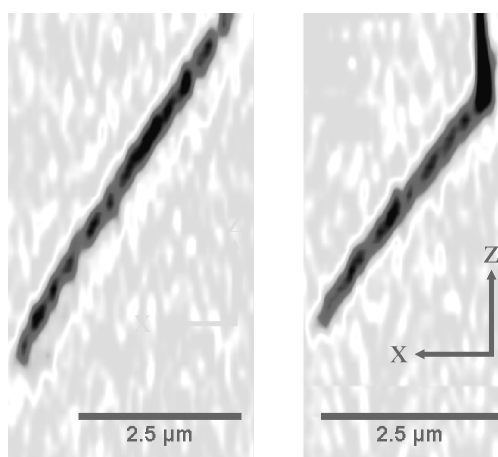
Figure 4-7: Alpha particles entering the FNTD, measured using SIM, undergoing no scattering (left) and strong scattering (right). In the absence of heavy collisions between alpha particles and atoms within the FNTD, the alpha particle follows a (close to) perfectly straight path (left). A strong collision with an atom will force to the alpha particle to be deviated from its original path (right). The images of the tracks are maximum intensity projections along the y-axis after

alignment of tracks with the x-axis. The relative scattering of the tracks in the left and right were respectively 0.004 and 0.29. Note the change in track intensity when the track angle changes in the right figure due to the change in illumination by the anisotropic excitation beam/spot.

CONCLUSION AND DISCUSSION

We have shown for the first time that SIM can be used for quantitative FNTD imaging. The maximum spatial resolution was almost doubled without increasing the scan time. The scan time for SIM could be further reduced by using three instead of five rotations of the illumination pattern, however this would lower the resolution of the reconstructed image and in addition, could lead to an increase of resolution anisotropy. Currently, SIM methods are being developed using different illumination patterns, which require fewer rotations, or no rotations (Chakrova et al., 2015; Schropp et al., 2017) at all and this would further reduce the scan time. Although SIM image reconstruction was computationally intensive and typically took the same amount of time as the image acquisition, the prospect of Graphics Processing Unit (GPU)-based image reconstruction (Lu-Walther et al., 2015; Müller et al., 2017) is expected to make real-time reconstruction possible in the near future. The proposed method for particle energy estimation based on track length showed an excellent energy resolution, which is required for proper alpha dosimetry. No significant improvement in energy resolution with SIM could be observed compared to CLSM. A significant difference was however visible in the relative spatial scattering of alpha track measurements between the two modalities. The difference in detour factor obtained using SIM versus the numbers obtained from NIST could be an indication that the current data from NIST might be overestimating the scattering of alpha particles in Al_2O_3 and that revision of the current cross section (a measure for interaction probability) might be necessary, but thorough determination of the uncertainty in scattering estimation using FNTDs is required before concrete conclusions can be made regarding the current NIST data. From these results, it is expected that the high resolution of SIM allows for more complex analyses of particle interactions, which can be of great value of the validation of the Monte Carlo simulation code and interaction cross section data. Since ion radiation therapy depends heavily on the accuracy of these simulation codes, the combination of SIM and FNTD imaging might find more applications in this field. Stimulated Emission Depletion (STED) was the only other super-resolution technique applied for FNTDs, but has yet to find its way to wider applications in part due to the long scanning time and technical hardships (Greilich et al., 2013; Niklas et al., 2017). SIM overcomes these challenges by offering super-resolution imaging at scanning speeds compatible with large-scale commercial read-out. The increased resolution can also be used for better detection of secondary particles in clinical carbon beams. Due to the low fluorescence intensity and often large angle of incidence of these secondary particles, their numbers are often underestimated when using CLSM for FNTD read-out

(Klimpki et al., 2016). SIM is therefore considered an excellent competitor for high resolution FNTD read-out, especially with the possibility of fast image acquisition and real-time SIM reconstruction in combination with automatic surface plane detection (Akselrod et al., 2014a). The FNTD/SIM combination paves the way for a new type of alpha dosimeter, both for research and personal dosimetry.

ACKNOWLEDGEMENTS

REFERENCES

Akselrod, M.S., Akselrod, A.E., Orlov, S.S., Sanyal, S., Underwood, T.H., 2003. Fluorescent aluminum oxide crystals for volumetric optical data storage and imaging applications. *J. Fluoresc.* 13, 503–511.

Akselrod, M.S., Yoder, R.C., Akselrod, G.M., 2006. Confocal fluorescent imaging of tracks from heavy charged particles utilising new Al2O3:C,Mg crystals. *Radiat. Prot. Dosimetry* 119(1–4), 357–362. https://doi.org/10.1093/rpd/nci664

Akselrod, G.M., Akselrod, M.S., Benton, E.R., Yasuda, N., 2006. A novel Al2O3 fluorescent nuclear track detector for heavy charged particles and neutrons. *Nucl. Instr. Methods B* 247(2), 295–306. https://doi.org/10.1016/j.nimb.2006.01.056

Akselrod, M.S., Fomenko, V.V., Bartz, J.A., Haslett, T.L., 2014. Automatic neutron dosimetry system based on Fluorescent Nuclear Track Detector Technology. *Radiat. Prot. Dosimetry* 161(1), 86–91.

Ball, G., Demmerle, J., Kaufmann, R., Davis, I., Dobbie, I.M., Schermelleh, L., 2015. SIMcheck: a Toolbox for Successful Super-resolution Structured Illumination Microscopy. *Sci. Rep.* 5(1), 15915. https://doi.org/10.1038/srep15915

Bandekar, A., Zhu, C., Jindal, R., Bruchertseifer, F., Morgenstern, A., Sofou, S., 2014. Anti-Prostate-Specific Membrane Antigen Liposomes Loaded with 225Ac for Potential Targeted Antivascular alpha-Particle Therapy of Cancer. *J. Nucl. Med.* 55(1), 107–114. https://doi.org/10.2967/jnumed.113.125476

Barendsen, G.W., Koot, C.J., Van Kersen, G.R., Bewley, D.K., Field, S.B., Parnell, C.J., 1966. The effect of oxygen on impairment of the proliferative capacity of human cells in culture by ionizing radiations of different LET. *Int. J. Radiat. Biol. Relat. Stud. Phys. Chem. Med.* 10(4), 317–27. https://doi.org/10.1080/09553006614550421

Bartz, J.A., Zeissler, C.J., Fomenko, V.V., Akselrod, M.S., 2013. An imaging spectrometer based on high resolution microscopy of fluorescent aluminum oxide crystal detectors. *Radiat. Meas.* 56, 273–276. https://doi.org/10.1016/j.radmeas.2013.01.041

Berger, M.J., Coursey, J.S., Zucker, M.A., Chang, J., 2005. ESTAR, PSTAR, and ASTAR: Computer Programs for Calculating Stopping-Power and Range Tables for Electrons, Protons, and Helium Ions (version 1.2.3), National Institute of Standards and Technology, Gaithersburg, MD ,USA.

Chakrova, N., Heintzmann, R., Rieger, B., Stallinga, S., 2015. Studying different illumination patterns for resolution improvement in fluorescence microscopy. *Opt. Express* 23(24), 31367. https://doi.org/10.1364/OE.23.031367

Chouin, N., Bitar, A., Lisbona, A., Chérel, M., Davodeau, F., Barbet, J., Bardiès, M., 2007. Implementation of a microdosimetric model for radioimmunotherapeutic alpha emitters. *Cancer Biother. Radiopharm.* 22(3), 387–392. https://doi.org/10.1089/cbr.2006.324

Cucinotta, F.A., Katz, R., Wilson, J.W., 1998. Radial distribution of electron spectra from high-energy ions. *Radiat. Environ. Biophys.* 37(4), 259–265. https://doi.org/10.1007/s004110050127

Elgqvist, J., Frost, S., Pouget, J.P., Albertsson, P., 2014. The Potential and Hurdles of Targeted Alpha Therapy – Clinical Trials and Beyond. *Front. Oncol.* 3, 324. https://doi.org/10.3389/fonc.2013.00324

Ferrari, A., Sala, P.R., Ranft, J., 2011. Fluka: a multi-particle transport code, Stanford Linear Accelerator Center, Stanford, CA, USA.

Franken, N. a P., ten Cate, R., Krawczyk, P.M., Stap, J., Haveman, J., Aten, J., Barendsen, G.W., 2011. Comparison of RBE values of high-LET α-particles for the induction of DNA-DSBs, chromosome aberrations and cell reproductive death. *Radiat. Oncol.* 6(1), 64. https://doi.org/10.1186/1748-717X-6-64

Greilich, S., Osinga, J.M., Niklas, M., Lauer, F.M., Klimpki, G.M., Bestvater, F., Bartz, J.A., Akselrod, M.S., Jäkel, O., 2013. Fluorescent nuclear track detectors as a tool for ion-beam therapy research. *Radiat. Meas.* 56, 267–272. https://doi.org/10.1016/j.radmeas.2013.01.033

Gustafsson, M.G.L., Shao, L., Carlton, P.M., Wang, C.J.R., Golubovskaya, I.N., Cande, W.Z., Agard, D.A., Sedat, J.W., 2008. Three-Dimensional Resolution Doubling in Wide-Field Fluorescence Microscopy by Structured Illumination. *Biophys. J.* 94(12), 4957–4970. https://doi.org/10.1529/biophysj.107.120345

ICRU, 1993. ICRU Report 49, Stopping Powers and Ranges for Protons and Alpha Particles.

Jadvar, H., Quinn, D.I., 2013. Targeted α-particle therapy of bone metastases in prostate cancer. *Clin. Nucl. Med.* 38(12), 966–71. https://doi.org/10.1097/RLU.0000000000000290

Klimpki, G.M., Mescher, H., Akselrod, M.S., 2016. Fluence-based dosimetry of proton and heavier ion beams using single track detectors. *Phys. Med. Biol.* 61(3), 1021–1040.

Kvinnsland, Y., Stokke, T., Aurlien, E., 2001. Radioimmunotherapy with alpha-particle emitters: microdosimetry of cells with a heterogeneous antigen expression and with various diameters of cells and nuclei. *Radiat. Res.* 155(2), 288–96.

Lewis, H.W., 1950. Multiple scattering in an infinite medium. *Phys. Rev.* 78(5), 526–529. https://doi.org/10.1103/PhysRev.78.526

Lu-Walther, H.-W., Kielhorn, M., Förster, R., Jost, A., Wicker, K., Heintzmann, R., 2015. fastSIM: a practical implementation of fast structured illumination microscopy. *Methods Appl. Fluoresc.* 3(1), 14001. https://doi.org/10.1088/2050-6120/3/1/014001

Lukosz, W., Marchand, M., 1963. Optischen Abbildung Unter Überschreitung der Beugungsbedingten Auflösungsgrenze. *Opt. Acta Int. J. Opt.* 10(3), 241–255. https://doi.org/10.1080/713817795

Müller, M., Markwirth, A., Mönkemöller, V., Lachetta, M., Wilking, A., Hübner, W., Huser, T., 2017. Video-rate, multi-color structured illumination microscopy with GPU-based, immediate image reconstruction, Biomolecular Photonics, Bielefield University, Bielefield, Germany.

Niklas, M., Henrich, M., Jäkel, O., Engelhardt, J., Abdollahi, A., Greilich, S., 2017. STED microscopy visualizes energy deposition of single ions in a solid-state detector beyond diffraction limit. *Phys. Med. Biol.* 62(9), N180–N190. https://doi.org/10.1088/1361-6560/aa5edc

R Core Development Team, 2011. R: A Language and Environment for Statistical Computing, R Foundation for Statistical Computing, Vienna, Austria.

Roeske, J.C., Stinchcomb, T.G., 1997. Dosimetric framework for therapeutic alpha-particle emitters. *J. Nucl. Med.* 38, 1923–1929.

Sartor, O., Maalouf, B.N., Hauck, C.R., Macklis, R.M., 2012. Targeted use of Alpha Particles: Current Status in Cancer Therapeutics. *J. Nucl. Med. Radiat. Ther.* 3(4). https://doi.org/10.4172/2155-9619.1000136

Schindelin, J., Rueden, C.T., Hiner, M.C., Eliceiri, K.W., 2015. The ImageJ ecosystem: an open platform for biomedical image analysis. *Mol. Reprod. Dev.* 82(7), 518–529. https://doi.org/10.1002/mrd.22489.The

Scholz, M., Kraft, G., 1996. Track structure and the calculation of biological effects of heavy charged particles. *Adv. Sp. Res.* 18(1–2), 5–14. https://doi.org/10.1016/0273-1177(95)00784-C

Schropp, M., Seebacher, C., Uhl, R., 2017. XL-SIM: Extending Superresolution into Deeper Layers. *Photonics* 4(2), 33. https://doi.org/10.3390/photonics4020033

Sgouros, G., Roeske, J.C., McDevitt, M.R., Palm, S., Allen, B.J., Fisher, D.R., Brill, A.B., Song, H., Howell, R.W., Akabani, G., Bolch, W.E., Brill, A.B., Fisher, D.R., Howell, R.W., Meredith, R.F., Sgouros, G., Wessels, B.W., Zanzonico, P.B., 2010. MIRD Pamphlet No. 22 (abridged): radiobiology and dosimetry of alpha-particle emitters for targeted radionuclide therapy. *J. Nucl. Med.* 51(2), 311–328. https://doi.org/10.2967/jnumed.108.058651

Sofou, S., Thomas, J.L., Lin, H., McDevitt, M.R., Scheinberg, D.A., Sgouros, G., 2004. Engineered liposomes for potential alpha-particle therapy of metastatic cancer. *J. Nucl. Med.* 45(2), 253–60.

Sykora, G.J., Akselrod, M.S., Benton, E.R., Yasuda, N., 2008. Spectroscopic properties of novel fluorescent nuclear track detectors for high and low LET charged particles. *Radiat. Meas.* 43, 422–426. https://doi.org/10.1016/j.radmeas.2007.11.009

Sykora, G.J., Akselrod, M.S., Vanhavere, F., 2009. Performance of fluorescence nuclear track detectors in mono-energetic and broad spectrum neutron fields. *Radiat. Meas.* 44(9–10), 988–991. https://doi.org/10.1016/j.radmeas.2009.10.027

Tracy, B.L., Stevens, D.L., Goodhead, D.T., Hill, M.A., 2015. Variation in RBE for Survival of V79-4 Cells as a Function of Alpha-Particle (Helium Ion) Energy. *Radiat. Res.* 184(1), 33–45. https://doi.org/10.1667/RR13835.1

Van Elburg, H.J., Kuypers, L.C., Decraemer, W.F., Dirckx, J.J.J., 2007. Improved correction of axial geometrical distortion in index-mismatched fluorescent confocal microscopic images using high-aperture objective lenses. *J. Microsc.* 228(1), 45–54. https://doi.org/10.1111/j.1365-2818.2007.01822.x

SUPPLEMENTAL FIGURE 1

Full field of view of FNTD irradiated with alpha radiation and imaged with CLSM and SIM. (A) Single image from the middle of a CLSM 3D-stack. (B) Max projection of the same 3D image stack. (C) Single image from the middle of a SIM 3D-stack. (D) Maximum projection of the same 3D image stack. The yellow boxes indicate the field of view shown in Figure 4-2. The CLSM images were cropped to match the field of view of the SIM data (75 µm x 75 µm). Scale bars are 10 micrometer.

SUPPLEMENTAL FIGURE 2
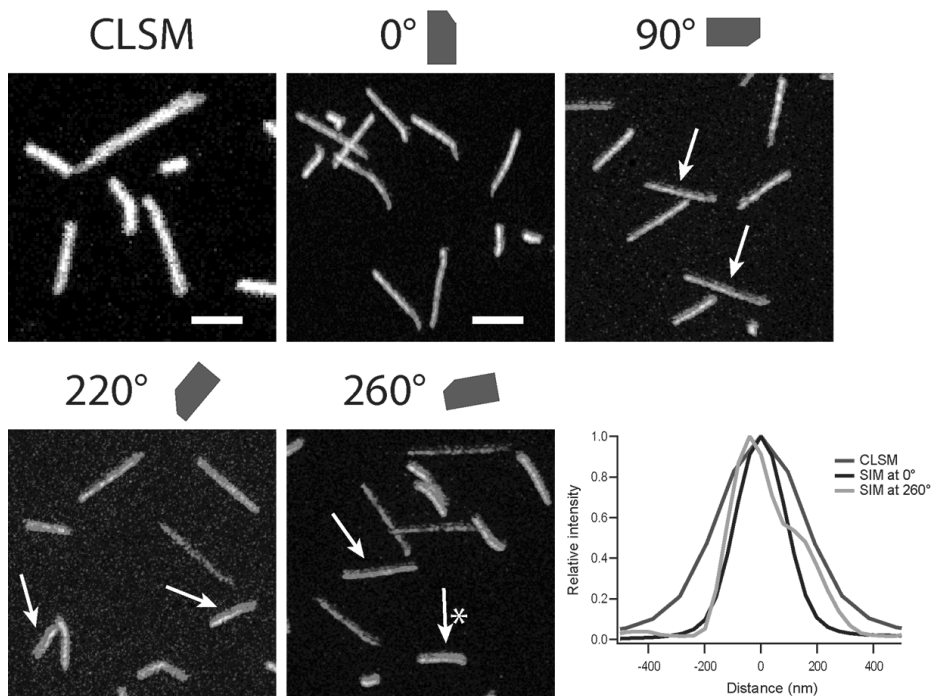
FNTD orientation-dependent shadow tracks. Maximum projections of SIM images obtained at the indicated FNTD sample orientation. Shadow tracks are indicated by arrows. CLSM image is shown for comparison. Scale bar is 2µm. Graph displays the average line plot across a single track for a FNTD at 260° (indicated by *). The lines are the average line plots for tracks imaged by CLSM and SIM (FNTD at 0°), respectively. The resolution of CLSM is too low to detect shadow tracks.

SUPPLEMENTAL FIGURE 3
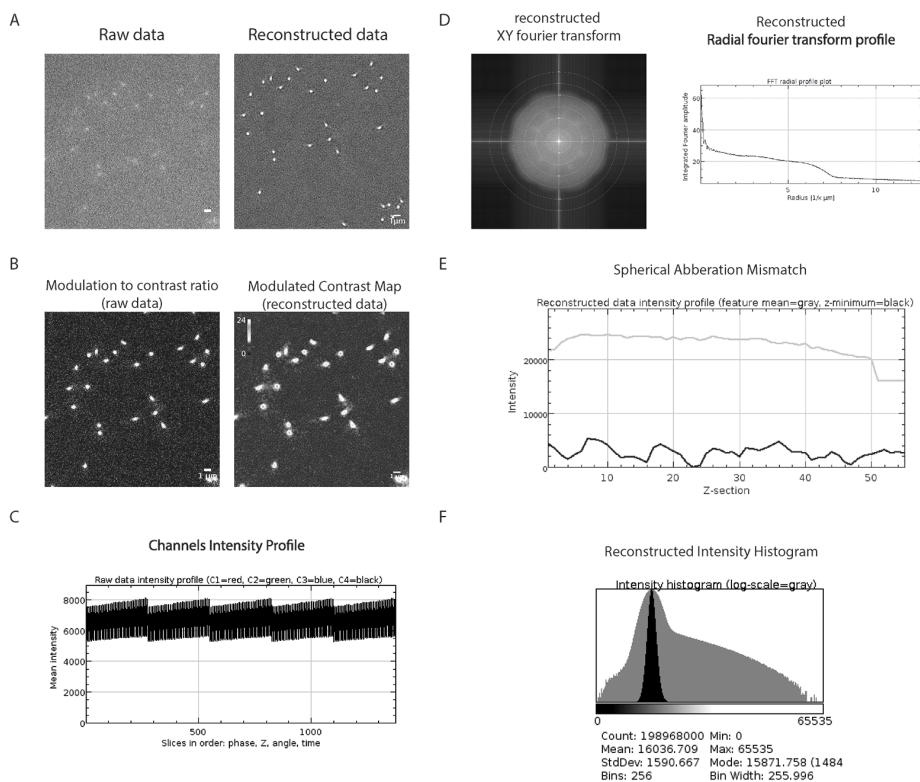
SIM check was performed on both raw and reconstructed data. A) Cropped area of raw and reconstructed data. The full image was used for SIMcheck. B) modulation contrast to noise ratio (MCNR) of raw and reconstructed data. MCNR is depicted on a grayscale, where light gray pixels indicate moderate to good modulation. C) Channels intensity profile of raw data, the total intensity variation measured is 30.5%. D) Fourier transform analysis of reconstructed data of both a lateral (x,y) and a radial view, no clear artifacts were observed. E) Spherical aberration mismatch analysis minimum values (black line) and maximum values (gray line) are depicted a z-minimum variation of 0.0523 was measured. F) Reconstructed intensity profile on a linear (black) and a logarithmic (gray) scale, a min-to-max intensity ratio of 3.30 was measured.

Chapter 5

Alpha Radiation Dosimetry using Fluorescent Nuclear Track Detectors

J.J.M. Kouwenberg[1], J.A. de Pooter[2], H.T. Wolterbeek[1], A.G. Denkova[1], A.J.J. Bos[1]

[1] Radiation, Science & Technology, Delft University of Technology, Mekelweg 15, Delft, the Netherlands
[2] VSL, Netherlands' national metrology institute, Thijsseweg 11, Delft, the Netherlands

ABSTRACT

To answer the need for better tools for alpha radiation radiobiology and microdosimetry research, a novel irradiation setup based on a honeycomb collimator, in combination with Fluorescent Nuclear Track Detectors (FNTD) for alpha radiation dosimetry and spectroscopy, was introduced. FNTDs are a novel type of small, crystalline detector that can visualize individual alpha particles and simultaneously measure their location, velocity direction and energy with good accuracy. The performance of FNTDs for alpha radiation dosimetry was evaluated for the first time and the results were compared to extrapolation chamber measurements and simulations. The surface dose rate to water of the irradiation setup for two different honeycomb collimators, measured using FNTDs, agreed with the extrapolation chamber measurements within 6%. The simulations underestimated the surface dose rate to water for the first collimator and overestimated the dose for the second collimator, indicating the sensitivity to manufacturing errors in the collimators of this irradiation setup. The dose homogeneity in the setup was measured using radiochromic film and showed variations of less than 5%, making this setup, in combination with the rich information obtained regarding the spatial, angular and energy distributions of the alpha particles, obtained using the FNTDs, ideal for microdosimetry and radiobiology experiments. The accuracy and ease-of-use of FNTDs in addition to the surface or absorbed dose and fluence of the radiation field indicate that these detectors are prime candidates for research applications in the field of alpha radionuclide therapy.

INTRODUCTION

While interest in alpha radionuclide therapy is still on the rise (Bandekar et al., 2014; Kratochwil et al., 2016; Pandya et al., 2016), the field of alpha radiobiology experiences a severe lack of proper tools. The high LET of alpha radiation leads to more complex DNA damage and repair mechanics (Franken et al., 2011; Prise et al., 1998; Rydberg, 2001) and microdosimetric effects (Huang et al., 2012; Lu and Kiger, 2009; Roeske and Stinchcomb, 1997; Stinchcomb and Roeske, 1992). Precise knowledge of the dose deposited in cells on a macro- and microscale by an alpha radiation field is required to perform these kinds of studies. Accurate alpha radiation (micro-)dosimetry does however remains difficult, partly due to alpha particles being unable to penetrate the walls of most radiation measurement equipment due to their short range (< 100 μm in water). (near-) Wall-less dosimeters like plastic nuclear track detectors (PNTD) (Wertheim et al., 2010), radiochromic film (Aydarous and Ghazaly, 2013), and alpha cameras (Back and Jacobsson, 2010), extrapolation chambers (EC) (Bohm et al., 1991) and simulation (Hamacher and Sgouros, 2001) are therefore commonly applied for alpha dosimetry. A recently introduced new type of detector called fluorescent nuclear track detector (FNTD) has shown to be an excellent alpha spectrometer (Bartz et al., 2013; Chapter 3; Chapter 4) and

gamma (Bartz et al., 2011a; Sykora and Akselrod, 2010b), neutron (Sykora and Akselrod, 2010b; Sykora et al., 2008b, 2009) and ion dosimeter (Greilich et al., 2013; Klimpki et al., 2016; Osinga et al., 2013, 2014b; Sawakuchi et al., 2016). FNTDs are small, cheap and reusable and have the ability to measure individual alpha tracks, yielding a rich amount of information regarding the location, track direction, energy and LET of individual particles. This combination has the potential to have the FNTD function simultaneously as alpha spectrometer, dosimeter and, possibly, microdosimeter. This versatile functionality is unique and can assist the study of radiobiology and microdosimetry for alpha particles greatly.

Radiobiological experiments often require relatively large doses (0.1 – 5 Gy) in large cell cultures (>30 mm diameter dishes) to yield statistically significant result (Franken et al., 2011; Tracy et al., 2015). However, commercially available alpha radiation sources with sufficient activity to induce the required doses within a reasonable timespan (<1 hour) are often much smaller than the used cell cultures, therefore requiring translation of the source to irradiate the whole target volume. In order to address this issue, a novel collimated alpha irradiation setup is introduced to enable uniform irradiation of large areas with a small source.

By combining this novel setup with FNTDs, an experimental setup for alpha radiobiology experiments with extensive knowledge of the radiation field characteristics is presented in order to answer the need for better tools for alpha radiobiology and microdosimetry. Since the FNTDs have not yet been used for alpha dosimetry, this work presents a novel method for alpha radiation dosimetry using these detectors. This method was validated by comparing the FNTD measured surface dose above the irradiation setup, with extrapolation chamber measurements and Monte Carlo simulations and by comparing the FNTD measured angular distribution of the alpha particles, with Monte Carlo calculated distributions.

MATERIALS AND METHODS

Irradiation setup

A setup capable of irradiating large areas with a collimated alpha source was required for future biological experiments. 241Am sources with high activities usually only cover a relatively small area (95 mm^2 for our source) and therefore require the source to be moved and collimated to evenly irradiate larger areas. For this research, a honeycomb collimator in combination with linear stages to move the collimated source to preset locations were used to irradiate areas up to 850 mm^2. A 1.1 cm diameter Americium-241 alpha source with an activity of 409.6 kBq ± 1.7% (20-03-1994) was obtained from the Czech Metrological Institute. A 2 µm gold layer covers the estimated 1.3 µm layer of americium oxide to prevent leakage. The source was placed on two digitally controlled linear stages and a lab jack purchased from Optics Focus Instruments Co. Ltd, China. The linear stages were controlled using a motion controller

purchased from the same supplier. The source assembly was placed inside a custom-made aluminum frame with a rail above the assembly for sample placement (see Figure 5-1). Sample holders for cell cultures and FNTDs were designed in-house and 3D printed using an Ultimaker 2+ with 200 µm layer height and PLA filament.

A collimator with honeycomb structures and wall height of 1800 µm (Figure 5-1, Figure 5-3) was designed to restrict the maximum angle of the alpha particles for reliable measurements with both the FNTDs and the extrapolation chamber.
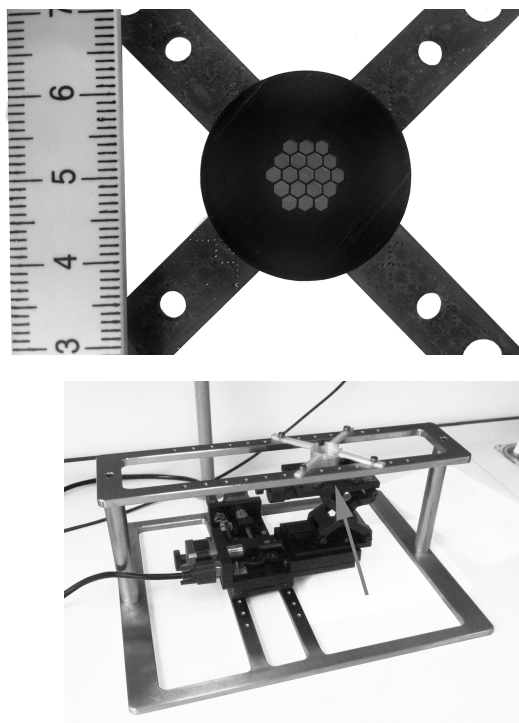
Figure 5-1: (top) 3D printed honeycomb collimator made using ABS plastic. The gold layer of the source is visible through the honeycomb structure. The given scale is in centimeters. (bottom) Photo of the aluminum frame with linear stages and a lab jack mounted on the linear stages for source position adjustment. The source (not visible, located at the arrow) was placed on top of the lab jack under the white sample holder.

To restrict the maximum angle even more a similar collimator with 2600 µm height was constructed as well. A honeycomb geometry was chosen because it features the same wall thickness throughout the whole geometry (0.2 mm, Figure 5-2) which leads to a homogeneous alpha radiation induced dose distribution starting from a specific distance above the collimator. This distance was determined using simulation and radiochromic film. The

collimators were printed using an EnvisionTEC PERFACTORY® 4 DSP high-resolution printer with 25 μm layer height and ABS filament. A 500 μm thick solid layer was printed on the honeycomb structure for support during printing, but was later removed via sanding. Residual burrs in the honeycomb structure were removed under a microscope using a scalpel. The collimators encapsulated the source and had 4 extending arms which were bolted to the surface of the linear stages. A 400 μm gap between the collimator and the active surface was added to avoid direct contact with the gold protection layer. A sketch of the collimator geometry is given in Figure 5-2 (top).
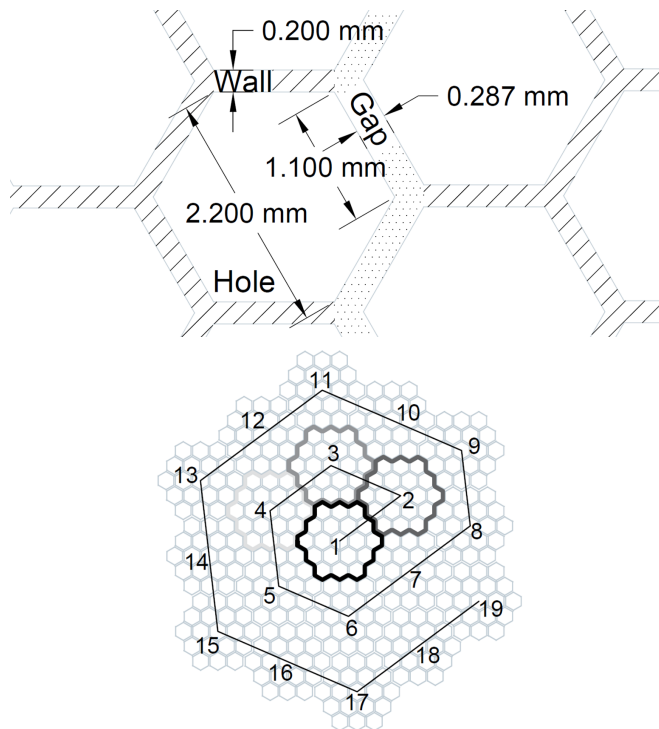
Figure 5-2: (top) Dimensions of the honeycomb structure as used in the collimators. A single collimator is 5 holes wide. The wall thickness between the holes (dashed) is 0.200 mm. The distance between collimator positions 1 and 2 shown on the right (gap, dotted) is 0.287 mm. A gap size of 0.287 mm instead of the 0.2 mm thickness of the physical walls was found to result in a more even dose distribution. (bottom) Positioning of the collimator to form an extended honeycomb structure, thereby creating a large virtual source. The zigzag black line numbered 1, 2, ... shows the movement of the collimator center. The dark outlines in the center represent the periphery of the collimator during the first few collimator positions

The positioning in the x,y-plane of the collimated source was done using an in-house build MATLAB interface and RS232 communication with the motion controller. The software placed

the collimated source at the indicated positions and the source was halted at each position for a time, chosen based on the desired total dose deposition. Movement between positions 1, 2, ... (see Figure 5-2, bottom) was relatively fast at less than 1 second per transition. By moving the collimated source so that the gap between adjacent collimator positions approximated the wall thickness of the physical collimator, a virtual scalable collimated source could be created (Figure 5-2, bottom). It was found that a virtual wall thickness of approximately 0.287 mm, instead of 0.2 mm, led to the most homogeneous dose distribution in radiochromic film, most likely due to small manufacturing errors. For the experiments in this research, only positions 1 through 7 were used. Positions 8 through 19 can be used to create a large field required for biological experiments.

Alignment of the collimated source and sample holder was done by placing 100 μm thick washers between the sample holder arms, so that a deviation of less than 100 μm from the desired distance between the collimator and the sample holder was realized. The deviation was measured at 4 positions on the collimated source: [-12,-12],[12,-12],[12,12],[-12,12] (x,y; mm from center).

Radiochromic Film

In order to find the required distance between the sample and the collimated source to reach a uniform dose distribution, 30 mm diameter slices of Gafchromic[tm] HD-V2 radiochromic film, kindly provided by PEO Radiation Technology, were irradiated with 60-100 Gy at various heights above each collimator. For each height the collimator was moved using collimator positions 1 to 7 (Figure 5-2, bottom). The radiochromic film was scanned with a HP Photosmart Premium C310 at 1200 ppi after which the red channel was isolated and converted to optical density using the image-processing software FIJI (Schindelin et al., 2012). The response in optical density, given by eq. (1) in Aydarous et al., of the red channel of the radiochromic film to exposure was shown to be linear in this dose range (Aydarous and Ghazaly, 2013).

FNTD Irradiation and read-out

FNTDs [8 x 4 x 1 (x,y,z) mm³] were irradiated with approximately 1 Gy above the 1800 and 2600 μm collimators at respectively 5.0 ± 0.1 mm and 7.0 ± 0.1 mm from the active surface. Since the measured area in the FNTDs is small compared to the sizes of the holes of the collimator, the angular distribution of incident alpha particles varied strongly between the irradiation positions. A simplified schematic overview for the first irradiation position above the 1800 μm collimator is given in Figure 5-3.
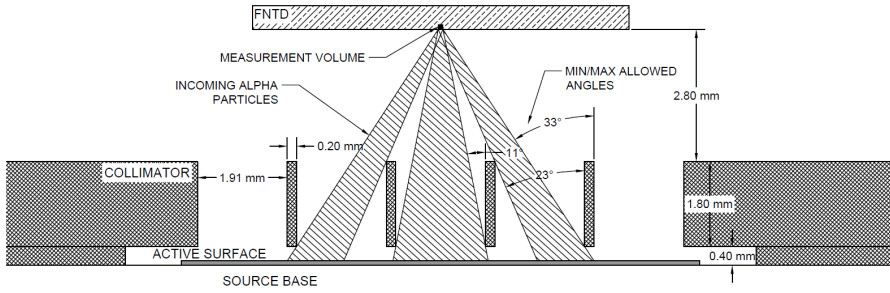
Figure 5-3: Schematic overview of possible alpha tracks through a 1.8 mm (1800 μm) thick collimator entering the measured area of the FNTD at position 1 (see Figure 5-5). A total of 9 irradiations positions were chosen to represent the angular distribution of the whole irradiation field. Note that since a total of 9 positions are used for the irradiation of FNTDs, the collective angular distribution of alpha tracks measured in the FNTDs will yield an angular distribution with less pronounced peaks than found when looking at individual irradiation positions as shown here.

A total of 9 FNTD irradiation positions were chosen based on sampling of the smallest elementary area (Figure 5-5, top), meaning that the whole collimator could theoretically be built by copying, scaling and rotating this area. The FNTD irradiation positions were distributed over the whole collimator in order to better represent the spatial variations in the extended radiation field, as illustrated in Figure 5-5 (bottom). During each FNTD irradiation, the collimated source was moved to positions 1 to 7 (Figure 5-2, bottom).

The center 100 x 100 x 12 μm³ volumes of FNTDs were read-out using a Leica SP5 confocal laser scanning microscope with Avalanche Photo Diodes (APD) (Figure 5-4). From the resulting fluorescent image stacks, the tracks induced by passing alpha particles in the measurement volume were reconstructed (Chapter 3). Track reconstruction yielded for each track l, its path length in the FNTD L_l, initial direction vector given by $x = \chi_l z$ and $y = \gamma_l z$, point of entrance (x_l, y_l, z_l) and corresponding entrance energy (Chapter 4). The angle of incidence of track l measured in an FNTD was calculated using eq. (5-1):

$$\theta_l = \tan^{-1}\left(\sqrt{\chi_l^2 + \gamma_l^2}\right)$$ (5-1)

Where χ_l and γ_l are the linear slopes between the depth z and respectively the x and y coordinate of track l.
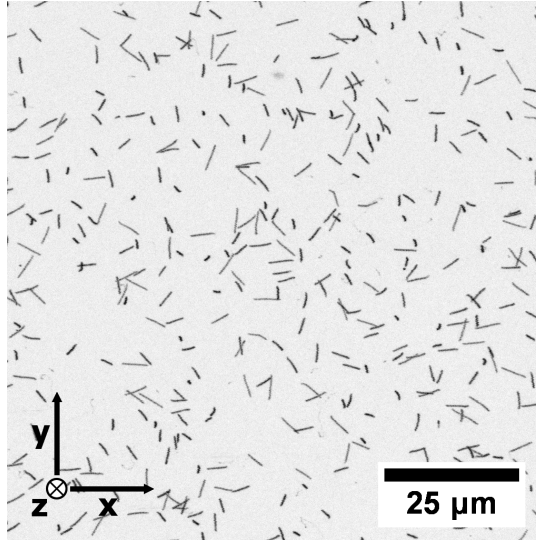
Figure 5-4: A 2D maximum intensity projection of the fluorescence measured in a 100 x 100 x 12 μm³ (x,y,z) volume with a confocal laser scanning microscope in a FNTD after irradiation with alpha particles. The apparent length of the tracks is related to the angle of incidence of the alpha particles. Individual tracks were analyzed using in-house build software, yielding the start- and endpoint, direction, relative scattering, fluorescence intensity and energy for each track.

FNTD Dosimetry

Using the energy and velocity vector of each particle upon entering the FNTD, the water equivalent absorbed dose rate at depth $z = 0$ in the FNTD was calculated via:

$$\dot{D} = \frac{s_{w,Al_2O_3}}{a \, \rho_{Al_2O_3} \, t} \frac{N_{total}}{N_{tracked}} \sum_{l=1}^{N_{tracked}} \frac{LET_{Al_2O_3,l}}{\cos(\theta_l)} \bigg|_{z=0} \tag{5-2}$$

where $s_{w,Al_2O_3} = 1.408 \pm 2.8\%$ is the stopping power ratio for alpha particles in aluminum oxide and water at 3.7 MeV (Berger et al., 2005; Ziegler, 1999), $N_{tracked}$ is the number of tracked tracks, N_{total} is the number of tracked tracks plus the number of missed tracks, $\rho_{Al_2O_3}$ is the density of aluminum oxide (3790 kg/m³), t is the irradiation time, a is the measurement surface area, $LET_{Al_2O_3,l}$ is the Linear Energy Transfer of track l in aluminum oxide upon entering the FNTD (derived from the particle energy) (Berger et al., 2005) and the term $1/\cos(\theta_l)$, in which θ_l is the angle of incidence for track l (eq. (5-1)), corrects for the increased dose deposition by tracks not aligned with the z-axis.
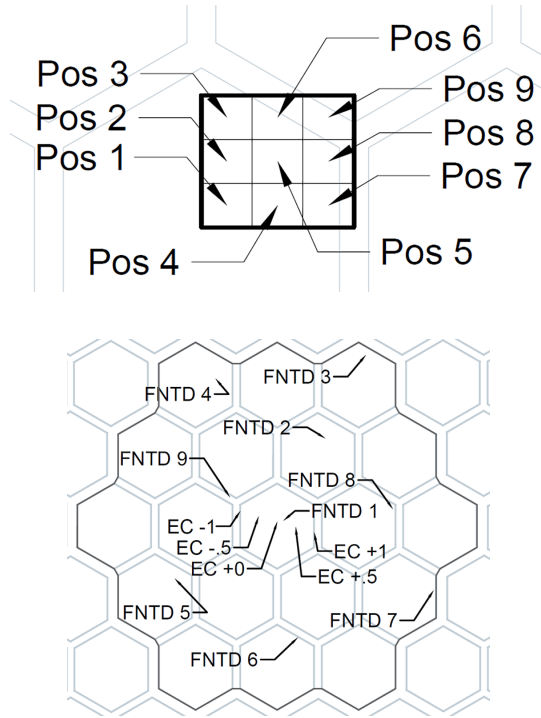
Figure 5-5: (top) The smallest elementary area (thick outline, 1.05 x 9.1 mm²) of the collimator and the 9 FNTD sampling positions. (bottom) Irradiation positions of the centers of the FNTDs divided over the whole collimator, together with the extrapolation chamber (EC) measurement positions. The dark black outline represents the outline of the first collimator position. Multiple collimator positions were only used during FNTD irradiation.

Since the tracking algorithm colors the reconstructed tracks, tracks missed by the algorithm, and therefore not included in dose calculation, were counted visually. Assuming that the uncertainties in χ_l and γ_l are negligible, the uncertainty of the surface dose estimation can be approximated as:

$$\frac{\sigma_D}{D} \approx \sqrt{\left(\frac{\delta s_{w,Al_2O_3}}{s_{w,Al_2O_3}}\right)^2 + \left(\frac{\delta N_{total}}{N_{total}}\right)^2 + \left(\frac{\delta LET_{Al_2O_3,l}}{LET_{Al_2O_3,l}}\right)^2} \tag{5-3}$$

where the first and second terms in the root are respectively the stopping power ratio and Poisson uncertainties. The last term, the relative uncertainty on LET for track l can be separated into two distinct components. The first component is the uncertainty of the tabulated LET values for alpha particles in matter, which was estimated at 2% for the materials used (Berger et al., 2005; Ziegler, 1999). The second component is the uncertainty of the

estimated initial energy of alpha particles entering the FNTD. As shown in an earlier chapter (Chapter 4), almost all particles are in the rising flank of the Bragg peak upon entering the FNTD. No significant bias was observed, but the uncertainty of the measured initial energy distribution was estimated at 200 keV from the difference in measured and simulated alpha particle energy spread of the collimated source. Using the relation between initial energy and LET from NIST's ASTAR, this spread results in a relative uncertainty in the LET of a single track of approximately 3%. The estimates of the initial energies of all individual tracks are fully uncorrelated. Therefore the contribution of this second component to the total uncertainty of the surface dose must be divided by $\sqrt{N_{total}}$, therefore this component is negligible compared to the Poisson (4.7% for single FNTD, 1.7% for the FNTDs combined) and stopping power uncertainties (2%).

Extrapolation Chamber

The surface dose rate to water for the 1800 (2600 μm) collimator at 5.0 ± 0.1 mm (7.0 ± 0.1 mm) from the active surface was measured at -1, -0.5, 0, 0.5 and 1 mm from the center using an extrapolation chamber since measurements of the extended radiation field were not possible in the extrapolation chamber setup (Figure 5-5, bottom). The extrapolation chamber, located at the Dutch Metrology Institute (VSL, Delft, the Netherlands), was similar to the setup used by Bohm et al. (Bohm et al., 1991). The chamber was covered by a 3.5 μm ± 10% polyethylene terephthalate (PE) film with an approximate 20 nm aluminum coating, obtained from Goodfellow Cambridge Ltd., England. By measuring the charge generated in the chamber as function of chamber height z, the absorbed dose rate $\dot{D}$ at $z = 0$ (surface dose) to water was given by eq. *(5-4)* (Bohm et al., 1991):

$$\dot{D} = \frac{s_{w,a}}{a} \frac{W}{\rho_{air}} \frac{W}{e} k_{mylar} \left. \frac{d(k_{ad} I)}{dz} \right|_{z=0} \tag{5-4}$$

where $s_{w,a} = 1.17 \pm 2.8\%$ is the stopping power ratio for alpha particles in air and water at 3.7 MeV (average entrance energy) (Berger et al., 2005; Ziegler, 1999), $W/e = 35.08\ J/C \pm 0.8\%$ is the quotient of the mean energy required to produce an ion pair in air (ICRU, 1979), $a = 0.8568\ mm^2 \pm 0.2\%$ is the collector surface area, ρ_{air} is the density of air under reference conditions, $k_{mylar} = 0.923 \pm 1.9\%$ is a correction factor for the increase in stopping power due to the presence of the entrance film (based on simulation and film thickness uncertainty), I is the measured current corrected for saturation effects (Böhm, 1976; Bohm et al., 1991) and k_{ad} is the correction for the deviation of the air density from ρ_0 (for standard pressure p₀ = 101.325 and temperature T₀ = 293.15 K) given by $k_{ad} = p_0 T / p T_0$, where T is the absolute temperature (in K) and p is the air pressure. The charge was measured for 120 (180) s using the 1800 (2600) μm collimator, with both positive and negative polarity, at $z =$

0.1, 0.2 .. 1.0 mm. Each measurement was repeated 4 times. $k_{ad} \cdot I$ was fitted to a linear curve using least squares minimization to obtain the slope $d(k_{ad} \, I)/dz$ and its respective uncertainty. FLUKA simulations of the sources within the extrapolation chamber setup showed negligible divergence in dose deposition up to 1 mm chamber heights.

FLUKA Simulation

Simulations of the sources with a 1 mm diameter, 10 μm high air filled cylindrical measurement volume were performed using FLUKA2011 version 2c.3 (Ferrari et al., 2011). The simulation geometry was very similar to Figure 5-3, but with the FNTD volume replaced by a cylindrical air filled volume. The source, collimator and setup dimensions mentioned in the 'Irradiation setup' section were used for the simulation geometry. The source was modeled as an infinitely thin layer halfway the americium oxide layer, which was modeled using the same density, but with gold atoms instead of americium atoms since higher Z atoms are not available in FLUKA. Each simulation ran for 1E6 particles and was repeated 5 times for uncertainty estimation. The approximate surface dose to water was calculated by multiplying the obtained dose in air with $s_{w,a}$. No extra dose measurements in the extended irradiation field, created by multiple collimators positions, were performed since simulations showed near-perfect dose uniformity over the whole extended field. The influence of the entrance film in the extrapolation chamber on the stopping power was determined by comparing the surface dose in air with and without aluminized mylar film in front of the air column. The absorbed dose in the mentioned air filled cylindrical measurement volume was obtained using the FLUKA USRBIN routine. A single bin spanning the entire measurement volume was used for the mean absorbed dose determination, while 15 x 15 x 10 μm³ bins spanning the cylindrical volume were used for dose homogeneity estimation. The angular distribution of particles entering the cylindrical volume was obtained using the USRBDX routine with 120 angle bins, spanning from 0 to 60° after conversion from solid angle to angle of incidence.

RESULTS

Radiochromic film

The dose inhomogeneity in the radiochromic film was found to drop below 5% (standard deviation) from 5.0 ± 0.1 mm (7.0 ± 0.1 mm) for the 1800 (2600 μm) collimator. FLUKA simulations for both collimators showed negligible spatial fluctuations (<0.5%) in surface dose at these heights. Contrast enhanced optical density maps of radiochromic film irradiated at these heights are shown in Figure 5-6. Intensity profiles along the white lines are given in Figure 5-7. Relative standard deviations in optical density of 4.4% and 4.6% for respectively the 1800 and 2600 μm collimator were measured in the films. The relative standard deviations

in optical density of unirradiated film was below 0.5%. No noise correction was applied to the images. Optical density to absorbed dose conversions were avoided due to the strong LET and angle dependency of the film.
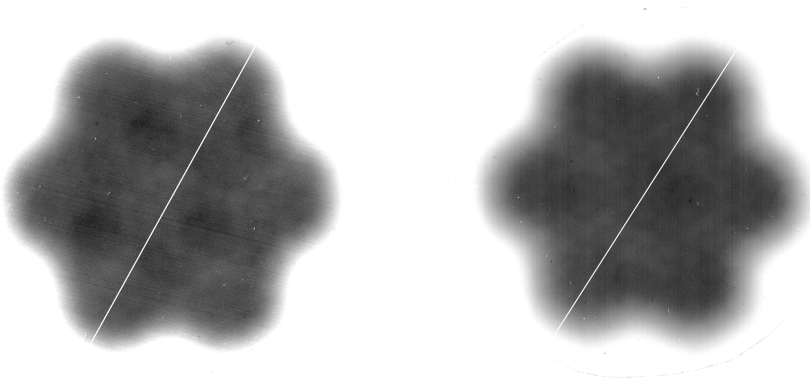
Figure 5-6: Optical density maps of Gafchromic^tm HD-V2 film irradiated using the 1800 μm (left) and 2600 μm (right) collimator, contrast enhanced to show the residual unevenness in dose distribution due to the honeycomb structure. Variations in dose distribution were below 5% for both collimators. The white lines are 30 mm long and indicate the position of the intensity profile in Figure 5-7. White specks are dust particles on the film during scanning.
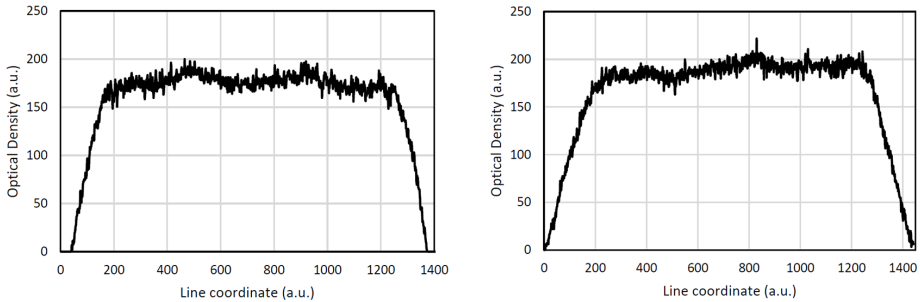
Figure 5-7: Contrast enhanced optical density maps of Gafchromic^tm HD-V2 film irradiated using the 1800 μm (left) and 2600 μm (right) collimator.

Angular Distributions

The measured average angular distributions of the irradiated FNTDs for both collimators are shown in Figure 5-8 together with the corresponding distribution estimated using FLUKA. The missing points near $\theta = 0°$ in the simulated distribution is the result of FLUKA's solid angle binning for angular distributions.
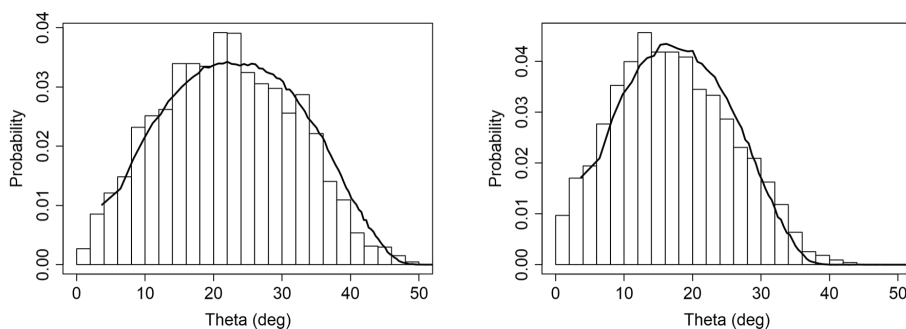
Figure 5-8: The average angular distribution of incoming alpha particles measured using multiple FNTDs irradiated at various positions above the 1800 μm (left) and 2600 μm (right) collimator. The black line represents the distribution obtained using FLUKA.

Dose Measurements

The uncertainties and variance weighted means of the surface dose rates measured using the extrapolation chamber are visualized in Figure 5-9. The uncertainty in the mean dose rate was given by the uncertainty of the constants given in eq. (5-4) and the standard deviation of the measurements at the given position. Uncertainties due to fluctuations in measured charge were small compared to others factors (<0.5%). The largest contributions to the uncertainties in the extrapolation chamber measurements were from the stopping power ratio (2.8%) and the mylar film correction (1.9%). Out of the 18 irradiated FNTDs, two measurements failed due to poor image quality. A total of 3348 (3251 tracks) were reconstructed while 6 (0) tracks were missed by the algorithm for the 1800 (2600) μm collimator measurements. The measured or estimated surface dose rates based on FNTD, extrapolation chamber and FLUKA data are given together with the respective fluences in Table 5-1. The uncertainties in the mean dose rates for the FNTD and extrapolation chamber measurements were given by the uncertainty of the constants given in respectively eq. (5-3) and eq. (5-4) and the standard deviation of the measurements at the various locations in the radiation field. The latter is related to the dose inhomogeneity in the radiation field, and the inhomogeneity therefore has an effect on the uncertainty of the mean dose rate. Uncertainties in the simulations were a combination of statistical uncertainty from the simulations and the source activity uncertainty. Uncertainties resulting from possible variations in source and collimator geometries due to manufacturing errors were not included in the simulation results.
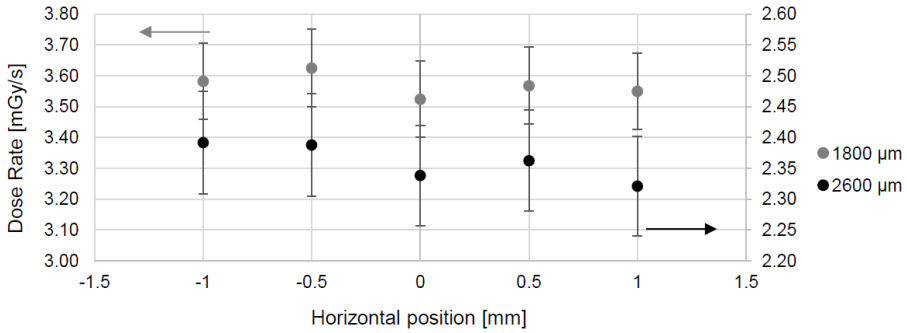
Figure 5-9: Surface dose rate to water measured using an extrapolation chamber at different horizontal positions above the collimator. Error bars indicate 1 standard deviation. Error bars indicate the combined uncertainty, taking into account the uncertainty of the constants given in eq. (5-4) and the standard deviation of the mean dose rate at the given position.

Table 5-1: Surface dose rates and fluences as measured or estimated using FNTDs, extrapolation chamber and FLUKA for the two collimators. The uncertainties are given by the standard deviation of the mean dose rate and the uncertainties given in eq. (5-3) and eq. (5-4).

	1800 μm Collimator		2600 μm Collimator	
	Dose rate (mGy/s)	Fluence (s⁻¹ cm⁻²)	Dose rate (mGy/s)	Fluence (s⁻¹ cm⁻²)
FNTD	3.36 ± 5.9% (5.3%*)	18201 ± 4.4%	2.22 ± 9.0% (5.4%*)	11846 ± 7.8%
Extrapolation Chamber	3.57 ± 3.8% (3.5%*)	-	2.36 ± 3.8% (3.5%*)	-
FLUKA	3.72 ± 5.0%	20744 ± 4.0%	2.06 ± 5.0%	11162 ± 4.0%

* Mean of the relative standard deviations of the individual measurements

DISCUSSION

FNTD measurements underestimated the extrapolation chamber measurements by 5.8% and 5.9% for respectively the 1800 and 2600 μm collimator. While these numbers are within the confidence intervals, the similarity in underestimation for both collimators suggests a systematic cause. A possible cause could be uncertainties in detected locations of the FNTD surfaces in the fluorescence images, leading to an under- or overestimation of the traversed distances of the tracks in the detectors. The maximum reflection intensity of an FNTD in the confocal laser scanning microscope can be used to find the location of the detector surface prior to scanning as shown in an earlier chapter (Chapter 3). The surface location for this set of FNTD scans was refined using a small portion of the tracks and the expected energy from the verified source geometry to allow for comparisons between different imaging methodologies (Chapter

4). When the source geometry is unknown, detection of the detector surface using only the maximum reflection intensity is, under ideal circumstances, accurate up to 200 nm (Akselrod et al., 2014a), which translates to an uncertainty in surface dose rate of approximately 3% for this irradiation setup. Other contributing factors might include missed or wrongly reconstructed tracks, overestimation of the stopping power ratio for alpha particles in aluminum oxide and water for the FNTD measurements, and possibly an overestimated value for W/e, with the current value for alpha radiation dating back to 1979 for the extrapolation chamber. While the atmospheric conditions were not measured during FNTD irradiations, it is expected that variations in air density did not have a significant impact on the energy, and therefore the stopping power, of the alpha particles upon entering the FNTD due to relatively short path length of the particles through the air. More research is required to find the possible cause of the apparent difference in surface dose rate.

Track overlap was not problematic at the applied dose (~1 Gy), but is expected to interfere with accurate track reconstruction from 2 - 5 Gy. Sykora et al. introduced the power spectrum integral (PSI) approach for high fluence dose estimation in FNTDs (Sykora and Akselrod, 2010c). However, this method suffers from LET dependency and the compatibility with high-LET alpha radiation is unknown. The penetration in the crystal is used to determine the track's initial energy. Therefore, when the source setup is unknown, the dose measurement method described here relies heavily on the correct determination of the detector's surface plane. An automated FNTD reader offers accurate surface plane detection within 200 nm (Akselrod et al., 2014a), which translates to an additional 1% uncertainty in LET (3.7 MeV, aluminum oxide). From this it is expected this method is reliable for alpha doses below 2 Gy.

Field inhomogeneity seen in the optical density of the radiochromic films (4.4 - 4.6%) and uncertainties obtained in FNTD measurements (5.9 – 9.0%) were large compared to the uncertainty in mean surface dose rate in the extrapolation chamber measurements (3.8%). The uncertainty of the extrapolation chamber measurements might realistically be higher due to several unknown factors like entrance window flatness and aluminum coating thickness. However, the relatively large difference in uncertainty between the FNTDs and the extrapolation chamber suggest that the inhomogeneity of the extended radiation field can partly be attributed to small errors in collimator positioning and manufacturing errors at the edge of the collimator. This is especially true for the 2600 μm collimator, where it is expected that the smaller maximum angle of incidence leads to a more localized dose deposition by individual holes in the collimator. Manufacturing errors in the collimator walls will therefore have a larger effect on the dose uniformity. This dose rate location dependency led to the relatively large uncertainty in surface dose rate found using FNTDs. This is reflected by the smaller uncertainties found in measurements of single FNTDs (5.3 – 5.4%). Future studies might benefit from elimination of this location factor and more repeated measurements to better estimate the dose uncertainty of this approach. The angular distributions measured

using FNTDs and estimated using FLUKA were in good overall agreement. Meanwhile, it was found that the collimator models in the simulations over- and underestimated the fluence and surface dose rates for the collimators. Possible adjustments to the simulated collimator geometry required to match the surface dose rates found using the extrapolation chamber and the simulations are shown in Table 5-2. Due to the limited resolution of the 3D printer (25-42 μm) and the additional sanding of the collimator, the indicated possible deviations in wall height and thickness from the design values are not unlikely. Since the simulations both under- and overestimated the surface dose rates, it was considered unlikely that the gold layer thickness differed from the used thickness since the change in attenuation of the alpha particles in the gold layer would have a comparable effect in both collimator simulations.

Table 5-2: Possible adjustments to the simulated collimator geometries to match the surface dose rates found using simulations and the extrapolation chamber measurements

	1800 μm Collimator		2600 μm Collimator	
	Wall height (μm)	**Wall Thickness (μm)**	**Wall height (μm)**	**Wall Thickness (μm)**
Planned geometry	1800	200	2600	200
Adjusted geometry	1823	206	2516	181

CONCLUSION

FNTD dosimetry was validated with both measurements and simulations. The angular distributions measured using FNTDs were in good overall agreement with simulated distributions. Analysis of the difference between measured and simulated surface dose rates showed that the induced dose rate is very sensitive to small variations in the collimator geometry. Surface dose rate measurement is therefore crucial for setups based on this geometry.

Surface dose rates, measured using FNTDs and extrapolation chamber, were in agreement for both collimator setups. However, uncertainties in surface dose rate due to field inhomogeneity and measurement uncertainties were high for the FNTD approach (5.9 – 9.0%) compared to the extrapolation chamber measurements (3.8%). Since extrapolation chamber measurements were performed in a smaller area than the FNTD measurements, it is expected that similar values could be reached with increased sample sizes, reduction of the dose inhomogeneity in the extended radiation field and further research on the uncertainties and improvement of surface location detection, track reconstruction, energy estimation, geometry and stopping power ratios involved with FNTD alpha dosimetry.

FNTDs nevertheless offer significant advantages. The detectors are small, robust, very cheap, can be read-out multiple times non-destructively and offer rich collection of data, including fluence, angular spectrum and energy. FNTDs can therefore readily be applied for dosimetry of very small (cell nuclei e.g.) volumes and alpha spectroscopy in addition to regular alpha dosimetry. These unique properties make FNTDs strong competitors in the field of alpha radiation dosimetry.

The dose uniformity in larger irradiated areas showed variations of less than 5%, making this setup, in combination with the rich information obtained regarding the spatial, angular and energy distributions of the alpha particles, obtained using the FNTDs, ideal for microdosimetry experiments, irradiation of larger cell cultures and other radiobiology experiments. The individually measured tracks together with the surface dose could be used to estimate the microdosimetric spectra of doses induced in cell nuclei, while the LET and angular spectra find their use in DNA damage and RBE studies. The obtained uncertainties in surface dose are expected to be sufficient for the application in radiobiology.

ACKNOWLEDGEMENTS

REFERENCES

Akselrod, M.S., Fomenko, V.V., Bartz, J.A., Haslett, T.L., 2014. Automatic neutron dosimetry system based on Fluorescent Nuclear Track Detector Technology. *Radiat. Prot. Dosimetry* 161(1), 86–91.

Aydarous, A., Ghazaly, M. El, 2013. Characterization of HD-V2 Gafchromic Film for Measurement of Spatial Dose Distribution from Alpha Particle of 5.5 MeV. *Int. J. Math. Comput. Phys. Electr. Comput. Eng.* 7(7), 1279–1281.

Back, T., Jacobsson, L., 2010. The alpha-Camera: A Quantitative Digital Autoradiography Technique Using a Charge-Coupled Device for Ex Vivo High-Resolution Bioimaging of alpha-Particles. *J. Nucl. Med.* 51(10), 1616–1623. https://doi.org/10.2967/jnumed.110.077578

Bandekar, A., Zhu, C., Jindal, R., Bruchertseifer, F., Morgenstern, A., Sofou, S., 2014. Anti-Prostate-Specific Membrane Antigen Liposomes Loaded with 225Ac for Potential Targeted Antivascular alpha-Particle Therapy of Cancer. *J. Nucl. Med.* 55(1), 107–114. https://doi.org/10.2967/jnumed.113.125476

Bartz, J.A., Sykora, G.J., Bräuer-Krisch, E., Akselrod, M.S., 2011. Imaging and dosimetry of synchrotron microbeam with aluminum oxide fluorescent detectors. *Radiat. Meas.* 46(12), 1936–1939. https://doi.org/10.1016/j.radmeas.2011.04.003

Bartz, J.A., Zeissler, C.J., Fomenko, V.V., Akselrod, M.S., 2013. An imaging spectrometer based on high resolution microscopy of fluorescent aluminum oxide crystal detectors. *Radiat. Meas.* 56, 273–276. https://doi.org/10.1016/j.radmeas.2013.01.041

Berger, M.J., Coursey, J.S., Zucker, M.A., Chang, J., 2005. ESTAR, PSTAR, and ASTAR: Computer Programs for Calculating Stopping-Power and Range Tables for Electrons, Protons, and Helium Ions (version 1.2.3), National Institute of Standards and Technology, Gaithersburg, MD ,USA.

Bohm, J., Ambrosi, P., Wernli, C., 1991. Measurement of the Depth-Dose Curve of 240Pu Alpha Particles. *Radiat. Prot. Dosimetry* 39(1), 191–194. https://doi.org/10.1017/CBO9781107415324.004

Böhm, J., 1976. Saturation corrections for plane-parallel ionization chambers. *Phys. Med. Biol.* 21(5), 754–759. https://doi.org/10.1088/0031-9155/21/5/004

Ferrari, A., Sala, P.R., Ranft, J., 2011. Fluka: a multi-particle transport code, Stanford Linear Accelerator Center, Stanford, CA, USA.

Franken, N. a P., ten Cate, R., Krawczyk, P.M., Stap, J., Haveman, J., Aten, J., Barendsen, G.W., 2011. Comparison of RBE values of high-LET α-particles for the induction of DNA-DSBs, chromosome aberrations and cell reproductive death. *Radiat. Oncol.* 6(1), 64. https://doi.org/10.1186/1748-717X-6-64

Greilich, S., Osinga, J.M., Niklas, M., Lauer, F.M., Klimpki, G.M., Bestvater, F., Bartz, J.A., Akselrod, M.S., Jäkel, O., 2013. Fluorescent nuclear track detectors as a tool for ion-beam therapy research. *Radiat. Meas.* 56, 267–272. https://doi.org/10.1016/j.radmeas.2013.01.033

Hamacher, K.A., Sgouros, G., 2001. Theoretical estimation of absorbed dose to organs in radioimmunotherapy using radionuclides with multiple unstable daughters. *Med. Phys.* 28(9), 1857–1874. https://doi.org/10.1118/1.1395026

Huang, C.Y., Guatelli, S., Oborn, B.M., Allen, B.J., 2012. Microdosimetry for targeted alpha therapy of cancer. Comput. *Math. Methods Med.* 2012. https://doi.org/10.1155/2012/153212

ICRU, 1979. Average Energy Required to Produce an Ion Pair, International Commission on Radiation Units and Measurements Washington. https://doi.org/10.1017/CBO9781107415324.004

Klimpki, G.M., Mescher, H., Akselrod, M.S., 2016. Fluence-based dosimetry of proton and heavier ion beams using single track detectors. *Phys. Med. Biol.* 61(3), 1021–1040.

Kratochwil, C., Bruchertseifer, F., Giesel, F.L., Weis, M., Verburg, F.A., Mottaghy, F., Kopka, K., Apostolidis, C., Haberkorn, U., Morgenstern, A., 2016. 225Ac-PSMA-617 for PSMA-Targeted alpha-Radiation Therapy of Metastatic Castration-Resistant Prostate Cancer. *J. Nucl. Med.* 57(12), 1941–1944. https://doi.org/10.2967/jnumed.116.178673

Lu, X.-Q., Kiger, W.S., 2009. Application of a novel microdosimetry analysis and its radiobiological implication for high-LET radiation. *Radiat. Res.* 171(6), 646–56. https://doi.org/10.1667/RR1612.1

Osinga, J.M., Akselrod, M.S., Herrmann, R., Hable, V., Dollinger, G., Jäkel, O., Greilich, S., 2013. High-accuracy fluence determination in ion beams using fluorescent nuclear track detectors. *Radiat. Meas.* 56, 294–298. https://doi.org/10.1016/j.radmeas.2013.01.035

Osinga, J.M., Brons, S., Bartz, J.A., Akselrod, M.S., Jäkel, O., Greilich, S., 2014. Absorbed dose in ion beams : Comparison of ionization- and fluence-based measurements. *Radiat. Prot. Dosimetry* 161(1–4), 387–392. https://doi.org/10.1093/rpd/ncu004

Pandya, D.N., Hantgan, R., Budzevich, M.M., Kock, N.D., Morse, D.L., Batista, I., Mintz, A., Li, K.C., Wadas, T.J., 2016. Preliminary therapy evaluation of 225Ac-DOTA-c (RGDyK) demonstrates that Cerenkov radiation derived from 225Ac daughter decay can be detected by optical imaging for in vivo tumor visualization. *Theranostics* 6(5), 698–709. https://doi.org/10.7150/thno.14338

Prise, K.M., Ahnström, G., Belli, M., Carlsson, J., Frankenberg, D., Kiefer, J., Löbrich, M., Michael, B.D., Nygren, J., Simone, G., Stenerlöw, B., 1998. A review of dsb induction data for varying quality radiations. *Int. J. Radiat. Biol.* 74(2), 173–184. https://doi.org/10.1080/095530098141564

Roeske, J.C., Stinchcomb, T.G., 1997. Dosimetric framework for therapeutic alpha-particle emitters. J. *Nucl. Med.* 38, 1923–1929.

Rydberg, B., 2001. Radiation-induced DNA damage and chromatin structure. *Acta Oncol.* (Madr). 40(6), 682–5. https://doi.org/10.1080/02841860152619070

Sawakuchi, G.O., Ferreira, F.A., McFadden, C.H., Hallacy, T.M., Granville, D.A., Sahoo, N., Akselrod, M.S., 2016. Nanoscale measurements of proton tracks using fluorescent nuclear track detectors. *Med. Phys.* 43(5), 2485–2490. https://doi.org/10.1118/1.4947128

Schindelin, J., Arganda-Carreras, I., Frise, E., Kaynig, V., Longair, M., Pietzsch, T., Preibisch, S., Rueden, C., Saalfeld, S., Schmid, B., Tinevez, J., White, D.J., Hartenstein, V., Eliceiri, K., Tomancak, P., Cardona, A., 2012. Fiji: an open-source platform for biological-image analysis. *Nat. Methods* 9(7), 676–682. https://doi.org/10.1038/nmeth.2019

Stinchcomb, T.G., Roeske, J.C., 1992. Analytic microdosimetry for radioimmunotherapeutic alpha emitters. *Med. Phys.* 19(6), 1385–93. https://doi.org/10.1118/1.596770

Sykora, G.J., Salasky, M., Akselrod, M.S., 2008. Properties of novel fluorescent nuclear track detectors for use in passive neutron dosimetry. *Radiat. Meas.* 43(2–6), 1017–1023. https://doi.org/10.1016/j.radmeas.2007.12.038

Sykora, G.J., Akselrod, M.S., Vanhavere, F., 2009. Performance of fluorescence nuclear track detectors in mono-energetic and broad spectrum neutron fields. *Radiat. Meas.* 44(9–10), 988–991. https://doi.org/10.1016/j.radmeas.2009.10.027

Sykora, G.J., Akselrod, M.S., 2010a. Novel fluorescent nuclear track detector technology for mixed neutron-gamma fields. *Radiat. Meas.* 45(3–6), 594–598. https://doi.org/10.1016/j.radmeas.2010.01.037

Sykora, G.J., Akselrod, M.S., 2010b. Spatial frequency analysis of fluorescent nuclear track detectors irradiated in mixed neutron-photon fields. *Radiat. Meas.* 45(10), 1197–1200. https://doi.org/10.1016/j.radmeas.2010.08.022

Tracy, B.L., Stevens, D.L., Goodhead, D.T., Hill, M.A., 2015. Variation in RBE for Survival of V79-4 Cells as a Function of Alpha-Particle (Helium Ion) Energy. *Radiat. Res.* 184(1), 33–45. https://doi.org/10.1667/RR13835.1

Wertheim, D., Gillmore, G., Brown, L., Petford, N., 2010. A new method of imaging particle tracks in solid state nuclear track detectors. *J. Microsc.* 237(1), 1–6. https://doi.org/10.1111/j.1365-2818.2009.03314.x

Ziegler, J.F., 1999. Comments on ICRU Report 49: Stopping Powers and Ranges for Protons and Alpha Particles. *Radiat. Res.* 152, 219–222. https://doi.org/10.1118/1.597176

Chapter 6

Fluorescent Nuclear Track Detectors for Alpha Radiation Microdosimetry

J.J.M. Kouwenberg[1], H.T. Wolterbeek[1], A.G. Denkova[1], A.J.J. Bos[1]

[1] Radiation, Science & Technology, Delft University of Technology, Mekelweg 15, Delft, the Netherlands

ABSTRACT

Background: While alpha microdosimetry dates back a couple of decades, the effects of localized energy deposition of alpha particles are often still unclear since few comparative studies have been performed. Most modern alpha microdosimetry studies rely for large parts on simulations, which negatively impacts both the simplicity of the calculations and the reliability of the results. A novel microdosimetry method based on the Fluorescent Nuclear Track Detector, a versatile tool that can measure individual alpha particles at sub-micron resolution, yielding accurate energy, fluence and dose rate measurements, was introduced to address these issues.

Methods: Both the detectors and U87 glioblastoma cell cultures were irradiated using an external Am241 alpha source. The alpha particle tracks measured with a Fluorescent Nuclear Track Detector were used together with high resolution 3D cell geometries images to calculate the nucleus dose distribution in the U87 glioblastoma cells. The experimentally obtained microdosimetry parameters were thereafter applied to simulations of 3D U87 cells cultures (spheroids) with various spatial distributions of isotopes to evaluate the effect of the nucleus dose distribution on the expected cell survival.

Results: The new experimental method showed good agreement with the analytically derived nucleus dose distributions. Small differences (<5%) in the relative effectiveness were found for isotopes in the cytoplasm and on the cell membrane versus external irradiation, while isotopes located in the nucleus or on the nuclear membrane showed a substantial increase in relative effectiveness (33 – 51%).

Conclusions: The ease-of-use, good accuracy and use of experimentally derived characteristics of the radiation field make this method superior to conventional simulation-based microdosimetry studies. Considering the uncertainties found in alpha radionuclide carriers in-vivo and in-vitro, together with the large contributions from the relative biological effectiveness and the oxygen enhancement ratio, it is expected that only carriers penetrating or surrounding the cell nucleus will substantially benefit from microdosimetry.

INTRODUCTION

The interest in alpha radionuclide therapy remains on the rise (Bandekar et al., 2014; Kratochwil et al., 2016; McLaughlin et al., 2013; Wang et al., 2014; Woodward et al., 2011), partly for its ability to deal with (micro-)tumours resistant to gamma and beta radiation attributed to the high LET of alpha particles (Franken et al., 2011; Jadvar and Quinn, 2013). Microdosimetry for alpha particles deals with the determination of the absorbed dose distribution in cell nuclei, the so called nucleus dose distribution (NDD) (Roeske and

Stinchcomb, 1997). The high LET of alpha particles, and therefore the relative low fluence per absorbed dose, in combination with the stochastic nature of radiation, leads to large variances in the NDD. This introduces anomalies when comparing the survival of cells in various alpha radiation fields (Charlton and Sephton, 1991). Microdosimetry methods already exist for alpha radiation (Roeske and Stinchcomb, 1997, 1999, Stinchcomb and Roeske, 1992, 1994). However, most of these methods require far-reaching assumptions regarding the radiation field and cell geometries, which have a negative impact of the accuracy and simplicity of these methods (Charlton and Sephton, 1991; Kvinnsland et al., 2001; Stinchcomb and Roeske, 1995). This paper utilizes a novel type of detector called the Fluorescent Nuclear Track Detectors (FNTD) (G. M. Akselrod et al., 2006; M. S. Akselrod et al., 2006), which allows for robust measurement of individual alpha particles with great accuracy (Bartz et al., 2014; Sykora et al., 2008). Using these detectors, the point of entrance, direction and energy of alpha particles tracks can be measured at sub-micrometer resolution (Chapter 3; Chapter 4). This detailed knowledge of the radiation field can be used to calculate the energy deposited in cell nuclei with relative ease and without the need for assumptions regarding the radiation field characteristics or geometry. The resulting microdosimetric spectra can be of great value for both cell survival studies as well as DNA damage and repair studies.

Alpha microdosimetry is also an area for which the criteria for application are not always clear, since very few studies exist that compare the effects of localized energy deposition of alpha particles for various scenarios (Charlton and Sephton, 1991; Roeske and Stinchcomb, 1996; Stinchcomb and Roeske, 1992). Since microdosimetry is often cumbersome, it is important to know under what conditions to apply and when to limit the time spend on microdosimetry during the design and evaluation of alpha radionuclide carriers (ARC). This study therefore extends the knowledge obtained using the FNTD experiments to simulation of virtual spheroids. Spheroids, a type of 3D cell culture that mimics the behavior of (micro-)tumors, are a better model to verify the effectiveness of ARCs than monolayers for alpha radiation therapy, both from a dosimetry and a radiobiology point of view (Charlton, 2000). Simulations for various types of sub-cellular alpha radionuclide distributions and alpha particle energies were performed to clarify the effect of NDD-based microdosimetry on the expected survival.

METHODS

Irradiation setup

An irradiation setup described in a previous chapter (Chapter 5) was built specifically for FNTD alpha (micro-)dosimetry. A 1.1 cm diameter 394 MBq Am241 source supplied by Czech Metrological Institute was placed inside a 3D printed honeycomb collimator and mounted on linear x,y-stages. The 1800 μm thick honeycomb collimator restricted the vertical angle of

alpha particles to 45 degrees to yield sufficient penetration in the FNTD for proper track measurement. The source was moved in the x,y-plane to uniformly irradiate areas up to 9 times the area of the source. Both cells and FNTDs were irradiated 5.0 ± 0.1 mm above the source, yielding a dose rate of 4.15 mGy/s ± 5.3% in the cell layer. This dose rate was checked with an independent measurement with an interpolation chamber.

Cell survival

U87 Glioblastoma cells were cultured in Dulbecco's Modified Eagle Medium supplemented with 10% Fetal Bovine Serum and 1% Penicillin-Streptomycin. 35 mm lumox® dishes (Sarstedt AG & Co., Nümbrecht, Germany) were modified to hold a 1.4 micron mylar film bottom, required for sufficient penetration of the alpha particles into the cell layer. The modified dishes were irradiated to 10 kGy from a Co-60 source for sterilization. U87 cells in culture flasks were resuspended using trypsin, pipetted repeatedly to avoid cell clumps and counted using a digital cell counter, after which 60.000 cells were transferred to mylar dishes. The cells were allowed to settle overnight and irradiated to 0, 125, 249, 498, 747 and 996 mGy (± 5.3%)(chapter 4). To minimize stress induced pH changes following atmospheric exposure, cells were irradiated in medium with 20 mM HEPES and each mylar dish was exposed to ambient air for an equal amount of time. After irradiation, 1900 – 5000 cells per well, depending on the expected survival, were transferred from the mylar dish onto 3 wells in a 24-well plate. The 24-well plates were incubated for 7 days after which the number of surviving cells were counted using the SRB assay (Voigt, 2005). The procedure was performed twice to improve reliability, which was deemed sufficient for the proof-of-principle of this work.

Cell geometry measurement and segmentation

U87 cells were transferred onto glass cover slips and allowed to settle overnight, after which they were fixated for 15 minutes at room temperature using 3.7% formaldehyde. The nucleus and cytoplasm were stained using respectively DAPI and Alexa Fluor 488 Phalloidin. A total of 15 cells were imaged using a Leica SP5 with a 63x 1.40 NA oil objective and a 96 x 96 x 490 nm^3 (x,y,z) voxel size. The measured slice thicknesses were corrected for the difference in reflective index(Van Elburg et al., 2007). The nuclei and cytoplasm in the images were segmented via thresholding using Fiji (Schindelin et al., 2012) yielding an image stack with 8-bit pixel values of 0, 182 and 201 for respectively the background, cytoplasm and nucleus.

Analytical estimation of microdosimetry-based survival

The number of particles hitting a nucleus is discreet. The probability distribution of a cell receiving a dose z can therefore be calculated from the Poisson distribution of the number of particles hitting the cell nucleus and a function describing the energy deposition by a single

track, the so called single hit nucleus dose distribution (SHNDD). Note that the NDD and SHNDD are both sometimes referred to as the specific energy. In this work, NDD and SHNDD will however be used for clarity. Let q be the mean dose of the SHNDD and therefore represent the average dose induced by a single particle in the nucleus, so that the number of tracks per nucleus, given an average dose $\bar{z}$, follows from the Poisson distribution via (ICRU, 1983):

$$p(i, \lambda = \bar{z}/q) = {\lambda^i e^{-\lambda}}/{i!} \qquad (6\text{-}1)$$

Where p is the Poisson distribution, giving the probability of i particles passing through a cell nucleus given an average number of particles λ hitting the cell nucleus at an average dose $\bar{z}$. The nucleus dose probability distribution for i particles hitting the cell nucleus can then be constructed via i convolutions of the SHNDD $f^{i=1}(z)$ (Stinchcomb and Roeske, 1992), which is described in Laplace space by:

$$f^i(z) = \mathcal{L}^{-1}\left\{ \mathcal{L}\{f^{i=1}(z)\}^i \right\} \qquad (6\text{-}2)$$

The SHNDD $f^{i=1}(z)$ is in this case obtained using either experimental methods or simulation. Let $f(z, \bar{z})$ be the NDD, representing the probability of a cell nucleus receiving a dose z given the average dose $\bar{z}$. One can find this probability by summing the contributions of the nucleus dose probability functions for i particles hitting the cell nucleus, $f^i(z)$, where i ranges from 0 to N particles. N is chosen as a very large number so that the likelihood of a cell nucleus being hit by N particles is very small. The NDD distribution then follows from (ICRU, 1983):

$$f(z, \bar{z}) = p(i, \lambda = \bar{z}/q)\delta(z) + \sum_{i=1}^{N} p(i, \lambda = \bar{z}/q)\, f^i(z) \qquad (6\text{-}3)$$

$\delta(z)$ is here the Dirac delta function, taking a value of 1 when the dose z is 0, and taking a value of 0 everywhere else. Now let the survival of a cell colony at absorbed dose x be given by $S(x) = e^{-\alpha x}$. Note that the term α is simply the first constant in the linear-quadratic equation for cell survival, i.e. we neglect the quadratic term. The cell survival based on the nucleus energy deposition distribution is then obtained by integrating over the NDD (Stinchcomb and Roeske, 1992):

$$S_z(\bar{z}) = \int_0^\infty f(z, \bar{z}) \cdot e^{-\alpha_z z}\, dz \qquad (6\text{-}4)$$

Where α_z is the microdosimetric survival slope. The survival $S_z^C(\bar{z})$ for a collection of cells then follows from the summation of eq. (6-4) for the collection C:

$$S_z^C(\bar{z}) = \frac{1}{M} \sum_{l=1}^{M} S_{z,l}(\bar{z}) \qquad\qquad (6\text{-}5)$$

where $l = 1..M$ represent the M cells in collection C with corresponding average absorbed dose induced by a single particle q_l. Using the previously mentioned survival equation, the expected survival from the classical approach can be calculated using the absorbed dose:

$$S_D(D = \bar{z}_n) = e^{-\alpha_D D} \qquad\qquad (6\text{-}6)$$

Where the survival slope α_D is the experimentally determined survival slope, which is only valid for the radiation field in which it was measured. Since the survival predicted via microdosimetry and the absorbed dose must be equal for the same radiation field, the microdosimetric survival slope α_z can be obtained by equating eq. (6-5) to eq. (6-6). This relation can be rewritten to:

$$\alpha_D \cdot D + ln[S_z^C(D = \bar{z}_n)] = 0 \qquad\qquad (6\text{-}7)$$

Since this equation cannot be solved analytically, α_z must be acquired numerically, in this case using the non-linear least squares algorithm as found in the software package R version 3.2.2 (R Core Development Team, 2011). This optimization will attempt to solve the following equation:

$$\min_{\alpha_z \in \mathbb{R}} \sum_j \alpha_D \cdot D_j + ln[S_z^C(D_j = \bar{z}_{n,j})] \qquad\qquad (6\text{-}8)$$

where D_j are the absorbed doses used during the biological survival experiments. For these experiments, the uncertainty in α_z is assumed to follow from the derivative of α_z to α_D and the experimental uncertainty of α_D, i.e. the standard error propagation.

FNTD irradiation, read-out and analysis

Eight FNTDs were irradiated at specific locations in the irradiation field to yield the best representation of irradiated area (Chapter 5). The 100 x 100 x 15 um³ (x,y,z) center region of each FNTD was read-out using a Leica SP5 with Avalanche Photo Diode (APD), a 63x 1.4 NA oil objective and a 96 x 96 x 490 nm³ (x,y,z) voxel size. FNTDs allow for the measurement of individual alpha particle tracks at a sub-micron resolution. An example of alpha tracks measured in a FNTD is given in Figure 5-4. For each track, the point of entrance, direction and energy upon entering the FNTD was determined. The energy resolution was determined in a previous chapter at approximately 100 – 200 keV (Chapter 4). Tracks ending in the outer 1 μm

rim of the image stack were removed since these tracks were likely to come to a halt outside the field of view, leading to incorrect track reconstruction.

FNTD specific energy calculation

In order to calculate the NDD of a cell, the segmented image stack was placed virtually in the radiation field, measured using the FNTDs. Given the initial direction and energy of a track, the dose deposited in a cell nucleus (Figure 6-1) could be calculated by combining the path length through the cell nucleus (τ_3) and the particle's LET in water (Berger et al., 2005), corrected for the energy loss during traversal of the mylar foil (τ_1) and the cytoplasm (τ_2). The total dose deposited D_{total} by the collection of tracks (N_{total} = 3348 tracks) in a 8 μm water layer (the average height of the measured cells) above the 1.4 μm mylar foil was calculated similar to Chapter 5. The dose deposited in the cell nucleus, given an absorbed dose $\bar{z}$, was calculated by randomly selection of N tracks (eq. (6-9)) and calculating the dose deposited in the cell nucleus by tracks hitting the nucleus.

$$N = \frac{\bar{z}}{D_{total}} N_{total} \qquad (6\text{-}9)$$

By repeating this process many times, each time with a different random selection of tracks, the NDD $f(z, \bar{z})$ as function of the absorbed dose $\bar{z}$ could be obtained. Both the cell nucleus and cytoplasm were assumed to have the stopping power and density of water for the dose calculations.
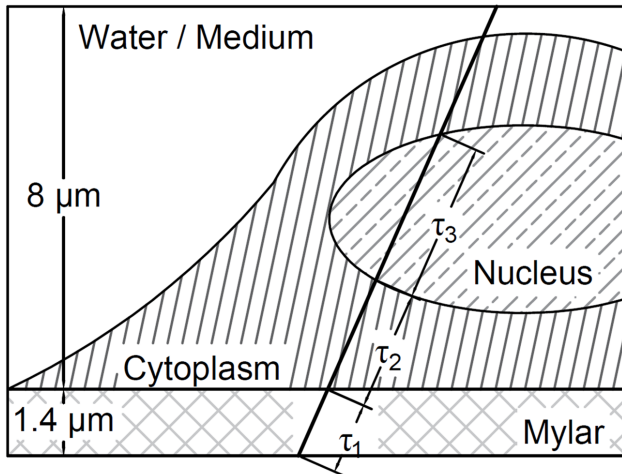
Figure 6-1: Illustration of an alpha track passing through a cell. Path lengths through the various media are indicated by τ_1 .. τ_3.

Spheroid microdosimetry simulation

Basic simulations of alpha emitting isotopes in U87 glioblastoma spheroids were performed to evaluate the effect of NDD-based microdosimetry on the expected survival. Virtual spherical U87 cells, with cytoplasm and nucleus volumes obtained from the cell images, were stacked using the Hexagonal Close Packing (HCP) geometry (Figure 6-2, left). For these simulation, it was assumed that there would be no interstitial fluid in the spheroid. Since the HCP geometry has a packing efficiency of $\eta \approx 0.740$, free space would remain between the cells when the geometry would be built using the radius of the cell as border between the spheres. By choosing a smaller radius of $R_{effective} \approx \sqrt[3]{0.740}\, R_{cell}$ as 'border' of the spheres in the geometry, the cytoplasm fills up all the volume between the nuclei, leaving zero interstitial fluid between the cells (Figure 6-2, right).
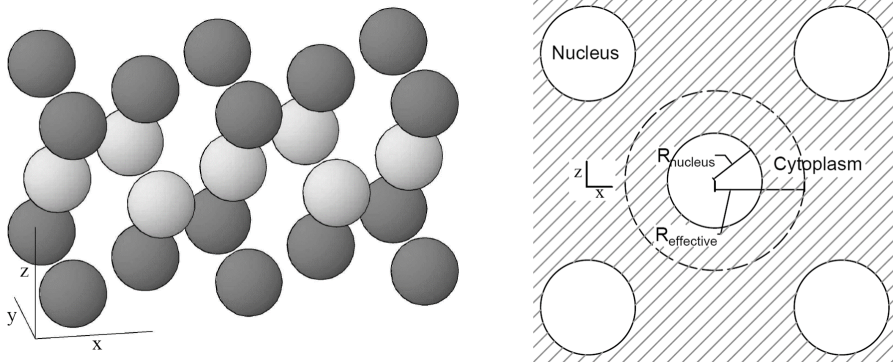
Figure 6-2: (left) 3D view of the virtual U87 nuclei in a HCP geometry. The dark and light grey spheres represent nuclei in respectively the even and uneven layers of the geometry. (right) 2D view of the hexagonal close packing geometry. The effective radius is indicated by R$_{effective}$. Note that the striped border is the not the cell membrane and that the cytoplasm (lines) fills all the space between the nuclei (solid circles) in these simulations. The cell membranes have not been drawn in this illustration.

Four different spatial distributions of isotopes were chosen to represent various ARCs: ARCs on cell membrane (Booth and Kim, 2014), ARCs evenly distributed in the cytoplasm (Borchardt et al., 2003; Sofou et al., 2010), ARCs on the nuclear membrane and ARCs evenly distributed in the nucleus (Nonnekens et al., 2016). The ARC distributions are here forth referred to as scenarios. During spheroid simulation, the origin (based on the given scenario) and direction of alpha particles originating from isotope decay events were randomly chosen.

When the simulated particle hits the nucleus located at the center of the virtual spheroid, the path lengths through the spheroid and nucleus located in the center were calculated together with dose deposited in the nucleus and cytoplasm (Berger et al., 2005). Simulations were performed for alpha particle energies between 4000 and 20.000 keV, and the HCP geometry was expanded to accommodate for the maximum range of the respective alpha particle energy. Each simulation was repeated till a total of 20.000 particles hitting the center nucleus was found. The statistical uncertainties of the mean absorbed doses in cell nuclei in these simulations were below 1.5%. The expected survival in the spheroid was calculated based on the SHNDD as described in an earlier section, together with the absorbed dose in the spheroid. Since this article only focusses on the significance of NDD-based microdosimetry, the dependency of the RBE on the LET was ignored in the survival calculations but is stated in the discussion of the results afterwards.

An overview of the complete workflow for this method, from the U87 glioblastoma cells and measured tracks in the FNTD to the values obtained with the spheroid simulations, is shown in Figure 6-3.
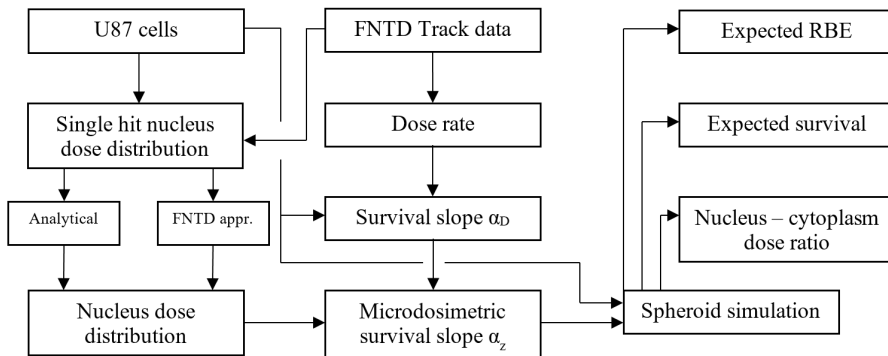
Figure 6-3: A diagram showing the work flow of this method, including the spheroid simulations that were performed using the parameters obtained using the FNTDs and U87 glioblastoma cells.

RESULTS AND DISCUSSION

Cell survival and geometry

The measured surviving fraction during the external irradiation, compared to the non-irradiated control, is given in Figure 6-4. Fitting eq. (6-6) for α_D on the data yields $\alpha_D = 1.66 \pm 0.13$ Gy^{-1}. The relatively high uncertainty was partly caused by the many steps involved in

transferring cells in and from the fragile irradiation dishes and the uncertainty in absorbed dose.
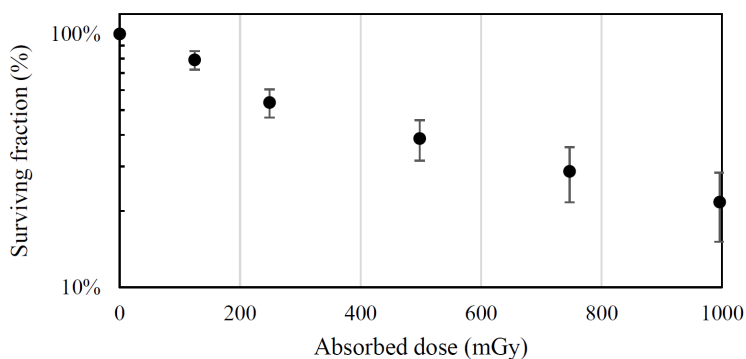
Figure 6-4: Measured surviving fraction as function of dose for U87 cells irradiated with an external Am241 source.

The middle slices of the 3D images of 2 out of the 15 imaged cells (designated as cell A and cell B), with corresponding cytoplasm/nucleus segmentation, are shown in Figure 6-6. The average nucleus volume of the 15 cells was 740 ± 150 μm³. While the displayed cells serve as examples for the NDDs in Figure 6-5 and Figure 6-7, the microdosimetry-based survival calculations involved all 15 cells.

Cell volume uncertainty

The imaging resolution was chosen so that the voxel size approximated half of the full width half maximum (FWHM) of the excitation spot, meaning that excitation spot was not solely confined to the imaged voxel and fluorescent dye in neighboring voxels would yield a (weakened) fluorescence response in the imaged voxel. The edge of the nucleus-cytoplasm border was visible as a smooth fluorescence intensity transition stretching approximately 2-3 voxels. The edge of the nucleus was chosen as the 50% fluorescence intensity decrease line (compared to the center of the nucleus). Since it was not possible to verify this assumption, a 1 voxel systematic uncertainty can be assumed. Given a voxel volume of 3.96E6 nm³ and an average nucleus volume of 740 μm³, the average nuclei consisted of 1.87E5 voxels, which translates to an average radius of 39 voxels (assuming a spherical nucleus volume). A systematic over- or underestimation of the nucleus edge by 1 voxel would therefore result in a relative error in nucleus volume of 5.1%. At the time of writing, it not possible to verify this number. It was therefore not included in the uncertainty calculations in this work. The reader is however advised to keep this possible source of uncertainty in mind when performing microdosimetry calculations and experiments.

Specific energy distributions

The SHNDD, given as probability densities, calculated using the FNTDs for the cells displayed in Figure 6-6 are given in Figure 6-5. The means of the SHNDD were respectively 0.070 and 0.109 J/kg per particle. The differences in spread and mean are the result of differences nucleus size and shape and the thickness of the cytoplasm layer between the mylar sheet and the cell nucleus. The average energy deposited by an alpha particle passing through the collection of 15 cell nuclei was determined at 115 ± 10 keV. The NDD for absorbed doses between 0.12 and 0.70 Gy for the two cells are given Figure 6-7. The histograms represent the FNTD approach for NDD calculation for the indicated mean absorbed dose D in the cell culture, while the black lines indicate the NDD based on the analytical approach (eq. (6-3)) and the single hit distributions given in Figure 6-5. The distinct peaks in the distributions are due to the discreet nature of the number of particles hitting the nucleus and are clearly visible up to 0.35 Gy. When the absorbed dose, and therefore the average number of particles hitting the cell nucleus, increases, the distribution becomes more and more Gaussian like, which is conform the Poisson distribution at large means. Both the calculated histograms and analytically derived NDD were in close agreement, as indicated by the root mean squared errors (RMSE) between the two approaches.
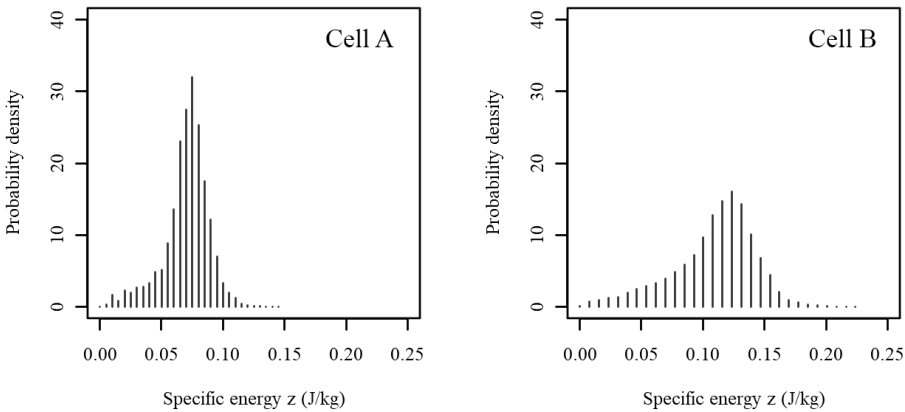
Figure 6-5: Specific energy distributions of nuclei hit by a single alpha particle while irradiated using an external Am241 source for cell A and B, respectively given in the left and right figure.
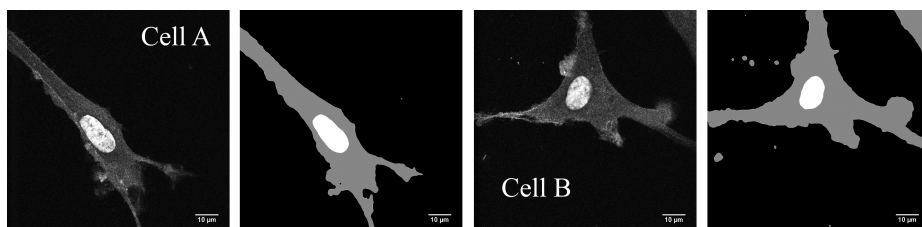
Figure 6-6: Examples of two U87 cells selected from the collection of imaged cells, stained for the cytoplasm (dark grey) and nucleus (light grey). Image scans are given on the left with the corresponding segmentation on the right.
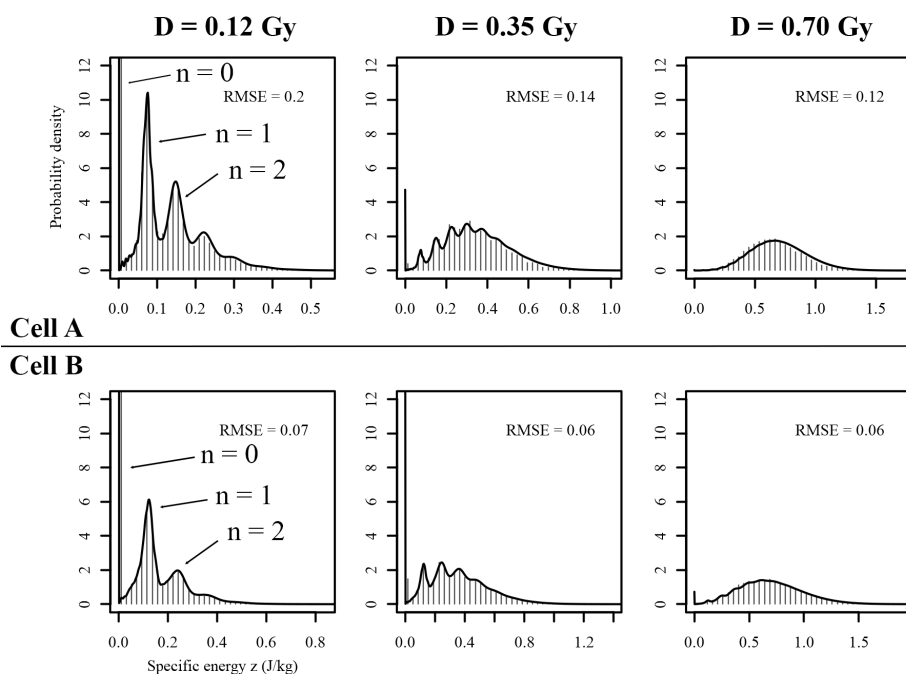
Figure 6-7: Specific energy distributions of cell nuclei at absorbed doses between 0.12 and 0.70 Gy. The histogram represents the distributions based on the FNTD approach, while the black line is given by the analytical method based on the single hit distributions given in Figure 6-5. Some of the peaks are indicated by the number of particles (n) hitting the nucleus that led to the formation of the respective peak. The vertical line at z = 0 represents the probability that a cell is not hit at all (n = 0).

127

Monolayer expected survival

Using the NDD given in the previous section, the microdosimetry-based survival could be estimated with and without correction for the survival slope α_z. The respective estimated survival curves are given in Figure 6-8. Fitting of α_z using $\alpha_D = 1.66 \pm 0.13$ Gy^{-1} and eq. (6-7) led to $\alpha_z = 1.92 \pm 0.15$ Gy^{-1}. Note that the possible systematic error in the nucleus volume estimation (5.1%) is not included in the uncertainty of α_z. The microdosimetric approach without survival slope correction yielded a 13% underestimation in radiosensitivity, which signifies the importance of correct usage of the primary survival slope. The obtained survival slope α_z was used for further calculations in spheroids. The exact uncertainty of α_z beyond the uncertainty inherited from α_D is not entirely known. Contributions from cell geometry alteration due to fixation, errors in cell segmentation and others can each have a contribution to the uncertainty and require further investigation to better quantity the uncertainty of α_z. However, it can be reasonably assumed that these uncertainties found in the FNTD will be smaller than uncertainties originating from the far-reaching assumptions made in modern microdosimetry simulation studies regarding the radiation field and the cell geometries. Note that while the used sample size of 15 cells was deemed sufficient for this proof of principle and the spheroid simulations, future studies looking to correlate microdosimetric parameters with biological indicators should increase the sample size to better reflect the whole culture population.
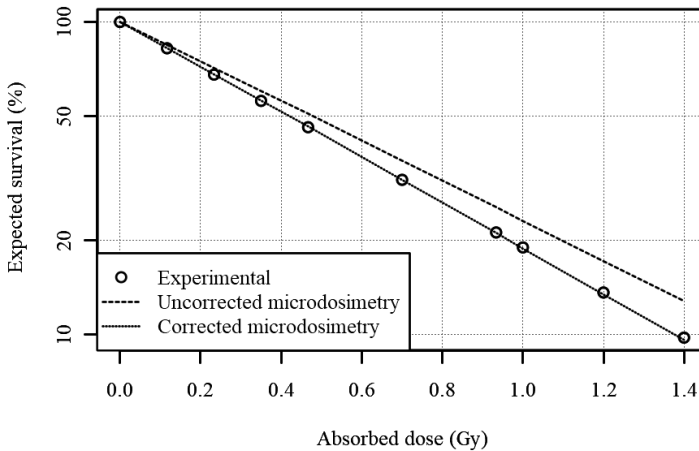
Figure 6-8: Expected survival based on the microdosimetry, both with and without survival slope correction, of externally irradiated U87 cells compared to experimental data.

Spheroid simulation

2D representations of the distribution of Am241 isotope decay events that yielded an alpha particle that hits the center are shown in Figure 6-9. Note that while it was assumed that there was no interstitial fluid in the spheroid, in order to simplify the calculation, the cell membrane for the 'Isotopes on the cell membrane'-scenario was taken as a sphere with a radius of $r = R_{eff}$, as given in the Methods section. One can see that the probability of hitting the center nucleus decreases with increasing distance, as is expected from the r-square law. Using the SHNDD calculated for the given scenarios together with $\alpha_z = 1.92$, the expected survival displayed in Figure 6-10 could be calculated. Note that RBE effects due to differences in LET between the different scenarios are ignored in these calculations. It was found that for low energy alpha particles, in some scenarios, a notable difference in absorbed dose in the nucleus and the cytoplasm was present. The nucleus – cytoplasm dose ratios for Am241 isotopes distributed according to the described scenarios are shown in Table 6-1, together with the relative effectiveness (without RBE contribution), given by the ratio of survival slopes obtained from Figure 6-10. The average LET in the cell nuclei and the LET-based RBE relative to the external irradiation (Tracy et al., 2015) are shown as well for comparison. Note that Tracy et al. reported a saturation effects for LETs above 130 keV, which lead to an average RBE in the spheroid calculations below that of the external radiation. However, isotopes in the cell nucleus and on the nuclear membrane show a substantial difference in expected survival with relative effectivenesses of respectively 151% and 133%. Considering the contributing (radio)biological factors found in spheroids like the Oxygen Enhancement Ratio (Barendsen et al., 1966; Sutherland et al., 1986) (OER), cell cycle changes and accompanying radiosensitivity(Gong et al., 2015; Hill, 1998), and the difficulty of accurate survival studies in spheroids, NDD-based microdosimetry has only a marginal effect on the survival for most ARCs in spheroids and micro-tumors based on the presented data. From these results it can be concluded that accurate determination of OER and cell cycle and LET based RBE effects should precede NDD-based microdosimetry in the process of translating monolayer survival experiments to the expected survival in spheroids and micro-tumors.

Table 6-1: Nucleus – cytoplasm dose ratio together with the relative effectiveness (found in Figure 6-10), the average LET and the relative LET-based RBE compared to the external irradiation for Am241 isotopes in virtual spheroid according to various isotope distributions.

Isotope distribution:	In Nucleus	In Cytoplasm	On Nuclear membrane	On Cell Membrane
Nucleus – Cytoplasm dose ratio	140 %	94 %	125 %	95 %
Relative effectiveness *	151 %	104 %	133 %	105 %
Average LET (keV/µm)	102 ± 36	128 ± 38	104 ± 49	129 ± 37
LET-based RBE *	0.91	0.93	0.85	0.93

* relative to the external irradiation

Isotopes in the nucleus

Isotopes in the cytoplasm

Isotopes on the nuclear membrane

Isotopes on the cell membrane
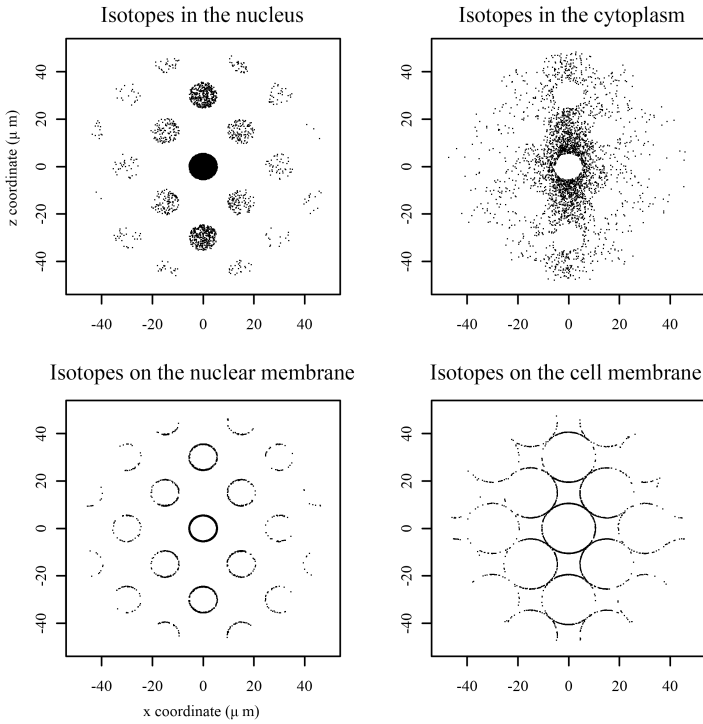
Figure 6-9: Spatial distributions of Am241 decay events which created alpha particles that deposited energy in the center nucleus for various isotope distributions visualized in 2D. Events within Y = ± 2 μm were selected to create a 2D representation of the 3D distribution, which means that spheres in 3D are visible as circles in the 2D figure.
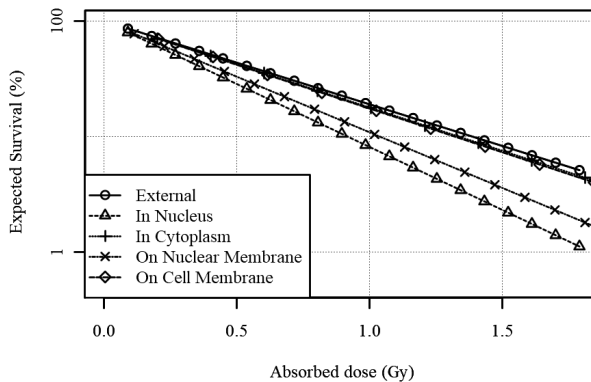
Figure 6-10: The expected survival as function of absorbed dose for virtual spheroids irradiated internally with Am241 isotopes distributed according to various scenarios, versus an externally irradiated monolayer.

In order to explore the limits of the effects of NDD-based microdosimetry, the nucleus – cytoplasm dose ratio was calculated for imaginary alpha emitting isotopes with alpha particle energies between 4000 and 20,000 keV. Figure 6-11 shows a distinct relation between the nucleus – cytoplasm dose ratio and the initial particle energy. Since a higher energy translates to a longer range in water and a lower initial LET, the dose deposited by single particle becomes less localized with increasing energy. A similar decrease in relative effectiveness was seen for the expected survival as function of particle energy. The nucleus – cytoplasm dose ratio reached values within the experimental error for particle ranges between 10 and 20 cell radii in all 4 scenarios. This is however above the maximum alpha particle energy in use (8784 keV, Po212) when using the U87 cell line used in these experiments. It is therefore expected that ARCs attached to, or penetrating, the nuclear membrane will benefit from NDD-based microdosimetry, especially considering the contribution of recoiling daughter radionuclides, an effect that was not included in these calculations (Wang et al., 2014).
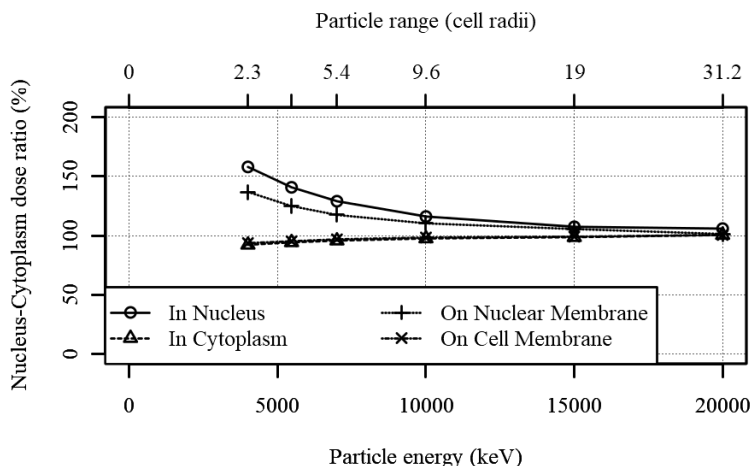
Figure 6-11: Nucleus – cytoplasm dose ratio as function of particle energy. The respective range of the particle in water is given as the range in number of U87 cell radii.

CONCLUSION

It was shown that the individual alpha tracks measured using FNTDs can be applied for microdosimetric purposes. By using 3D scans of the investigated cells, microdosimetric spectra could be obtained with great detail and with relative easy. While only small discrepancies were observed between the analytical and experimental approach for NDD estimation as indicated by the small RMSE, validation of the obtained NDD was not yet possible due to a lack of comparable tools for NDD estimation. Since no assumptions regarding the radiation field or target geometry were required, the method is expected to be more reliable and easier

compared to analytical or Monte Carlo approaches. The FNTD approach has potential to be of great tool for DNA damage and repair studies with alpha radiation, since FNTDs offer, in addition to the fluorescent tracks, a biocompatible surfaces on which live cells can be grown, irradiated and imaged (Niklas et al., 2016). The multi-cell approach proved to be a good estimator for the NDD and the survival of the whole cell culture, and allowed for calculation of α_z as function of the measured survival parameter α_D, making this approach the first of its kind to do so. Simulations of Am241 isotopes in the virtual U87 spheroids showed that the NDD- has a marginal effect on the expected survival for ARCs in the cytoplasm and on the cell membrane compared to other contributing factors found in the dosimetry and radiobiology of spheroids and micro-tumors. A substantial difference in both expected survival and nucleus-cytoplasm dose ratio was observed for isotopes in the cell nucleus and on the nuclear membrane. These effects were found to vanish for alpha particles with ranges in water from 10 to 20 cell radii. However, since these ranges corresponds to alpha particle energies between 10.000 and 16.000 keV, which are above the maximum alpha particle energy of alpha particle emitting radionuclides (8784 keV, Po212), it is expected that ARCs that attach to, or penetrate, the nucleus membrane will benefit from localized energy deposition effects.

Availability of data and material

FNTD processing, specific energy calculation and spheroid simulation was done using a combination of R 3.2.2 (R Core Development Team, 2011) and Java 1.8. Both the code (uuid:8dd8a61b-ca67-447a-ac20-e2d23472142e) and FNTD plus cell scans (uuid:684161d8-fbd4-4276-93f9-a3cc1e7ed360) are freely available from the 4TU.Centre for Research Data repository (*https://data.4tu.nl/*). The library used for FNTD processing is a modified version of a 2016 fork of the public FNTD package available at *https://github.com/FNTD* (Chapter 3).

Acknowledgements

REFERENCES

Akselrod, G.M., Akselrod, M.S., Benton, E.R., Yasuda, N., 2006. A novel Al2O3 fluorescent nuclear track detector for heavy charged particles and neutrons. *Nucl. Instruments Methods Phys. Res. B* 247(2), 295–306. https://doi.org/10.1016/j.nimb.2006.01.056

Akselrod, M.S., Yoder, R.C., Akselrod, G.M., 2006. Confocal fluorescent imaging of tracks from heavy charged particles utilising new Al2O3:C,Mg crystals. *Radiat. Prot. Dosimetry* 119(1–4), 357–362. https://doi.org/10.1093/rpd/nci664

Bandekar, A., Zhu, C., Jindal, R., Bruchertseifer, F., Morgenstern, A., Sofou, S., 2014. Anti-Prostate-Specific Membrane Antigen Liposomes Loaded with 225Ac for Potential Targeted Antivascular alpha-Particle Therapy of Cancer. *J. Nucl. Med.* 55(1), 107–114. https://doi.org/10.2967/jnumed.113.125476

Barendsen, G.W., Koot, C.J., Van Kersen, G.R., Bewley, D.K., Field, S.B., Parnell, C.J., 1966. The effect of oxygen on impairment of the proliferative capacity of human cells in culture by ionizing radiations of different LET. *Int. J. Radiat. Biol. Relat. Stud. Phys. Chem. Med.* 10(4), 317–27. https://doi.org/10.1080/09553006614550421

Bartz, J.A., Kodaira, S., Kurano, M., Yasuda, N., Akselrod, M.S., 2014. High resolution charge spectroscopy of heavy ions with FNTD technology. *Nucl. Instruments Methods Phys. Res. B* 335, 24–30. https://doi.org/10.1016/j.nimb.2014.05.019

Berger, M.J., Coursey, J.S., Zucker, M.A., Chang, J., 2005. ESTAR, PSTAR, and ASTAR: Computer Programs for Calculating Stopping-Power and Range Tables for Electrons, Protons, and Helium Ions (version 1.2.3), National Institute of Standards and Technology, Gaithersburg, MD ,USA.

Booth, R., Kim, H., 2014. Permeability Analysis of Neuroactive Drugs Through a Dynamic Microfluidic In Vitro Blood-Brain Barrier Model. *Ann. Biomed. Eng.* 42(12), 2379–2391. https://doi.org/10.1007/s10439-014-1086-5

Borchardt, P.E., Yuan, R.R., Miederer, M., Mcdevitt, M.R., Scheinberg, D. a, 2003. Targeted Actinium-225 in Vivo Generators for Therapy of Ovarian Cancer. *Cancer Res.* 63(17), 5084–5090.

Charlton, D.E., Sephton, R., 1991. A Relationship between Microdosimetric Spectra and Cell Survival for High-LET Irradiation. *Int. J. Radiat. Biol.* 59(2), 447–457. https://doi.org/10.1080/09553009114550401

Charlton, D.E., 2000. Radiation effects in spheroids of cells exposed to alpha emitters. *Int. J. Radiat. Biol.* 76(11), 1555–1564. https://doi.org/10.1080/09553000050176315

Franken, N. a P., ten Cate, R., Krawczyk, P.M., Stap, J., Haveman, J., Aten, J., Barendsen, G.W., 2011. Comparison of RBE values of high-LET α-particles for the induction of DNA-DSBs, chromosome aberrations and cell reproductive death. *Radiat. Oncol.* 6(1), 64. https://doi.org/10.1186/1748-717X-6-64

Gong, X., Lin, C., Cheng, J., Su, J., Zhao, H., Liu, T., Wen, X., Zhao, P., 2015. Generation of multicellular tumor spheroids with microwell-based agarose scaffolds for drug testing. *PLoS One* 10(6), 1–18. https://doi.org/10.1371/journal.pone.0130348

Hamacher, K.A., Sgouros, G., 2001. Theoretical estimation of absorbed dose to organs in radioimmunotherapy using radionuclides with multiple unstable daughters. *Med. Phys.* 28(9), 1857–1874. https://doi.org/10.1118/1.1395026

Hill, A.A., 1998. Cell cycle related effects on the radiation survival responses of human tumor cells. https://doi.org/10.1017/CBO9781107415324.004

ICRU, 1983. Microdosimetry (Report 36).

Jadvar, H., Quinn, D.I., 2013. Targeted α-particle therapy of bone metastases in prostate cancer. *Clin. Nucl. Med.* 38(12), 966–71. https://doi.org/10.1097/RLU.0000000000000290

Kratochwil, C., Bruchertseifer, F., Giesel, F.L., Weis, M., Verburg, F.A., Mottaghy, F., Kopka, K., Apostolidis, C., Haberkorn, U., Morgenstern, A., 2016. 225Ac-PSMA-617 for PSMA-Targeted alpha-Radiation Therapy of Metastatic Castration-Resistant Prostate Cancer. *J. Nucl. Med.* 57(12), 1941–1944. https://doi.org/10.2967/jnumed.116.178673

Kvinnsland, Y., Stokke, T., Aurlien, E., 2001. Radioimmunotherapy with alpha-particle emitters: microdosimetry of cells with a heterogeneous antigen expression and with various diameters of cells and nuclei. *Radiat. Res.* 155(2), 288–96.

McLaughlin, M.F., Woodward, J., Boll, R.A., Wall, J.S., Rondinone, A.J., Kennel, S.J., Mirzadeh, S., Robertson, J.D., 2013. Gold Coated Lanthanide Phosphate Nanoparticles for Targeted Alpha Generator Radiotherapy. *PLoS One* 8(1), 2–9. https://doi.org/10.1371/journal.pone.0054531

Niklas, M., Zimmermann, F., Schlegel, J., Schwager, C., Debus, J., Jäkel, O., Abdollahi, A., Greilich, S., 2016. Registration procedure for spatial correlation of physical energy deposition of particle irradiation and cellular response utilizing cell-fluorescent ion track hybrid detectors. *Phys. Med. Biol.* 61(17), N441–N460. https://doi.org/10.1088/0031-9155/61/17/N441

Nonnekens, J., van Kranenburg, M., EMT Beerens, C., Suker, M., Doukas, M., van Eijck, C.H., de Jong, M., van Gent, D.C., 2016. Potentiation of Peptide Receptor Radionuclide Therapy by the PARP Inhibitor Olaparib. *Theranostics* 6(611), 1821–1832. https://doi.org/10.7150/thno.15311

R Core Development Team, 2011. R: A Language and Environment for Statistical Computing, R Foundation for Statistical Computing, Vienna, Austria.

Roeske, J.C., Stinchcomb, T.G., 1996. Relationships between cell survival and specific energy spectra for therapeutic alpha-particle emitters. *Radiat. Res.* 145(3), 268–273. https://doi.org/10.2307/3578981

Roeske, J.C., Stinchcomb, T.G., 1997. Dosimetric framework for therapeutic alpha-particle emitters. *J. Nucl. Med.* 38, 1923–1929.

Roeske, J.C., Stinchcomb, T.G., 1999. The use of microdosimetric moments in evaluating cell survival for therapeutic alpha-particle emitters. *Radiat. Res.* 151(1), 31–38. https://doi.org/10.2307/3579744

Schindelin, J., Arganda-Carreras, I., Frise, E., Kaynig, V., Longair, M., Pietzsch, T., Preibisch, S., Rueden, C., Saalfeld, S., Schmid, B., Tinevez, J., White, D.J., Hartenstein, V., Eliceiri, K., Tomancak, P., Cardona, A., 2012. Fiji: an open-source platform for biological-image analysis. *Nat. Methods* 9(7), 676–682. https://doi.org/10.1038/nmeth.2019

Sofou, S., Enmon, R., Palm, S., Kappel, B., Zanzonico, P., Mcdevitt, R., Scheinberg, D.A., Sgouros, G., 2010. Large anti-HER2/neu liposomes for potential targeted intraperitoneal therapy of micrometastatic cancer. *J. Liposome Res.* 20(4), 330–340. https://doi.org/10.3109/08982100903544185.Large

Stinchcomb, T.G., Roeske, J.C., 1992. Analytic microdosimetry for radioimmunotherapeutic alpha emitters. *Med. Phys.* 19(6), 1385–93. https://doi.org/10.1118/1.596770

Stinchcomb, T.G., Roeske, C., 1994. Analysis of Survival of C-18 Cells after in Suspension Irradiation Analysis with and Ionic Bismuth-212 Chelated Using Microdosimetry. *Radiat. Res.* 140(1), 48–54.

Stinchcomb, T.G., Roeske, J.C., 1995. Survival of Alpha Particle Irradiated Cells as a Function of the Shape and Size of the Sensitive Volume (Nucleus). *Radiat. Prot. Dosimetry* 62(3), 157–164. https://doi.org/10.1017/CBO9781107415324.004

Sutherland, R.M., Sordat, B., Gabbert, H., Bourrat, B., Mueller-Klieser, W., 1986. Oxygenation and differentiation in multicellular spheroids of human colon carcinoma. *Cancer Res.* 46(10), 5320–5329.

Sykora, G.J., Akselrod, M.S., Benton, E.R., Yasuda, N., 2008. Spectroscopic properties of novel fluorescent nuclear track detectors for high and low LET charged particles. *Radiat. Meas.* 43, 422–426. https://doi.org/10.1016/j.radmeas.2007.11.009

Tracy, B.L., Stevens, D.L., Goodhead, D.T., Hill, M.A., 2015. Variation in RBE for Survival of V79-4 Cells as a Function of Alpha-Particle (Helium Ion) Energy. *Radiat. Res.* 184(1), 33–45. https://doi.org/10.1667/RR13835.1

Van Elburg, H.J., Kuypers, L.C., Decraemer, W.F., Dirckx, J.J.J., 2007. Improved correction of axial geometrical distortion in index-mismatched fluorescent confocal microscopic images using high-aperture objective lenses. *J. Microsc.* 228(1), 45–54. https://doi.org/10.1111/j.1365-2818.2007.01822.x

Voigt, W., 2005. Sulforhodamine B assay and chemosensitivity. *Methods Mol. Med.* 110, 39–48. https://doi.org/10.1385/1-59259-869-2:039

Wang, G., Kruijff, R.M. De, Rol, A., Thijssen, L., Mendes, E., Morgenstern, A., Bruchertseifer, F., Stuart, M.C.A., Wolterbeek, H.T., Denkova, A.G., 2014. Retention studies of recoiling daughter nuclides of in polymer vesicles Ac. *Appl. Radiat. Isot.* 85, 45–53. https://doi.org/10.1016/j.apradiso.2013.12.008

Woodward, J., Kennel, S.J., Stuckey, A., Osborne, D., Wall, J., Rondinone, A.J., Standaert, R.F., Mirzadeh, S., 2011. LaPO4 nanoparticles doped with actinium-225 that partially sequester daughter radionuclides. *Bioconjug. Chem.* 22(4), 766–776. https://doi.org/10.1021/bc100574f

Chapter 7

Evaluation of the Pharmacokinetics and Dosimetry of 225Ac Alpha Radionuclide Carriers

J.J.M. Kouwenberg[1], H.T. Wolterbeek[1], A.G. Denkova[1]

[1] Radiation, Science & Technology, Delft University of Technology, Mekelweg 15, Delft, the Netherlands

ABSTRACT

Introduction: The use of 225Ac for alpha radionuclide therapy is a relatively novel approach, where the dense energy deposition of alpha radiation is used to treat cancer more effectively. 225Ac has, compared to conventional radionuclides, a long half-life of 10 days and a long decay chain, yielding 4 alpha particles, 2 beta particles and several gamma rays. This long decay chain presents new challenges. Daughter radionuclides that separate from the radionuclide carrier during radioactive decay can end up freely circulating through the body, potentially causing significant harm to healthy tissue.

Methods: In this work, a model for the kinetics of free radionuclides is presented and the effects of circulation time and the retention of daughter radionuclides via recoil retention and internalization in cells are evaluated for various 225Ac radionuclide carriers that are administered intravenously.

Results and Conclusions: It was found that retention of daughter radionuclides is generally preferred, but that some loss of daughter radionuclides can actually be beneficial, since the non-retained fraction of daughter radionuclides is likely to decay away from the critical organ, lowering the total absorbed dose in this area. In the presented model, internalization of alpha radionuclide carriers in cells reduced organ doses induced by freely circulating radionuclides up to 60%, by partly trapping the free radionuclides released from the radionuclides inside the cells. Internalization also yielded a near 4 fold increase in the tumor dose for alpha radionuclide carriers without recoil retention, indicating that carrier internalization is paramount for this type of carrier. While the maximum injectable activity was limited by the absorbed dose in the kidneys for most carriers, the red bone marrow was the critical organ for nanovesicles carriers due to their long circulation time and retention of daughter radionuclides. The presented model gives insight in the various mechanisms involved in alpha radionuclide therapy, allowing researchers to fine tune their carrier for maximum effect in the clinic.

INTRODUCTION

The demand of 225Ac has increased drastically in the last two decades due to the come-back of alpha radionuclide therapy to the clinic. The decay chain of 225Ac yields 4 alpha particles, 2 beta particles and several gamma's, together accounting for nearly 30 MeV kinetic energy. 225Ac has a long half-life of 10 days. 225Ac has half-life of 10 days which makes it easier to use in the clinic without loss due to transportation from the site of production to the hospital. Alpha particles have high energy deposition densities with an average Linear Energy Transfers (LET) of ~140 keV/μm in water (5 MeV particle) (Berger et al., 2005), which is about a factor 25 and 1000 times larger than for respectively proton and beta particles at similar energies. This high

energy deposition leads to more clustered damage to the genetic material in cells, thereby significantly impeding DNA repair and reducing the chance of the cell survival (Franken et al., 2011; Prise et al., 1998). An indicator for the biological effectiveness of radiation type is the so-called Relative Biological Effectiveness (RBE). The RBE is given by the ratio of doses required to reach a certain level of cell death for the radiation type of interest and a reference source, usually x-ray. For alpha radiation, RBE values up to 20 have been reported (Franken et al., 2011; Tracy et al., 2015), which means that for certain cell types, only 1/20 of the x-ray dose was required to reach an equal level of cell death. Following the large LET of alpha particles, their range in water is very short no more than 100 μm in water (~10 cell diameters). Due to this short range, energy deposited by alpha particles around the alpha radionuclide carrier is very localized. While this can be used to spare healthy tissue surrounding the malignant site, it also means that proper tumor penetration and distribution become more significant.
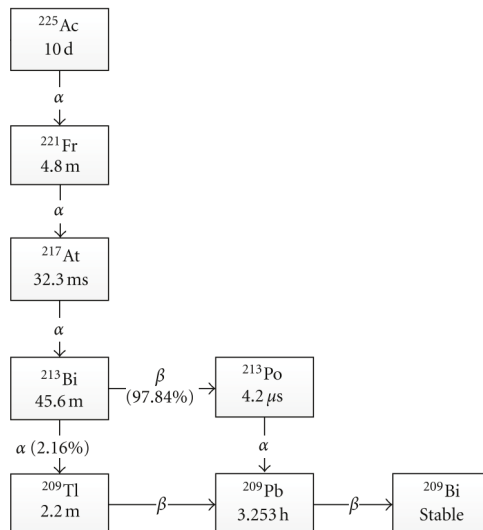
Figure 7-1: Decay chain of 225Ac leading to final stable 209Bi (Huang et al., 2012).

Characteristic for 225Ac is the long decay chain, containing multiple alpha emitting daughter isotopes (Figure 7-1). During each alpha decay, the daughter isotopes receives a 'kick' after emission of the alpha particle, referred to as the recoil effect. From the preservation of momentum and energy, it can be deduced that the daughter nuclei in the 225Ac decay chain receive about 2% of the total emitted energy, which translates to 100 – 180 keV of kinetic energy. These values far exceed the strength of a chemical bond (< 10 eV), leading to separation of the daughter nuclei from the radionuclide carrier.

225Ac carriers for radionuclide therapy can be categorized as follows: (small) molecular carriers (proteins, ligands) (Kratochwil et al., 2016; Pandya et al., 2016), antibody targeting agents (Ballangrud et al., 2004; Borchardt et al., 2003; McDevitt, 2001; McLaughlin et al., 2013; Miederer et al., 2004; Schwartz et al., 2005; Woodward et al., 2011) and nanovesicles and other nano-particles (Chang et al., 2008; Chow et al., 2009; Sofou et al., 2004; Wang et al., 2014). Some examples are given in Figure 7-2.

(a) (b) (c)
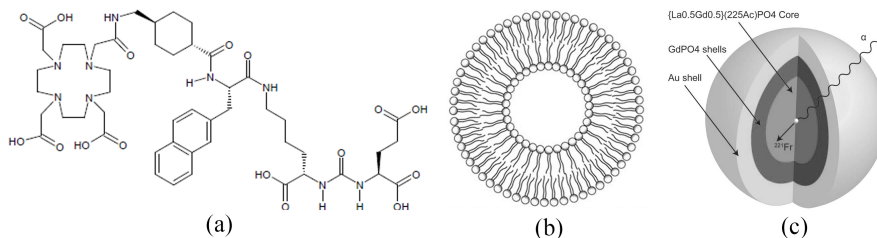
Figure 7-2: (a) Chemical structure of DKFZ-PSMA-617 (Sharifi et al., 2016). 225Ac isotopes are chelated in the DOTA structure, shown in the outer-most left side of the image. Image downloaded from http://www.internetchemie.info/chemie-lexikon/stoffe/p/psma-617.php (b) Illustration of a bilayer vesicle (liposomes/polymersomes) (Åkesson et al., 2012). Radionuclides are loaded in the aquatic cavity. (c) An illustration of a LaPO4 gold coated nanoparticle, loaded with 225Ac in the center. The diameter of these particles is about 25 nm (McLaughlin et al., 2013).

Molecular carriers, like ligands and proteins, are characterized by fast tumor uptake and blood clearance in the order of several minutes. The 225Ac isotopes are usually bound to these targeting agent via the chelating agent 1,4,7,10-tetraazacyclododecane-1,4,7,10-tetraacetic acid (DOTA). The chemical bonds between 225Ac and DOTA are weak compared to the energy released during alpha decay (i.e. energy recoil >100 keV vs. a few eV of chemical bonds), resulting in the loss of daughter radionuclides from the targeting entity. This process can lead to possible unwanted organ toxicity due to the accumulation of, and irradiation by, free isotopes. As of yet, only a few molecular targeting agents are available in the clinic, limiting the use of molecular carriers for 225Ac to a few types of cancer.

Antibody targeting agents exploit the overexpression of antigens and proteins by certain types of cancer cells. Antibodies targeting agents are orders of magnitude larger than small molecular targeting agents like the prostate specific membrane antigen (PSMA), and have much longer blood circulation times, ranging from hours to days instead of minutes. Antibody targeting agents have been used together with DOTA or with specially designed nanoparticles for 225Ac binding, where the latter is able to retain some of the daughter radionuclides after decay of the mother isotope. Both molecular and antibody targeting agents have been used extensively in the past for both the detection and treatment of cancer using gamma, beta minus

and positron emitting isotopes. Pharmacokinetic data of these targeting agents is therefore abundant, which is of great benefit for researchers looking to apply these targeting agents for alpha radionuclide therapy.

Nanovesicles are small vesicles, using either a lipids (liposomes) or amphiphilic synthetic block copolymers (polymersomes) to create a membrane surrounding an aquatic core. Nanovesicles often rely on the enhanced permeability and retention effect (EPR) for tumor targeting. Exploiting the short range in water of recoiling daughter radionuclides, these vesicles utilize the membrane and the volume of aqueous solution in the core to naturally retain (some of the) recoiling daughter isotopes. Retention probability of these vesicles is therefore proportional to the size (diameter) of the vesicles. Efforts to build additional structures inside the vesicles for increased retention are ongoing (de Kruijff et al., 2017).

As shown, some types of carriers rely on fast and/or highly specific targeting to minimize normal tissue complications, while others attempt to retain the daughter isotopes to minimize the irradiation of healthy tissue by free radionuclides. As of yet, no comparative study of the effects of circulation time, targeting efficiency, carrier internalization and recoil retention on tumor treatment efficiency and normal tissue complication probability has been performed. A clear picture of these effects and the pros and cons of the available approaches is however crucial for researchers looking to use or design 225Ac radionuclide carriers for alpha radionuclide therapy. This work therefore attempts to predict the absorbed dose in major organs after injection of the radionuclide carrier. Biodistribution, blood circulation time, excretion and recoil retention for the various carriers was based on data presented in mentioned publications or estimated when unavailable. A revised model for free isotope pharmacokinetics and biodistribution by Hamacher et al. (Hamacher and Sgouros, 2001) is introduced to estimate the normal tissue burden due to free circulating isotopes. Doses induced by carrier-bound and free isotopes were calculated, together with the critical organ for the respective carrier and the expected required tumor uptake for successful treatment. Based on these results, recommendations for the application of 225Ac in alpha radionuclide therapy, and the presentation of research data in future studies, could be made. An overview of the current state of the art is presented, exposing areas requiring further research for the maturation of alpha radionuclide therapy.

METHODS

Biodistribution and recoil retention

Radionuclide carriers

Biodistributions of the following intravenously injected (potential) alpha radionuclide carriers were collected (abbreviations given between brackets): HUM195 antibody (H195) (Miederer et al., 2004), PEGylated liposomes 100 nm (LPS) (Chang et al., 2008; Chow et al., 2009; Sofou et al., 2004), Trastuzumab Antibody (TRAS) (Borchardt et al., 2003), Polymersomes (PLMS) (Wang et al., 2014), Monoclonal antibody 201B labelled LaPO4 nanoparticles (regular (LAPO4) (Woodward et al., 2011) and gold coated (GOLD) (McLaughlin et al., 2013)) and PSMA (PSMA) (Afshar-Oromieh et al., 2016; Kratochwil et al., 2016; Pfob et al., 2016; Sharifi et al., 2016).

The HUM195 antibody study followed monkeys injected with humanized antibody 195 labelled with 225Ac for several months. Proper blood concentrations curves were presented and no specific binding in the monkeys was observed, leading to the assumption that organ irradiation was the result of free isotopes produced by the labelled antibody. No organ activities were presented and renal toxicity was estimated from the 225Ac and 213Bi concentrations. Since no biostability data or excretion data was given, the compound was assumed to be fully stable and cleared via urine in accordance with the blood concentration curves, despite the fact that intact HUM195 is probably too large for glomerular filtration.

A study on 100 nm PEGylated liposomes by Chow et al. contained extensive data on the biodistribution of 111In labelled liposomes together with blood concentration curves and tumor uptake. Manual conversion from %ID/g to %ID per organ, based on the average organ weights of NOD/SCID mice, was required. The liposomes were assumed to be completely biostable during circulation, immune to excretion and to internalize in all soft tissue.

Biodistribution data of 80 nm polymersomes was assumed to be equal to the 100 nm PEGylated liposomes due to the lack of proper data for polymersomes.

Trastuzumab, an anti-HER-2/neu antibody for ovarian cancer, was extensively studied in-vitro and in 4-8 week old female athymic nude mice. The internalized fraction on SKOV3-NMP2 cell monolayers was given together with the biodistribution in mice 4 and 24 hours after injection and free isotope concentrations in several organs up to 120 hours after injection. Uptake data for most organs was given in %ID/g which required manual conversion. Since no biostability data was given, the antibody was assumed to be biostable during circulation and after internalization. It was assumed that the antibody only internalized in tumor tissue (female reproduction organs are not included in this work).

The studies on antibody conjugated LaPO4 nanoparticles was performed on 5 week old female BALB/c mice. Biodistribution data was limited to the liver, spleen, kidney and lung at 3 time points and was expressed in %ID/g, which required manual conversion to %ID. No blood clearance data was shown. Since the studies contained too little data to form a model for this algorithm, the biodistribution of Trastuzumab was used instead. The nanoparticles were assumed to be internalizing in tumor tissue and to be biostable.

Since the study on 225Ac labelled PSMA did not contain data on the biodistribution over time, this data was obtained from another study on DKFZ-PSMA-617 (Figure 7-2, left, a PSMA-DOTA conjugate) labelled with 68Ga in Syrian rats. The latter published %ID/g values after 15, 30, 60 and 120 minutes for various organs. No definitive numbers for clearance were given. Since no biostability data was given, the compound was assumed to be biostable during circulation and after internalization. Given that an estimated 70% and 92% of the injected activity was unaccounted for after respectively 15 and 120 minutes, it was assumed that ~20% of the compound was cleared during this time.

Two virtual carriers have been included in this study to visualize the effects of carrier internalization. Both virtual carriers, given by VIRT1 (internalizing) and VIRT2 (non-internalizing), were assumed to instantaneously accumulate and remain in tumor tissue.

Generalized biodistribution models, based on the available data, were created for the various carriers since the available data in the shown publications was often insufficient for pharmacokinetic and dosimetry modelling. %ID values 24 hours post-injection were estimated from the presented data, except for PSMA, for which 60 minutes post-injection was used due to its fast clearance. The resulting values are shown in Table 7-3.

Recoil retention

The retention of daughter radionuclides after decay in the 225Ac chain for the various radionuclides carriers are given in Table 7-4. Retention of the complete chain was only available for polymersomes. Since no retention data for the 100 nm PEGylated liposomes was given, the retention was assumed to be equal to 100 nm zwitterionic liposomes (Sofou et al., 2004), which reported no retention of 213Bi isotopes. Given that no retention data for the intermediate isotopes 221Fr and 217At was published, retention of these isotopes was assumed to be small at 25% and 12.5% respectively, loosely based on 80 nm polymersomes data available in the literature. 50% and 88% retention of daughters was reported for respectively the non-coated (Woodward et al., 2011) and gold coated (McLaughlin et al., 2013) LaPO4 nanoparticles. Carriers relying on chemical bonds for retention, including the virtual carriers, were set to have no daughter retention.

Free isotopes

Biodistribution data for free Francium (via Cesium), Bismuth, Thallium and Lead were obtained from an extensive study using intravenously injected salts in male Sprague-Dawley rats (Gregus and Klaassen, 1986). Organ concentrations were measured 2 hours post-injection while the total excretion was measured over a period of 4 days. Data for actinium was obtained from a study on intravenously injected Actinium nitrate in male Marshall-August hybrid rats, measured 24h post-injection (Taylor, 1970). The biodistributions of 217At and 213Po were assumed to be equal to their parents' due to their short half-lives. Since most studies publish uptake results in the form of %ID/g (percentage of injected dose per gram of organ tissue) without publishing corresponding total organ masses, values were multiplied by the reference organ masses for the respective rat strain (Kanerva et al., 1983; Schoeffner et al., 1999) to obtain the %ID per organ. The fraction of injected dose unaccounted for by the major organs and excretion was attributed to the residual body mass. It was assumed that isotopes internalize (enter cells) in the target organs and sites, expect for the blood, excretion and bone.

Pharmacokinetics

Radionuclide carriers

Since insufficient data was available to create more complex compartment models to describe the pharmacokinetics of the various carriers, a simple exponential model was assumed, which is the simplest solution for a 1 compartment model with no wash out (k2 = 0) (Watabe et al., 2006). The blood and organ concentrations were given by:

$$c_{i=blood}^{carrier}(t) = \frac{N_{carrier}}{V_{i=blood}} \, 2^{-t/\tau_{carrier}} \tag{7-1}$$

$$c_i^{carrier}(t) = \frac{N_{carrier}}{V_i} \, B_i \left(1 - 2^{-t/\tau_{carrier}}\right) = \frac{B_i}{V_i} \left(1 - V_{i=blood} \, c_{i=blood}^{carrier}(t)\right) \tag{7-2}$$

where $c_{i=blood}^{carrier}$ and $c_i^{carrier}$ are carrier concentrations in respectively the blood and organ i, $N_{carrier}$ is the total number of injected carriers, $V_{i=blood}$ and V_i are the volumes of respectively the blood and organ i, $\tau_{carrier}$ is the blood circulation half-life and B_i is the fraction of accumulated carriers in organ i as given in Table 7-3. This means that carriers remained in the organs of residence indefinite, which is most likely a wrong representation for at least the molecular and antibody carriers. However, since no biodistribution data for such carriers for time points exceeding 24 hours post-injection could be found at the time of writing, no attempt was made to improve this model.

Free isotopes

The pharmacokinetics of the free isotopes were based on a publication by Hamacher et al. (Hamacher and Sgouros, 2001), but instead of an analytical approach, a step-wise computational approach was chosen to allow for more complex processes.

There are two ways in which free, unbound, isotopes can be created: via recoil from the carrier of a radionuclide, or via radioactive decay of an already unbound radionuclide. The free daughter isotopes was set to be produced at the location of the parent. If this location was either within the interstitial fluid, blood or bone, the daughter is assumed not to be internalized in a cell and was therefore presumed to diffuse randomly via Brownian motion. Taking an average diffusion coefficient of $2 \cdot 10^{-9}$ m^2/s (Sato et al., 1996) and a maximum distance to the nearest capillary of 50 µm (Baish et al., 2011), calculating the mean diffusion time for isotopes near the furthest cells yields less than 1 second. Given that the time it takes blood to circulate the body is between 10 and 16 seconds (Tarr et al., 1933), the diffusion of non-internalized free isotopes to the target organ of residence (Table 7-2) is likely fast compared to the decay times (except for 217At and 213Po) and therefore assumed to be instant.

In cases where the free isotope was produced within a cell, the probability of it passing through the cellular membrane before decaying is required. Due to the short half-lives of 217At, 213Po and 209Tl, these isotopes were assumed to always decay at the location of the parent. Yao et al. performed a study where anti-CD5 antibody radiolabeled with bismuth and lead were internalized in various cell lines to measure the release of catabolized compound over time (Yao et al., 2001). Bismuth and lead retention stabilized at respectively 10% and 15% loss of internalized compound after 2 hours. This is in agreement with the reported accumulation of bismuth in-vitro reported by Hong et al. (Hong et al., 2015). While the ICRP and other organizations have published numerous reports regarding the biodistribution and dosimetry of ingested, inhaled and injected radionuclides data for isotopes originating from inside tissue as the result of decay of the mother isotope is still scarce. Therefore, since studies for actinium and francium retention could not be found, an attempt to approximate the retention of 225Ac and 221Fr in cells was made using a novel approach, combining compartment analysis theorem (Watabe et al., 2006) and membrane perfusion data.

For this approach, let the flow J of a compound passing through a cell membrane be given by:

$$J = -D\frac{\Delta c}{\Delta x} = -D\frac{c_{interstitial} - c_{intracellular}}{\Delta x} = P_{app}\,\Delta c \qquad (7\text{-}3)$$

Where Δc is the concentration difference between the intracellular and interstitial fluid, D is the compound-specific diffusion constant, Δx is the thickness of the cellular membrane and P_{app} is the apparent permeability of the cellular membrane for the compound, a value often

found in pharmacological studies (Palumbo et al., 2008). Using a two-compartment model, the flow to the interstitial fluid (k_4) can be measured for PET tracers in various tissues (Watabe et al., 2006). These values can be defined as:

$$c_{intracellular} \cdot k_4 = -\frac{dc_{intracellular}}{dt} \tag{7-4}$$

Using the surface area exposed to the interstitial fluid of all the cells in a tissue, eq. (7-3) and eq. (7-4) can be related:

$$P_{app,in \to out} \, c_{intracellular} \cdot A = c_{intracellular} \cdot k_4 \cdot V_{intracellular} \tag{7-5}$$

Where P_{app} has now been replaced by the directional apparent permeability, A is the exposed cellular surface area per unit volume of tissue and $V_{interstitial}$ and $V_{intracellular}$ are respectively the interstitial and intracellular fluid volumes area per unit volume of tissue. Note that is equation is simply a formulation for the flow of mass. $A/(V_{interstitial} + V_{intracellular})$ is equal to the surface-to-volume ratio (S/V), which was estimated at 0.55 μm^{-1} for a murine glioma model in-vivo (Reynaud et al., 2017). Rewriting eq. (7-5) yields:

$$k_4 = P_{app,in \to out} \frac{A}{V_{intracellular}} = P_{app,in \to out} \frac{S/V \, (V_{interstitial} + V_{intracellular})}{V_{intracellular}} \tag{7-6}$$

Which gives a relation between the apparent permeability $P_{app,in \to out}$ inside a specific tissue and the outflux rate k_4. The apparent permeabilities of actinium and francium are unknown. Following the closest achievable chemical similarity, the (uni-directional) values for calcium ($2 \cdot 10^{-8}$ m/s (Feher and Briggs, 1982), instead of actinium, rabbit skeletal muscle cells) and potassium ($2 \cdot 10^{-9}$ m/s (Dawson et al., 1986), instead of francium, mouse Langerhans cells) ions are therefore used instead together with $V_{interstitial}$ = 0.2 L/L and $V_{intracellular}$ = 0.8 L/L (human) (Lei et al., 2015), yielding approximate k_4 values of respectively 0.5 and 0.05 min^{-1}. By combining the radioactive decay and the flow from the interstitial fluid, the fraction of isotopes that are likely to decay within the cell they were produced is calculated via:

$$N_{ratio} = \int_0^\infty e^{-(\lambda + k_4)\,t} dt \Big/ \int_0^\infty e^{-\lambda\,t} dt = \frac{\lambda}{\lambda + k_4} \tag{7-7}$$

Where λ is the decay constant of the isotope in question. Calculating these ratios based on the presented values yields that respectively >1% and 73% of the 225Ac and 221Fr isotopes produced within a cell are likely to decay within the same cell before diffusing from through the cellular membrane. A summary of the retention and decay probabilities is given in Table 7-1.

Table 7-1: Fraction of isotopes produced within a cell that is likely to decay within the same cell before diffusing through the cellular membrane (i.e. retention probability)

	225Ac	221Fr	217At	213Bi	213Po	209Th	209Pb
Retention probability	0 %	73 %	100 %	85 %	100 %	100 %	90%

Pharmacokinetics model

An iterative program to follow the radionuclide carriers and free isotopes concentrations in various organs was written in the software package R 3.2.2 (R Core Development Team, 2011).

A brief overview of the structure of the code is given below:

General structure of the pharmacokinetics code

```
–   For each time point t
        –   Distribute carriers according to eqs. (7-1) and  (7-2),
            internalize according to Table 7-3
        –   For each organ i
            –   Process decay of isotopes contained in the carriers
                    –   Place non-retained recoiled daughters in a
                        temporary pool in the organ of production
                        according to the internalization state of the
                        carrier
                    –   Update contents of carriers following decay
                        and recoil
            –   Process decay of free isotopes
                    –   Place the produced daughters in the temporary
                        pool for daughters produced inside cells
            –   For the pool of produced daughters inside cells
                (internalized)
                    –   Place the fraction of daughters likely to
                        decay outside the parent cell (Table 7-1) in
                        the pool for non-internalized daughters
                    –   Store the remaining fraction inside the organ
                        till decay occurs
            –   For the pool of daughters in the interstitial fluid
                (non-internalized)
                    –   Distribute daughters according to their
                        eventual biodistribution (Table 7-2) and
                        store the them inside the organ till decay
                        occurs
```

Calculations were performed with time intervals of 60 seconds for 4 hours, 1 and 7 days, with the exception of PSMA for which only 4 hours was used. The time interval was chosen so that the error in total number of decays was below 0.1%. The source code is freely available from *https://github.com/Yskaa91/AlphaRadPharmacokinetics*.

Dosimetry

Using the mentioned algorithm, the cumulative decays of the various isotopes per organ were calculated after 4 hours, 1 and 7 days. Due to the short range of alpha particles and the relative

low fraction of energy deposited by the beta radiation present in the 225Ac chain, it was assumed that the contribution of decays in the blood and cross-irradiations between organs were negligible. The only exception is the red bone marrow, for which it was assumed that it contained 1500 mL of blood. The cumulative energy of the decay events within this volume of the blood were included in the absorbed dose in the red bone marrow following the EANM recommendation (Hindorf et al., 2010):

$$\#Decays_{RBM,total} \approx \#Decays_{RBM,specific} + \frac{V_{RBM}}{V_{blood}} \#Decays_{blood} \cdot RMBLR \qquad (7\text{-}8)$$

Where $\#Decays_{RBM,total}$ and $\#Decays_{RBM,specific}$ are respectively the total and red bone marrow-specific number of decay events in the red bone marrow, V_{RBM} and V_{blood} are respectively the red bone marrow and blood volume, $\#Decays_{blood}$ is the total number of decay events in the blood and $RMBLR$ is the red bone marrow-to-blood activity concentration ratio, estimated at 0.36 (Sgouros, 1993). All doses are expressed in mGy/MBq injected activity and no radiation quality corrections were applied.

Normal tissue tolerances for alpha radiation are not available. Hobbs et al. therefore created a formalism to convert normal tissue tolerance doses exposed to x-rays in 2 Gy fractions to tolerance doses for alpha emitters (Hobbs et al., 2014). From this work a conversion factor was used so that:

$$TD_{5/5}^{\alpha} \approx \frac{TD_{5/5}^{x-ray}}{RBE2(\alpha/\beta)} \qquad (7\text{-}9)$$

Where $TD_{5/5}^{\alpha}$ and $TD_{5/5}^{x-ray}$ are the doses resulting in a 5% probability of complication within 5 years of treatment for respectively alpha and x-ray (external) irradiation and $RBE2(\alpha/\beta)$ is a conversion factor. Since no organ specific conversion data is available, a general value for alpha radiation of 4.5 is assumed (Hobbs et al., 2014). $TD_{5/5}^{x-ray}$ values, shown in Table 7-2, were obtained from multiple sources. From these dose limits, the critical organ and respective maximum injectable dose for each radionuclide carrier could be estimated using the calculated absorbed dose per injected activity values. To estimate the required uptake in tumors for tumor control with normal tissue complication, let the required injected activity ending up in the tumor, A_{tumor}, for tumor control be given by:

$$A_{tumor} \approx D_{tumor} \Big/ \frac{Gy}{MBq}\Big|_{tumor} \qquad (7\text{-}10)$$

Where D_{tumor} is the absorbed dose required for tumor control and $\frac{Gy}{MBq}\Big|_{tumor}$ is the absorbed

dose per injected activity in the tumor. Tumor control alpha dose D_{tumor} = 20 Gy (90 Gy x-ray equivalent after RBE2 correction) and tumor mass M_{tumor} = 10 g were used for tumor uptake calculation. The tumor mass was chosen small so that specific uptake of carriers inside the tumor did not have a substantial impact on the uptake of major organs.

RESULTS AND DISCUSSION

Absorbed doses per injected MBq for the various carriers after 4 hours, 24 hours and 7 days are given in Table 7-5, Table 7-6 and Table 7-7. Table 7-8 shows the doses induced by members of the 225Ac decay chain in various organs, expressed as percentage of the total dose, for the virtual carriers. The critical organs, together with maximum injectable activity without normal tissue complication and the required tumor uptake given an injection of the maximum injectable dose are given in Table 7-9. The results are discussed per carrier category.

VIRT1 and VIRT2

The virtual particles (VIRT1: internalizing, VIRT2: non-internalizing) were included to visualize the effect of internalization on tumor and normal tissue doses as determined from the presented model. Lack of internalization yielded between 120% and 250% higher doses in normal tissues. Not shown in the tables are the absorbed doses in the tumor. Absorbed doses in a 10 g tumor were estimated at 170 and 46 Gy/MBq after 7 days for respectively VIRT1 and VIRT2, showing a near 3.7 fold increase in tumor irradiation efficiency for internalized carriers compared to non-internalized carriers. Manual calculation of the fraction of decay energy for both internalized and non-internalized carriers using the decay energies, retention probabilities (Table 7-1) and decay probabilities (Figure 7-1) yields a similar factor 3.7 higher energy deposition fraction for internalized carrier, serving as a validation for this part of the algorithm. The maximum injectable dose is given by the maximum tolerable dose in the critical organ, in this case the kidneys for both VIRT1 and VIRT2 (Table 7-9). Given the higher tumor irradiation efficiency together with the higher injectable dose due to the lower absorbed dose per injected activity in the kidneys, a near 9 fold decrease in required tumor uptake for tumor control for VIRT1 versus VIRT2 could be observed (Table 7-9). Table 7-8 was included to show the contribution of each member of the decay chain to the absorbed doses in the organs and tissues. Looking at the isotope contributions in the most exposed organs from Table 7-7 (heart, intestine, kidneys, liver, pancreas, spleen, stomach), it is clearly visible that in this model, the francium biodistribution dominates the normal tissue exposure, especially for the non-internalizing carrier (VIRT2). This is not unexpected since it was assumed that isotopes internalize in their organs of residence (Table 7-3). The retention of the daughters of 221Fr was assumed to be high, resulting in most of the isotopes remaining at the site of the francium mother isotope. VIRT1 shows a more 'diverse' normal tissue exposure since it releases free

isotopes from the tumor tissue in steps, irradiating the primary sites of accumulation of the long-lived isotopes (221Fr, 213Bi, 209Pb) more equally.

HUM195

Miederer et al. reported (severe) damage in the myocardial tissue, liver, gastric mucosa, kidneys and bone marrow in the monkeys exposed to the 225Ac-labeled HUM195 antibody (Miederer et al., 2004). During these experiments, the human equivalent of approximately 28 MBq 225Ac was injected, yielding organ doses of 0.77 Gy (heart), 2.53 Gy (intestine), 2.68 Gy (kidneys), 1.22 Gy (liver) and 0.69 Gy (red bone marrow) after 7 days according to the presented HUM195 model. To obtain the doses after complete decay, these values should be multiplied by 2.6. Multiplying by the alpha-to-x-ray conversion factor $RBE2(\alpha/\beta)$, yields x-ray equivalent doses of 9 Gy (heart), 30 Gy (intestine), 31 Gy (kidneys), 14 Gy (liver) and 8 Gy (red bone marrow) after complete decay. Comparing these values to the normal tissue complication $TD_{5/5}$ values shown in Table 7-2 indicates that there is a general agreement between the algorithm and the reported normal tissue complications in the monkeys. A more detailed comparison is unfeasible due to the relatively large variations and small sample size in the HUM195 study and the uncertainties present in this algorithm. It does however serve as an indicator that the fundamentals of the algorithms are correct.

TRAS, LAPO4 and GOLD

TRAS (225Ac-labeled trastuzumab antibody model), $LAPO_4$ (antibody-conjugated LaPO4 nanoparticles labeled with 225Ac model) and GOLD (antibody-conjugated gold covered $LaPO_4$ nanoparticles labeled with 225Ac model) were assumed to have the same biodistribution. While the normal tissue exposure from free isotopes was less for GOLD than for the $LAPO_4$ model, the exposure from carrier-bound isotopes was significantly higher for carriers with recoil retention. This lead to an increased exposure in primarily the kidneys for the nanoparticle models compared to TRAS. While the kidneys were identified as critical organ for all three carrier models, a 50-70% increase in required tumor uptake for the nanoparticle models compared to TRAS was observed. This can be explained by the lower maximum injectable doses due to higher doses in the kidneys following daughter radionuclide retention in the nanoparticles. This indicates that lack of recoil retention is not necessarily an unwanted process and can have a 'smoothing' effect on the overall dose distribution, distributing the exposure over multiple organs and relieving the critical organ. Secondly, while it is assumed that the carriers are immune to excretion, between 30-40% of the non-internalized free isotopes are excreted, thereby decreasing the overall exposure when daughters are not retained.

LPS and PLMS

Major organ exposure for the LPS (liposomes) and PLMS (polymersomes) models was comparable to the antibody models. However, the long circulation time combined caused a 5-10 fold increase in red bone marrow dose, making this the critical organ for the nanovesicle models. The red bone marrow exposure yielded poor tumor irradiation efficiency and maximum activity tolerance levels. Required tumor uptake was higher than for the conjugated nanoparticle models, which could be problematic since these carriers usually lack targeting agents and rely on the so-called EPR effect for tumor targeting. This type of carrier is however an option for treatment of malignancies for which no specific targeting agents are available. Reduction of the circulation time or other methods to protect the red bone marrow from exposure are however likely required for successful treatment without complications.

PSMA

The PSMA model showed the best performance in normal tissue exposure, maximum tolerable activity and required tumor uptake. However, note that over 70% of the injected compound accumulated in the residual body mass in this model. While this fraction has little effect on the exposure from carrier-bound isotopes, the fraction does produce a significant amount of free isotopes that end up in the bloodstream. It is therefore unsurprising that free isotopes irradiation is the largest contributor to the normal tissue exposure is most of the organs. The release of francium, thallium and lead are likely the reason of the high kidney exposure, making it the critical organ for this model. Kratochwil et al. performed a clinical study in Ac225-PSMA-617 and reported absorbed doses in the salivary glands, kidneys and bone marrow of respectively 466, 148, and 10 mGy/MBq (converted from Sv_{RBE5}/MBq) (Kratochwil et al., 2017), which indicates that the presented model strongly underestimates the absorbed dose in the salivary glands. A likely cause of this is the very low uptake in the salivary glands reported by Sharifi et al. (Sharifi et al., 2016). It is unknown whether this is due to low absolute activity values causing large uncertainties, or differences in PSMA pharmacokinetics between rats and humans. Incorporation of carrier release from organs and the residual body mass over time is expected to have a significant effect on the calculated maximum injectable doses. However, insufficient data is currently available to reliably model such processes.

MODEL UNCERTAINTIES

The reader is correct to question the global validity of the presented dosimetry data for the models in question. Lack of consistency in data given by alpha radionuclide carrier reports is problematic and makes direct comparison of carriers hard. Moreover, organ masses used for %ID/g calculation are rarely shown, making a reliable conversion to %ID in animals, and

especially humans, virtually impossible. Also, the retention and release kinetics of high Z atoms in-vitro, and especially in-vivo, are rarely known, but are crucial for accurate dosimetry of elements with long decay chains. Hamacher et al. chose values for the transition times from and to the blood based on a model for antibodies (Sgouros, 1992), while there is no evidence that the kinetics of the relatively large antibodies are comparable to individual ions. Accurate dosimetry of 225Ac is therefore, at the time of writing, very difficult due to the following factors:

- Limited knowledge of the biodistributions of 225Ac and its daughters

- Very limited data regarding the kinetics of the isotopes on a cellular level

- Uncertainties in normal tissue tolerances to alpha radiation exposure

- Uncertainties regarding the blood-to-organ contribution for alpha radiation

- (Very) limited pharmacokinetics data published in carrier studies

More research regarding the biodistribution of mainly free actinium and francium is necessary. Studies regarding bismuth and lead are more readily available, but are almost solely in the context of (metal) compounds. It is therefore unclear to what extend these can be applied to the free isotopes. Evident from Table 7-5, Table 7-6 and Table 7-7 is the significant contribution of accumulation of, and irradiation by, free isotopes. Free isotopes levels in tissue are strongly dependent on the internal decay probabilities as presented in Table 7-1. As mentioned, data membrane perfusion rates of free isotopes is almost non-existent at the time of writing. An attempt to estimate the internal decay probabilities was presented, but the accuracy of this approach is yet unclear. Research regarding the retention of free isotopes in (various types of) cells is paramount for safe use of 225Ac.

While several authors and institutions have already addressed the issue of normal tissue tolerance to alpha radiation and blood-to-organ dose contributions (Bolch et al., 2009; Hobbs et al., 2014; Meredith et al., 2008; Misdaq et al., 2000; Sgouros et al., 2010), no consensus regarding these numbers has yet been reached. Lastly, building pharmacokinetic models as a researcher not involved in the respective research, based on the data presented in studies of 225Ac carriers, proved to be difficult.

A complete analysis would require the following data:

- Carrier concentration in blood over time

- Critical organ uptake (multiple time points, preferably both %ID and %ID/g)

- Internalized fraction in target organ/tissue

- Biostability in blood

- Excretion over time (at least urine)

- Recoil retention (ex vitro)

- Free isotope accumulation in critical organs

None of the studies used for this work satisfied all these requirements, leading to educated guesses for missing data and often problematic %ID/g to %ID conversion.

CONCLUSIONS

Models for the pharmacokinetics and daughter radionuclide retention probabilities of 225Ac radionuclide carriers were used to investigate the effects of carrier internalization, recoil retention, tumor targeting and blood circulation time on normal tissue exposure and tumor control probability. Also, an improved model for free radionuclide pharmacokinetics was introduced to estimate normal tissue exposure due to the recoiling daughter radionuclides of 225Ac. Using these, it was shown that molecular radionuclide carriers (proteins, ligands) and antibody targeting agents perform best in terms of normal tissue exposure and required tumor targeting efficiency for tumor control. From calculations on theoretical carriers, it was concluded that carrier internalization is paramount for efficient tumor irradiation, potentially yielding up a 4 fold increase in tumor dose and between 120% and 250% higher doses in major organs for non-internalized carriers versus internalized carriers. Contrary to initial expectations recoil retention was not always beneficial in this model. Targeting agents that accumulate in major organs (kidney, liver e.g.), can benefit from the loss of some daughter radionuclides since it alleviates the organ by distributing the radiation exposure throughout the body. Long circulation times showed overall negative effects, leading to a high concentrations of free radionuclides in major organs and significant red bone marrow exposure. It was found maximum injectable doses for nanovesicles like liposomes and polymersomes were therefore limited by red bone marrow exposure. Nevertheless these carriers might find their use in radionuclide therapy of cancers for which no antibody or molecular targeting agents are available. Reduced blood circulation time and improved targeting efficiency could greatly benefit the applicability of nanovesicles carriers. While this work focused on currently available alpha radionuclide carriers, the presented models can be used to study the effects of, for example, biostability and carrier retention over time, allowing researchers to fine tune the properties of their alpha radionuclide carriers for maximum effect.

In addition to these conclusions, it was found that more research regarding the pharmacokinetics and biodistributions and free radionuclides is paramount for the applicability of 225Ac in clinical settings. Currently available data is severely lacking, which

makes patient risk estimation difficult. Also, recommendations for data representation in 225Ac carrier publications are given, since currently available data is often insufficient for further calculations by external parties.

Table 7-2: Reference human organ masses, tolerance doses and biodistribution data for intravenously injected free isotopes. Clearance data is given by the cumulate excretion over 4 days.

	Human mass (g) or volume (mL)	Actinium (%ID)	Francium[2] (%ID)	Bismuth (%ID)	Thallium (%ID)	Lead (%ID)	X-Ray dose tolerance[4] (Gy)
Adrenals	14	-	-	-	-	-	90 [5]
Blood	5500	0.08	0.31	0.64	0.36	3.63	-
Bone	5000	11.52[4]	5.10	15.29	8.40	3.83	52 [6]
Brain	1400	-	0.02	0.01	0.04	0.01	45 [6]
Heart	330	-	0.65	0.02	0.25	0.06	40 [6]
Intestines	1000	-	6.42	0.63	3.71	1.64	40 [6]
Kidneys	310	2.37	1.63	7.05	2.05	1.63	23 [6]
Liver	1800	37.3	5.41	2.12	2.81	15.96	30 [6]
Lungs	1000	-	0.38	0.17	0.26	0.27	17.5 [6]
Muscles	30000	-	8.29	1.60	10.11	1.67	-
Pancreas	100	-	0.16	0.03	0.17	-	50 [5]
Prostate	13	-	-	-	-	-	unknown
Red bone marrow[2]	1500	-	-	-	-	-	2 [5]
Salivary glands	85	-	-	-	-	-	10 [5]
Spleen	180	0.17	0.21	0.06	0.21	0.24	unknown
Stomach	150	-	0.31	0.08	0.26	0.08	50 [6]
Thyroid	20	-	-	-	-	-	45 [5]
Residual body[1]	24588	37.74	32.76	32.79	22.96	25.94	-
Clearance	-	11.20	37.74	38.24	47.70	37.79	-
Tumor	10	-	-	-	-	-	-

[1] Residual body mass represents the mass unaccounted for by the major organs.

[2] Assuming similar behavior as Cesium.

[3] Specific binding only. Not accounting for irradiation from the blood.

[4] Based on $TD_{5/5}$ values for whole organ x-ray irradiation with 2 Gy fractions.

[5] (Herrmann et al., 2006), [6] (Bentzen et al., 2012)

Table 7-3: Simplified biodistribution models for various alpha radionuclide carriers. Values expressed in %ID 24 h post-injection, except for PSMA, which is given at 60 min post-injection.

	HUM195 Antibody	Liposomes and polymersomes	Trastuzumab and LaPO$_4$ nanoparticles	PSMA[1]	Theoretical particle, internalizing	Theoretical particle, non-internalizing
Indicator	*H195*	*LPS, PLMS*	*TRAS, LAP04, GOLD*	*PSMA*	*VIRT1*	*VIRT2*
Blood half-life	*12 days*	*16 hours*	*8 hours*	*8 minutes*	*-*	*-*
Internalizing in	*-*	*All soft tissues*	*Tumor*	*Tumor, prostate, salivary glands*	*Tumor*	*-*
Biostable	*Yes*	*Yes*	*Yes*	*Yes*	*Yes*	*Yes*
Adrenals	-	-	-	>0.1	-	-
Blood	94.4	35	12.5	0.6		
Bone	-	-	-	0.4	-	-
Brain	-	-	-	-	-	-
Heart	-	-	1.8	>0.1	-	-
Intestines	-	7.1	11.4	0.3	-	-
Kidneys	-	3.3	7.0	6.7	-	-
Liver	-	21.3	29.8	0.5	-	-
Lungs	-	1.9	4.4	0.1	-	-
Muscles	-	14.9	13.1	1.5	-	-
Pancreas	-	-	-	>0.1	-	-

[1] Biodistribution data based on the time-integrated activity coefficients of ^{68}Ga-PSMA-11.

[2] Specific binding only. Not accounting for carriers in the blood located at the bone marrow.

Table 7-3 continued

Prostate	-	-	-	>0.1	-	-
Red bone marrow²	-	3.2	-	-	-	-
Salivary glands	-	-	-	>0.1	-	-
Spleen	-	0.6	0.9	>0.1	-	-
Stomach	-	-	-	>0.1	-	-
Thyroid	-	-	-	>0.1	-	-
Residual body	-	12.3	19.3	70.2	-	-
Clearance	5.6	-	-	20	-	-
Tumor	n.a.	n.a.	n.a.	n.a.	100	100

Table 7-4: Recoil retention. Values expressed as the percentage of daughter isotopes retained compared to the initial number of 225Ac isotopes.

Retention (%)	HUM195 Antibody	Liposomes[1]	Polymersomes	Trastuzumab	LaPO4
225Ac	-	-	-	-	-
221Fr	0	25	35	0	50
217At	0	12.5	-	0	25
213Bi	0	0	20	0	12.5
213Po	0	0	20	0	12.5
209Th	0	0	11	0	6.25
209Pb	0	0	11	0	6.25
	Gold coated LaPO4	PSMA	Theoretical particles		
225Ac	-	-	-		
221Fr	88	0	0		
217At	77	0	0		
213Bi	68	0	0		
213Po	68	0	0		
209Th	46	0	0		
209Pb	46	0	0		

[1] Since no data before Bismuth was given, 25% retention was assumed

Table 7-5: Absorbed dose per injected MBq for various models of 225Ac carriers 4 hours post-injection induced by the carrier-bound and free circulating isotopes.

mGy/MBq	H195			TRAS			LAPO4		
	Carrier	Free	Total	Carrier	Free	Total	Carrier	Free	Total
Adrenal	0	0	0	0	0	0	0	0	0
Bone	0	**3.76E-1**	**3.76E-1**	0	**3.78E-1**	**3.78E-1**	0	**3.55E-1**	**3.55E-1**
Brain	0	6.40E-3	6.40E-3	0	6.43E-3	6.43E-3	0	3.62E-3	3.62E-3
Heart	0	**8.61E-1**	**8.61E-1**	**1.27E-1**	**8.64E-1**	**9.92E-1**	**2.57E-1**	**5.01E-1**	**7.58E-1**
Intestine	0	**2.82**	**2.82**	**2.73E-1**	**2.83**	**3.10**	**5.52E-1**	**1.59**	**2.14**
Kidneys	0	**2.82**	**2.82**	**5.41E-1**	**2.84**	**3.38**	**1.10**	**2.96**	**4.06**
Liver	0	**1.34**	**1.34**	**3.96E-1**	**1.35**	**1.74**	**8.02E-1**	**9.46E-1**	**1.75**
Lung	0	**1.70E-1**	**1.70E-1**	**1.05E-1**	**1.71E-1**	**2.75E-1**	**2.12E-1**	**1.49E-1**	**3.61E-1**
Muscle	0	**1.22E-1**	**1.22E-1**	1.05E-2	**1.22E-1**	**1.33E-1**	2.12E-2	6.96E-2	9.08E-2
Pancreas	0	**7.05E-1**	**7.05E-1**	0	**7.08E-1**	**7.08E-1**	0	**3.71E-1**	**3.71E-1**
Prostate	0	0	0	0	0	0	0	0	0
RBM	**8.88E-1**	2.11E-2	**9.09E-1**	**7.55E-1**	2.12E-2	**7.76E-1**	**1.48**	**2.36E-1**	**1.71**
Salivary glands	0	0	0	0	0	0	0	0	0
Spleen	0	**5.17E-1**	**5.17E-1**	**1.17E-1**	**5.19E-1**	**6.36E-1**	**2.36E-1**	**3.39E-1**	**5.75E-1**
Stomach	0	**9.14E-1**	**9.14E-1**	0	**9.18E-1**	**9.18E-1**	0	**4.89E-1**	**4.89E-1**
Thyroid	0	0	0	0	0	0	0	0	0
Residual body	0	**6.11E-1**	**6.11E-1**	1.88E-2	**6.13E-1**	**6.32E-1**	3.80E-2	**3.91E-1**	**4.29E-1**

Cells are style coded for better data visualization: **1-10 mGy/MBq**, **0.1-1 mGy/MBq**, <0.1 mGy/MBq.

Table 7-5 continued

mGy/MBq	GOLD			LPS			PLMS		
	Carrier	Free	Total	Carrier	Free	Total	Carrier	Free	Total
Adrenal	0	0	0	0	0	0	0	0	0
Bone	0	**2.20E-1**	**2.20E-1**	0	**3.84E-1**	**3.84E-1**	0	**3.03E-1**	**3.03E-1**
Brain	0	1.75E-3	1.75E-3	0	4.85E-3	4.85E-3	0	4.13E-3	4.13E-3
Heart	**4.15E-1**	**2.38E-1**	**6.53E-1**	0	**6.17E-1**	**6.17E-1**	0	**5.34E-1**	**5.34E-1**
Intestine	**8.90E-1**	**7.48E-1**	**<u>1.64</u>**	**1.64E-1**	**<u>2.29</u>**	**<u>2.45</u>**	**2.55E-1**	**<u>1.94</u>**	**<u>2.20</u>**
Kidneys	**<u>1.77</u>**	**<u>1.86</u>**	**<u>3.63</u>**	**2.41E-1**	**<u>3.26</u>**	**<u>3.50</u>**	**3.74E-1**	**<u>2.56</u>**	**<u>2.93</u>**
Liver	**<u>1.29</u>**	**4.94E-1**	**<u>1.79</u>**	**2.74E-1**	**<u>1.42</u>**	**<u>1.69</u>**	**4.25E-1**	**<u>1.17</u>**	**<u>1.60</u>**
Lung	**3.42E-1**	8.24E-2	**4.25E-1**	4.48E-2	**1.96E-1**	**2.41E-1**	6.95E-2	**1.60E-1**	**2.29E-1**
Muscle	3.42E-2	3.31E-2	6.73E-2	1.14E-2	**1.07E-1**	**1.18E-1**	1.78E-2	8.97E-2	**1.07E-1**
Pancreas	0	**1.70E-1**	**1.70E-1**	0	**5.15E-1**	**5.15E-1**	0	**4.44E-1**	**4.44E-1**
Prostate	0	0	0	0	0	0	0	0	0
RBM	**<u>2.31</u>**	**1.61E-1**	**<u>2.47</u>**	**<u>1.14</u>**	**2.13E-1**	**<u>1.36</u>**	**<u>1.72</u>**	1.62E-2	**<u>1.74</u>**
Salivary glands	0	0	0	0	0	0	0	0	0
Spleen	**3.80E-1**	**1.71E-1**	**5.52E-1**	8.30E-2	**5.09E-1**	**5.92E-1**	**1.29E-1**	**4.22E-1**	**5.51E-1**
Stomach	0	**2.27E-1**	**2.27E-1**	0	**6.74E-1**	**6.74E-1**	0	**5.79E-1**	**5.79E-1**
Thyroid	0	0	0	0	0	0	0	0	0
Residual body	6.13E-2	**2.03E-1**	**2.64E-1**	1.15E-2	**5.05E-1**	**5.17E-1**	1.79E-2	**4.23E-1**	**4.41E-1**

Cells are style coded for better data visualization: **<u>1-10 mGy/MBq</u>**, **0.1-1 mGy/MBq**, <0.1 mGy/MBq.

Table 7-5 continued

mGy/MBq	PSMA			VIRT1			VIRT2		
	Carrier	Free	Total	Carrier	Free	Total	Carrier	Free	Total
Adrenal	1.09E-2	**3.07E-1**	**3.18E-1**	0	**1.55E-1**	**1.55E-1**	0	**3.78E-1**	**3.78E-1**
Bone	0	5.21E-3	5.21E-3	0	1.86E-3	1.86E-3	0	6.43E-3	6.43E-3
Brain	1.96E-2	**7.01E-1**	**7.20E-1**	0	**2.35E-1**	**2.35E-1**	0	**8.64E-1**	**8.64E-1**
Heart	3.88E-2	**<u>2.29</u>**	**<u>2.33</u>**	0	**7.75E-1**	**7.75E-1**	0	**<u>2.83</u>**	**<u>2.83</u>**
Intestine	**<u>2.80</u>**	**<u>2.30</u>**	**<u>5.10</u>**	0	**<u>1.17</u>**	**<u>1.17</u>**	0	**<u>2.84</u>**	**<u>2.84</u>**
Kidneys	3.59E-2	**<u>1.09</u>**	**<u>1.13</u>**	0	**3.86E-1**	**3.86E-1**	0	**<u>1.35</u>**	**<u>1.35</u>**
Liver	1.55E-2	**1.38E-1**	**1.54E-1**	0	4.91E-2	4.91E-2	0	**1.71E-1**	**1.71E-1**
Lung	6.56E-3	9.92E-2	**1.06E-1**	0	3.40E-2	3.40E-2	0	**1.22E-1**	**1.22E-1**
Muscle	2.59E-2	**5.74E-1**	**6.00E-1**	0	**1.96E-1**	**1.96E-1**	0	**7.08E-1**	**7.08E-1**
Pancreas	9.95E-2	**2.33E-1**	**3.32E-1**	0	0	0	0	0	0
Prostate	4.50E-2	1.72E-2	6.22E-2	0	8.05E-3	8.05E-3	0	2.12E-2	2.12E-2
RBM	3.04E-2	7.12E-2	**1.02E-1**	0	0	0	0	0	0
Salivary glands	2.16E-2	**4.21E-1**	**4.43E-1**	0	**1.46E-1**	**1.46E-1**	0	**5.19E-1**	**5.19E-1**
Spleen	3.45E-2	**7.44E-1**	**7.79E-1**	0	**2.57E-1**	**2.57E-1**	0	**9.18E-1**	**9.18E-1**
Stomach	6.47E-2	0	6.47E-2	0	0	0	0	0	0
Thyroid	**3.70E-1**	**4.97E-1**	**8.67E-1**	0	**1.89E-1**	**1.89E-1**	0	**6.13E-1**	**6.13E-1**
Residual body	1.09E-2	**3.07E-1**	**3.18E-1**	0	**1.55E-1**	**1.55E-1**	0	**3.78E-1**	**3.78E-1**

Cells are style coded for better data visualization: **<u>1-10 mGy/MBq</u>**, **0.1-1 mGy/MBq**, <0.1 mGy/MBq.

Table 7-6: Absorbed dose per injected MBq for various models of 225Ac carriers <u>24 hours post-injection</u> induced by the carrier-bound and free circulating isotopes.

mGy/MBq	H195			TRAS			LAPO4		
	Carrier	Free	Total	Carrier	Free	Total	Carrier	Free	Total
Adrenal	0	0	0	0	0	0	0	0	0
Bone	0	**2.36**	**2.36**	0	**2.42**	**2.42**	0	**2.20**	**2.20**
Brain	0	4.23E-2	4.23E-2	0	4.35E-2	4.35E-2	0	2.42E-2	2.42E-2
Heart	0	**5.65**	**5.65**	2.76	**5.81**	**8.57**	5.70	4.72	<u>**1.04E1**</u>
Intestine	0	<u>**1.85E1**</u>	<u>**1.85E1**</u>	5.93	<u>**1.90E1**</u>	<u>**2.49E1**</u>	<u>**1.22E1**</u>	<u>**1.36E1**</u>	<u>**2.58E1**</u>
Kidneys	0	<u>**1.94E1**</u>	<u>**1.94E1**</u>	<u>**1.18E1**</u>	<u>**1.99E1**</u>	<u>**3.17E1**</u>	<u>**2.43E1**</u>	<u>**2.53E1**</u>	<u>**4.96E1**</u>
Liver	0	**8.88**	**8.88**	8.62	**9.12**	<u>**1.77E1**</u>	<u>**1.78E1**</u>	<u>**1.06E1**</u>	<u>**2.84E1**</u>
Lung	0	**1.12**	**1.12**	2.28	**1.15**	**3.43**	4.70	2.11	6.82
Muscle	0	8.01E-1	8.01E-1	2.28E-1	8.24E-1	**1.05**	4.70E-1	5.78E-1	1.05
Pancreas	0	**4.64**	**4.64**	0	**4.77**	**4.77**	0	2.48	2.48
Prostate	0	0	0	0	0	0	0	0	0
RBM	5.05	1.33E-1	**5.19**	2.21	1.37E-1	**2.35**	4.49	7.76E-1	5.26
Salivary glands	0	0	0	0	0	0	0	0	0
Spleen	0	**3.41**	**3.41**	2.53	**3.51**	**6.04**	5.22	3.52	8.74
Stomach	0	**6.02**	**6.02**	0	**6.19**	**6.19**	0	3.28	3.28
Thyroid	0	0	0	0	0	0	0	0	0
Residual body	0	**4.06**	**4.06**	4.08E-1	**4.17**	**4.58**	8.41E-1	2.81	3.65

Cells are style coded for better data visualization: <u>**10-100 mGy/MBq**</u>, **1-0.1 mGy/MBq**, <1 mGy/MBq.

Table 7-6 continued

	GOLD			LPS			PLMS		
	Carrier	Free	Total	Carrier	Free	Total	Carrier	Free	Total
Adrenal	0	0	0	0	0	0	0	0	0
Bone	0	**1.40**	**1.40**	0	**2.13**	**2.13**	0	**1.68**	**1.68**
Brain	0	1.18E-2	1.18E-2	0	2.62E-2	2.62E-2	0	2.23E-2	2.23E-2
Heart	9.43	2.53	**1.20E1**	0	3.26	3.26	0	2.82	2.82
Intestine	**2.02E1**	7.03	**2.73E1**	4.41	**1.92E1**	**2.36E1**	7.03	**1.57E1**	**2.27E1**
Kidneys	**4.02E1**	**1.64E1**	**5.66E1**	6.46	**2.95E1**	**3.60E1**	**1.03E1**	**2.29E1**	**3.32E1**
Liver	**2.94E1**	6.28	**3.57E1**	7.35	**1.94E1**	**2.68E1**	**1.17E1**	**1.52E1**	**2.70E1**
Lung	7.78	1.32	9.11	1.20	2.97	4.18	1.92	2.32	4.23
Muscle	7.78E-1	2.99E-1	**1.08**	3.07E-1	**1.06**	**1.37**	4.90E-1	8.50E-1	**1.34**
Pancreas	0	**1.14**	**1.14**	0	**2.74**	**2.74**	0	**2.36**	**2.36**
Prostate	0	0	0	0	0	0	0	0	0
RBM	7.29	5.27E-1	7.82	5.71	1.32	7.03	9.01	9.18E-2	9.10
Salivary glands	0	0	0	0	0	0	0	0	0
Spleen	8.65	2.01	**1.07E1**	2.23	6.28	8.51	3.55	4.96	8.51
Stomach	0	**1.52**	**1.52**	0	**3.60**	**3.60**	0	**3.09**	**3.09**
Thyroid	0	0	0	0	0	0	0	0	0
Residual body	1.39	1.50	2.90	3.10E-1	3.28	3.59	4.94E-1	2.70	3.20

Cells are style coded for better data visualization: **10-100 mGy/MBq**, **1-0.1 mGy/MBq**, <1 mGy/MBq.

Table 7-6 continued

mGy/MBq	PSMA			VIRT1			VIRT2		
	Carrier	Free	Total	Carrier	Free	Total	Carrier	Free	Total
Adrenal	5.63E-1	0	5.63E-1	0	0	0	0	0	0
Bone	6.62E-2	**1.95**	**2.01**	0	**1.08**	**1.08**	0	**2.42**	**2.42**
Brain	0	3.48E-2	3.48E-2	0	1.28E-2	1.28E-2	0	4.35E-2	4.35E-2
Heart	1.19E-1	**4.65**	**4.77**	0	**1.58**	**1.58**	0	**5.81**	**5.81**
Intestine	2.36E-1	**<u>1.52E1</u>**	**<u>1.55E1</u>**	0	**5.24**	**5.24**	0	**<u>1.90E1</u>**	**<u>1.90E1</u>**
Kidneys	**<u>1.70E1</u>**	**<u>1.60E1</u>**	**<u>3.31E1</u>**	0	**8.70**	**8.70**	0	**<u>1.99E1</u>**	**<u>1.99E1</u>**
Liver	2.19E-1	**7.32**	**7.54**	0	**2.68**	**2.68**	0	**9.12**	**9.12**
Lung	9.45E-2	9.24E-1	**1.02**	0	3.37E-1	3.37E-1	0	**1.15**	**1.15**
Muscle	3.99E-2	6.60E-1	7.00E-1	0	2.30E-1	2.30E-1	0	8.24E-1	8.24E-1
Pancreas	1.58E-1	**3.82**	**3.98**	0	**1.33**	**1.33**	0	**4.77**	**4.77**
Prostate	6.06E-1	**1.64**	**2.24**	0	0	0	0	0	0
RBM	4.50E-2	1.10E-1	1.55E-1	0	5.83E-2	5.83E-2	0	1.37E-1	1.37E-1
Salivary glands	1.85E-1	5.01E-1	6.86E-1	0	0	0	0	0	0
Spleen	1.31E-1	**2.81**	**2.94**	0	**1.00**	**1.00**	0	**3.51**	**3.51**
Stomach	2.10E-1	**4.96**	**5.17**	0	**1.75**	**1.75**	0	**6.19**	**6.19**
Thyroid	3.94E-1	0	3.94E-1	0	0	0	0	0	0
Residual body	**2.25**	**3.35**	**5.60**	0	**1.33**	**1.33**	0	**4.17**	**4.17**

Cells are style coded for better data visualization: **<u>10-100 mGy/MBq</u>**, **1-0.1 mGy/MBq**, <1 mGy/MBq.

Table 7-7: Absorbed dose per injected MBq for various models of 225Ac carriers 7 days post-injection induced by the carrier-bound and free circulating isotopes.

mGy/MBq	H195			TRAS			LAPO4		
	Carrier	Free	Total	Carrier	Free	Total	Carrier	Free	Total
Adrenal	0	0	0	0	0	0	0	0	0
Bone	0	**1.18E1**	**1.18E1**	0	**1.41E1**	**1.41E1**	0	**1.13E1**	**1.13E1**
Brain	0	2.14E-1	2.14E-1	0	2.56E-1	2.56E-1	0	1.39E-1	1.39E-1
Heart	0	**2.86E1**	**2.86E1**	2.53E1	**3.42E1**	**5.95E1**	5.23E1	3.43E1	**8.66E1**
Intestine	0	**9.37E1**	**9.37E1**	5.43E1	**1.12E2**	**1.66E2**	**1.12E2**	9.38E1	**2.06E2**
Kidneys	0	**9.91E1**	**9.91E1**	**1.08E2**	**1.18E2**	**2.26E2**	**2.23E2**	**1.65E2**	**3.88E2**
Liver	0	**4.51E1**	**4.51E1**	7.89E1	**5.39E1**	**1.33E2**	**1.63E2**	8.26E1	**2.45E2**
Lung	0	5.69	5.69	**2.09E1**	6.79	**2.77E1**	4.31E1	1.78E1	**6.09E1**
Muscle	0	4.06	4.06	2.09	4.85	6.94	4.31	3.92	8.23
Pancreas	0	**2.35E1**	**2.35E1**	0	**2.81E1**	**2.81E1**	0	**1.45E1**	**1.45E1**
Prostate	0	0	0	0	0	0	0	0	0
RBM	2.50E1	6.76E-1	**2.56E1**	2.51	8.04E-1	3.31	5.09	1.36	6.45
Salivary glands	0	0	0	0	0	0	0	0	0
Spleen	0	**1.73E1**	**1.73E1**	2.32E1	**2.07E1**	**4.39E1**	4.79E1	2.66E1	**7.45E1**
Stomach	0	**3.05E1**	**3.05E1**	0	**3.65E1**	**3.65E1**	0	**1.90E1**	**1.90E1**
Thyroid	0	0	0	0	0	0	0	0	0
Residual body	0	**2.06E1**	**2.06E1**	3.74	**2.46E1**	**2.84E1**	7.71	**1.68E1**	**2.45E1**

Cells are style coded for better data visualization: **>100 mGy/MBq**, **10-100 mGy/MBq**, <10 mGy/MBq.

Table 7-7 continued

	GOLD			LPS			PLMS		
	Carrier	Free	Total	Carrier	Free	Total	Carrier	Free	Total
Adrenal	0	0	0	0	0	0	0	0	0
Bone	0	7.13	7.13	0	7.69	7.69	0	6.31	6.31
Brain	0	6.68E-2	6.68E-2	0	8.90E-2	8.90E-2	0	7.63E-2	7.63E-2
Heart	**8.67E1**	**1.94E1**	<u>**1.06E2**</u>	0	**1.08E1**	**1.08E1**	0	9.38	9.38
Intestine	<u>**1.86E2**</u>	**5.09E1**	<u>**2.37E2**</u>	**5.66E1**	<u>**1.48E2**</u>	<u>**2.05E2**</u>	**9.04E1**	<u>**1.17E2**</u>	<u>**2.07E2**</u>
Kidneys	<u>**3.69E2**</u>	<u>**1.08E2**</u>	<u>**4.77E2**</u>	**8.30E1**	<u>**2.28E2**</u>	<u>**3.11E2**</u>	<u>**1.33E2**</u>	<u>**1.77E2**</u>	<u>**3.09E2**</u>
Liver	<u>**2.70E2**</u>	**5.08E1**	<u>**3.21E2**</u>	**9.44E1**	<u>**2.06E2**</u>	<u>**3.00E2**</u>	<u>**1.51E2**</u>	<u>**1.58E2**</u>	<u>**3.09E2**</u>
Lung	**7.15E1**	**1.15E1**	**8.30E1**	**1.54E1**	**3.30E1**	**4.85E1**	**2.47E1**	**2.53E1**	**5.00E1**
Muscle	7.15	2.12	9.27	3.95	9.43	**1.34E1**	6.30	7.32	**1.36E1**
Pancreas	0	6.59	6.59	0	9.17	9.17	0	7.91	7.91
Prostate	0	0	0	0	0	0	0	0	0
RBM	8.29	9.07E-1	9.20	**2.37E1**	7.97	**3.17E1**	**3.77E1**	3.50E-1	**3.81E1**
Salivary glands	0	0	0	0	0	0	0	0	0
Spleen	**7.95E1**	**1.59E1**	**9.53E1**	**2.86E1**	**6.37E1**	**9.23E1**	**4.57E1**	**4.91E1**	**9.48E1**
Stomach	0	8.80	8.80	0	**1.21E1**	**1.21E1**	0	**1.04E1**	**1.04E1**
Thyroid	0	0	0	0	0	0	0	0	0
Residual body	1.28E1	9.07	**2.19E1**	3.98	**1.72E1**	**2.12E1**	6.35	**1.39E1**	**2.02E1**

*Cells are style coded for better data visualization: <u>**>100 mGy/MBq**</u>, **10-100 mGy/MBq**, <10 mGy/MBq.*

Table 7-7 continued

mGy/MBq	PSMA			VIRT1			VIRT2		
	Carrier	Free	Total	Carrier	Free	Total	Carrier	Free	Total
Adrenal	3.25	0	3.25	0	0	0	0	0	0
Bone	3.82E-1	**1.13E1**	**1.17E1**	0	6.37	6.37	0	**1.41E1**	**1.41E1**
Brain	0	2.05E-1	2.05E-1	0	7.58E-2	7.58E-2	0	2.56E-1	2.56E-1
Heart	6.90E-1	**2.74E1**	**2.80E1**	0	9.29	9.29	0	**3.42E1**	**3.42E1**
Intestine	1.37	**8.96E1**	**9.10E1**	0	**3.09E1**	**3.09E1**	0	**1.12E2**	**1.12E2**
Kidneys	**9.86E1**	**9.48E1**	**1.93E2**	0	**5.21E1**	**5.21E1**	0	**1.18E2**	**1.18E2**
Liver	1.26	**4.31E1**	**4.44E1**	0	**1.59E1**	**1.59E1**	0	**5.39E1**	**5.39E1**
Lung	5.46E-1	5.44	5.99	0	2.00	2.00	0	6.79	6.79
Muscle	2.31E-1	3.88	4.11	0	1.36	1.36	0	4.85	4.85
Pancreas	9.11E-1	**2.25E1**	**2.34E1**	0	7.84	7.84	0	**2.81E1**	**2.81E1**
Prostate	3.50	9.70	**1.32E1**	0	0	0	0	0	0
RBM	4.50E-2	6.47E-1	6.92E-1	0	3.50E-1	3.50E-1	0	8.04E-1	8.04E-1
Salivary glands	1.07	2.97	4.04	0	0	0	0	0	0
Spleen	7.59E-1	**1.65E1**	**1.73E1**	0	5.93	5.93	0	**2.07E1**	**2.07E1**
Stomach	1.21	**2.92E1**	**3.04E1**	0	**1.03E1**	**1.03E1**	0	**3.65E1**	**3.65E1**
Thyroid	2.28	0	2.28	0	0	0	0	0	0
Residual body	**1.30E1**	**1.97E1**	**3.27E1**	0	7.86	7.86	0	**2.46E1**	**2.46E1**

*Cells are style coded for better data visualization: **>100 mGy/MBq**, **10-100 mGy/MBq**, <10 mGy/MBq.*

Table 7-8: Doses induced in various organs and tissues by radionuclides in the 225Ac decay chain, expressed as percentage of the total absorbed dose in the respective organ/tissue.

% of Total Dose	225Ac	221Fr	217At	213Bi	213Po	209Tl	209Pb
VIRT1							
Adrenal	0	0	0	0	0	0	0
Bone	0	21.44	23.90	8.27	45.70	0.04	0.65
Brain	0	25.25	28.14	6.63	36.60	0.40	2.98
Heart	0	28.39	31.64	5.74	31.68	0.31	2.24
Intestine	0	27.86	31.05	5.87	32.43	0.32	2.47
Kidneys	0	13.51	15.06	10.20	56.34	0.55	4.34
Liver	0	25.25	28.14	6.27	34.66	0.34	5.33
Lung	0	25.51	28.43	6.52	36.02	0.36	3.16
Muscle	0	27.23	30.34	6.07	33.53	0.35	2.48
Pancreas	0	27.33	30.45	6.07	33.54	0.35	2.26
Prostate	0	0	0	0	0	0	0
RBM	0	23.02	25.66	6.18	34.16	0.03	10.95
Salivary glands	0	0	0	0	0	0	0
Spleen	0	26.36	29.38	6.19	34.20	0.35	3.52
Stomach	0	26.79	29.86	6.20	34.23	0.34	2.59
Thyroid	0	0	0	0	0	0	0
Tumor	26.53	21.05	23.46	4.17	23.03	0.21	1.55
Residual body	0	22.62	25.21	7.40	40.88	0.40	3.48

Table 7-8 continued

% of Total Dose	225Ac	221Fr	217At	213Bi	213Po	209Tl	209Pb
VIRT2							
Adrenal	0	0	0	0	0	0	0
Bone	0	35.81	39.91	3.68	20.33	0.02	0.25
Brain	0	27.66	30.83	5.95	32.89	0.32	2.34
Heart	0	28.58	31.85	5.69	31.44	0.30	2.14
Intestine	0	28.44	31.69	5.73	31.64	0.30	2.20
Kidneys	0	22.08	24.60	7.64	42.23	0.40	3.05
Liver	0	27.69	30.86	5.86	32.35	0.31	2.93
Lung	0	27.75	30.92	5.92	32.71	0.31	2.39
Muscle	0	28.26	31.49	5.78	31.95	0.31	2.21
Pancreas	0	28.28	31.52	5.78	31.95	0.31	2.15
Prostate	0	0	0	0	0	0	0
RBM	0	37.17	41.42	2.66	14.69	0.01	4.05
Salivary glands	0	0	0	0	0	0	0
Spleen	0	28.02	31.22	5.82	32.17	0.31	2.46
Stomach	0	28.13	31.35	5.82	32.15	0.31	2.23
Thyroid	0	0	0	0	0	0	0
Tumor	100	0	0	0	0	0	0
Residual body	0	26.76	29.82	6.22	34.36	0.33	2.51

Table 7-9: Maximum injectable dose with corresponding critical organ (the organ to first reach the dose threshold), 7 days after irradiation, together with the minimum tumor SUV to reach 20 Gy (90 Gy x-ray equivalent after RBE2(α/β) correction) in a tumor.

	Critical organ/tissue	Maximum injectable activity (MBq)	Req. tumor uptake (% on maximum injected dose)
TRAS	Kidney	23	0.56
LAPO4	Kidney	13	0.84
GOLD	Kidney	11	0.95
LPS	Red bone marrow	14	0.93
PLMS	Red bone marrow	12	1.07
PSMA	Kidney	26	0.44
THEOR1	Kidney	98	0.12
THEOR2	Kidney	43	1.01

REFERENCES

Afshar-Oromieh, A., Hetzheim, H., Kubler, W., Kratochwil, C., Giesel, F.L., Hope, T.A., Eder, M., Eisenhut, M., Kopka, K., Haberkorn, U., 2016. Radiation dosimetry of 68Ga-PSMA-11 (HBED-CC) and preliminary evaluation of optimal imaging timing. *Eur. J. Nucl. Med. Mol. Imaging* 43(9), 1611–1620. https://doi.org/10.1007/s00259-016-3419-0

Åkesson, A., Lind, T., Ehrlich, N., Stamou, D., Wacklin, H., Cárdenas, M., 2012. Composition and structure of mixed phospholipid supported bilayers formed by POPC and DPPC. *Soft Matter* 8(20), 5658. https://doi.org/10.1039/c2sm00013j

Baish, J.W., Stylianopoulos, T., Lanning, R.M., Kamoun, W.S., Fukumura, D., Munn, L.L., Jain, R.K., 2011. Scaling rules for diffusive drug delivery in tumor and normal tissues. *Proc. Natl. Acad. Sci. U. S. A.* 108(5), 1799–1803. https://doi.org/10.1073/pnas.1018154108

Ballangrud, Å.M., Yang, W.H., Palm, S., Enmon, R., Borchardt, P.E., Pellegrini, V.A., McDevitt, M.R., Scheinberg, D.A., Sgouros, G., 2004. Alpha-particle emitting atomic generator (actinium-225)-labeled trastuzumab (Herceptin) targeting of breast cancer spheroids: Efficacy versus HER2/neu expression. *Clin. Cancer Res.* 10(13), 4489–4497. https://doi.org/10.1158/1078-0432.CCR-03-0800

Bentzen, S.M., Dörr, W., Gahbauer, R., Howell, R.W., Joiner, M.C., Jones, B., Jones, D.T.L., Van Der Kogel, A.J., Wambersie, A., Whitmore, G., 2012. Bioeffect modeling and equieffective dose concepts in radiation oncology-Terminology, quantities and units. *Radiother. Oncol.* 105(2), 266–268. https://doi.org/10.1016/j.radonc.2012.10.006

Berger, M.J., Coursey, J.S., Zucker, M.A., Chang, J., 2005. ESTAR, PSTAR, and ASTAR: Computer Programs for Calculating Stopping-Power and Range Tables for Electrons, Protons, and Helium Ions (version 1.2.3).

Bolch, W.E., Eckerman, K.F., Sgouros, G., Thomas, S.R., 2009. MIRD pamphlet No. 21: a generalized schema for radiopharmaceutical dosimetry--standardization of nomenclature. *J. Nucl. Med.* 50(3), 477–484. https://doi.org/10.2967/jnumed.108.056036

Borchardt, P.E., Yuan, R.R., Miederer, M., Mcdevitt, M.R., Scheinberg, D. a, 2003. Targeted Actinium-225 in Vivo Generators for Therapy of Ovarian Cancer. *Cancer Res.* 63(17), 5084–5090.

Chang, M.Y., Seideman, J., Sofou, S., 2008. Enhanced loading efficiency and retention of 225Ac in rigid liposomes for potential targeted therapy of micrometastases. *Bioconjug. Chem.* 19(6), 1274–1282. https://doi.org/10.1021/bc700440a

Chow, T.H., Lin, Y.Y., Hwang, J.J., Wang, H.E., Tseng, Y.L., Wang, S.J., Liu, R.S., Lin, W.J., Yang, C.S., Ting, G., 2009. Improvement of biodistribution and therapeutic index via increase of polyethylene glycol on drug-carrying liposomes in an HT-29/luc xenografted mouse model. *Anticancer Res.* 29(6), 2111–2120.

Dawson, C.M., Croghan, P.C., Scott, A.M., Bangham, J.A., 1986. Potassium and rubidium permeability and potassium conductance of beta-cell membrane in mouse islets of langerhans. *Q. J. Exp. Physiol.* 71, 205–222.

de Kruijff, R.M., Drost, K., Thijssen, L., Morgenstern, A., Bruchertseifer, F., Lathouwers, D., Wolterbeek, H.T., Denkova, A.G., 2017. Improved 225Ac daughter retention in InPO4 containing polymersomes. *Appl. Radiat. Isot.* 128(March), 183–189. https://doi.org/10.1016/j.apradiso.2017.07.030

Feher, J.J., Briggs, F.N., 1982. The effect of calcium load on the calcium permeability of sarcoplasmic reticulum. *J. Biol. Chem.* 257(17), 10191–10199.

Franken, N.A.P., ten Cate, R., Krawczyk, P.M., Stap, J., Haveman, J., Aten, J., Barendsen, G.W., 2011. Comparison of RBE values of high-LET α-particles for the induction of DNA-DSBs, chromosome aberrations and cell reproductive death. *Radiat. Oncol.* 6(64), 1–8. https://doi.org/10.1186/1748-717X-6-64

Gregus, Z., Klaassen, C.D., 1986. Disposition of metals in rats: A comparative study of fecal, urinary, and biliary excretion and tissue distribution of eighteen metals. *Toxicol. Appl. Pharmacol.* 85(1), 24–38. https://doi.org/10.1016/0041-008X(86)90384-4

Hamacher, K.A., Sgouros, G., 2001. Theoretical estimation of absorbed dose to organs in radioimmunotherapy using radionuclides with multiple unstable daughters. *Med. Phys.* 28(9), 1857–1874. https://doi.org/10.1118/1.1395026

Herrmann, T., Baumann, M., Dorr, W., 2006. Klinische Strahlenbiologie, 4th ed. Elsevier, Munich.

Hindorf, C., Glatting, G., Chiesa, C., Lindén, O., Flux, G., 2010. EANM dosimetry committee guidelines for bone marrow and whole-body dosimetry. *Eur. J. Nucl. Med. Mol. Imaging* 37(6), 1238–1250. https://doi.org/10.1007/s00259-010-1422-4

Hobbs, R.F., Howell, R.W., Song, H., Baechler, S., Sgouros, G., 2014. Redefining Relative Biological Effectiveness in the Context of the EQDX Formalism: Implications for Alpha-Particle Emitter Therapy. *Radiat. Res.* 181(1), 90–98. https://doi.org/10.1016/j.micinf.2011.07.011.Innate

Hong, Y., Lai, Y.-T., Chan, G.C.-F., Sun, H., 2015. Glutathione and multidrug resistance protein transporter mediate a self-propelled disposal of bismuth in human cells. *Proc. Natl. Acad. Sci. U. S. A.* 112(11), 3211–3216. https://doi.org/10.1073/pnas.1421002112

Huang, C.Y., Guatelli, S., Oborn, B.M., Allen, B.J., 2012. Microdosimetry for targeted alpha therapy of cancer. *Comput. Math. Methods Med.* 2012. https://doi.org/10.1155/2012/153212

Kanerva, R.L., Lefever, F.R., Alden, C.L., 1983. Comparison of fresh and fixed organ weights of rats. *Toxicol. Pathol.* 11(2), 129–131. https://doi.org/10.1177/019262338301100204

Kratochwil, C., Bruchertseifer, F., Giesel, F.L., Weis, M., Verburg, F.A., Mottaghy, F., Kopka, K., Apostolidis, C., Haberkorn, U., Morgenstern, A., 2016. 225Ac-PSMA-617 for PSMA-Targeted alpha-Radiation Therapy of Metastatic Castration-Resistant Prostate Cancer. *J. Nucl. Med.* 57(12), 1941–1944. https://doi.org/10.2967/jnumed.116.178673

Kratochwil, C., Bruchertseifer, F., Rathke, H., Bronzel, M., Apostolidis, C., Weichert, W., Haberkorn, U., Giesel, F.L., Morgenstern, A., 2017. Targeted Alpha Therapy of mCRPC with 225Actinium-PSMA-617:

Dosimetry estimate and empirical dose finding. *J. Nucl. Med.* 58(10), jnumed.117.191395. https://doi.org/10.2967/jnumed.117.191395

Lei, Y., Han, H., Yuan, F., Javeed, A., Zhao, Y., 2015. The brain interstitial system: Anatomy, modeling, in vivo measurement, and applications. *Prog. Neurobiol.* https://doi.org/10.1016/j.pneurobio.2015.12.007

McDevitt, M.R., 2001. Tumor Therapy with Targeted Atomic Nanogenerators. *Science.* 294(5546), 1537–1540. https://doi.org/10.1126/science.1064126

McLaughlin, M.F., Woodward, J., Boll, R.A., Wall, J.S., Rondinone, A.J., Kennel, S.J., Mirzadeh, S., Robertson, J.D., 2013. Gold Coated Lanthanide Phosphate Nanoparticles for Targeted Alpha Generator Radiotherapy. *PLoS One* 8(1), 2–9. https://doi.org/10.1371/journal.pone.0054531

Meredith, R., Wessels, B., Knox, S., 2008. Risks to Normal Tissues From Radionuclide Therapy. *Semin. Nucl. Med.* 38(5), 347–357. https://doi.org/10.1053/j.semnuclmed.2008.05.001

Miederer, M., Mcdevitt, M.R., Sgouros, G., Kramer, K., Cheung, N. V, Scheinberg, D.A., 2004. Pharmacokinetics, Dosimetry, and Toxicity of the Targetable Atomic Generator, 225Ac-HuM195, in Nonhuman Primates. *J. Nucl. Med.* 45, 129–137.

Misdaq, M.A., Merzouki, A., Elabboubi, D., Aitnouh, F., Berrazzouk, S., 2000. Determination of radon equivalent alpha-doses in different human organs from water ingestion using SSNTD and dosimetric compartmental models. *J. Radioanal. Nucl. Chem.* 256(3), 513–520. https://doi.org/10.1023/A

Palumbo, P., Picchini, U., Beck, B., Van Gelder, J., Delbar, N., DeGaetano, A., 2008. A general approach to the apparent permeability index. *J. Pharmacokinet. Pharmacodyn.* 35(2), 235–248. https://doi.org/10.1007/s10928-008-9086-4

Pandya, D.N., Hantgan, R., Budzevich, M.M., Kock, N.D., Morse, D.L., Batista, I., Mintz, A., Li, K.C., Wadas, T.J., 2016. Preliminary therapy evaluation of 225Ac-DOTA-c (RGDyK) demonstrates that Cerenkov radiation derived from 225Ac daughter decay can be detected by optical imaging for in vivo tumor visualization. *Theranostics* 6(5), 698–709. https://doi.org/10.7150/thno.14338

Pfob, C.H., Ziegler, S., Graner, F.P., Köhner, M., Schachoff, S., Blechert, B., Wester, H.J., Scheidhauer, K., Schwaiger, M., Maurer, T., Eiber, M., 2016. Biodistribution and radiation dosimetry of 68Ga-PSMA HBED CC—a PSMA specific probe for PET imaging of prostate cancer. *Eur. J. Nucl. Med. Mol. Imaging* 43(11), 1962–1970. https://doi.org/10.1007/s00259-016-3424-3

Prise, K.M., Ahnström, G., Belli, M., Carlsson, J., Frankenberg, D., Kiefer, J., Löbrich, M., Michael, B.D., Nygren, J., Simone, G., Stenerlöw, B., 1998. A review of dsb induction data for varying quality radiations. *Int. J. Radiat. Biol.* 74(2), 173–184. https://doi.org/10.1080/095530098141564

R Core Development Team, 2011. R: A Language and Environment for Statistical Computing, R Foundation for Statistical Computing, Vienna, Austria.

Reynaud, O., Winters, K.V., Hoang, D.M., Zaim, Y., Novikov, D.S., Kim, S.G., 2016. Surface-to-volume ratio mapping of tumor microstructure using oscillating gradient diffusion weighted imaging. *Magn. Reson. Med.* 76(1), 237–247. https://doi.org/10.1002/mrm.25865.Surface-to-volume

Sato, H., Yui, M., Yoshikawa, H., 1996. Ionic Diffusion Coefficients of Cs+, Pb2+, Sm3+, Ni2+, SeO2- 4 and TcO- 4 in Free Water Determined from Conductivity Measurements. *J. Nucl. Sci. Technol.* 33(12), 950–955. https://doi.org/10.1080/18811248.1996.9732037

Schoeffner, D.J., Warren, D.A., Muralidhara, S., Bruckner, J. V, Simmons, J.E., Carolina, N., 1999. Organ weights and fat volume in rats as a function of strain and age. *J. Toxicol. Enviromental Heal. Part A* 56, 449–462.

Schwartz, J., Jaggi, J.S., O'Donoghue, J.A., Ruan, S., McDevitt, M., Larson, S.M., Scheinberg, D.A., Humm, J.L., 2005. Renal uptake of bismuth-213 and its contribution to kidney radiation dose following administration of actinium-225-labeled antibody. *Biophys. Chem.* 257(5), 2432–2437. https://doi.org/10.1016/j.immuni.2010.12.017.Two-stage

Sgouros, G., 1993. Bone Marrow Dosimetry for Radioimmunotherapy : Theoretical Considerations. *J. Nucl. Med.* 34, 689–695.

Sgouros, G., Roeske, J.C., McDevitt, M.R., Palm, S., Allen, B.J., Fisher, D.R., Brill, A.B., Song, H., Howell, R.W., Akabani, G., Bolch, W.E., Brill, A.B., Fisher, D.R., Howell, R.W., Meredith, R.F., Sgouros, G., Wessels, B.W., Zanzonico, P.B., 2010. MIRD Pamphlet No. 22 (abridged): radiobiology and dosimetry of alpha-particle emitters for targeted radionuclide therapy. *J. Nucl. Med.* 51(2), 311–328. https://doi.org/10.2967/jnumed.108.058651

Sharifi, M., Yousefnia, H., Zolghadri, S., Bahrami-Samani, A., Naderi, M., Jalilian, A.R., Geramifar, P., Beiki, D., 2016. Preparation and biodistribution assessment of 68Ga-DKFZ-PSMA-617 for PET prostate cancer imaging. *Nucl. Sci. Tech.* 27(6), 1–9. https://doi.org/10.1007/s41365-016-0134-2

Sofou, S., Thomas, J.L., Lin, H., McDevitt, M.R., Scheinberg, D.A., Sgouros, G., 2004. Engineered liposomes for potential alpha-particle therapy of metastatic cancer. *J. Nucl. Med.* 45(2), 253–60.

Tarr, L., Oppenheimer, B., Sager, R., 1933. The circulation time in various clinical conditions determined by the use of sodium dehydrochlorate. *Am. Heart J.* 8, 766–786.

Taylor, D.M., 1970. The metabolism of actinium in the rat. Health Phys. 19(Sept.), 411–418.

Tracy, B.L., Stevens, D.L., Goodhead, D.T., Hill, M.A., 2015. Variation in RBE for Survival of V79-4 Cells as a Function of Alpha-Particle (Helium Ion) Energy. *Radiat. Res.* 184(1), 33–45. https://doi.org/10.1667/RR13835.1

Wang, G., Kruijff, R.M. De, Rol, A., Thijssen, L., Mendes, E., Morgenstern, A., Bruchertseifer, F., Stuart, M.C.A., Wolterbeek, H.T., Denkova, A.G., 2014. Retention studies of recoiling daughter nuclides of 225Ac in polymer vesicles. *Appl. Radiat. Isot.* 85, 45–53. https://doi.org/10.1016/j.apradiso.2013.12.008

Watabe, H.W., Koma, Y.I., Imura, Y.K., Aganawa, M.N., Hidahara, M.S., 2006. PET kinetic analysis — compartmental model. *Ann. Nucl. Med.* 20(9), 583–588.

Woodward, J., Kennel, S.J., Stuckey, A., Osborne, D., Wall, J., Rondinone, A.J., Standaert, R.F., Mirzadeh, S., 2011. LaPO4 nanoparticles doped with actinium-225 that partially sequester daughter radionuclides. *Bioconjug. Chem.* 22(4), 766–776. https://doi.org/10.1021/bc100574f

Yao, Z., Garmestani, K., Wong, K.J., Park, L.S., Dadachova, E., Yordanov, A., Waldmann, T.A., Eckelman, W.C., Paik, C.H., Carrasquillo, J.A., 2001. Comparative Cellular Catabolism and Retention of Astatine-, Bismuth-, and Lead-Radiolabeled Internalizing Monoclonal Antibody. *J. Nucl. Med.* 42(10), 1538–1545.

Summary and outlook

Alpha radionuclide therapy has great potential for effective treatment of metastatic with reduced normal tissue complications. (Pre-clinical) research of alpha radiation of therapy does however suffer from a lack of proper tools for spectroscopy, (micro-) dosimetry and radiobiology. An attempt was made to develop and verify methods for the application of fluorescent nuclear track detectors (FNTD) for alpha radiation, to create an affordable and versatile 4 in 1 tool.

Chapter 2 summarized the current state of the FNTD technology. It was shown that significant advancements have been made in the application of these detectors for gamma, proton and heavy ion radiation. The ability to visualize individual tracks at a sub-micron scale enabled simultaneous spectroscopy and dosimetry of various beams. The novel technique were cell monolayers were grown on top of the FNTD to localize DNA damage and repair with ion tracks, both after fixation and in live cells, has great potential in future efforts to unravel the kinetics of DNA damage and repair.

Chapter 3 described in detail the first step of FNTD track analysis: the reconstruction of 3D tracks from the 2D fluorescence images produced using a fluorescence microscope of the detectors. The old algorithm lacked accuracy when dealing with crowded samples and heavily scattering ions. A new algorithm to connect the fluorescent spots in the 2D images based on intensity, track velocity, track direction, drift and scattering was introduced. Significant improvements in tracking of primary and secondary particles was seen in samples irradiated in the SOBP of a carbon beam. The algorithm was successfully applied to samples irradiated with alpha radiation.

Chapter 4 introduces two novelties: the first application of a fast super-resolution microscopy technique, structured illumination microscopy (SIM), for FNTD read-out, and advanced track analysis of alpha particles with scattering and energy measurement algorithms. Since the depth resolution of the used microscopy techniques has a significant effect on the maximum achievable energy resolution in alpha particle track measurement, SIM was used to measure FNTDs samples at twice the resolution of conventional confocal laser scanning microscopy (CLSM). Both techniques were compared, but no significant increase in energy resolution could be observed. It was theorized that the proposed algorithm for track endpoint determination based on track length and track intensity was sufficient to achieve super-resolution endpoint determination with both techniques. Secondly, the simulated energy distribution used for evaluation of the energy estimation algorithm, most likely underestimated the broadness of the distribution due to the absence of manufacturing errors in the collimators. The alpha track energy resolution limit of the proposed method was therefore estimated between 100 and 200 keV. However, the superior resolution of SIM did show a significant reduction in measured scattering of the alpha tracks. The difference in scattering obtained using SIM versus the numbers obtained from NIST indicates that the current data from NIST might be

overestimating the scattering of alpha particles in Al_2O_3 and that revision of the current cross section (a measure for interaction probability) might be necessary. It also shows the potential for SIM to analyze large quantities of FNTD data for Monte Carlo code validation of (heavy) ion beams.

Chapter 5 explored the application of FNTDs for alpha radiation dosimetry. A novel irradiation setup, build to use commercially available alpha source with large cell cultures, was combined with FNTD technology, to create a setup for alpha radiobiology research. The surface dose rates above the setup were measured using FNTDs and validated using extrapolation chamber measurements. Surface dose rates measured using FNTDs and extrapolation chamber were in agreement for the two different collimator setups. Uncertainties in absorbed alpha radiation dose rates using the FNTD approach (5.9 – 9.0%) were higher than for the extrapolation chamber measurements (3.8%). It is however expected that similar values could be reached with increased sample sizes, removal of the spatial dose dependency and further research on the uncertainties and improvement of surface location detection, track reconstruction, energy estimation, geometry and stopping power ratios involved with FNTD alpha dosimetry. The dose uniformity in larger irradiated areas showed variations of less than 5%, making this setup, in combination with the rich information obtained regarding the spatial, angular and energy distributions of the alpha particles ideal for microdosimetry and radiobiology experiments in large cell cultures (required for statistical significance).

Chapter 6 built upon chapter 5 by investigating the localized energy deposition of alpha irradiated U87 glioblastoma cells. The nucleus dose spectra of monolayers above the irradiation setup were experimentally estimated using tracks measured with the FNTDs and 3D images of cell geometries. This method for experimental alpha dosimetry is a first of its kind and can have many applications in radiobiology experiments, taking advantage of the known dose rate, LET, angular direction of the tracks and the nucleus dose spectra in cells to better quantify, for example, RBE, OER and DNA damage and repair factors. The experimentally determined (microdosimetry) survival parameters were used to predict the effect of localized energy deposition on the survival of cells in spheroids, a model for small tumors or metastases. While the number of publications on this subject is relatively large, studies evaluating these effects could not be found at the time of writing. The simulations showed that the contribution of localized energy deposition to the survival for various alpha radionuclide carrier distributions (e.g. on the nuclear membrane or in the cytoplasm), was only significant for carriers located in and on the cell nucleus. RBE, OER, cell cycle and pharmacokinetic factors are expected to trump the effects of localized energy deposition when it comes to cell killing efficacy for carriers located in the cytoplasm and on the cellular membrane in modern studies. On the other, the pronounced effect of localized energy deposition for carriers located in and on the nucleus might indicate that internalized carriers will have an edge in tumor kill efficiency compared to tissues complications in tissues where the carrier is not internalized.

Chapter 7 delved into the pharmacokinetics and dosimetry of currently available 225Ac radionuclide carriers that utilize different mechanisms to minimize healthy tissue exposure. A model for the kinetics of free radionuclides was presented. The goal was to analyze the effects of circulation time and the retention of daughter radionuclides via recoil retention and internalization in cells on tumor and healthy tissue exposure. It was found that while retention of the daughter radionuclides was generally preferred, radionuclide carriers that suffer from high aspecific uptake can benefit from some loss of daughter radionuclides. Internalization of the carriers greatly benefit both the tumor and normal tissue exposure as was expected. It was shown that the kidneys are the critical organ for most carriers, with the exception of nanovesicles carriers with long circulation time for which the exposure of the red bone marrow was the most critical. While the presented model did give insight in the various mechanisms involved in alpha radionuclide therapy, it was also concluded that the currently available data regarding the (long-term) pharmacokinetics and biostability of radionuclide carriers, as well as the kinetics of internalized free radionuclides, is currently (severely) lacking. Since the analyses showed the importance of free circulating radionuclides for normal tissue exposure and maximum injectable doses, more research regarding these topics is paramount before 225Ac radionuclide carriers can be safely applied in the clinic.

The FNTD has proven to be a very versatile tool for alpha radiation research. Methods for tracking, spectroscopy, dosimetry and microdosimetry using individual particles were developed with success. However, an investigation of previously published work on alpha radionuclide carriers showed that a lot of work is yet to be done before therapy based on alpha radiation can face widespread adoption in the clinic.

Samenvatting en vooruitzicht

Alfa-radionuclidentherapie biedt potentie voor de effectieve behandeling van uitzaaiingen. (Pre-klinisch) onderzoek van alfastraling voor therapie lijdt echter aan een gebrek aan geschikte hulpmiddelen voor de spectroscopie, (micro-) dosimetrie en radiobiologie van alfastraling. In dit werk werden methoden voor de toepassing van fluorescent nuclear track detectors (FNTD, fluorescentie nucleaire sporen detectoren) voor alfastraling ontwikkeld en geverifieerd, om zo een betaalbaar en veelzijdig hulpmiddel voor onderzoek naar alfastraling te creëren.

Hoofdstuk 2 vatte de huidige stand van de FNTD-technologie samen. In dit hoofdstuk is zichtbaar geworden dat er aanzienlijke vooruitgang is geboekt bij de toepassing van deze detectoren voor gamma-, proton- en zware ionenstraling. Het feit dat deze detectoren individuele sporen op een sub-micronschaal kunnen visualiseren maakt gelijktijdige spectroscopie en dosimetrie van verschillende bundels mogelijk. Een nieuw ontwikkelde techniek maakte het mogelijk om cellen op FNTD's te kweken, om op die manier schade aan, en reparatie van, het DNA in levende cellen te relateren aan sporen gemeten in de FNTD's. Deze nieuwe ontwikkelingen kunnen een belangrijke rol gaan spelen in toekomstig onderzoek naar de mechanieken betrokken bij schadevorming en reparatie in DNA.

Hoofdstuk 3 beschreef in detail de eerste stap van de analyse van sporen in FNTD's: de reconstructie van sporen in 3D met behulp van de 2D fluorescentieafbeeldingen geproduceerd door een fluorescentiemicroscoop. Het oude algoritme was niet nauwkeurigheid genoeg voor detectoren met een hoge spoordichtheid en/of sterk verstrooiende ionen. Een nieuw algoritme dat de fluorescente spots in de 2D-beelden verbindt op basis van intensiteit, snelheid, richting en verstrooiing werd daarom geïntroduceerd. Significante verbeteringen in de reconstructie van sporen van primaire en secundaire deeltjes kon worden waargenomen in FNTD's bestraald in de zogenaamde spread-out Bragg peak (SOBP) van koolstofionenbundels. Het algoritme kon met succes worden toegepast voor FNTD's bestraald met alfastraling.

Hoofdstuk 4 introduceert twee noviteiten: de eerste poging om een snelle superresolutie microscopietechniek genaamd structured illumination microscopy (SIM) te gebruiken voor de uitlezing van FNTD's, en een nieuwe methode voor geavanceerde spooranalyse van alfadeeltjes met algoritmen voor het meten van de verstrooiing en energie van alfadeeltjes in FNTD's. De resultaten werden vergeleken met metingen gedaan met de conventionele manier van FNTD uitlezen: confocal laser scanning microscopy (CLSM). Ondanks de hogere resolutie van SIM, kon er geen significante toename in energieresolutie worden waargenomen. De hypothese hiervoor is dat het gepresenteerde algoritme voor de bepaling van het eindpunt van sporen in de FNTD's voldoende was om ook met de conventionele non-superresolutie microscoop het eindpunt van sporen zeer nauwkeurig te bepalen. Daarnaast onderschatte de gesimuleerde energieverdeling die werd gebruikt voor de evaluatie van het algoritme hoogstwaarschijnlijk de breedte van de distributie omdat mogelijke fabricagefouten in de collimators niet waren

meegenomen in de simulaties. De daadwerkelijke onzekerheid in de gemeten energie van individuele sporen via de voorgestelde methode werd geschat tussen de 100 en 200 keV. De superieure resolutie van SIM resulteerde echter in een significante vermindering in gemeten verstrooiing van de alfa-sporen. Het verschil in verstrooiing verkregen met behulp van SIM vergeleken met de getallen gepubliceerd door het NIST geeft aan dat de huidige gegevens van het NIST mogelijk de verstrooiing van alfadeeltjes in Al_2O_3 overschat. Dit is een indicatie dat herziening van de huidige interactiedoorsneden (een maat voor interactiekans) nodig zou kunnen zijn. De snelle uitlezen en hoge resolutie van SIM kan, in combinatie met FNTD's, in de toekomst gebruikt worden voor de validatie van Monte Carlo-codes van (zware) ionenbundels.

Hoofdstuk 5 onderzocht de toepassing van FNTD's voor alfadosimetrie. Een nieuwe bestralingsopstelling, ontwikkeld om commercieel verkrijgbare alfabronnen te kunnen gebruiken voor grote celculturen, werd gecombineerd met FNTD-technologie om een opstelling te creëren voor radiobiologisch onderzoek. Het oppervlaktedosistempo boven de opstelling werd gemeten met behulp van FNTD's en gevalideerd via extrapolatiekamermetingen. Oppervlaktedosistempo's gemeten met behulp van de FNTD's en de extrapolatiekamer waren in overeenstemming voor de twee verschillende collimatoropstellingen. Onzekerheden in de geabsorbeerde alfadosistempo's voor de FNTD methode (5,9 – 9,0%) waren hoger dan voor de extrapolatiekamermetingen (3,8%). Naar verwachting kunnen vergelijkbare waarden worden bereikt met meer metingen, vermindering van de plaatsafhankelijkheid van het dosistempo, verder onderzoek naar de onzekerheden, verbetering van detectie van het oppervlak van de FNTD's en meer data voor de spoorreconstructie, energieschatting, opstellingsgeometrie en energieverliezen voor alfadeeltjes die zijn betrokken bij FNTD-alfadosimetrie. De uniformiteit van de dosis in grote bestraalde gebieden vertoonde variaties van minder dan 5%, waarmee deze opstelling, in combinatie met de grote hoeveelheid informatie verkregen over de ruimtelijke, hoek- en energieverdelingen van de alfadeeltjes, ideaal voor microdosimetrie en radiobiologie-experimenten in grote celculturen.

Hoofdstuk 6 bouwde voort op hoofdstuk 5 door de effecten van gelokaliseerde energiedepositie van alfadeeltjes op de overleving van U87-glioblastomacellen te onderzoeken. De celkerndosisdistributies van monolagen boven de bestralingsopstelling werden experimenteel geschat met behulp van sporen gemeten met de FNTD's en 3D-beelden van celgeometrieën. Deze methode voor experimentele alfadosimetrie is nieuw en kan vele toepassingen hebben in radiobiologie-experimenten, gebruikmakend van dosistempo, LET, hoekrichting van de sporen en celkerndosisdistributies om bijvoorbeeld RBE-, OER- en DNA-schade en reparatiefactoren beter te kwantificeren. De experimenteel bepaalde (microdosimetrie-)overlevingsparameters werden gebruikt om de effecten van gelokaliseerde energiedepositie van alfadeeltjes op de overleving van cellen in sferoïden (een model voor kleine tumoren of metastasen) te voorspellen. Hoewel het aantal publicaties over dit

onderwerp relatief groot is, konden er maar weinig studies gevonden worden die deze effecten evalueren. De simulaties toonden aan dat de bijdrage van de celkerndosisdistributie aan de overleving voor verschillende spatiele distributies van alfa-radionuclidedragers (bijvoorbeeld op het kernmembraan of in het cytoplasma) alleen significant was voor dragers die zich in en rondom de celkern bevinden. RBE, OER, celcyclus en farmacokinetische factoren zullen naar verwachting de effecten van gelokaliseerde energiedepositie overschaduwen als het gaat om de effectiviteit van celdoding voor dragers die zich in het cytoplasma en op het celmembraan bevinden. Anderzijds kunnen de uitgesproken effecten van gelokaliseerde energiedepositie voor in en op de kern gelegen dragers erop wijzen dat geïnternaliseerde dragers een voordeel hebben. De hogere celdoding zal dan enkel voorkomen in weefsel waar de drager internaliseert, wat betekend dat gezond weefsel mogelijk zo gespaard kan worden.

Hoofdstuk 7 ging dieper in op de farmacokinetiek en dosimetrie van de momenteel beschikbare 225Ac-radionuclidedragers, welke gebruikmaken van verschillende mechanismen om blootstelling aan gezonde weefsels te minimaliseren. Een model voor de kinetiek van vrije radionucliden werd gepresenteerd. Het doel was om de effecten van circulatietijd en het behoud van dochterradionucliden op de geabsorbeerde dosis in de tumor en gezond weefsel te analyseren. Uit deze analyse bleek dat, terwijl retentie van de dochter radionucliden in het algemeen de voorkeur heeft, radionuclidedragers die lijden aan een hoge aspecifieke opname in organen kunnen profiteren van enig verlies van dochterradionucliden. Zoals verwacht komt de internalisatie van radionuclidedragers ten goede aan de bestraling van de tumor als zowel de blootstelling van gezond weefsel. Ook werd aangetoond dat de nieren het kritieke orgaan zijn voor de meeste radionuclidedragers. De uitzondering hierop waren nanodeeltjes met lange circulatietijd. Voor deze deeltjes was de blootstelling van het beenmerg het meest kritisch. Hoewel het gepresenteerde model goed inzicht gaf in de verschillende mechanismen die betrokken zijn bij alfa-radionuclidetherapie, werd ook geconcludeerd dat de momenteel beschikbare gegevens over de farmacokinetiek en biostabiliteit van radionuclidendragers, evenals de kinetiek van geïnternaliseerde vrije radionucliden, flink beperkt zijn. Gezien deze analyse het belang aantoonde van vrij circulerende radionucliden voor normale weefselblootstelling en maximale injecteerbare doses, is meer onderzoek met betrekking tot deze onderwerpen van cruciaal belang alvorens 225Ac-radionuclidendragers veilig in de kliniek kunnen worden toegepast.

Ter conclusie. Het is bewezen dat de FNTD een zeer veelzijdig hulpmiddel is voor alfastralingsonderzoek. Methoden voor de reconstructie van alfasporen in FNTD's en voor spectroscopie, dosimetrie en microdosimetrie met behulp van individuele alfadeeltjes zijn gepresenteerd in dit werk. Een onderzoek naar eerder gepubliceerd werk met alfa-radionuclidedragers heeft echter aangetoond dat er nog veel werk moet worden verzet alvorens therapie met behulp van alfastraling veilig kan worden toegepast in de kliniek.

Addendum

List of common abbreviations

List of publications

List of presentations

PhD portfolio

Dankwoord

LIST OF COMMON ABBREVIATIONS

225Ac	Actinium-225
APD	Avalanche Photo Diode
CLSM	Confocal Laser Scanning Microscopy
DNA	DeoxyriboNucleic Acid
DSB	Double Strand Break
EC	Extrapolation Chamber
EPR	Enhanced Permeability and Retention effect
FHWM	Full Width Half Maximum
FIJI	Fiji Is Just ImageJ (software)
FNTD	Fluorescent Nuclear Track Detector
HCP	Hexagonal Close Packing
HEPES	(4-(2-hydroxyethyl)-1-piperazineethanesulfonic acid)
LET	Linear Energy Transfer
NDD	Nucleus Dose Distribution
OSLD	Optically Stimulated Luminescence Dosimeter
PLA	PolyLactic Acid
PNTD	Plastic Nuclear Track Detector
PSI	Power Spectrum Integral
PSMA	Prostate-Specific Membrane Antigen
RBE	Relative Biological Effectiveness
SIM	Structured Illumination Microscopy
SNR	Signal to Noise Ratio
SOBP	Spread Out Bragg Peak
SRB	Sulforhodamine B
SHNDD	Single Hit Nucleus Dose Distribution
TLD	ThermoLuminescence Dosimeter

LIST OF PUBLICATIONS

J. J. M. Kouwenberg, L. Ulrich, O. Jäkel, and S. Greilich, "A 3D feature point tracking method for ion radiation", *Physics in Medicine and Biology*, vol. 61, no. 11, pp. 4088–4104, 2016.

S. Greilich, J. Jansen, M. K. Grischa, J. J. M. Kouwenberg, A. Neuholz, T. Pfeiler, S. Rahmanian, A. Stadler, and L. Ulrich, "Dosimetry for ion-beam therapy using fluorescent nuclear track detectors and an automated reader", pp. 1–36, 2017, arXiv:1610.05054.

J.J.M. Kouwenberg, G.J. Kremers, J.A. Slotman, H.T. Wolterbeek, A.B. Houtsmuller, A.G. Denkova, A.J.J. Bos, "Alpha particle spectroscopy using FNTD and SIM super-resolution microscopy", *Journal of Microscopy,* 2018. doi:10.1111/jmi.12686.

J. J. M. Kouwenberg, H. T. Wolterbeek, A. G. Denkova, and A. J. J. Bos, "Fluorescent Nuclear Track Detectors for Alpha Radiation Microdosimetry", 2018. (*Accepted at Radiation Oncology*)

J. J. M. Kouwenberg, J. A. de Pooter, H. T. Wolterbeek, A. G. Denkova, and A. J. J. Bos, "Alpha Radiation Dosimetry using Fluorescent Nuclear Track Detectors,", *Radiation Measurements*, vol. 113, no. June, pp. 25-32, 2018.

M. A. Akselrod, J. J. M. Kouwenberg, "Fluorescent Nuclear Track Detectors – review of past, present and future of the technology", 2018. (Accepted under conditions at *Radiation Measurement*)

R. M. de Kruijff, A. van der Meer, A. G. Denkova, C. Windmeijer, F. Bruchertseifer, J. J. M. Kouwenberg, A. Morgenstern and P. Sminia, "Biodistribution and therapeutic efficacy of 225Ac loaded polymersomes in 2D and 3D in vitro glioma models", E*uropean Journal of Pharmaceutics and Biopharmaceutics*, vol. 127, no. June, pp. 85-91, 2018.

LIST OF CONFERENCE PRESENTATIONS

Talk: "Alpha Microdosimetry using novel Fluorescent Nuclear Track Detectors", 17th International Symposium on Microdosimetry, Venice, Italy (October, 2017)

Talk: "SIM Super-Resolution Microscopy for individual Alpha Particle Track Measurement using FNTD", 27th International Conference on Nuclear Tracks and Radiation Measurements, Strasbourg, France (August 2017)

Talk: "Experimental Alpha Microdosimetry using Fluorescent Nuclear Track Detectors", 10th International Symposium on Targeted Alpha Therapy, Kanazawa, Japan (May 2017)

Poster: "Individual Alpha Particle Measurement using FNTD and SIM Super-Resolution Microscopy", 10th International Symposium on Targeted Alpha Therapy, Kanazawa, Japan (May 2017)

PHD PORTFOLIO

Name PhD student:	Jasper J. M. Kouwenberg
Department:	Applied Radiation & Isotopes, Radiation Science & Technology, TU Delft
Research School:	TU Delft Graduate School
Contract period:	July 2015 – February 2018
Promotor:	Prof. Dr. H. T. Wolterbeek
Copromotors:	Dr. ir. A. G. Denkova
	Dr. A. J. J. Bos
Project funding:	Technologiestichting STW, project number 13577

Graduate school

Transferrable skills

Course	GS credits
C9.M4: How-to keep motivated after your GO? Regain your flow!	1
T1.A9: Scientific text processing with LaTeX	1
T1.B5: Managing the academic publication review process	1
T2.D1: Leadership, teamwork and group dynamics	1.5
T4.B3: Time Management II - Self-management to the max	1
T4.G4: Career Development - Looking for Work in the Netherlands	1
T4.G6: Career Development - Preparing for a company	1
R1.A3: Making an impact with Open Science	2
R2.B2: Speedreading and Mindmapping	1.5
Japanese I (Leiden University)	4
Total:	15

Discipline related skills

Course	GS credits
Basic FLUKA course, Pohang Accelerator Laboratory (2017)	5
CUDA programming course, University of Oxford (2017)	5
ESTRO Basic Radiobiology, Paris (2017)	5
Total:	15

Learning-on-the-job activities

Course	GS credits
Addressing a major international audience	2 x 1
Addressing a small audience	1 x 0.5
BSc/MSc students supervision	6
First journal article	4
Poster presentation, major audience	1 x 1
Teaching assistance: designing examination assignments	2 x 1
Total:	15.5

DANKWOORD

Allereerst gaat mijn voornaamste dankzegging naar Dr. Ir. Antonia Denkova. In januari 2013 verdedigde ik mijn bachelor thesis al onder jou, en hoewel jij het waarschijnlijk niet wil horen, heb ik altijd tegen jou op gekeken. Bedankt voor de begeleiding, discussies en de vrijheid die jij mij gaf. Ik heb erg genoten van werken met jou, en ik zal dat dan ook het meeste gaan missen wanneer ik het RID verlaat.

Ik ben Dr. Adrie (Bos) zeer dankbaar voor zijn begeleiding. U heeft mij gestuurd om de puntjes op de i te zetten en het geheel naar een hoger niveau te brengen. Ondanks dat ik tijdens onze discussie misschien wat eigenwijs en koppig kon zijn, hoop ik dat u weet dat ik uw advies altijd ten harte heb genomen.

Mijn dank gaat uit naar Prof. Dr. Bert Wolterbeek voor zijn begeleiding en adviezen tijdens dit werk. Hoewel het gros van onze conversaties die mij bij zijn gebleven over alles gingen behalve onderzoek, zal ik nooit uw volgende wijsheid vergeten: "Een goed wetenschappers trekt soms zijn schoenen uit en legt zijn voeten op tafel, om zo eens goed na te kunnen denken over zijn werk." (vrije verwoording).

De vliegende start van dit proefschrift zou niet hebben bestaan zonder de onschatbare hulp van Dr. Steffen Greilich en zijn team aan het Deutsches Krebsforschungszentrum (DKFZ). Mijn dank gaat uit naar Julia en Shirin voor het op weg helpen met de FNTD's, en in het bijzonder naar Leonie Ulrich, met wie ik samen het tracking algoritme heb ontwikkeld. Ik heb een enorm gave tijd gehad in Heidelberg, en dank daarom ook mijn vrienden Christiaan, Alexander, Kathrin, Raya, Yanick hartelijk voor hun warmte en gastvrijheid. In het speciaal wil ik Nina bedanken. Ik hoop dat wij nog lang vrienden zullen blijven en elkaar kunnen blijven steunen tijdens de minder leuke perioden van academisch onderzoek.

Ik wil Dr. Mark Akselrod bedanken voor het delen van zijn kennis tijdens het project en het gezamenlijk schrijven van hoofdstuk 2. Mijn dank gaat ook uit naar de partners binnen het STW project voor hun participatie en hun donaties van materialen.

Gezien de sterke focus op de natuurkunde in dit proefschrift, was het fijn soms op de harde feiten omtrent de complexiteit van de biologie te worden gedrukt door Dr. Jeroen Essers, Dr. Dick van Gent en Stefan Roobol, MSc. Ik dank jullie voor jullie bereidheid jullie kennis te delen en ik heb genoten van ons samenwerken binnen het project.

Voornamelijk hoofdstuk 4 was niet mogelijk geweest zonder de expertise en inzet van Dr. Gert-Jan Kremers, Dr. Johan Slotman en Prof. Dr. Adriaan Houtsmuller. Ik blijf mij erover verbazen. Jullie vertelden mij dat jullie eens SIM hadden getest voor de uitlezing van FNTD's, en dat het

al vrij snel werkte. Alles alsof het niets was. Ik ben jullie veel verontschuldigd voor het initiatief dat jullie hebben genomen en ik ben trots dat wij dit mooie werk hebben kunnen publiceren.

Mijn dank gaat uit naar Dr. Jacco de Pooter, Ing. Bartel Jansen, Dr. Leon de Prez en Dr. Marc Pieksma voor hun gastvrijheid en onmisbare bijdrage aan het werk in hoofdstuf 5. Ik heb diep respect voor jullie kennis, expertise en oog voor detail. Zonder jullie was een groot deel van dit werk niet bestaan.

Ik wil in het bijzonder Ing. Marcel Schouwenburg bedanken voor zijn luisterend oor. Meerdere keren ben ik enthousiast jouw kamer binnengerend met theorieën over de wiskunde van celkerndosisdistributie. Jouw luisterend oor, expertise, en met name geduld, heb ik zeer gewaardeerd.

Voor hun hulp bij de begeleiding van studenten en werk in het lab ben ik Ing. Adrie Laan, Ing. Baukje Terpstra, Folkert Geurink en, met name, Ing. Astrid van der Meer zeer dankbaar. Zonder jullie zou ARI niet zijn wat het is.

Ik wil de SBD bedanken voor hun, soms ondankbare, taak van het veilig houden van de werkomgeving. Voornamelijk Koos van Kammen en Henk van Doorn wil bedanken voor de erg leuke tijd die ik met jullie heb mogen meemaken aan het RID. Jullie zijn topgasten!

Ir. Coen Windmeijer, Ing. Sanne Treep, Ing. Olivier Nijhout, Ing. Ewout van Laarhoven, ik heb erg genoten van onze projecten samen. Ik dank jullie hartelijk voor het plezier en het vertrouwen dat jullie hadden in mij. Ik wens jullie veel succes in de toekomst.

Ik heb ook kunnen genieten van de goede sfeer die er heerst op de afdeling applied radiation & isotopes, en ik ben dat ik blij hiervan deel uitgemaakt te mogen hebben. In het bijzonder wil ik mijn (ex-)kamergenoten Ir. Robin de Kruijff en Dr. Eelco Lens bedanken. Jullie hebben mij soms op mijn slechts meegemaakt. Ik ben dankbaar voor onze vriendschap.

Als laatste wil ik mijn familie en vrienden bedanken. Ik ben erg dankbaar voor de hechte familie die ik heb ontvangen, alsook de vele vrienden die ik vaak al meer dan 20 jaar ken. Ik vermoed dat voor velen van jullie deze dissertatie de eerste keer is dat jullie iets lezen/horen over de inhoud van mijn onderzoek, gezien ik promoveren altijd simpelweg gezien heb als een baan. Iets waar je je voor inzet, zoals jullie dat allen doen. Ik heb een diep respect voor jullie. Jullie maken mij tot wie ik ben.

Fluorescent Nuclear Track Detectors for Alpha Particle Measurement

Jasper Johannes Marcellianus KOUWENBERG